UNIVERSITY OF CALIFORNIA SAN DIEGO

High-Strength Steel Reinforcement in Critical Regions of Earthquake-Resistant Bridges

A dissertation submitted in partial satisfaction of the requirements for the degree of Doctor of Philosophy

in

Structural Engineering

by

Koorosh Hossein Lotfizadeh

Committee in charge:

Professor José I. Restrepo, Chair
Professor Joel P. Conte
Professor John McCartney
Professor David Sandwell
Professor P. Benson Shing

2019

The Dissertation of Koorosh Hossein Lotfizadeh is approved, and it is acceptable in quality and form for publication on microfilm and electronically:

Chair

University of California San Diego

2019

DEDICATION

To my mother, Fatemeh,

whose encouragement and support made this possible.

EPIGRAPH

We cannot solve our problems with the same thinking we used when we created them.

Albert Einstein

TABLE OF CONTENTS

LIST OF SYMBOLS

a	Reinforcing bar rib height
α	Linear factor for computation of L_p
A_g	Cross-section gross area
β	Angle of transverse reinforcing bar rib relative to longitudinal direction; Linear factor for computation of L_p, equivalent yield penetration term; Shear retention factor (Chapter 3)
c	Thickness of concrete cover above top of pile longitudinal reinforcement
c_1, c_2	Menegotto-Pinto constitutive steel model parameters
c_{ts}	Tension stiffening parameter
d_b	Reinforcing bar diameter
d_e	Measured external reinforcing bar diameter (top of rib)
d_{EN}, d_{ES}	Relative displacement measured by potentiometers on the north and south side of the east face of the column
d_{WN}, d_{WS}	Relative displacement measured by potentiometers on the north and south side of the west face of the column
d_{CR}	Distance between centers of rotation in buckled reinforcement
d_{POI}	Distance between points of inflection in buckled reinforcement
δ	Distance between north and south potentiometer sets; Standard deviation (Chapter 5)
D_c	Column diameter
D_i	Stiffness modulus for smeared formulation in mode i
Δ	Displacement measured at top of column
Δ_c	Displacement measured at top of column at each displacement ductility level by string potentiometers

Δ_{cf}	Displacement measured at top of column due to column flexure
Δ_{cs}	Displacement measured at top of column due to pile shaft flexure and shear displacements
Δ_{FE}	Displacement measured at top of column due to fixed-end rotation
Δ_{Slip}	Measured slip at top of bar
Δ_{y}	Displacement at first yield
$\Delta\varepsilon_{t-c}$	Smeared strain amplitude, $\varepsilon_{st} - \varepsilon_{sc}$
$\Delta\varepsilon_{vK}$	von Karman strain amplitude, $\varepsilon_{st} - \varepsilon_{vK}$
ε_0	Strain at zero-stress state following the maximum reversal in tension
ε_c	Extreme compressed fiber strain
ε_{E-C}	Strain at onset of buckling (Engesser- Considère strain)
ε_h	Strain measured in column transverse hoop
ε_{kv}	Strain in fiber in the concave side of the critical section of the buckled shape
ε_{kx}	Strain in fiber in the convex side of the critical section of the buckled shape
ε_{amp}	Strain amplitude, difference between extreme tensile and compressive strains
ε_{max}	Extreme tensile strain
ε_{min}	Extreme compressive strain
ε_{nbe}	Maximum strain measured by strain gage near the embedded bar end
ε_s	Strain measured at top of bar at each slip
ε_{sc}	Maximum smeared strain in compression
ε_{sh}	Strain at the onset of strain-hardening
ε_{st}	Smeared strain demand in tension

ε_{su}	Measured strain at ultimate strength
ε_{sue}	Expected strain at ultimate strength
ε_u^R	Reduced uniform strain as defined in Caltrans SDC 2.0
ε_{vK}	Strain at which peak compressive strain is reached (von Karman strain)
ε_y	Steel reinforcement yield strain
ε_{yh}	Hoop transverse reinforcement yield strain
ε_N, ε_S	Average smeared strains within each deformation panel in the north and south side of the column
F_i	Ideal lateral force accounting for P-Delta effect
F_y	Reinforcing bar yield force
f_c'	Concrete compressive strength
f_{cs}	Concrete splitting (tensile) strength
f_R	Relative rib ratio of reinforcing bar
f_{Rm}	Measured relative rib ratio of reinforcing bar
f_U	Concrete unloading factor controlling crack closure stiffness
f_y	Steel reinforcement measured yield strength
f_{ye}	Steel reinforcement expected yield strength
$f_{s4\%}$	Steel reinforcement stress at 4% strain
f_{su}	Steel reinforcement measured ultimate strength
f_{sue}	Steel reinforcement expected ultimate strength
φ_i	Curvature obtained from deformation panel at level i
φ_y	Column yield curvature
ϕ_k	Peak curvature at cracking

$\bar{\phi}$	Smeared curvature
G	Elastic shear modulus
G_c	Effective shear stiffness
G_{fc}	Concrete compressive fracture energy
G_{ft}	Concrete tensile fracture energy
h	Incremental height along column
H_c	Column shear span (column height)
ℓ	Unsupported length of reinforcing bar
ℓ_d	Tension development length of reinforcing bar
$\ell_{d,SDC}$	Required tension development length of reinforcing bar as prescribed in SDC 2.0
$\ell_{d,ACI}$	Required tension development length of reinforcing bar as prescribed in ACI 318-19
ℓ_e	Embedment length of reinforcing bar
λ	Modification factor accounting for lightweight or normal-weight concrete (ACI 318-19)
λ_{CR}	Ratio between strain amplitude in concave side, and smeared strain amplitude between centers of rotation in a buckled bar
L	Column height
L_{ac}	Development length of column longitudinal reinforcement into bent cap
L_i	Gage length of deformation panel at level i
L_{nbe}	Length from top of bar to strain gage near the embedded bar end
L_P	Analytical plastic hinge length
$L_{P\varepsilon}$	Smeared strain compatible equivalent plastic hinge length
L_{Pi}	Assumed smeared height of the column plastic hinge

L_{Py}	Strain penetration length
L_{req}	Required development length of column longitudinal reinforcement into bent cap
L_{ep}	Equivalent strain penetration depth
L_{yp}	Yield penetration length
M	Column section bending moment
M_{cr}	Column section cracking moment
M_i	Ideal moment, moment capacity computed with simplified flexure theory and using measured material properties
M_y	Column section bending moment at first yield
$2N_f$	Number of reversals to failure
n_{bar}	Number of longitudinal reinforcing bars in column cage
Ω_{fac}	Bauschinger effect shape factor
P	Strain-hardening exponent
ρ_l	Longitudinal reinforcement ratio
ρ_s	Volumetric reinforcement ratio (Chapter 5)
ρ_v	Volumetric reinforcement ratio
R	Menegotto-Pinto model parameter for Bauschinger effect
s	Spacing between column transverse reinforcement; Longitudinal spacing of the reinforcing bar ribs
s_F	Concrete shear factor
S_R	Clear spacing between bar deformations
T/Y	Tensile to yield strength ratio
θ_{FE}	Angle of rotation from fixed-end rotation

μ	Mean value
μ_Δ	Displacement ductility level
ν	Poisson's ratio
W_{ft}	Total dissipated energy
w_d	Critical compression displacement parameter
Ψ_e	Modification factor for epoxy-coated or zinc and epoxy dual-coated reinforcement (ACI 318-19)
Ψ_{eyp}	Equivalent strain penetration term
Ψ_g	Modification factor for reinforcement grade (ACI 318-19)
Ψ_t	Modification factor accounting for casting position (ACI 318-19)
Ø	Outer diameter measurement

LIST OF FIGURES

LIST OF TABLES

ACKNOWLEDGMENTS

First and foremost, I would like to thank Professor Restrepo for his incredible mentorship. His guidance, advice, and support over the years has taught me not only to be a better researcher and engineer, but also to be a better and more well-rounded individual.

I would like to express my deepest gratitude to my fellow graduate students: Dr. Rodrigo Carreño, Dr. Arpit Nema, Ricardo Bustamante, and Valentina Vásquez to name a few. Their encouragement, help, and support, technical and otherwise, is sincerely appreciated and will never be forgotten.

I would like to especially thank Han-Mei Chen for her patience, constant support, and encouragement throughout the years, and standing by my side through some of the most challenging of times.

Many thanks to the Powell lab staff: Dr. Chris Latham, Messrs. Darren McKay, Michael Sanders, Noah Aldrich, Abdullah Hamid, and Andrew Sander for their invaluable help and advice during the many experimental parts of my research.

Also, I would like to thank the SE department staff, especially Lindsay Walton, who always went above and beyond and out of her way to help with everything, and always checking to make sure I was doing alright and had everything I needed.

Funding for the research work presented here was supplied by the California Department of Transportation (Caltrans), contract number 65A0562. I am grateful for their financial support. Technical input from Dr. Charles Sikorsky and Mr. Issam Noureddine is also greatly appreciated.

All Grade 80 reinforcement used in the experiments were donated by Nucor Steel Seattle and Gerdau Rancho Cucamonga, with special thanks to Messrs. Erik Nissen, Matthew Heath, and Michael Mayer for their continuous help and support with procurement of reinforcing bars. I would also like to thank Mr. Christian Dahl at Headed Reinforcement Corp. (HRC) for providing the friction-welded headers for some of the test specimens, and Mr. Jesus Osuna who assisted with the experimental work in the laboratory.

Finally, I want to thank the members of my committee for the time they dedicated and their valuable contribution to define the objectives for this dissertation.

Chapter 2, in part, is currently being prepared for submission for publication of the material. Lotfizadeh, Koorosh H.; Restrepo, José I. The dissertation author was the primary investigator and author of this material.

Chapter 3, in part, is currently being prepared for submission for publication of the material. Lotfizadeh, Koorosh H.; Vásquez, Valentina A.; Restrepo, José I. The dissertation author was the primary investigator and author of this material.

Chapter 4, in part, is currently being prepared for submission for publication of the material. Lotfizadeh, Koorosh H.; Bustamante, Ricardo; Restrepo, José I. The dissertation author was the primary investigator and author of this material.

Chapter 5, in part, is currently being prepared for submission for publication of the material. Lotfizadeh, Koorosh H.; Carreño, Rodrigo; Restrepo, José I. The dissertation author was the primary investigator and author of this material.

VITA

2011	Bachelor of Science in Structural Engineering.
	University of California, San Diego
2012	Master of Science in Structural Engineering
	University of California, San Diego
2013	Structural Engineer
	Black & Veatch, Overland Park, Kansas
2014-2019	Teaching Assistant, Department of Structural Engineering.
	University of California, San Diego
2016-2019	Graduate Student Researcher
	University of California, San Diego
2019	Doctor of Philosophy in Structural Engineering
	University of California, San Diego

PUBLICATIONS

Carreño, R., **Lotfizadeh, K.**, Conte, J. P., & Restrepo, J. I. (accepted for publication). Material Model Parameters for the Giuffrè-Menegotto-Pinto Uniaxial Steel Stress-Strain Model.

Lotfizadeh, K., Restrepo, J. I. (in-preparation). Yield Penetration of Large Diameter Bars in Confined Concrete

Lotfizadeh, K., Vásquez, V., Restrepo, J. I. (in-preparation). Development of Large Diameter Grade 80 Reinforcement in Enlarged Bridge Column Pile Shafts.

Lotfizadeh, K., Bustamante, R., Restrepo, J. I. (in-preparation). High-Strength Grade 80 Reinforcement in Bridge Column-Bent Cap Connections.

Lotfizadeh, K., Carreño, R., R., Restrepo, J. I. (in-preparation). Plastic Buckling-Straightening Fatigue of High-Strength Grade 80 Reinforcement.

Carreño, R., **Lotfizadeh, K.**, Conte, J. P., & Restrepo, J. I. (in-preparation). Implementation of Improved Dodd-Restrepo Constitutive Stress-strain relationship.

ABSTRACT OF THE DISSERTATION

High-Strength Steel Reinforcement in Critical
Regions of Earthquake-Resistant Bridges

by

Koorosh Hossein Lotfizadeh

Doctor of Philosophy in Structural Engineering

University of California San Diego, 2019

Professor José I. Restrepo, Chair

Large diameter bars are often used in large civil infrastructure projects such as bridges, power stations, large mat footings, and are occasionally used as reinforcement in buildings where the use of smaller size reinforcement would cause excessive congestion.

The use of high-strength Grade 80 reinforcement can reduce the number of bars required in construction, likely reducing congestion, thereby reducing construction time. Current design guidelines only allow the use of A706 Grade 60 reinforcing bars in seismic critical members (SCMs), while allowing the use of straight A706 Grade 80 bars only in capacity protected members. The use of high-strength large-diameter bars in SCMs requires experimental validation since extrapolation of current prescriptive requirements for Grade 60 reinforcement cannot always be deemed satisfactory or appropriate. The research work presented herein comprises of a comprehensive investigation, which addresses, at the bar, bar-to-concrete, and at the component levels, the main areas of research needed to implement the use of ASTM A706 Grade 80 high-strength reinforcement into bridge seismic design practice, and presents findings from proof-of-concept experiments in support of this implementation.

This dissertation presents an experimental and analytical investigation to characterize the response of large-diameter ASTM A706 Grade 80 reinforcement embedded in confined concrete, replicating the boundary conditions of bars developed into extended shafts, bent caps, and footings. The equivalent strain penetration term for this type of reinforcement, which is used to calculate the analytical plastic hinge length of columns, is determined and recommendations are provided to more closely represent experimentally measured results.

The proof-of-concept experiments supporting the implementation of high-strength Grade 80 reinforcement in future design codes consist of a full-scale bridge column extending into an enlarged Type II pile shaft, and a ¾-scale exterior column of a multi-

column bent cap connection, both reinforced entirely with ASTM A706 Grade 80 bars. Findings from these experiments are used to calibrate and validate detailed finite element models which can be used to aid future bridge design practice.

At the bar level, to characterize the buckling behavior, post-buckling fracture mechanism, and cyclic fatigue life of large-diameter Grade 80 reinforcing bars, a set of experiments were performed on both commonly available ASTM A706 Grade 80 bars and newly developed Grade 80 bars with a more smoothed-rib-radius. An extensive finite element study is also conducted to develop a simplified equation for design to prevent premature plastic buckling and subsequent fracture of column longitudinal reinforcement.

Chapter 1.

INTRODUCTION

1.1. Motivation

Since 2009, the American Society for Testing and Materials (ASTM) has incorporated Grade 80 reinforcement in the A706 specification. As is the case in countries with high seismicity such as Japan and New Zealand, interest in using higher strength reinforcements in construction has been increasing over the years. Currently, AASHTO LRFD Specifications[1] allows the use of ASTM A706 Grade 80 and even ASTM A1035 Grade 100 reinforcing bars in capacity protected members, where plastic hinging will not develop. There is a knowledge-gap that exists regarding the cyclic response, low-cycle fatigue, post-buckling fatigue life, and the tensile development characteristics of high-strength Grade 80 and 100 reinforcement. Due to this knowledge-gap, the use of these higher-strength reinforcing bars in regions of structures where plastic hinges develop during seismic events is still prohibited. With more research and investigation into the

mechanical properties, prediction of crack widths, and anchorage characteristics of high-strength reinforcement such as A706 Grade 80, the availability and usage of these reinforcing bars is expected to increase significantly. As the seismic performance of higher-strength reinforcement is detailed in regions of plasticity is better understood, ASTM A706 Grade 80 reinforcement could eventually supersede A706 Grade 60 bars, similar to how using Grade 60 reinforcement replaced Grade 40 in the 1950s. Incorporation of Grade 80 reinforcement rather than the currently widely used Grade 60, requires a comprehensive analytical and experimental investigation.

1.2. Background

The use of Grade 75 bars as transverse reinforcement for shear, and Grade 115 bars for confinement and to provide resistance against buckling of longitudinal bars has been allowed by the New Zealand Standard since 1995[2]. In 2006, New Zealand allowed the use of nominally Grade 80 longitudinal reinforcement in critical elements where plastic hinges were expected to develop[3]. In Japan, high-strength reinforcement has been used as longitudinal and transverse reinforcement in building columns for over ten years[4]. Both New Zealand and Japan are countries with high seismicity, and expectedly have stringent requirements for seismic design of buildings and bridges.

In 2013, NIST[5] recommended in a report that ASTM A706 Grade 80 reinforcement could be used, with minor changes in codes like ACI 318, as longitudinal reinforcement in critical elements of structures where plastic hinging is expected to occur. The report recommended a number of changes to the ACI 318 building code and also highlighted a few areas requiring further research. These findings, along with the

knowledge gained from the extensive experimental and analytical work by Trejo et al.[6] in 2014 on half-scale bridge columns reinforced with A706 Grade 80 bars, suggest with confidence that ASTM A706 Grade 80 reinforcement could be incorporated into critical elements of bridges in California. In the context of bridge seismic design in California, the main areas of research are in the low-cycle fatigue life of large diameter bars, on the development length of bars subjected to cyclic loading, and on the expected material stress-strain characteristics and overstrength needed to capacity protect other regions and elements in the structure.

Most bridge design in California relies on ductility at selected regions in bridges to survive a rare but strong intensity earthquake, for which probabilistic and deterministic criteria is given. This ductility is often achieved through the development of plastic hinges in columns, which are capacity designed to ensure that the desired mechanism of inelastic deformation can develop and be maintained throughout a strong intensity earthquake. Current design recommendations have proven satisfactory through experiments conducted on bridge columns in recent studies.

In 2010, a full-scale reinforced concrete bridge column designed in accordance with Caltrans SDC 1.6[7] was tested at the Large High-Performance Outdoor Shake Table (LHPOST) of the University of California at San Diego. Progressively increasing intensity ground motions were applied, and the response of the column was closely monitored. The column clearly developed a plastic hinge at its base when subjected to a ground motion corresponding to the design earthquake[8]. As the column experienced nearly 5% drift ratio (displacement ductility of approximately 4), axial strains in the longitudinal reinforcement

at the base of the column reached 3% in tension and 1.5% in compression. Although concrete spalling occurred in the plastic hinge region, strains measured in the hoops barely exceeded yielding, and no longitudinal bar buckling was observed. Subsequently, a stronger than the design earthquake ground motion was imposed on the test column, inducing a drift ratio of 7.8% at the top. Axial strains in the longitudinal reinforcement at the base of the column reached 4.7% in tension, and 1.6% in compression, and the hoops experienced a tensile strain of 2.5%. The onset of longitudinal bar buckling was observed during this test. With further higher-intensity ground motion testing, a significant number of longitudinal bars fractured. Buckling prior to fracture had occurred along two sets of hoops, and cracks developed on the concave (compressed) face of the buckled bars, which ultimately led to fracture with no signs of necking. Cracking at the root of bar deformations occur in the plastic hinges that develop in the buckled region of the bar. The failure mode observed in this test suggests that the deformation capacity of bridge columns designed in accordance with Caltrans SDC 1.6[7], may ultimately be limited by bar fracture following buckling.

The differential movement of the hot-rolled steel core and the outer-most part of the bar during manufacturing, induces tensile strains and small defects on the bar surface, a phenomenon known as “wiping”. It is believed that the tensile stresses and small defects induced on reinforcing bars due to this phenomenon shorten the low-cycle fatigue life of buckled bars and cause the development of compressive cracks, which propagate and ultimately lead to bar fracture upon buckling. Since the relative velocity between the hot-rolled steel core and the outer surface is greater in larger diameter bars during

manufacturing, the defects induced by wiping may be more prevalent in larger diameter bars. The phenomena of wiping and its effects on the low-cycle fatigue life of longitudinal bars that buckle should be well understood for higher strength reinforcement such as Grade 80, and in particular, for large diameter bars that are commonly specified as longitudinal reinforcement in bridge columns where plastic hinging is expected to occur during the design earthquake loading. The incorporation of Grade 80 large diameter reinforcement in seismic critical members in design guidelines such as Caltrans SDC requires that the mechanical and low-cycle fatigue characteristics of this reinforcement to be well established and validated through experimental investigations.

Furthermore, the significant catastrophic consequences of bar pullout failures, such as that observed during the 1971 San Fernando earthquake, has heightened the importance of research into assessing whether the current tensile development length requirements set forth by AASHTO LRFD Specifications[1] is directly applicable to high-strength reinforcement or if some modification is necessary.

1.3. Objectives and Scope

The research work presented herein comprises of a comprehensive investigation, which addresses, at the bar, bar-to-concrete, and at the component levels, the main areas of research needed to implement the use of ASTM A706 Grade 80 high-strength reinforcement into bridge seismic design practice, and presents findings from proof-of-concept experiments in support of this implementation.

Initially, the yield penetration, bond strength, and cyclic bond-slip behavior of large diameter ASTM A706 Grade 80 reinforcement embedded in confined concrete is

investigated. Murcia-Delso et al.[9] was the first to investigate the cyclic bond-slip of large diameter bars (#11, #14, and #18), and determine the minimum embedment length required for ASTM A706 Grade 60 column longitudinal reinforcement extending into a Type II pile shaft, and the transverse reinforcement required in the bar anchorage regions of these shafts. To date, no research has been conducted to establish the yield penetration and bond strength of high-strength large diameter ASTM A706 Grade 80 bars (#14 and #18) embedded in confined concrete. By means of an experimental and analytical study, the yield penetration of these bars was studied, and a revised expression for approximating the analytical plastic hinge length of columns extending into Type II pile shafts is recommended for design engineers.

A full-scale bridge column extending into a Type II pile shaft reinforced entirely with ASTM A706 Grade 80 reinforcement was built and quasi-statically tested applying reversed cyclic loading. The column longitudinal reinforcing bars were embedded in the pile shaft at a reduced length based on findings from earlier experimental work by Murcia-Delso et al. regarding columns reinforced with A706 Grade 60 bars. Results from this experiment, along with newly calibrated bond-slip models from the earlier experimentation, were used to develop a nonlinear finite element model. This adds knowledge to the limited existing literature of testing, which is comprised of only half-scale column specimens.

To date no seismic testing has been reported on integral column-bent cap connections entirely reinforced with Grade 80 reinforcement. Implementation in practice of reinforcement type in California requires experimental evidence showing that critical

parts of bridges such as integral column-bent cap connections perform adequately during, and exceeding, the design earthquake. The use of high-strength Grade 80 reinforcement in bridge column-bent cap connections is ideal since it has been found that the reinforcement ratios in the column and bent caps are rather high when designed with Grade 60 reinforcement. A ¾-scale integral column-bent cap connection representing an exterior column of a multi-column bent and reinforced entirely with ASTM A706 Grade 80 bars is tested. An exterior column of a multi-column bent was selected for this research due to the variable axial load applied on the column during cyclic testing.

Characterizing the buckling and subsequent fracture mechanism of high-strength reinforcement is critical in determining the suitability of using such reinforcement in seismic critical members. The plastic buckling-straightening fatigue life, commonly referred to as low-cycle fatigue, of large diameter ASTM A706 Grade 80 reinforcement is investigated through an extensive series of cyclic tests. Although exhaustive experimental and analytical research has been conducted on Grade 60 large-diameter bars in the past, no such research is available for higher-strength reinforcement, in particular Grade 80. Furthermore, adapting the finite element analysis framework, originally developed by Carreño et al.[10], to consider Grade 80 reinforcement, the influence of transverse reinforcement in the post-buckling response of longitudinal reinforcement of ordinary bridge columns is characterized and recommendations for design are proposed.

1.4. Outline of the Dissertation

This section provides a brief overview of the six chapters included in this dissertation:

- Chapter 1: Introduction

  This chapter includes the motivation, background, objectives and scope of the research work, including an outline of the content in the dissertation

- Chapter 2: Strain Penetration of High-Strength Large Diameter Bars

  This chapter presents the experimental and analytical research conducted on ASTM A706 Grade 80 large-diameter (#14 and #18) reinforcing bars, to investigate the bond-slip behavior and determine the yield penetration of these bars in confined concrete of different strengths. The specimen design, test setup, experimental test results, and a recommendation for the equivalent yield penetration is provided in this chapter.

- Chapter 3: Development of Large Diameter Grade 80 Reinforcement in Enlarged Bridge Column Pile Shafts

  Results from a full-scale bridge column extending into a Type II pile shaft reinforced entirely with ASTM A706 Grade 80 bars is presented in this chapter. The column longitudinal reinforcement is embedded in the pile shaft at a reduced length than that required by current design codes. Findings from this experiment are used in conjunction with newly

determined bond-slip relationships (from Chapter 2) to calibrate a detailed finite element model. A brief summary of the parametric study performed to calibrate the finite element model is also presented.

- Chapter 4: High-Strength Grade 80 Reinforcement in Bridge Column-Bent Cap Connections

  Experimental findings from a first-of-its-kind ¾-scale integral column-bent cap connection entirely reinforced with Grade 80 bars is presented in this chapter. To date no seismic testing has been reported on integral column-bent cap connections reinforced with Grade 80 reinforcement. An exterior column of a multi-column bent cap connection, with varying axial load, is tested to determine the suitability of using Grade 80 reinforcement in such members, which would ultimately reduce congestion within the heavily reinforced column-bent cap connection. The specimen design, test setup, and experimental results are presented in this chapter.

- Chapter 5: Plastic Buckling-Straightening Fatigue of High Strength Grade 80 Reinforcement

  This chapter describes the experimental research conducted on large-diameter ASTM A706 Grade 80 reinforcement to characterize the buckling behavior, post-buckling fracture mechanism, and cyclic fatigue life of large diameter high-strength reinforcing bars. Reinforcement manufactured with

a more smoothed-rib-radii are tested along with commonly available bars manufactured per current ASTM requirements, to compare their cyclic fatigue life. Description of the test apparatus, test preparation and setup, and findings from this extensive set of experiments are presented in this chapter. Adaptation of the finite element analysis framework by Carreño et al. for Grade 80 reinforcement, and the extensive finite element study performed to develop a simplified equation for design preventing premature plastic buckling and subsequent fracture of column longitudinal reinforcement is presented.

- Chapter 6: Conclusions

  A description of the main findings and conclusions from this research, as well as suggestions for future work are presented in this chapter.

Chapter 2.

STRAIN PENETRATION OF HIGH-STRENGTH LARGE DIAMETER BARS

2.1. Abstract

The Department of Transportation of California funded a large experimental work to validate the use of higher-grade reinforcement, such as Grade 80 reinforcement, in large civil infrastructure projects. A task within this project was to characterize the response of large-diameter ASTM A706 Grade 80 bars embedded in confined concrete, thus replicating the boundary conditions of bars developed into extended shafts, bent caps, and footings. A direct outcome of this study is the determination of the equivalent strain-penetration term for this reinforcement type, which is used in the calculation of the analytical plastic hinge length of columns. This chapter describes experimental test setup, procedure, and presents the main findings, conclusions and recommendations derived from this task.

2.2. Introduction

The last decade has seen a push by industry and code committees to provide prescriptive requirements for the use of Grade 80 and 100 reinforcement in construction of reinforced concrete structures in the United States[11]. To achieve this objective, a significant amount of research was carried out to determine the adequacy of the high-grade reinforcement for use in seismic systems[12]–[20], paralleling the comprehensive effort done in Japan in the 1990s[4], where high-grade reinforcement has widespread use nowadays. The recently issued ACI 318-19 building code[21] allows the use of Grades 80 and 100 reinforcement manufactured to ASTM A706 as longitudinal reinforcement in special seismic systems. The new edition of the Caltrans Seismic Design Code, SDC 2.0[22], only allows the use of straight A706 Grade 80 bars in seismic critical members (SCM) only in capacity protected members.

Most of the research carried out thus far on the high-grade reinforcement has focused on small and medium bar sizes. Large diameter bars are often used in the construction of large civil infrastructure projects such as bridges, power stations, large mat footings, where the use of smaller size reinforcement would cause excessive congestion. The use of high-strength large-diameter bars in SCMs requires experimental validation since extrapolation of current prescriptive requirements for Grade 60 reinforcement should not always be deemed appropriate. For example, the development length of large diameter bars could exhibit a size effect. Furthermore, the plastic hinge length often used to calculate the displacement capacity of bridge columns has a term that represents the strain

penetration (Caltrans SDC 2.0 §5.3.4[22]). This term is a function of the expected yield strength of the reinforcement.

Shake table tests of full-scale reinforced concrete bridge columns subjected to large lateral displacements have shown that longitudinal bars tend to buckle and then fracture after attaining a tensile strain of approximately 4 to 5% in the plastic hinges[8]. The longitudinal reinforcement at the column ends needs to be properly developed to sustain these levels of strains. In California, such reinforcement is typically developed as straight bars into well-confined concrete in the bent-caps, extended shafts, and footings. The California Department of Transportation (Caltrans) funded a research program into the seismic performance of bridge columns built incorporating ASTM A706 Grade 80 reinforcement. This paper presents the findings from one of the tasks set out to investigate the development of large diameter bars embedded in confined concrete representing the confinement typically used in the design of bridge columns in California and the corresponding strain penetration of these bars. These variables were studied through the cyclic push-pull testing of four full scale test specimens, built with different combinations of reinforcing bar size and concrete strength. This chapter discusses the experimental test setup, procedure, findings, and presents the main conclusions and recommendations from the tests.

2.3. Research Significance

The use of high strength large diameter reinforcement will likely become the predominant reinforcement in future construction of reinforced concrete buildings in the

United States. This reinforcement may reduce congestion in bridge construction, large mat footings, and other civil infrastructure projects where specials seismic systems are used, thereby reducing construction time. This investigation provides an insight on the development and strain penetration of ASTM A706 Grade 80 large diameter reinforcing bars with straight embedment in confined concrete.

2.4. Experimental Investigation Test Program

Four specimens were built at full-scale to investigate the strain penetration and bar development of large diameter A706 Grade 80 reinforcement embedded in well-confined concrete, see Figure 2.1. Each test specimen consisted of a 3 ft (0.9 m) diameter by 7 ft (2.1 m) high column and a 3'-4" (1 m) by 4'-4½" (1.3 m) by 3' (0.9 m) high footing, cast in the upright orientation. All test specimens were identically reinforced except for a centrally embedded #14 (43 mm) or #18 (57 mm) bar, which was a test variable, and had a cage of 8 #11 (36 mm) ASTM A706 Grade 80 longitudinal bars and #5 (16 mm) ASTM A706 hoops spaced at 5 in. (127 mm) and providing a volumetric confining ratio of $\rho_v = 0.79\%$. Two of the test specimens were built with specified 5000 psi (34.5 MPa) concrete compressive strength whereas the other two were built with 8000 psi (55.2 MPa) concrete.

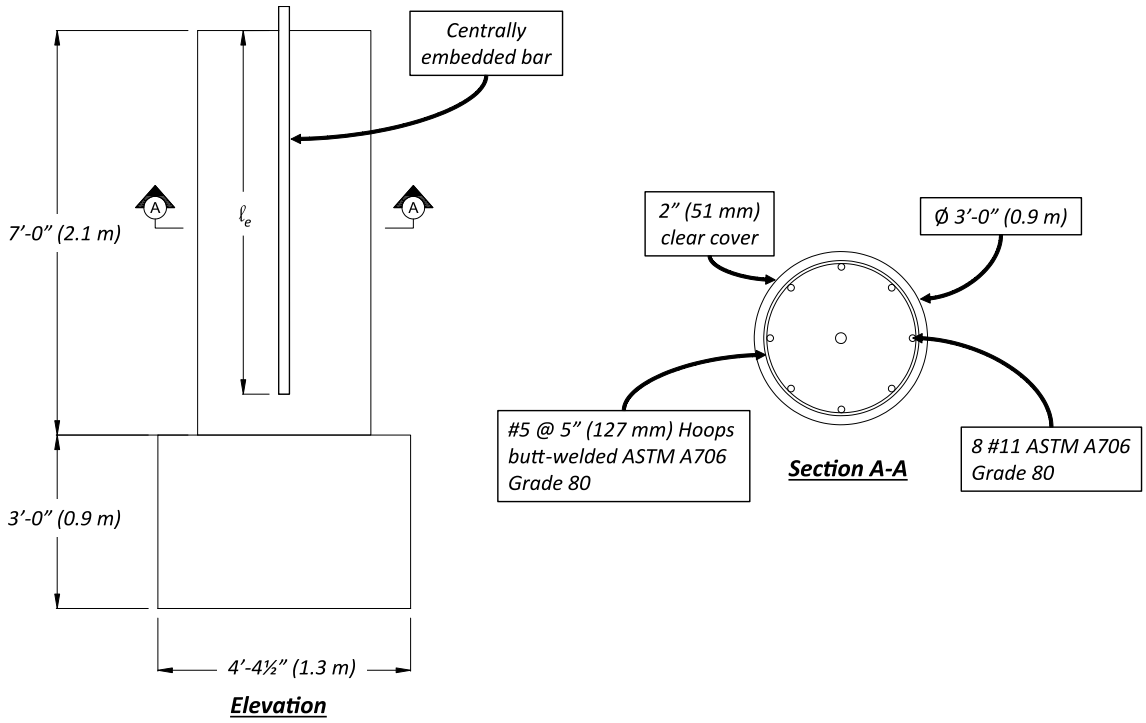

Figure 2.1: Test Specimen Design, Elevation and Plan View

Three monotonic tensile tests were performed on sample bars from the same heat as the test bars to obtain their mechanical properties. Testing was performed in accordance with ASTM A370-17[23] and ASTM E8-16a[24] using a closed-loop active hydraulic SATEC universal testing machine (UTM). Strains were measured using a 2 in. (51 mm) gage length high-precision extensometer positioned at the center of the bar. Dividing the forces recorded from the UTM by the nominal cross-section area of the bar, stresses were obtained. The complete monotonic stress-strain responses of the bars were recorded and are presented in Figures 2.2 and 2.3.

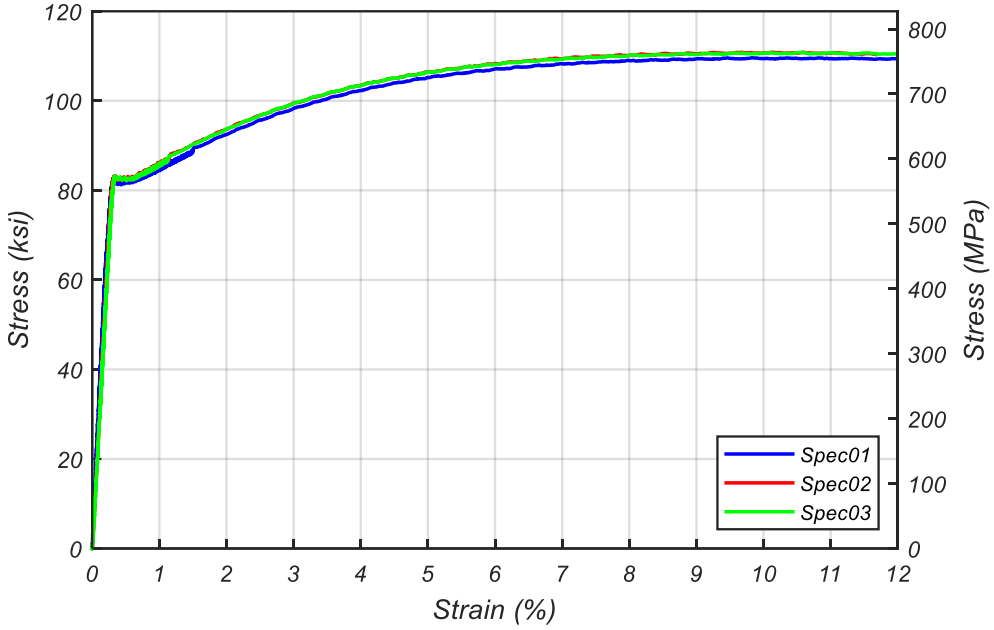

Figure 2.2. Monotonic Stress-Strain Response of ASTM A706 Grade 80 #18 Bars

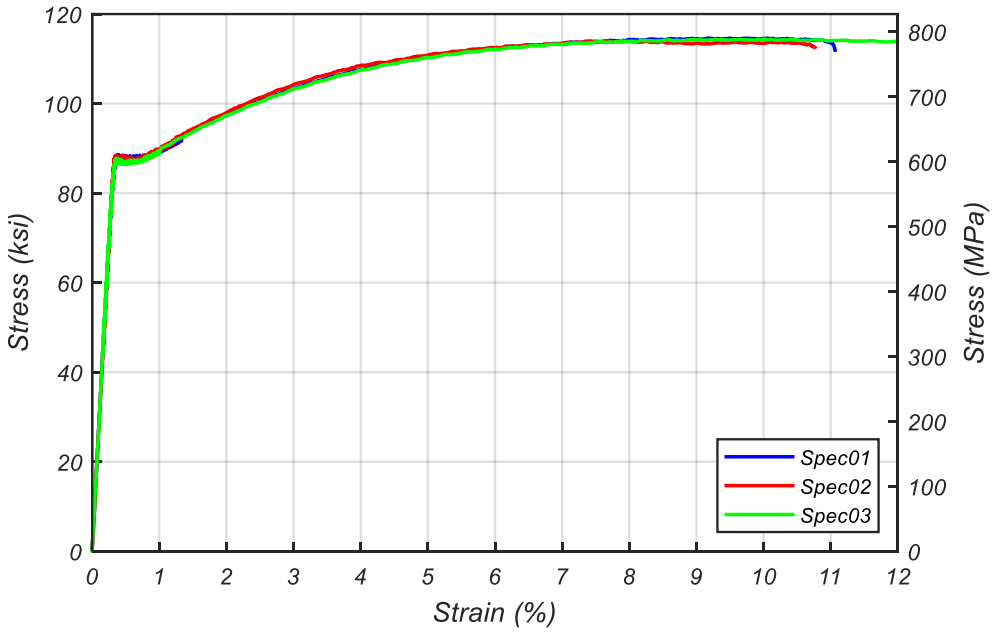

Figure 2.3. Monotonic Stress-Strain Response of ASTM A706 Grade 80 #14 Bars

The hoops were resistance-welded and were tested for adequacy in accordance to California Test 670[25], which provides a step-by-step procedure for cutting and straightening sample specimens from resistance-welded hoops and tensile testing them in the Universal Testing Machine (UTM). The validation procedure involves meticulous measurements, with 1 mil (0.025 mm) precision, of 8 in. (203 mm) and $2d_b$ gage lengths surrounding the weld, both before and after tensile testing, see Figure 2.4. Samples are deemed satisfactory if fracture occurs after bar necking, while the weld remains intact

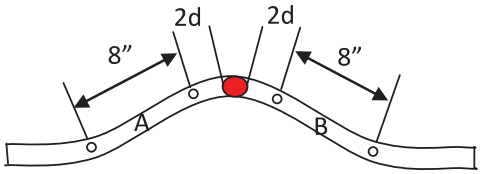

Figure 2.4. California Test 670 Hoop Weld Validation Sample (California Test 670)

Key mechanical properties including the power term, P, obtained from a least-squares optimization between each recorded strain hardening branch and the formulation for the corresponding curve proposed by Mander[26], are listed in Table 2.1.

Table 2.1. Reinforcing Test Bar Material Properties

Bar ID	f_y (ksi) [MPa]	$f_{s4\%}$ (ksi) [MPa]	f_{su} (ksi) [MPa]	ε_y (%)	ε_{sh} (%)	ε_{su} (%)	$\frac{f_{su}}{f_y}$	$\frac{f_{s4\%}}{f_y}$	$\frac{f_{su}-f_y}{f_y}$	P†
#5§	87.8 [605]	-	114.6 [790]	-	-	-	1.31	-	0.31	-
#14	87.3 [602]	107.9 [744]	114.2 [787]	0.31	0.74	9.0	1.31	1.24	0.31	2.84
#18	82.1 [566]	103.0 [710]	110.3 [760]	0.28	0.57	10.3	1.34	1.25	0.34	3.09

§ Information obtained from mill certificate

† Strain-hardening power, found through optimization. from Mander et al. (1983) Eq. 2.6

To obtain the mechanical properties of the concrete in each test specimen, several 6 in. (152 mm) by 12 in. (305 mm) sample cylinders were taken during concrete placement per ASTM C192-18[27]. The sample cylinders were capped using high-strength gypsum cement paste in accordance with ASTM C617-15[28] and tested in sets of three using the UTM per ASTM C39-18[29] throughout the curing process to monitor the compressive strength gain. Strains were measured using a compressometer, and the compressive stresses were calculated by dividing the recorded forces from the UTM by the cross-section area of the sample cylinders. The splitting tensile strength of the concrete was also obtained by performing split-cylinder tests in accordance with ASTM C496-17[30]. Key mechanical properties, such as the concrete compressive strength, f_c', and splitting tensile strength, f_{cs}, are listed in Table 2.2.

Table 2.2. Test Specimen Concrete Material Properties

Specimen	Max. Aggregate Size (in.) [mm]	w/cm Ratio (%)	Age of Concrete at DOT (days)	f_c' (ksi) [MPa]	f_{cs} (ksi) [MPa]
1	1 [25.4]	45	82	5.13 [35.4]	0.41 [2.83]
2	1 [25.4]	45	94	5.42 [37.4]	0.49 [3.38]
3	0.375 [9.5]	34	99	8.45 [58.3]	0.60 [4.14]
4	0.375 [9.5]	34	120	8.90 [61.4]	0.61 [4.21]

Table 2.3 lists the geometric properties for the test bars as defined by Metelli and Plizzari[31] and Table 2.4 lists the proportion of the embedment length provided in each test specimen with respect to that required by AASHTO LRFD Bridge Design Specifications §5.10.8.2[1] and ACI 318-19 §25.4[21], respectively. The embedment length in all four tests were significantly smaller than the development length required by SDC 2.0 and by ACI

318-19, ranging from 56% to 79% of code requirements. One of the goals of this research is the effect of concrete strength on the bond-slip behavior of reinforcing bars embedded in well-confined concrete. Hence, two of the test specimens were built with specified 5000 psi (34.5 MPa) concrete compressive strength whereas the other two were built with 8000 psi (55.2 MPa) concrete. Furthermore, columns with each concrete strength had two different size reinforcing bars centrally embedded, #14 and #18 mimicking the earlier Caltrans funded project reported by Murcia-Delso et al.[32] This arrangement resulted in the test matrix of reinforcing bar sizes and concrete strengths listed in Table 2.4.

Table 2.3. Reinforcing Test Bar Geometric Properties

Bar ID	d_b (in.) [mm]	f_{Rm}	d_e (in.) [mm]	β (degrees)	s (in.) [mm]	a (in.) [mm]
#14	1.693 [43]	0.109	1.779 [45.2]	72	0.967 [24.6]	0.107 [2.7]
#18	2.257 [57]	0.092	2.379 [60.4]	65	1.136 [28.9]	0.104 [2.6]

Table 2.4. Bond-Slip Test Matrix and Properties

		Specimen 1	Specimen 2	Specimen 3	Specimen 4
Specified f'_c (ksi) [MPa]		5 [34.5]	5 [34.5]	8 [55.2]	8 [55.2]
Bar Size		#18	#14	#18	#14
d_b (in.) [mm]		2.26 [57.3]	1.69 [43]	2.26 [57.3]	1.69 [43]
$\frac{\ell_e}{d_b}$		33.6	34.3	33.6	34.3
SDC 2.0‡	$\left(\frac{\ell_d}{d_b}\right)_{SDC}$	55.5	57.1	42.8	45.8
	$\frac{\ell_e}{\ell_{d,SDC}}$ **(%)**	60.5	60.1	78.5	74.9
ACI 318-19†	$\left(\frac{\ell_d}{d_b}\right)_{ACI}$	59.6	59.6	44.7	44.7
	$\frac{\ell_e}{\ell_{d,ACI}}$ **(%)**	56.4	57.6	75.2	76.7

‡ Development length requirements in AASHTO LRFD BDS and SDC 2.0 are identical

† ACI 318-19 Table 25.4.2.3: $\ell_d = \left(\frac{f_y \psi_t \psi_e \psi_g}{20\lambda\sqrt{f'_c}}\right) d_b$

A 500 kip (2224 kN) hydraulic actuator hanging vertically from a steel loading frame was affixed to the exposed end of the centrally embedded reinforcing bar and used to cyclically push and pull the bar until fracture occurred, see Figure 2.5.

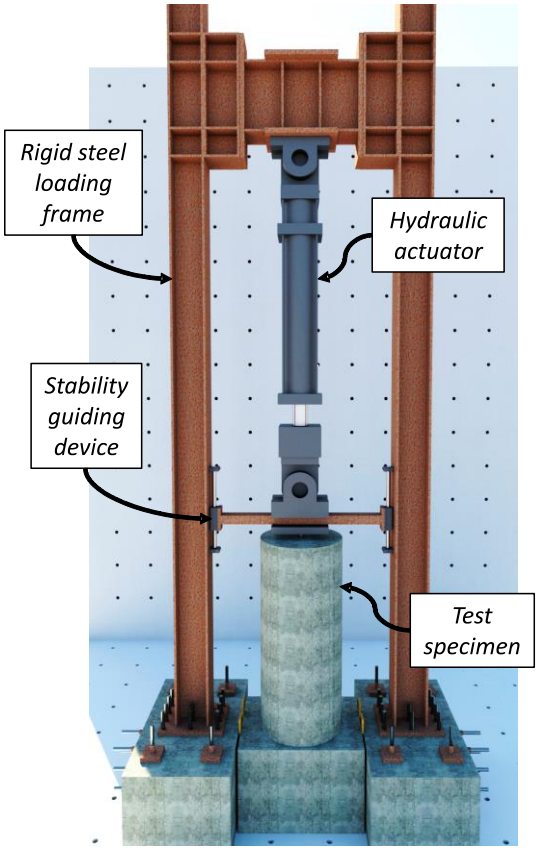

Figure 2.5. 3D Rendering of Test Setup

To connect the bar with the hydraulic actuator, a threaded header was friction-welded to the exposed end of the reinforcing bar, see Figure 2.6. A 3 in. (76 mm) thick, 7 in. (178 mm) diameter round steel nut was sandwiched between two steel plates which were post-tensioned to the moving end of the hydraulic actuator. To prevent lateral instability of the actuator/test bar during the push load cycles resulting in compression in the bars, a guiding frame was incorporated in the loading apparatus. The guiding frame comprised of 3 ft (0.9 m) long 2 in. (51 mm) diameter brushed stainless steel rods mounted along the height of the loading frame on each side, where linear sleeve bearings connected by a concrete-filled 6 in. (152 mm) by 4 in. (102 mm) hollow steel tube attached to the actuator head glide along, see Figure 2.6.

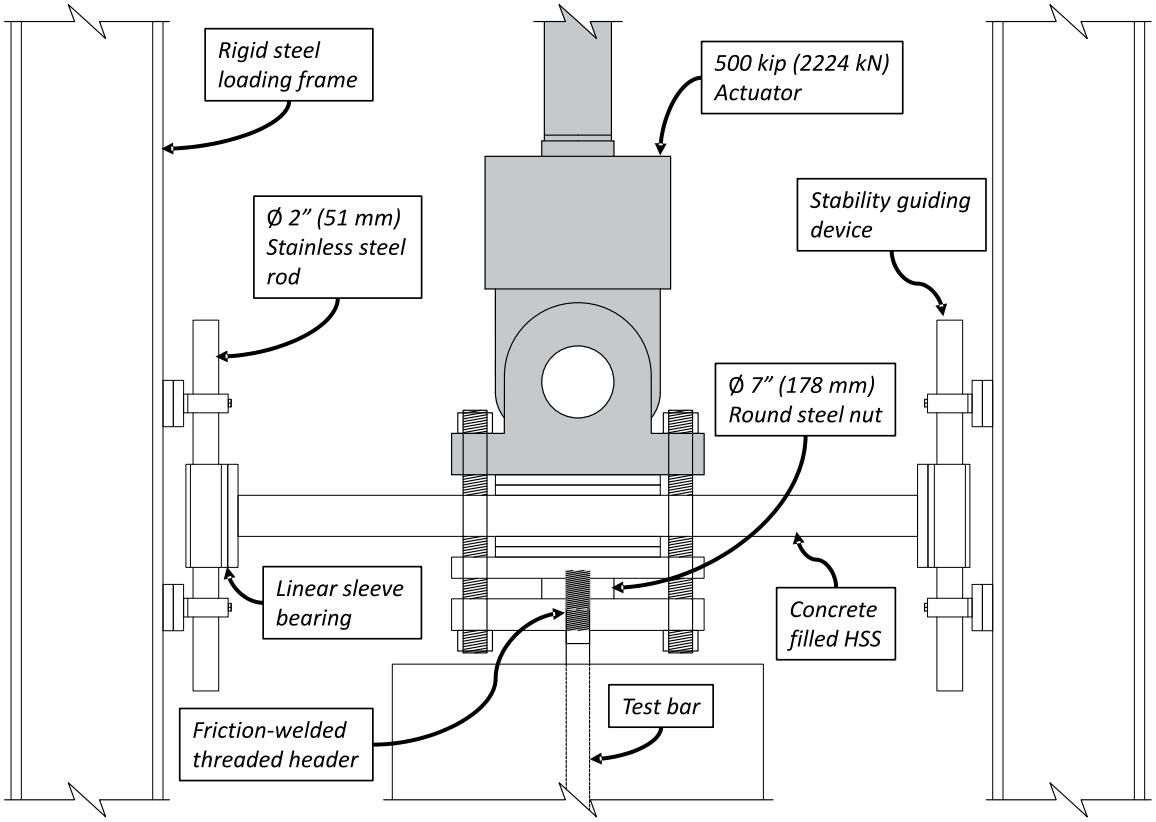

Figure 2.6. Actuator-Test Bar Connection with Stability Guiding Device

The strain in the longitudinal and transverse reinforcement in each of the test specimens was monitored with an array of 0.2 in. (5 mm) 120 Ohm high-elongation electrical-foil strain gages. Particular attention was given to the instrumentation of the test bar, notwithstanding that most of the strain gages in these bars will be mechanically damaged as a result of bond-slip. Although the loss of these strain gages was expected, the decision to carefully instrument the test bar was taken since during the early load cycles, the strain gages provide precise strains. The loss of the strain gages gave a rough indication of the magnitude of the bar bond-slip, where negligible bar bond-slip occurred when the strain gages functioned. Expecting the loss of strain-gages, an innovative approach was

planned and executed to retrieve the peak strains along the length of the bars using diameter measurements after careful extraction of the bars post-test.

After testing, the test units were carefully demolished to expose the centrally embedded test bars. Upon careful extraction of the test bars, all residual concrete dust between the ribs was removed and the bars were cleaned without altering the bar geometry. The diameter of each was measured with a 1 mil (0.025 mm) resolution digital micrometer at various locations along the bar length. Since previous experience with Digital Image Correlation techniques had shown that the strain distribution between the ribs of reinforcing bars is non-uniform, special care was taken to measure the diameter at precisely the same location between the ribs along the length of the bar and obtain residual transverse strains. Figure 2.7 illustrates the measurement location selected. To eliminate measurement bias, the diameter was measured ten times at each location and an average value was obtained. Similarly, to obtain a benchmark, diameters of spare reinforcing bars from the same heat were measured.

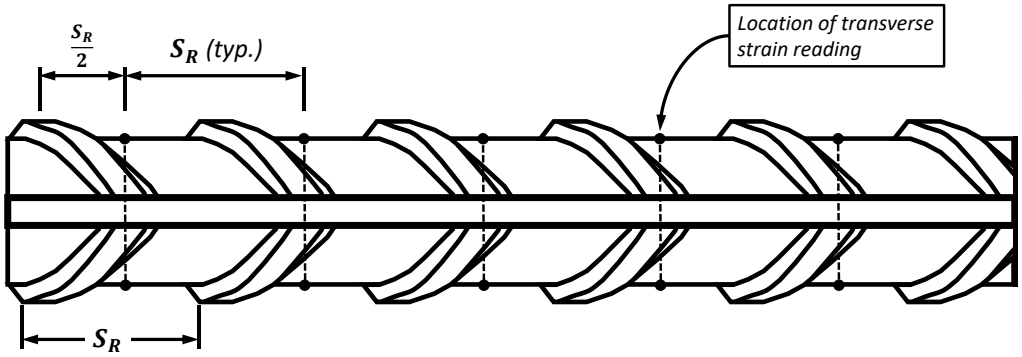

Figure 2.7. Consistent Measurement Location Between Deformations on Bar

These spare reinforcing bars were instrumented with high-elongation electrical-foil strain gages and were tensile-tested in the Universal Testing Machine. The load protocol

for these tests was set up such that the test would pause at a specific load limit to allow for the measurement of the bar diameter at peak strain, then the system would return to a zero-load state allowing for the measurement of the bar diameter at the residual strain limit. This loading scheme and diameter measurement was repeated for peak strain limits of 3%, 5%, 7%, and 9%, see Figure 2.8. After completing the 9% load and unload cycle, the bar was tensioned until fracture.

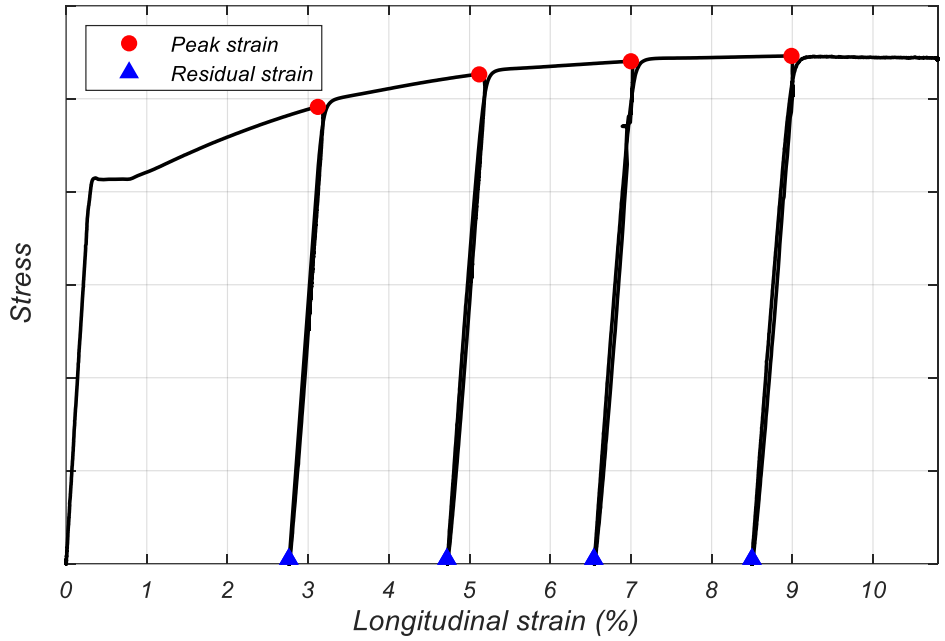

Figure 2.8. Loading Scheme for Virgin Bar Tests

Since the strain gages recorded the residual strain in the bar after each unload cycle, a relationship between the peak and residual longitudinal strains was obtained for each virgin bar test. The observed changes in diameter were converted to transverse strains using the initial virgin bar diameter measurements as a reference and a relationship between the residual transverse and peak longitudinal strain was developed, see Figure 2.9. The measured bar diameters from the post-test extracted bars were also converted to transverse strains. Since these diameter measurements were taken after the test at an unloaded state, the calculated strains obtained represented the residual transverse strains. These residual transverse strains along the length of the post-test bars were then converted to peak longitudinal strains using the strain relationship developed earlier from the virgin bar tensile tests.

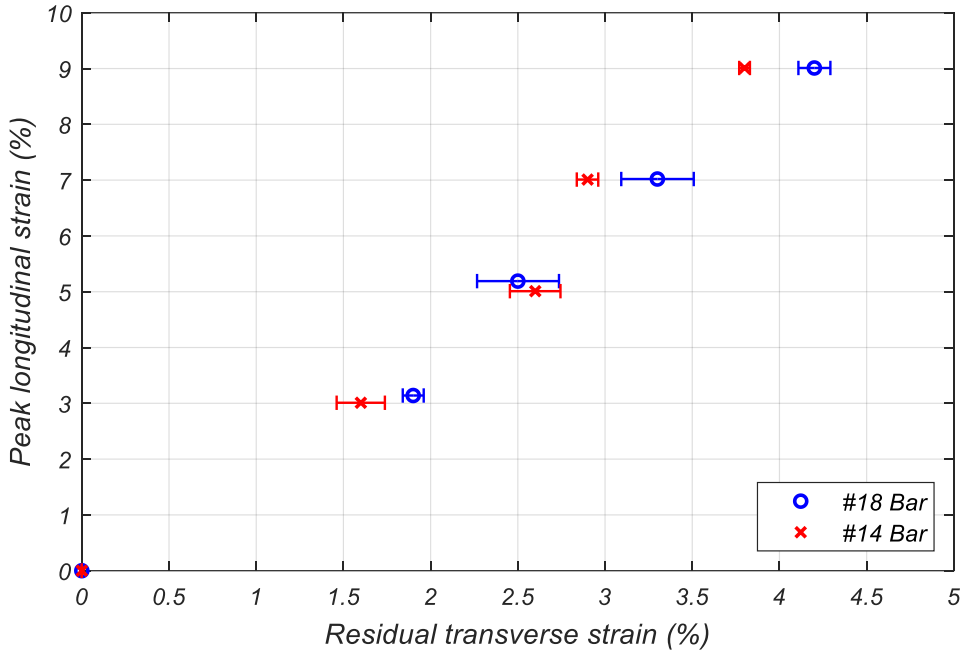

Figure 2.9. Relationship Between Measured Residual Transverse and Peak Longitudinal Strains

Using this innovative approach to obtain peak longitudinal strains along the bar length provides invaluable information previously unavailable regarding the strains exhibited on the bar during testing such as the complete strain profile of the test bar even in regions where strain gages had not survived, see Figure 2.10. As demonstrated in Figure 2.10, the peak longitudinal strains obtained from this approach match closely with the readings from the remaining strain gages. The test results from the specimens are discussed in the following section.

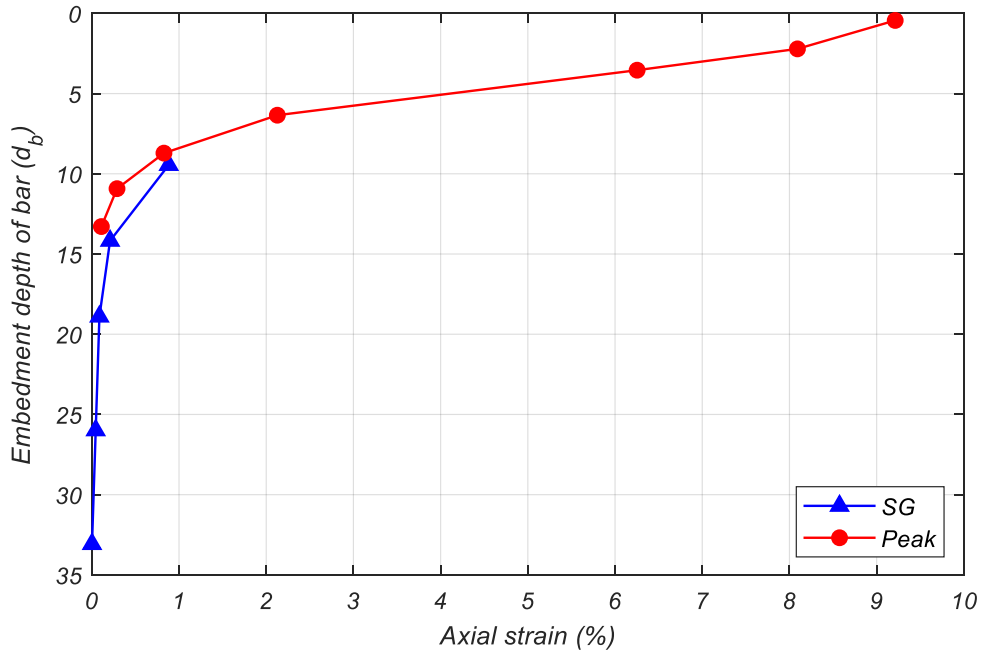

Figure 2.10. Strain Profile of Test Bar Including Measured Peak Strains Post-Test

2.5. Experimental Test Results

The loading protocol was set up such that the compression cycles would only apply 50% of the expected yield force of the bar to prevent unwanted plastic buckling at the anchorage. The tension cycles however were initially force-controlled and incrementally applied as a function of the expected tension yield force until yielding was observed in the bar, then the loading scheme was changed to displacement-controlled for the remainder of the test. The loading protocol used for all tests is shown in Figure 2.11.

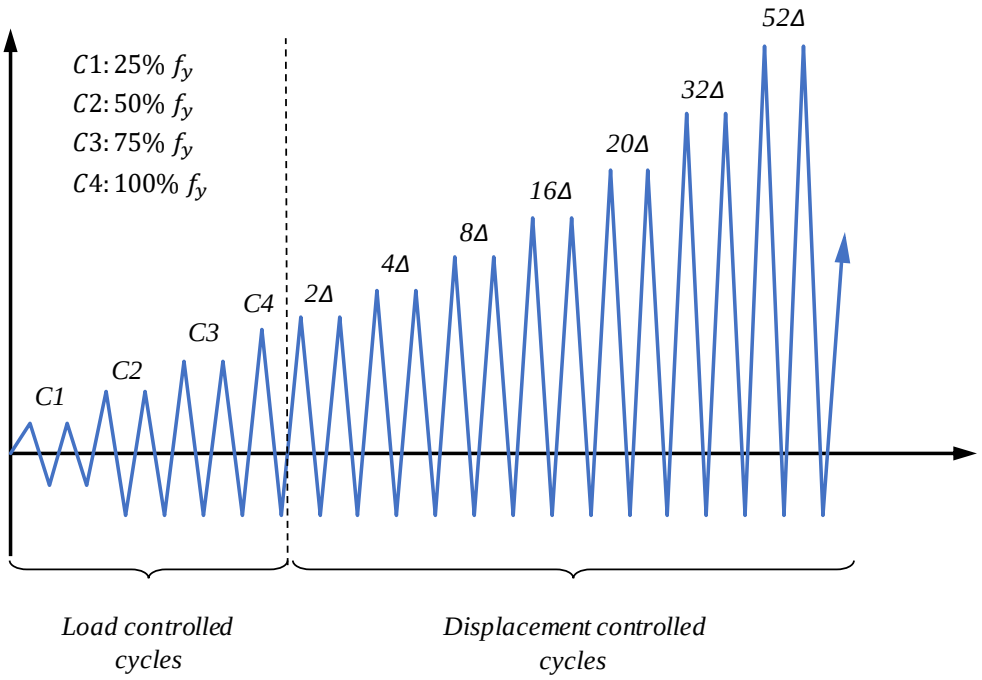

Figure 2.11. General Loading Protocol for All Test Specimens

Test results for all test specimens are presented as bar stress with respect to the slip of the bar measured at the anchorage in Figure 2.12 (a) through (d).

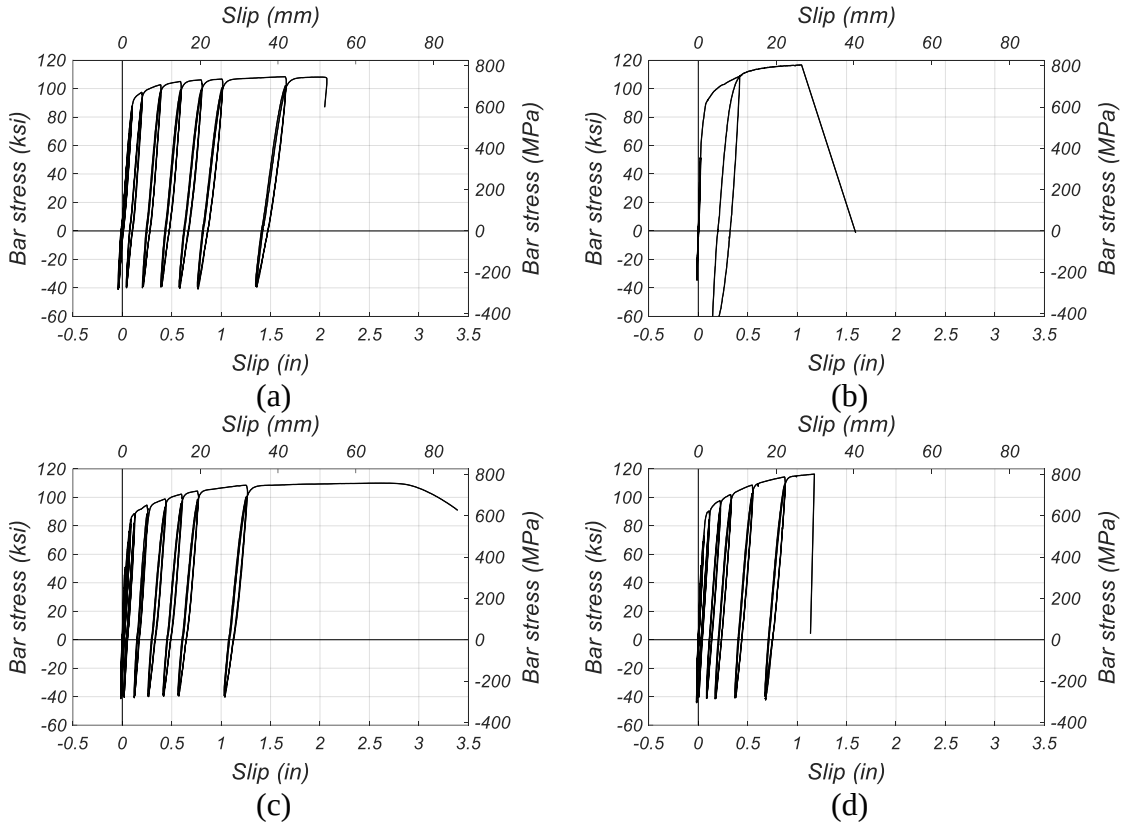

Figure 2.12. Bar Stress vs. Slip Response of (a) Test Specimen #1; (b) Test Specimen #2; (c) Test Specimen #3; (d) Test Specimen #4

2.5.1. Test Results: Specimen 1

During the force-controlled loading cycles, prior to bar yielding, the stiffness in tension and compression were very similar. The #18 bar yielded in tension at a slip of about 0.1 in. (2.5 mm) and sustained significant inelastic deformation throughout the loading cycles. After yielding, bar slip increased substantially with little incremental increase in the pull force. The maximum pull force was reached at a slip of 1.65 in. (42 mm), at which point the bar experienced 98% of its measured tensile strength. After reaching this high

pull force, in the following load cycle, visible necking occurred in the friction-welded header resulting in fracture prior to bar pulling out of the concrete, see Figure 2.13.

(a) (b)

Figure 2.13. Fracture of Friction-Welded Header in Specimen #1: (a) Damage at Bar-Concrete Interface; (b) Closeup View of Header Post-Fracture

Radial splitting cracks developed along the surface from the bar extending to the outer perimeter of the concrete column, and ultimately the transfer of the tensile force from the test bar to the surrounding concrete resulted in a cone-shaped fracture of the immediately surrounding concrete. Rather than using crude approximations to characterize the damage at the failure surface atop the test specimen, a detailed 3D point cloud model of the cone-shaped fracture surface was developed. Using this 3D point cloud model, the depth of the concrete cone failure was measured to be approximately 2.77 in. (70.4 mm), which equates to $1.23d_b$, as shown Figure 2.14.

(a) (b)

Figure 2.14. 3D Point Cloud Model of Fracture Surface of Test Specimen #1: (a) Plan View; (b) Cone Shaped Fracture

Observing the measured strains at various slip levels throughout the test, significant plastic strain penetration along the embedded length was evident. Plastic strains were measured at a depth of $18.75d_b$ at a slip of 1.65 in. (42 mm) in the last cycle prior to the friction-welded header necking, see Figure 2.15. Since the total embedment depth of the #18 bar was $33.6d_b$, it is shown that the lowest $14.85d_b$ of the embedment depth was enough to develop the yield stress in the test bar. All perimeter longitudinal and transverse hoop reinforcement in the test specimen remained elastic throughout testing, as shown in Figure 2.16.

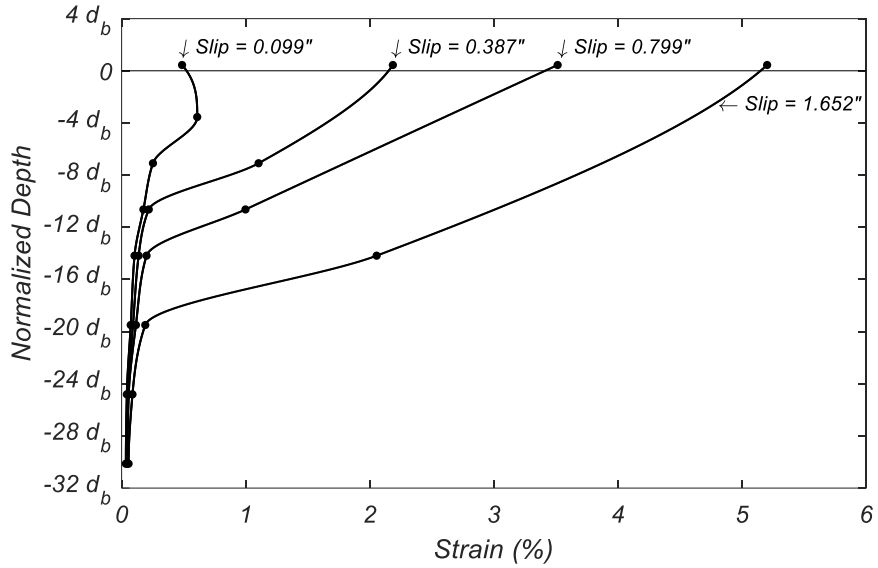

(a)

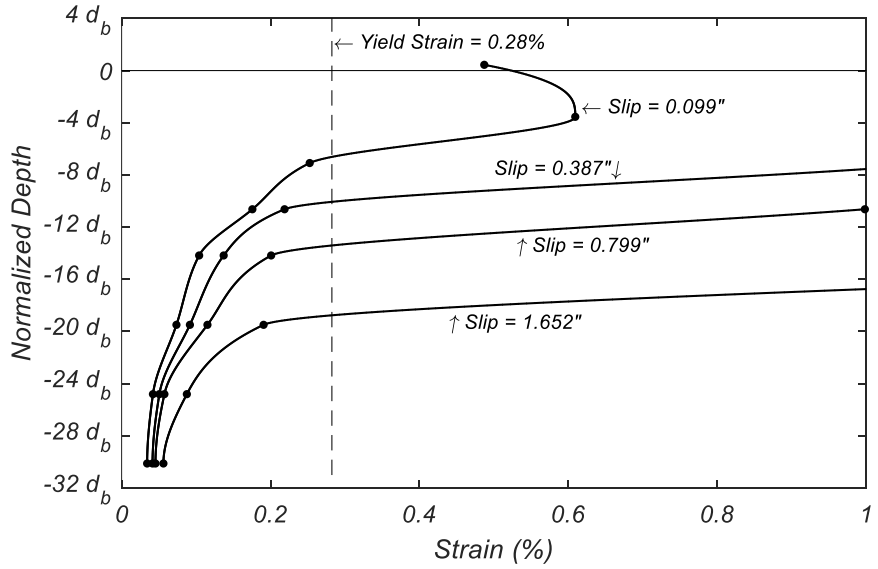

(b)

Figure 2.15. Strain Profile of Test Bar in Specimen #1: (a) Overall; (b) Closeup View Displaying Yield Penetration

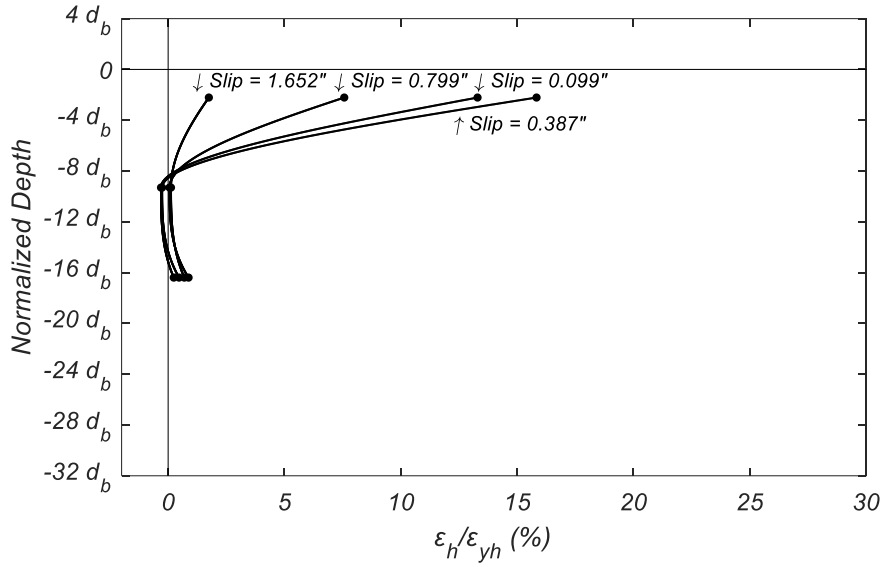

Figure 2.16. Transverse Hoop Strain Profile in Specimen #1

2.5.2. Test Results: Specimen 2

As with the behavior observed in the first test specimen, the stiffness in tension and compression during the force-controlled loading cycles were very similar for this specimen. The #14 bar yielded in tension at a slip of approximately 0.07 in. (1.8 mm) and sustained significant inelastic deformation throughout the displacement-controlled loading cycles. Upon yielding, the bar slip increased aggressively with incremental increases in the pull force. The maximum pull force was reached at a slip of 1.05 in. (27 mm), which equates to 102% of the bar's measured tensile strength, just prior to fracture. Immediately following the point of maximum pull force, the bar fractured at the interface with the friction-welded header without any visible necking prior to the bar pulling out from the concrete, see Figure 2.17.

(a) (b)

Figure 2.17. Fracture at Interface of Friction-Welded Header in Specimen #2: (a) Damage at Bar-Concrete Interface; (b) Closeup View of Header Post-Fracture

Similarly, splitting cracks developed and were visible at the top surface of the column, radiating from the bar to the outer perimeter of the concrete column. Transfer of the tensile forces from the bar to the surrounding concrete resulted in a cone-shaped fracture of the surrounding concrete. With the use of a 3D point cloud model of the specimen post-test, the depth of the concrete cone failure was measured to be approximately 4.65 in. (118 mm), which equates to $2.75d_b$, as shown in Figure 2.18.

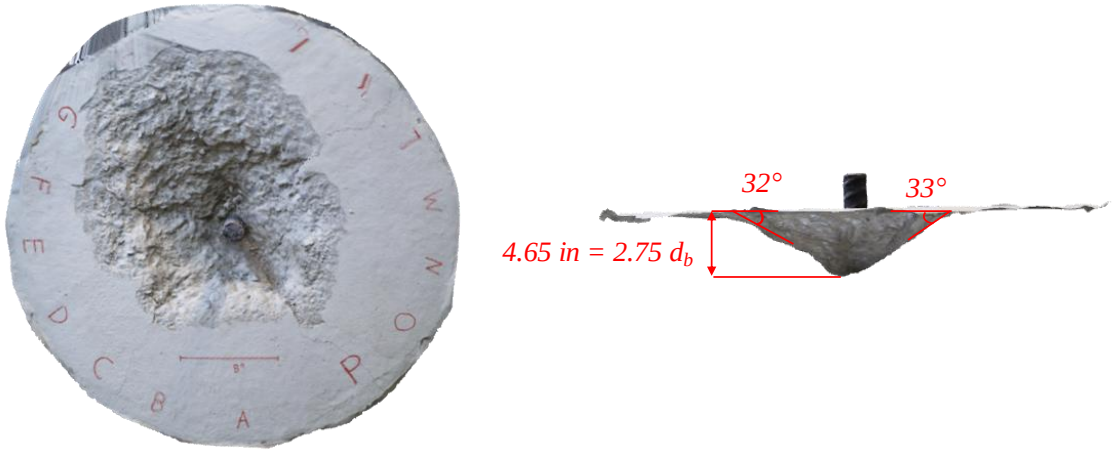

(a) (b)

Figure 2.18. 3D Point Cloud Model of Fracture Surface of Test Specimen #2: (a) Plan View; (b) Cone Shaped Fracture

Larger bars with larger rib deformations generally impose larger splitting forces on concrete, however, although the test bar in Specimen #2 was a smaller size than the bar in Specimen #1, the damage induced on the concrete in Specimen #2 was more severe. This can most likely be attributed to the necking and subsequent fracture of the friction-welded header in Specimen #1, preventing the full transfer of forces to concrete at the end of the test.

From the strain profile measured along the embedded length of the bar, significant plastic strain penetration was evident. Plastic strains were measured at a depth of $13.5d_b$ at a slip of 1.05 in. (27 mm) in the last cycle prior to bar fracture at the friction-welded header interface, see Figure 2.19. Since the total embedment depth of the #14 bar was $34.3d_b$, it is shown that the lowest $20.8d_b$ of the embedment depth was enough to develop the yield stress in the test bar. All perimeter longitudinal and transverse hoop reinforcement in the test specimen remained elastic throughout testing, as shown in Figure 2.20.

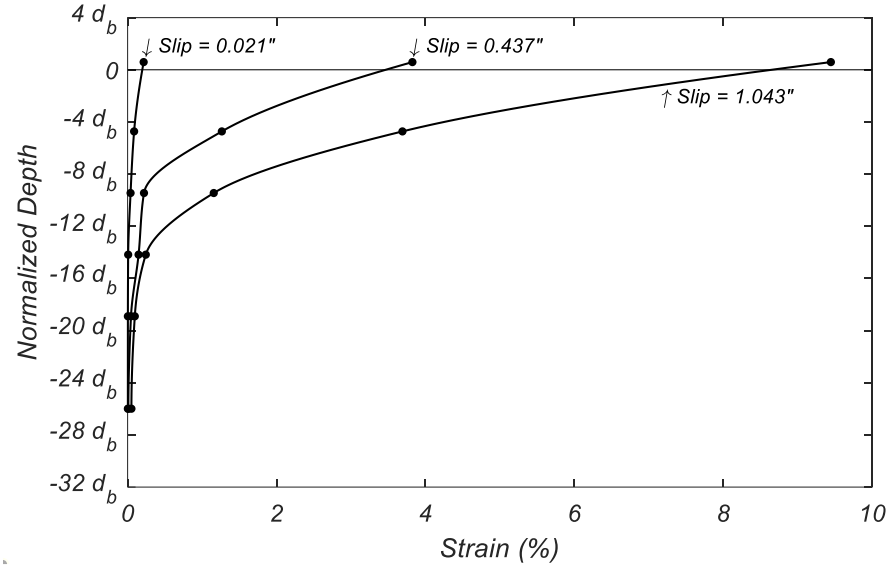

(a)

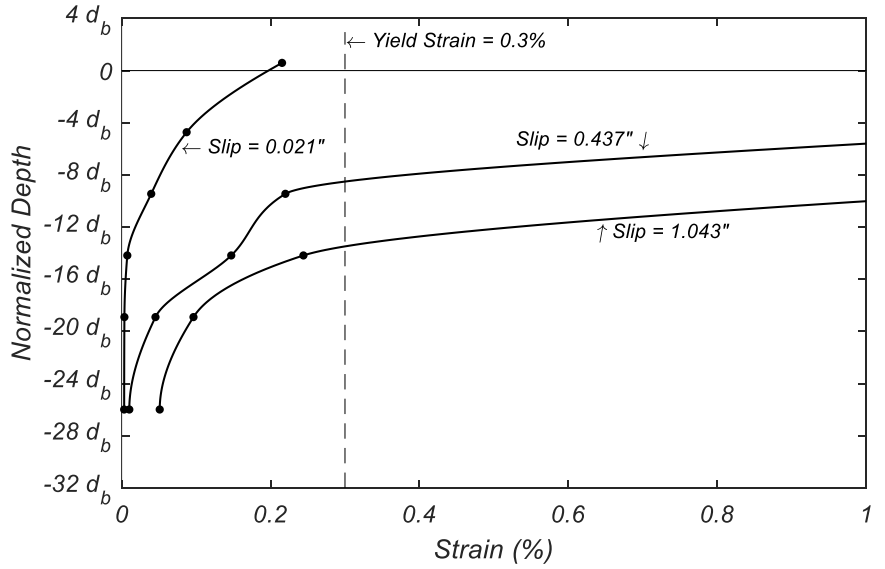

(b)

Figure 2.19. Strain Profile of Test Bar in Specimen #2: (a) Overall; (b) Closeup View Displaying Yield Penetration

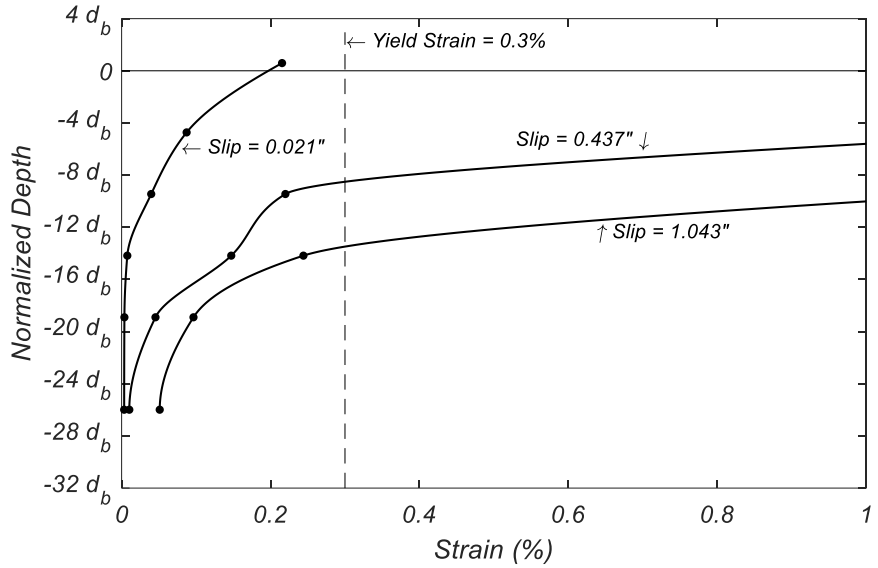

Figure 2.20. Transverse Hoop Strain Profile in Specimen #2

2.5.3. Test Results: Specimen 3

Specimen #3 behaved similarly, during the force-controlled loading cycles, prior to yielding, the stiffness in tension and compression was very similar. The #18 bar yielded in tension at a slip of approximately 0.08 in. (2 mm) and sustained significant inelastic deformation throughout the displacement-controlled loading cycles. After yielding, the bar slip increased substantially with incremental increases in the pull force. The maximum pull force was reached at a slip of 2.65 in. (67 mm), which equates to more than 99% of the bar's measured tensile strength, just prior to fracture. Immediately following the point of maximum pull force, the bar fractured within the concrete below the top surface of the column, without any visible necking, see Figure 2.21.

(a) (b)

Figure 2.21. Bar Fracture Beneath the Concrete Surface in Specimen #3: (a) Damage at Top of Column; (b) Closeup View of Severe Splitting Cracks

Severe splitting cracks developed at the top of the column, radiating from the bar to the outer perimeter of the concrete, extending vertically about 4 in. (102 mm) down from the top surface. Additionally, a horizontal circumferential crack was observed at that same depth. Transfer of the tensile forces from the bar to the surrounding concrete resulted in a cone-shaped fracture of the surrounding concrete. Upon completion of the test, the severely crushed concrete at the top of the column was removed, and a 3D point cloud model of the failure surface was developed. The depth of the concrete cone failure was measured to be approximately 7.1 in. (180 mm), which equates to $3.2d_b$, as shown in Figure 2.22. The damage induced on the concrete in this test specimen was the most severe of all tests.

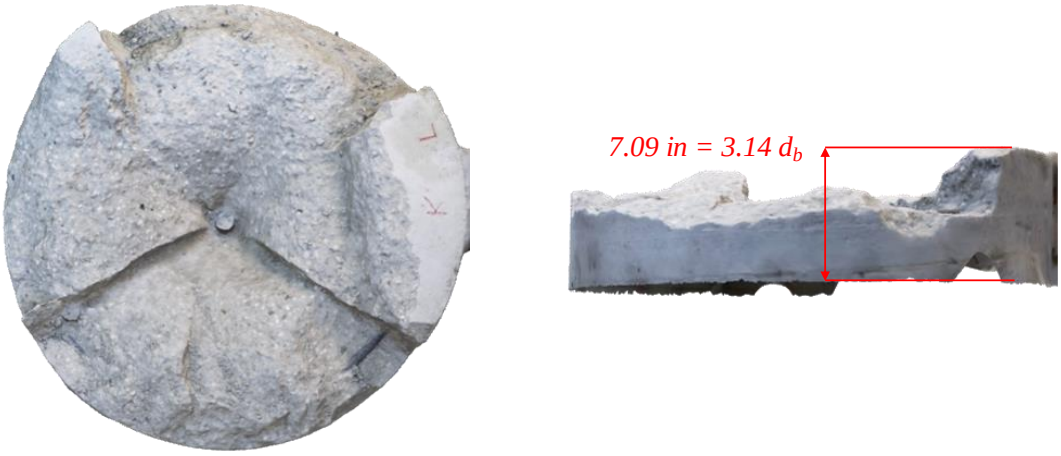

(a) (b)

Figure 2.22. 3D Point Cloud Model of Fracture Surface of Test Specimen #3: (a) Plan View; (b) Cone Shaped Fracture

The measured strains at various slip levels throughout the test show significant plastic strain penetration along the embedded length. Plastic strains were measured at a depth of approximately $10d_b$ at a slip of 1.31 in. (33 mm), after which the strain gages applied on the bar were damaged and no further strain measurements were obtained, see Figure 2.23. Since the total embedment depth of the #18 bar was $33.6d_b$, it is shown that the lowest $23.6d_b$ of the embedment depth was enough to develop the yield stress in the test bar. Given that no strain measurements were obtained beyond a slip of 1.31 in. (33 mm), the plastic strain penetration at higher slip values is likely higher. A post-test investigation provides more insight on the strain penetration along the bars, which is explained in Section 2.6. Although the damage induced on the concrete was extensive, all perimeter longitudinal and transverse hoop reinforcement in the test specimen remained elastic throughout testing, as shown in Figure 2.24.

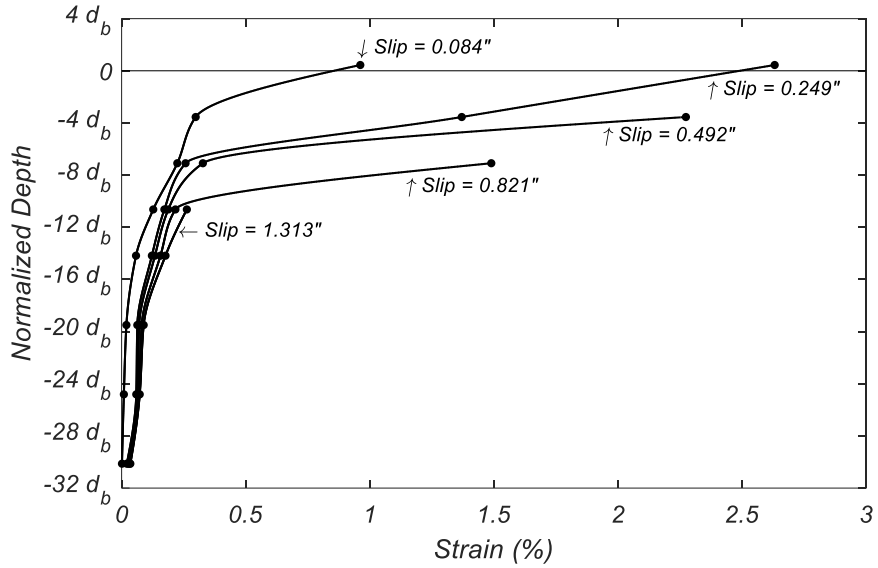

(a)

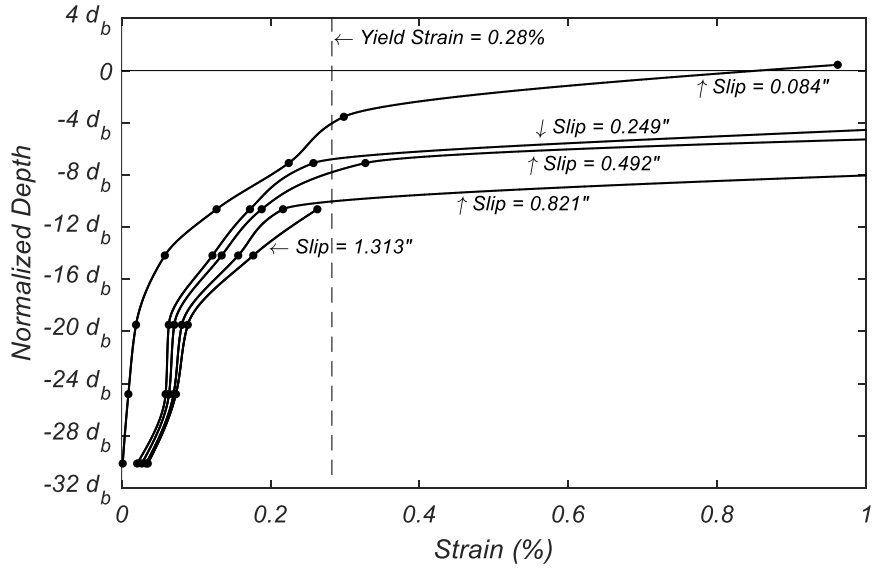

(b)

Figure 2.23. Strain Profile of Test Bar in Specimen #3: (a) Overall; (b) Closeup View Displaying Yield Penetration

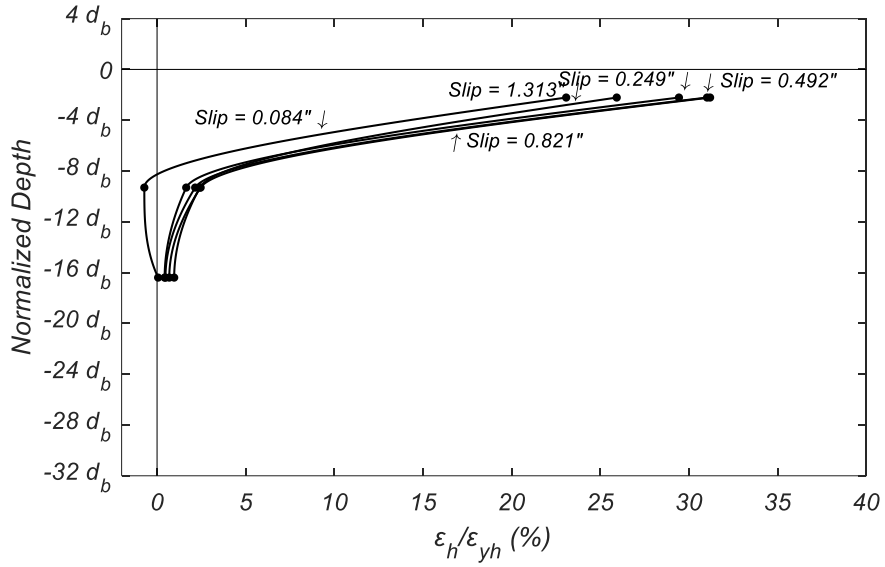

Figure 2.24. Transverse Hoop Strain Profile in Specimen #3

2.5.4. Test Results: Specimen 4

As with all previous tests, prior to bar yielding, the stiffness in tension and compression was very similar. During the test, the #14 bar yielded in tension at a slip of approximately 0.08 in. (2 mm), and sustained significant inelastic deformation throughout the loading cycles, reached and exceeded its ultimate tensile strength, then fractured prior to pulling out of the concrete, see Figure 2.25.

Figure 2.25. Damage Surface at Top of Column in Specimen #4

The expected tensile strength of the bar was reached at a slip of 0.85 in. (21.6 mm). No visible necking was observed, which corresponds to the slight increase in strength in the subsequent tension cycle prior to fracture. The bar fractured just below the friction-welded header at a slip of 1.18 in. (30 mm). Severe radial splitting cracks developed along the surface from the bar extending to the outer perimeter of the concrete column, and ultimately the transfer of the tensile force from the test bar to the surrounding concrete resulted in a cone-shaped fracture of the immediately surrounding concrete with a depth of approximately 3.75 in. (95 mm) which equates to $2.25d_b$, as shown in the 3D point cloud model in Figure 2.26.

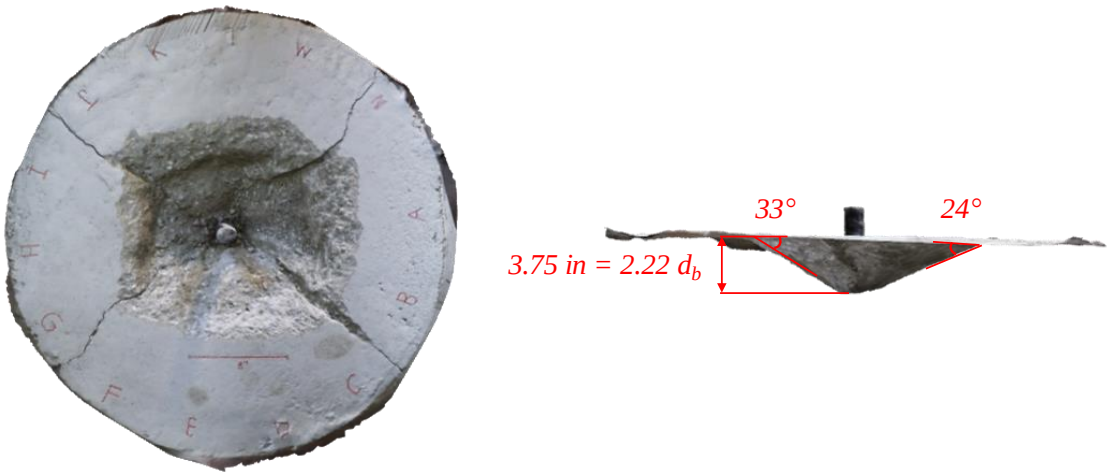

(a) (b)

Figure 2.26. 3D Point Cloud Model of Fracture Surface of Test Specimen #4: (a) Plan View; (b) Cone Shaped Fracture

The measured strains along the embedded length of the test bar provide valuable insight into the strain penetration and bond deterioration of the reinforcing bar. Observing the measured strains at various slip levels throughout the test, significant plastic strain penetration along the embedded length was evident. Plastic strains were measured at a depth of $13.25d_b$ at a slip of 1.17 in. (29.7 mm) just prior to fracture, see Figure 2.27. Since the total embedment depth was $34.3d_b$, it is shown that the lowest $20d_b$ of the embedment depth was enough to develop the yield stress in the test bar. All perimeter longitudinal and transverse hoop reinforcement in the test specimen remained elastic throughout testing, see Figure 2.28.

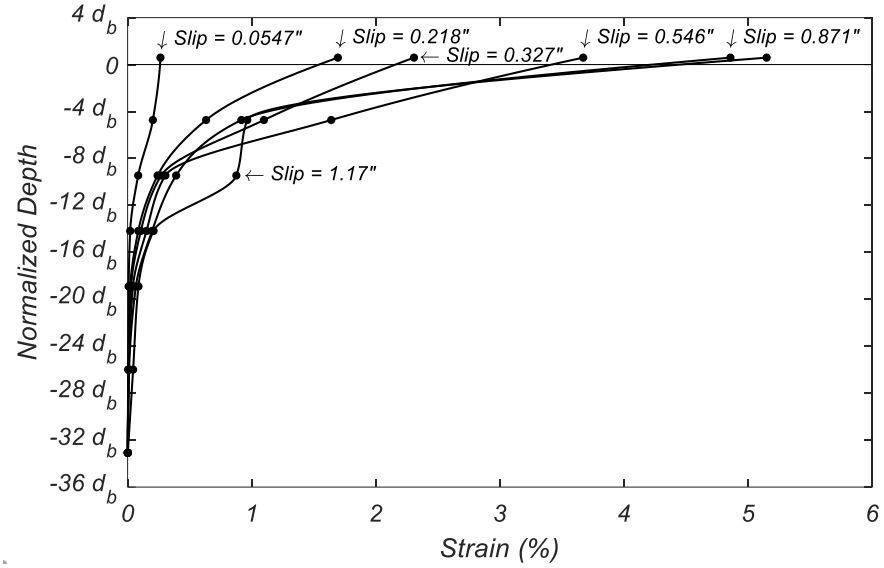

(a)

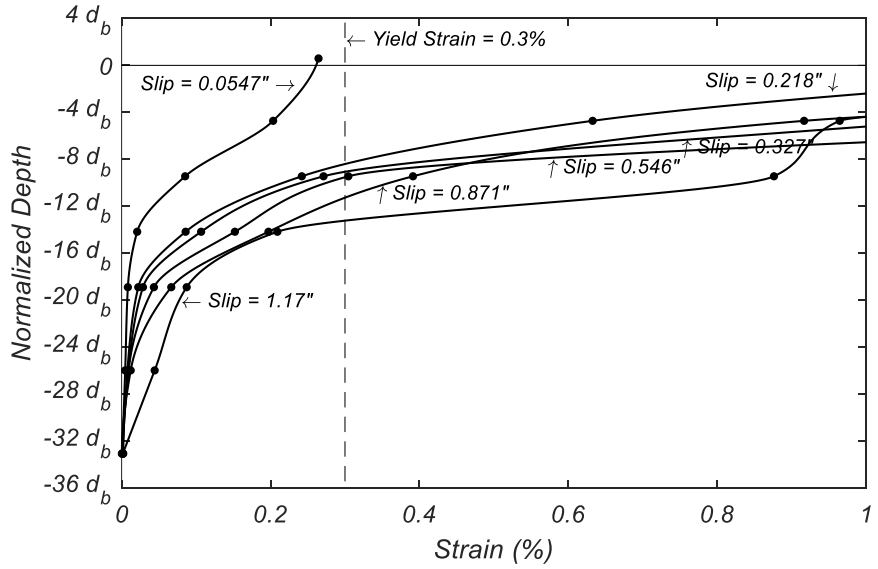

(b)

Figure 2.27. Strain Profile of Test Bar in Specimen #4: (a) Overall; (b) Closeup View Displaying Yield Penetration

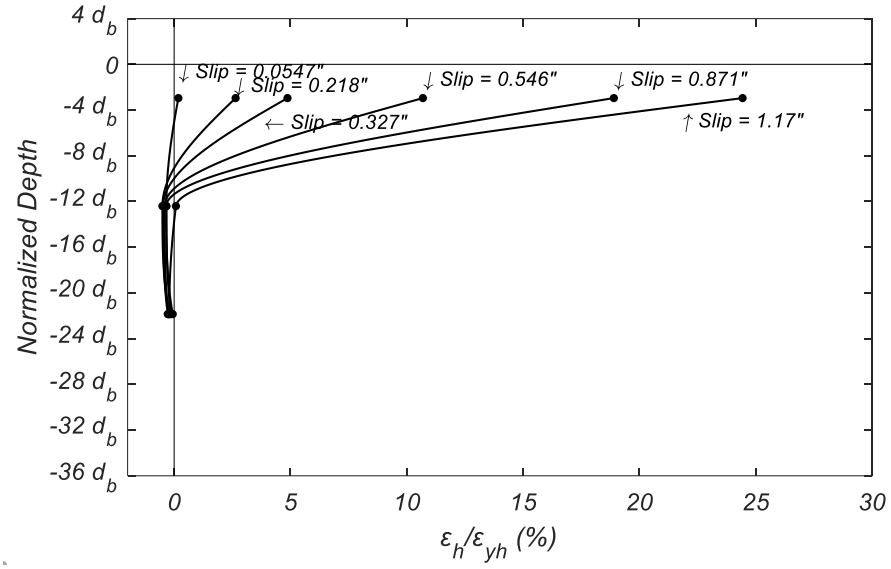

Figure 2.28. Transverse Hoop Strain Profile in Specimen #4

2.6. Data Processing and Interpretation

In all tests, the bars experienced forces between 98% and 102% of their corresponding tensile strength measured from bare bars in a calibrated Universal Testing Machine (UTM) prior to fracture. The bars fractured in the heat-affected region near the friction-welded header in all tests but one, where the bar fractured beneath the surface within the concrete. Table 2.5 summarizes the maximum tensile stress and strain, and the maximum yield penetration observed at the largest measured slip during each test. The maximum strain measured by the strain gages near the embedded bar end, ε_{nbe}, is also tabulated in Table 2.5. Since the largest strains measured near the embedded bar end ranged from 1% to less than 25% of the yield strain, the assumption that negligible bar slippage occurs at the embedded end is confirmed. The pre- and post-yield average bond stresses for each test are presented in Table 2.6. It is observed that as expected, the pre-yield average

bond stress was higher than the post-yield average bond stress. The post-yield average bond stress ranges between 25% and 51% of the pre-yield average bond stress, see Table 2.6. Some minor variation between the average bond stress for similar size bars embedded in concrete with different compressive strength is observed. However, due to the lack of data from more tests, no conclusions can be made regarding what the main variables causing this slight variation are.

Table 2.5. Summary of Key Test Bar Stresses and Strains

Specimen	Maximum Slip (in) [mm]	Maximum Tensile Strain (%)	Maximum Tensile Stress (ksi) [MPa]	Yield Penetration Length, L_{yp} (d_b)	$\frac{L_{nbe}}{d_b}$	$\frac{\varepsilon_{nbe}}{\varepsilon_y}$ (%)
1	2.07 [53]	6.7	108.3	18.5	30	23
2	1.04 [27]	8.9	116.6	14	26	17
3	2.68 [68]	8.5	109.9	18.5	30	15
4	1.17 [30]	9.2	116.3	13.5	33	0.8

Table 2.6. Comparison of Pre- and Post-Yield Average Bond Stress for All Tests

Specimen	Yield Force F_y (kips) [kN]	Maximum Tensile Force (kips) [kN]	Average Bond Stress		
			Pre-Yield (ksi) [MPa]	Post-Yield (ksi) [MPa]	Post-Yield/ Pre-Yield (%)
1	328.4 [1461]	433.2 [1927]	1.359 [9.4]	0.354 [2.4]	26
2	196.4 [874]	262.4 [1167]	1.075 [7.4]	0.523 [3.6]	49
3	328.4 [1461]	439.9 [1957]	1.359 [9.4]	0.377 [2.6]	28
4	196.4 [874]	261.7 [1164]	1.049 [7.2]	0.537 [3.7]	51

As mentioned above, many of the strain gages along the length of the test bar did not survive the larger amplitude load cycles carried towards the end of the tests. Combining the peak strains obtained through the post-test investigation along with the peak strains measured by the strain gages at the end of the test, a complete strain profile for each test bar was developed, see Figure 2.29. Having the strain profile and the measured slip at the peaks of every cycle during the test provides the opportunity to investigate the bond stress-slip behavior of the test bar.

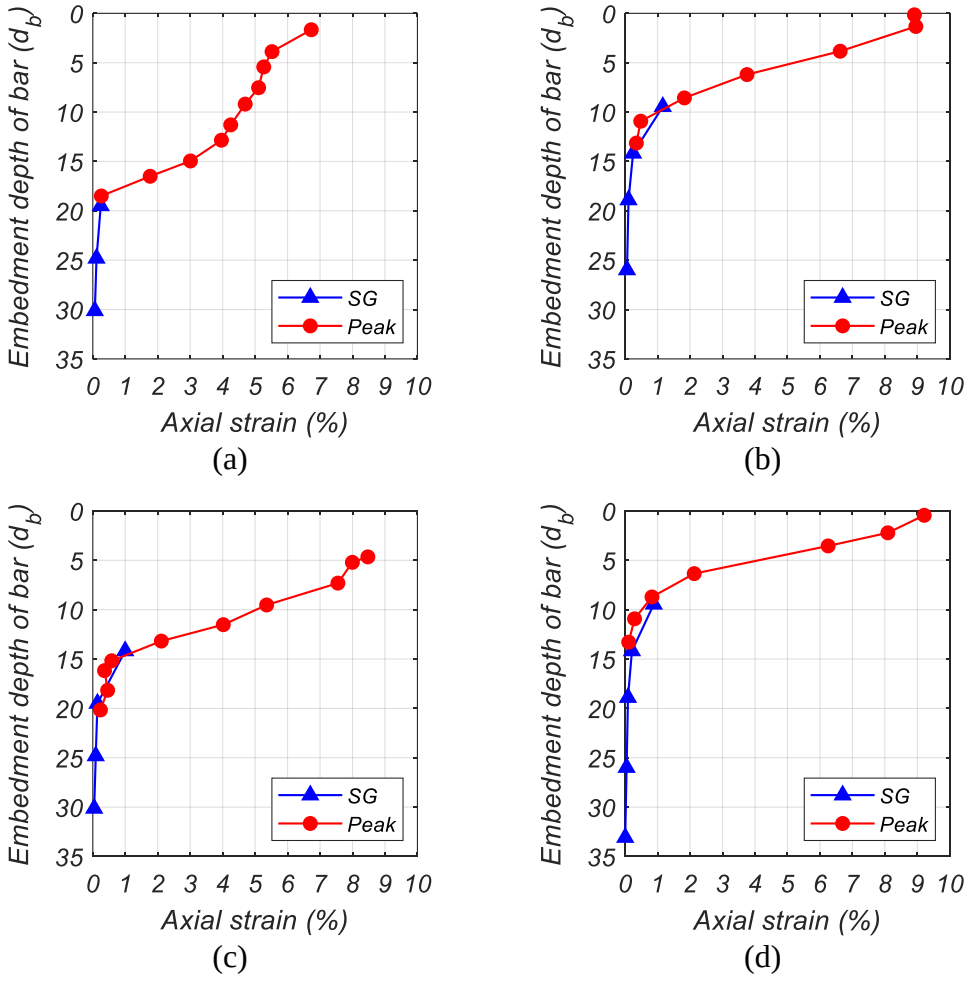

Figure 2.29. Strain Profile of Test Bar Including Measured Peak Strains Post-Test: (a) Specimen #1; (b) Specimen #2; (c) Specimen #3; (d) Specimen #4

Interpolating from previously obtained tensile test data of bars from the same heat, the bar stress profile, and the bar tensile force profile is calculated at all cycle peaks. The bond force at any embedment depth is the difference between the bar tensile force at that, and the consecutive depth. The bond stress at each embedment depth is then calculated by dividing the bond force by the corresponding bar surface area at which its applied, which corresponds to the surface area along the depth between two consecutive measurement locations. The integral of the strains along the embedment length starting from the bar end of the test bar produces the slip profile. Bond stresses and measured slips are obtained and categorized by measurement depth and concrete strength. It is worth mentioning that during the yield plateau of the test bar, pure slippage occurs and since no bond stress can develop, some “zero-stress” or apparently odd “low-stress” values are visible on the bond stress-slip relationship, as presented in Figure 2.30. Although this test setup was not designed to obtain the complete bond stress-slip relationship, the discrete points obtained give an indication of such a relationship.

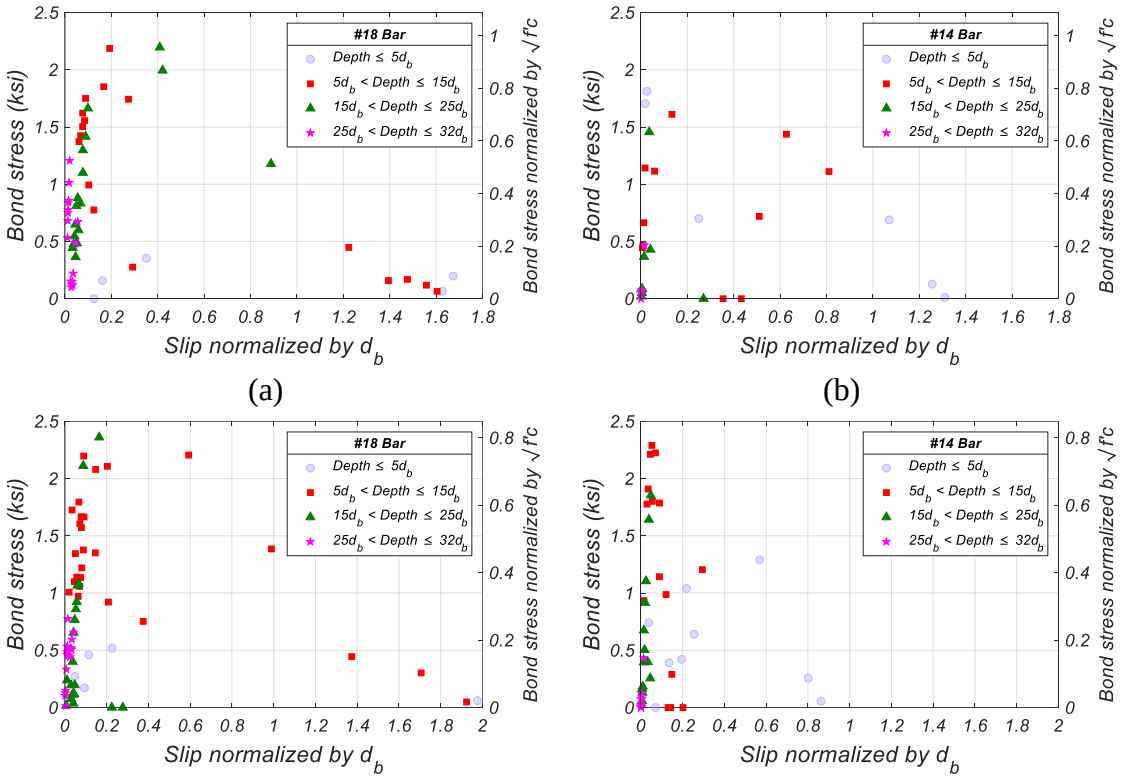

Figure 2.30. Bond Stress-Slip Relationship: (a) Specimen #1; (b) Specimen #2; (c) Specimen #3; (d) Specimen #4

Table 2.7 lists the bond strengths and approximate bar slip when the bond strength was attained in the four test specimens. Comparing the bond stress-slip relationship for both concrete strengths, it is evident that the bond strength is not significantly influenced by the concrete compressive strength. The higher strength 8000 psi (55.2 MPa) concrete specimens reached a bond strength of 2.4 ksi (16.5 MPa) and 2.3 ksi (15.9 MPa) for #18 and #14 bar sizes respectively, whereas the 5000 psi (34.5 MPa) concrete reached a bond strength of 2.2 ksi (15.2 MPa) and 1.9 ksi (13.1 MPa) accordingly. Notably, the bond strength was reached at a substantially smaller slip in the specimens with #14 bars than their #18 bar counterparts.

Table 2.7. Bond Strength Observed in Each Test

	Specimen #1	Specimen #2	Specimen #3	Specimen #4
Bond Strength (ksi) [MPa]	2.2 [15.2]	1.9 [13.1]	2.4 [16.5]	2.3 [15.9]
Slip (in.) [mm]	0.44 [11.2]	0.043 [1.1]	0.37 [9.4]	0.089 [2.3]

According to the prescriptive requirements set out in Caltrans SDC 2.0[22] and ACI[21], it was expected that the bond strength would be proportional to $\sqrt{f_c'}$, however based on the findings from this experiment, this was not necessarily the case. Without the availability of a large enough population of experimental data, it cannot be concluded that the bond strength is not proportional to $\sqrt{f_c'}$. Findings from a comprehensive experimental study by Alavi-Fard and Marzouk[33] however, have shown that the bond of high strength concrete is more appropriately proportional to $\sqrt[3]{f_c'}$ as prescribed in the British Code BS 8110 (BSI 1985)[34] and the findings from this experiment suggest a similar proportional relationship.

Furthermore, geometric properties of reinforcing bars such as the relative rib ratio, commonly referred to as the bond index, also significantly influence the bond strength. The relative rib ratio is defined as the ratio between the rib area above the core, projected on a plane perpendicular to the bar axis. Metelli and Plizzari[31] performed an extensive literature review and an exhaustive experimental investigation regarding the effect of the relative rib ratio on the bond strength of bars. Through experimental work, it was shown that the bond strength increases with the bond index and decreases with the bar diameter. Therefore, it is expected that the bond strength of the bars used in this experiment to be

lower due to their large diameter (#14 and #18), however since the bars have a relative rib ratio, f_R, of 0.11 and 0.09 respectively, the maximum bond strengths observed are comparable to those presented by Metelli and Plizzari[31].

An important aspect of bridge column seismic design is the analytical plastic hinge length, L_P, which is defined as the equivalent length of the column over which the plastic curvature is assumed constant for estimating plastic rotations. The analytical plastic hinge length is evaluated by considering the contributions from the spread of plasticity along the member length and the amount of strain penetration. Mander et al.[26] first observed that a plastic hinge length of a column or a member framing into an elastic element exhibits some strain penetration. Based on experimental work, in 1983, these researchers proposed that the effect of strain penetration in the plastic hinge length, termed here as the equivalent strain penetration, L_{ep}, to be:

$$\frac{L_{ep}}{d_b} = \frac{32}{\sqrt{d_b}} \qquad 2.1$$

Per the findings from Mander et al.[26], the yield penetration would decrease with an increase in bar size. In 1990, Park and Paulay[35] proposed an empirical expression for the yield penetration which remains constant regardless of the bar diameter, see Equation 2.2.

$$\frac{L_{ep}}{d_b} = 6 \qquad 2.2$$

In 1996, Priestley et al.[36] presented an expression for evaluating the strain penetration which was made proportional to the bar expected yield strength, f_{ye}, see Equation 2.3.

$$\begin{cases} \frac{L_{ep}}{d_b} = 0.022 f_{ye} & (f_{ye} \text{ in MPa}) \\ \frac{L_{ep}}{d_b} = 0.15 f_{ye} & (f_{ye} \text{ in ksi}) \end{cases} \quad 2.3$$

Caltrans SDC[22] has since adopted this expression directly from Priestley et al.[36] Current design guidelines in Caltrans SDC 2.0 §5.3.4[22] present an expression to calculate this analytical plastic hinge length in columns supported on footings or Type II shafts. This expression has two components, first, a geometric term related to the height of the column, and second, an equivalent strain penetration term dependent on the bar diameter and expected yield strength, see Equation 2.4.

$$L_P = \begin{cases} 0.08L + 0.15 f_{ye} d_b \geq 0.3 f_{ye} d_b & \text{(in, ksi)} \\ 0.08L + 0.022 f_{ye} d_b \geq 0.044 f_{ye} d_b & \text{(mm, MPa)} \end{cases} \quad 2.4$$

The equivalent yield penetration depth is defined by considering a constant strain, equal to the measured strain at the top of the bar for a given slip, along an equivalent depth, L_{ep}, measured from the top of the bar. The area under this equivalent rectangle is equal to the measured slip, which is obtained from the integral of the bar strain profile along its entire embedded length, as shown in Figure 2.31.

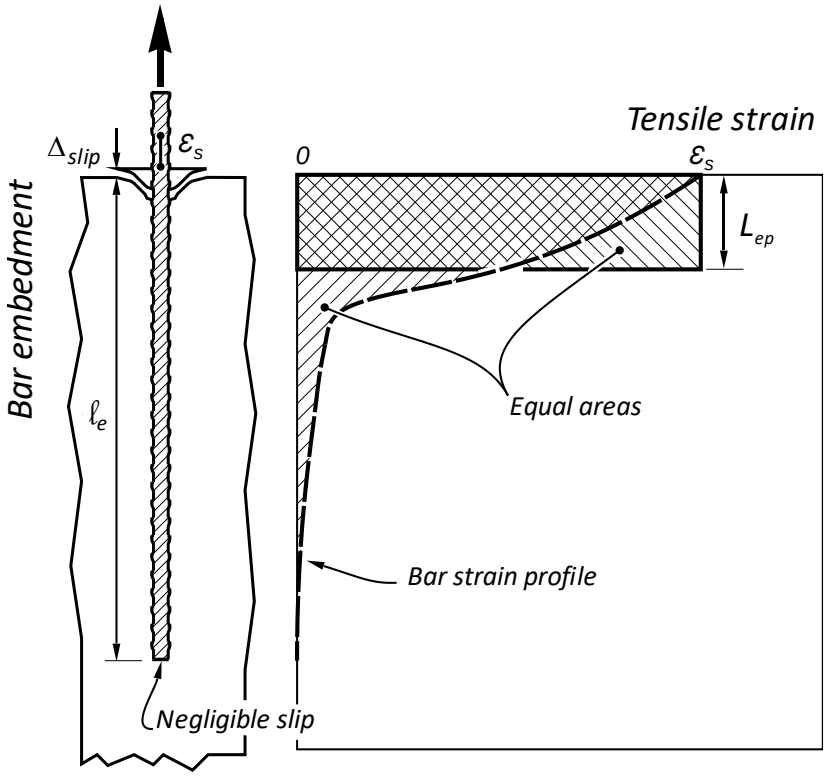

Figure 2.31. Visual Representation of Equivalent Yield Penetration

By equating the area of this equivalent rectangle to the integral of the measured strain profile of the bar, the equivalent yield penetration depth, L_{ep}, is determined to be:

$$\int_0^{\ell_e} \varepsilon_s dz = L_{ep}\varepsilon_s \qquad 2.5$$

$$\Delta_{Slip} = L_{ep}\varepsilon_s \qquad 2.6$$

$$L_{ep} = \frac{\Delta_{Slip}}{\varepsilon_s} \qquad 2.7$$

where ε_s is the measured strain, and Δ_{Slip} is the measured slip at the top of the bar. The equivalent yield penetration was evaluated for all test specimens including tests obtained from similar testing on ASTM A706 Grade 60 reinforcement by Murcia-Delso et al.[32] To properly compare the findings from both sets of tests, the equivalent yield

penetration term for all tests were normalized by $d_b \cdot (f_{sue} - f_{ye})/f_{ye}$, see Figures 2.32 and 2.33.

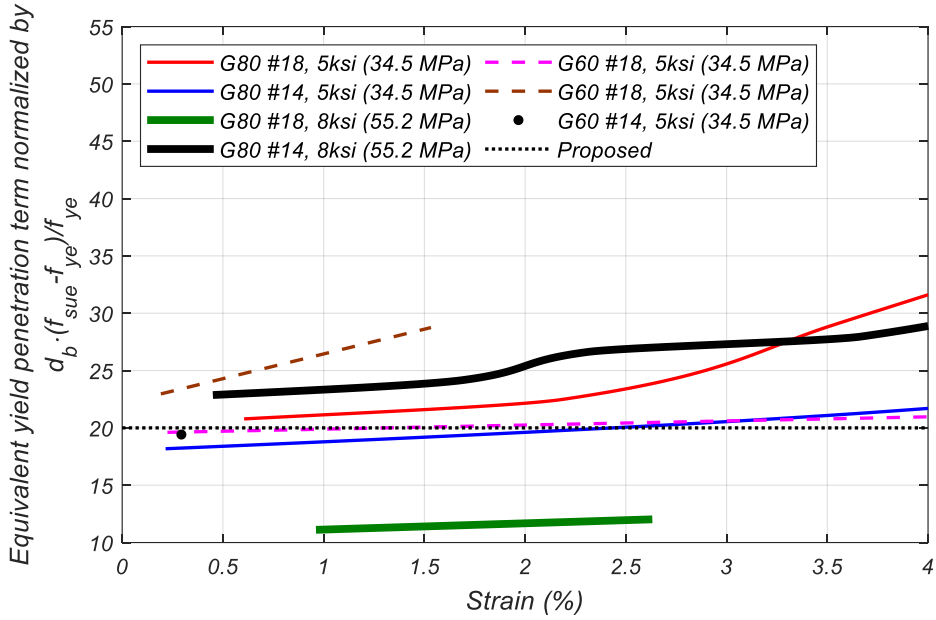

Figure 2.32. Comparison of Equivalent Yield Penetration Term for all Tests Including Grade 60

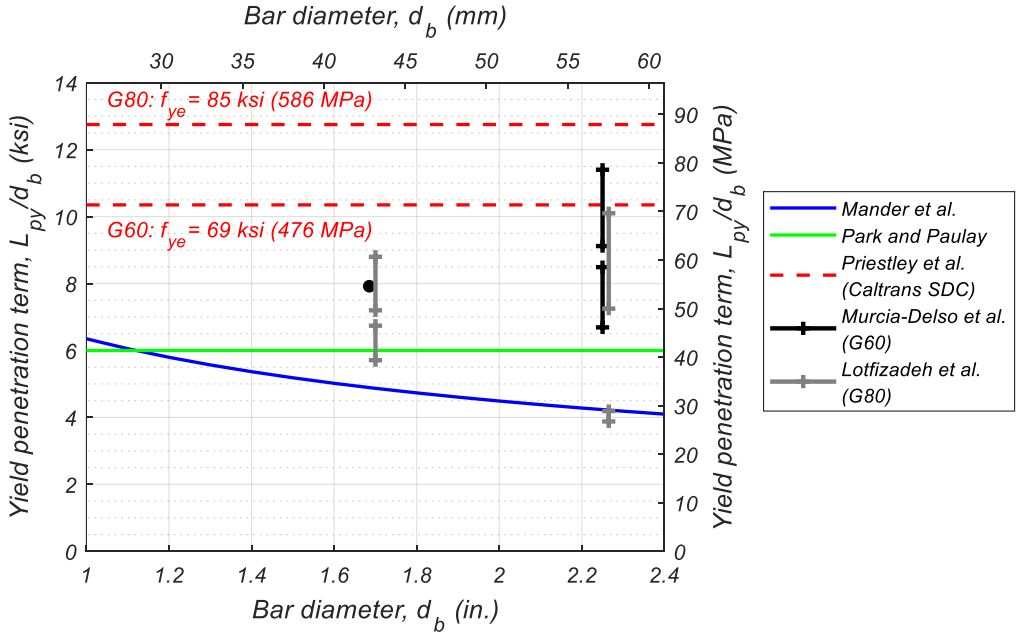

Figure 2.33. Comparison of Equivalent Yield Penetration Term Normalized by Bar Diameter

Findings from this experiment have shown that the strain penetration is not sensitive to the bar yield strength, f_y, as presented by Priestley et al.[36], and does not appear to be sensitive to the bar diameter either, as the approach by Mander et al.[26] had originally suggested. Since sensitivity to f_y and d_b are not observed in this experiment, also, since no direct correlation between bar size and concrete strength is observed in the tests, a modified expression is proposed for the equivalent yield penetration term, hereto referred as Ψ_{eyp}, where the analytical plastic hinge length expression is given by:

$$L_P = 0.08L + \Psi_{eyp} d_b \qquad 2.8$$

The authors propose the following expression for the equivalent yield penetration term:

$$\Psi_{eyp} = 20 \cdot \frac{f_{sue} - f_{ye}}{f_{ye}} \qquad 2.9$$

which is dependent on the expected ultimate strength, f_{sue}, and expected yield strength, f_{ye}, of the bar. The justification for such a dependency comes from the satisfaction of the boundary condition that if the bar has no hardening, the ultimate strength would be equal to the yield strength, and therefore yielding cannot penetrate into the region where the bar in anchored.

The $(f_{sue} - f_{ye})/f_{ye}$ ratio, varies for different bars. Experimental tensile test data for bars of various sizes between #5 and #18 of both Grade 60 and 80, were collected from various experimental work[8],[20],[32],[37]–[40], compared, and are presented in Tables 2.8 and 2.9 respectively.

Table 2.8. Key Mechanical Properties of ASTM A706 Grade 60 Bars (27 Samples)

	f_{ye} (ksi) [MPA]	f_{sue} (ksi) [MPa]	ε_{sue} (%)	$\frac{f_{sue}-f_{ye}}{f_{ye}}$
Minimum	59.9 [413]	84.8 [585]	9.5	0.34
Maximum	75.2 [519]	104.3 [719]	23.4	0.68
Mean	66.6 [459]	95.6 [659]	13.1	0.44
Median	67.0 [462]	94.9 [654]	12.2	0.42
STD	3.8 [26.2]	4.9 [33.8]	3.1	0.08

Table 2.9. Key Mechanical Properties of ASTM A706 Grade 80 Bars (27 Samples)

	f_{ye} (ksi) [MPA]	f_{sue} (ksi) [MPa]	ε_{sue} (%)	$\frac{f_{sue}-f_{ye}}{f_{ye}}$
Minimum	79.0 [545]	105.0 [724]	8.4	0.26
Maximum	88.3 [609]	119.1 [821]	15.5	0.44
Mean	84.6 [583]	112.6 [776]	10.3	0.33
Median	86 [593]	113.9 [785]	9.7	0.33
STD	2.8 [19.3]	3.7 [25.5]	1.5	0.04

It is observed that while this ratio is generally greater for the Grade 60 bars, the mean values show an inverse relationship with respect to the bar grade. That is, the $(f_{sue}-f_{ye})/f_{ye}$ ratio for Grade 80 to Grade 60 is equal to $3/4$ as shown in Equation 2.10.

$$\frac{\left[\frac{f_{sue}-f_{ye}}{f_{ye}}\right]_{G80}}{\left[\frac{f_{sue}-f_{ye}}{f_{ye}}\right]_{G60}} = \frac{0.33}{0.44} = 0.75 \qquad 2.10$$

This further confirms the validity of the proposed equivalent yield penetration term, Ψ_{eyp}. Therefore, the proposed analytical plastic hinge length expression is:

$$L_P = 0.08L + \Psi_{eyp} d_b \qquad 2.11$$

where, based on experimental results from both Grade 60 and 80 reinforcement:

$$\Psi_{eyp} = \begin{cases} 8.8 & \text{for Grade 60} \\ 6.6 & \text{for Grade 80} \end{cases} \quad 2.12$$

The proposed analytical plastic hinge length equation, Equations 2.11-2.12, is believed to be very useful since it no longer requires prior knowledge of the expected yield strength, f_{ye}, to evaluate the analytical plastic hinge length, while reducing the complexity and potential for designer error by eliminating the need for different multiplicative constants dependent on the design units as currently required in Equation 2.4.

2.7. Summary and Conclusions

The development of high strength A706 Grade 80 large diameter bars for use in large civil infrastructure projects such as bridge substructures, power stations, and large mat footings has been studied in this research. To validate the use of prescriptive requirements in current design codes by extrapolation for Grade 80 reinforcement, experiments were conducted on large diameter Grade 80 bars embedded in well confined concrete. These experiments have confirmed that extrapolation of current prescriptive requirements for the development of A706 Grade 80 reinforcement is satisfactory in design. Bars in all test specimens were able to yield, sustain significant inelastic strain, and reach the ultimate strength without pull-out from the concrete, despite their significantly shorter development length than specified by SDC 2.0[22] and ACI 318-19[21]. In some cases, the failure mechanism occurred in the friction-welded header since the header material was weaker than the Grade 80 test bar itself.

The bond stress-slip relationship of large diameter A706 Grade 80 in two different concrete strengths was investigated. Bars embedded in higher strength 8000 psi (55.2 MPa)

concrete show a marginal increase in bond strength as well as a slightly stiffer initial bond stress-slip response when compared with similar bars embedded in 5000 psi (34.5 MPa) concrete. Apart from those findings, no other noticeable differences were observed between concrete types.

Lastly, the currently prescribed expression for the calculation of the analytical plastic hinge length of columns supported on footings or Type II shafts is updated and a modification has been presented to simplify the expression while more closely representing experimentally measured results. The proposed expression is normalized with respect to the steel strength, which allows its use for both A706 Grade 60 and 80 reinforcing bars.

Chapter 2, in part, is currently being prepared for submission for publication of the material. Lotfizadeh, Koorosh H.; Restrepo, José I. The dissertation author was the primary investigator and author of this material.

Chapter 3.

DEVELOPMENT OF LARGE DIAMETER GRADE 80 REINFORCEMENT IN ENLARGED BRIDGE COLUMN PILE SHAFTS

3.1. Abstract

The Department of Transportation of California funded a large experimental work to validate the use of higher-grade reinforcement, such as Grade 80 reinforcement, in large civil infrastructure projects. A task within this project was to experimentally validate the replacement of ASTM A706 Grade 60 reinforcing steel with large diameter ASTM A706 Grade 80 bars in bridge columns extending into Type II pile shafts and calibrate a nonlinear finite element analysis model permitting the extrapolation of laboratory tests. This chapter describes the experimental test setup and procedure and presents the main findings and conclusions from this task, as well as the development and calibration of the nonlinear

finite element analysis model, and a comparison of the model results with the experimental findings.

3.2. Introduction

Many types of foundations are used to support bridge columns in modern bridge construction. Cast-in-drilled hole (CIDH) piles are one of the most common and preferred foundation types used in bridge construction due to their significantly smaller footprint when compared with spread footings. This smaller footprint can reduce costs by simplifying construction while reducing the environmental impact of construction.

Current design guidelines such as AASHTO[1] and Caltrans SDC[22] differentiate CIDH piles in two categories: (1) Type I, and (2) Type II, with the difference being the cross-sectional confined core diameter of the underground pile, as presented in Figure 3.1. Type I piles have the same confined core diameter as the bridge column, allowing a continuous reinforcement cage for the column and the pile, whereas Type II piles are designed such that the confined core diameter of the pile is larger than the bridge column, requiring separate reinforcement cages for the column and pile. During a large seismic event, it is expected that the plastic deformation in columns is concentrated in the plastic hinge region, where the bending moment is most significant. When using a uniform cross-section for the column and pile (Type I), the plastic hinge region tends to develop below ground level due to the soil surrounding the pile acting as springs rather than a perfectly fixed boundary condition. The development of the plastic hinge beneath ground level makes post-earthquake inspection and repairs rather challenging and costly. When using a Type II pile, where the cross-section of the pile is larger than the column, the plastic hinge

develops at the base of the column above the column-pile interface, simplifying future inspections and repairs. For this reason, Type II CIDH piles are the preferred foundation type for bridge construction in seismic regions.

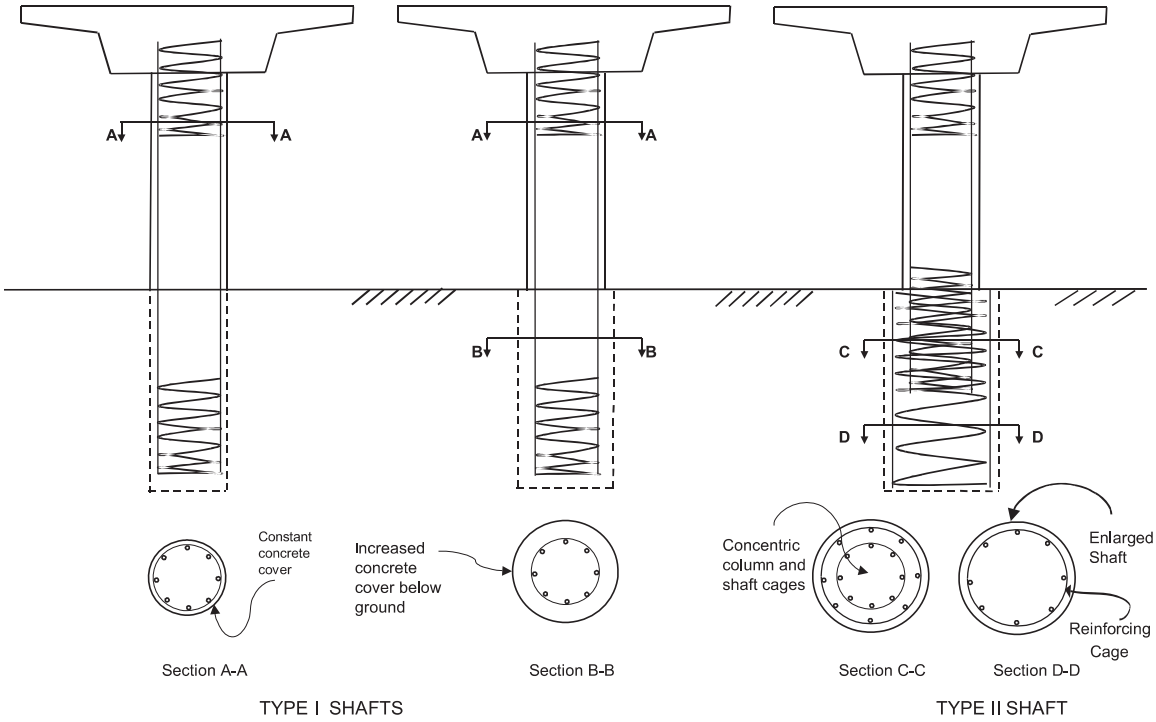

Figure 3.1. Columns Extending into Type I and Type II Pile Shafts (Caltrans SDC 2.0)

Due to the difference in cross-section between the column and pile, the column longitudinal reinforcement extending into the pile must form a non-contact splice with the pile longitudinal reinforcement to transfer forces into the foundation. Current design codes have explicit provisions regarding the required embedment depth of the column longitudinal bars into Type II pile shafts to develop and transfer loads fully. Experimental studies investigating the development and lap splice length of bars subjected to cyclic loading have been carried out in the past by Lukose et al. (1982)[41] and Sagan et al. (1991)[42]. Furthermore, McLean and Smith (1997)[43] and Tran et al. (2013)[44] conducted

an extensive reduced-scale experimental study on the development of column longitudinal reinforcement in Type II pile shafts. It is worth noting that in the experiments conducted by Tran et al. (2013)[44], the column longitudinal reinforcement was embedded in the pile shaft using bar headers, which differ from other investigations. Murcia-Delso et al. (2016)[45] continued and elaborated on this topic with an extensive experimental study to determine the minimum embedment length of column longitudinal reinforcement extending into Type II pile shafts as well as determining the amount of transverse reinforcement required along the bar anchorage region of the pile shaft to prevent premature anchorage failures. Murcia-Delso et al.[45] tested four full-scale column-shaft specimens under quasi-static cyclic loading, three of which had embedment lengths significantly shorter than the prescribed lengths provided by AASHTO[1] and Caltrans SDC[22]. Formulas to determine embedment lengths and amount of transverse reinforcement in the anchorage region were proposed and presented by Murcia-Delso et al.[45], and the experimental study showed that the reduced embedment length was sufficient to fully develop and transfer loads through the non-contact splice, see Equation 3.1.

However, due to the lack of experimentation, current design codes only allow the use of ASTM A706 Grade 60 and lower longitudinal reinforcement within the non-contact splice region. To date, no experimental investigation has been done to verify and validate the use of ASTM A706 Grade 80 reinforcement in Type II CIDH piles for bridge construction in seismic regions. This chapter presents findings from an experimental test program of a full-scale column-pile connection entirely reinforced with ASTM A706

Grade 80 bars, as well as a comparison of the experimental results with a nonlinear finite element (FE) model using newly calibrated bond-slip models from experimental work presented in Chapter 2.

3.3. Research Significance

Use of large diameter Grade 80 reinforcement in Type II CIDH piles reduces construction time and cost. This research provides insight on the viability of using high-strength large diameter bars in the non-contact splice region of Type II piles through full-scale experimental testing of a column extending into a Type II pile. The experimental test results are used to validate a nonlinear finite element (FE) model using commercially available finite element analysis software, ATENA® by Cervenka Consulting, incorporating newly calibrated bond-slip and material models. The validation of this FE model will be invaluable for future work, as nonlinear finite element analyses are increasingly used to predict the behavior of structures.

3.4. Experimental Investigation Test Program

A full-scale test specimen was built and tested to investigate the behavior of large diameter Grade 80 reinforcing bars in the plastic hinge and non-contact splice regions of columns extending into Type II piles, see Figure 3.2.

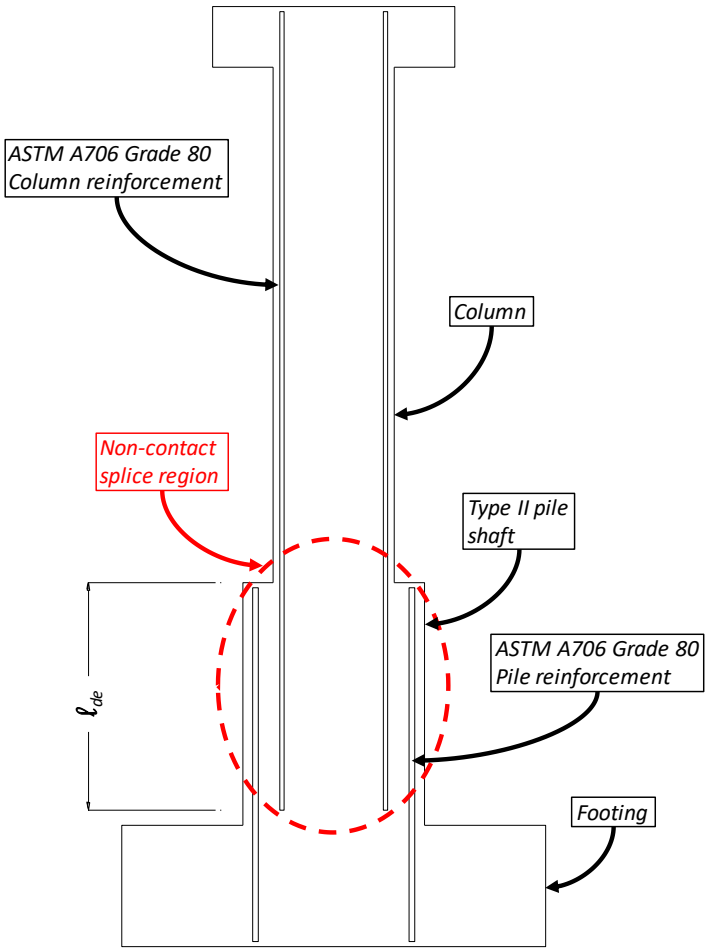

Figure 3.2. Non-Contact Splice Region in Type II Pile Shaft

The specimen consisted of a 4 ft (1.2 m) diameter by 17 ft (5.2 m) high column extending into a 6 ft (1.8 m) diameter by 8 ft (2.4 m) high pile resting on a 8 ft (2.4 m) by 14 ft (4.3 m) by 4 ft (1.2 m) high footing, with a 8 ft (2.4 m) by 8 ft (2.4 m) by 2 ft (0.6 m) deep load stub at the top of the column to apply the axial and lateral loads, all cast in the upright orientation, see Figure 3.3. The specimen was reinforced entirely with ASTM A706 Grade 80 bars, as shown in Figures 3.3 and 3.4. The column was reinforced with 14 #14 bars longitudinally, for a reinforcement ratio of $\rho_l = 1.74\%$, and double #5 butt-welded hoops spaced at 5 in. (127 mm), for a volumetric reinforcement ratio of $\rho_v = 1.14\%$. The

pile longitudinal reinforcement consists of 20 #18 bars, for a reinforcement ratio of $\rho_l = 1.96\%$, with #7 hoops butt-welded hoops spaced at 5 in. (127 mm) on center, for a volumetric reinforcement ratio of $\rho_v = 0.74\%$.

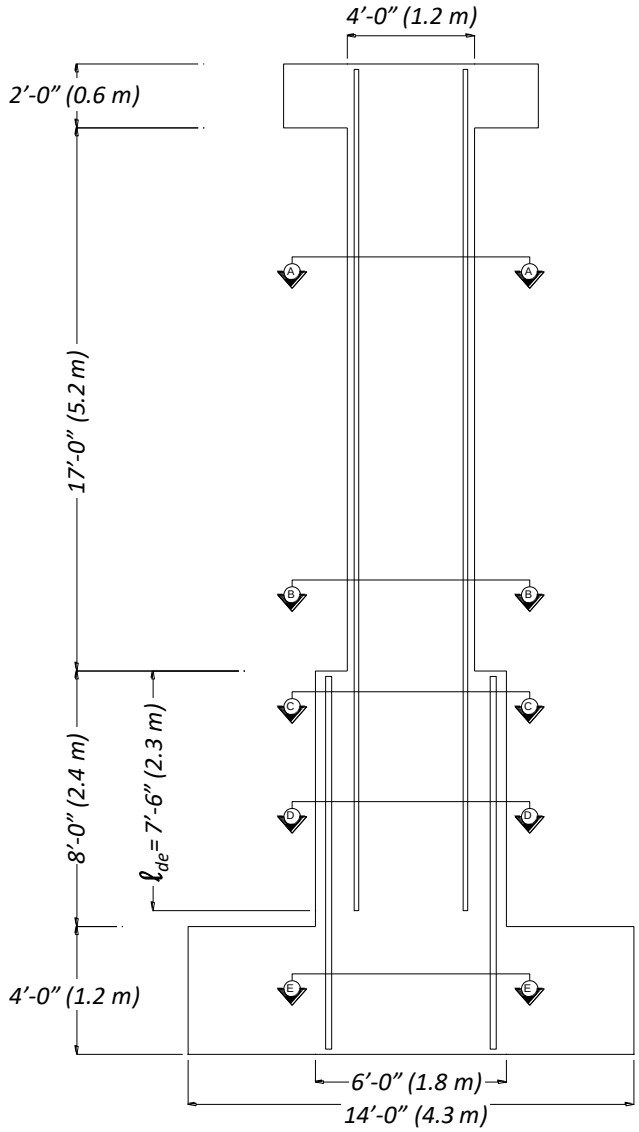

Figure 3.3. General Dimensions of Test Specimen (Elevation View)

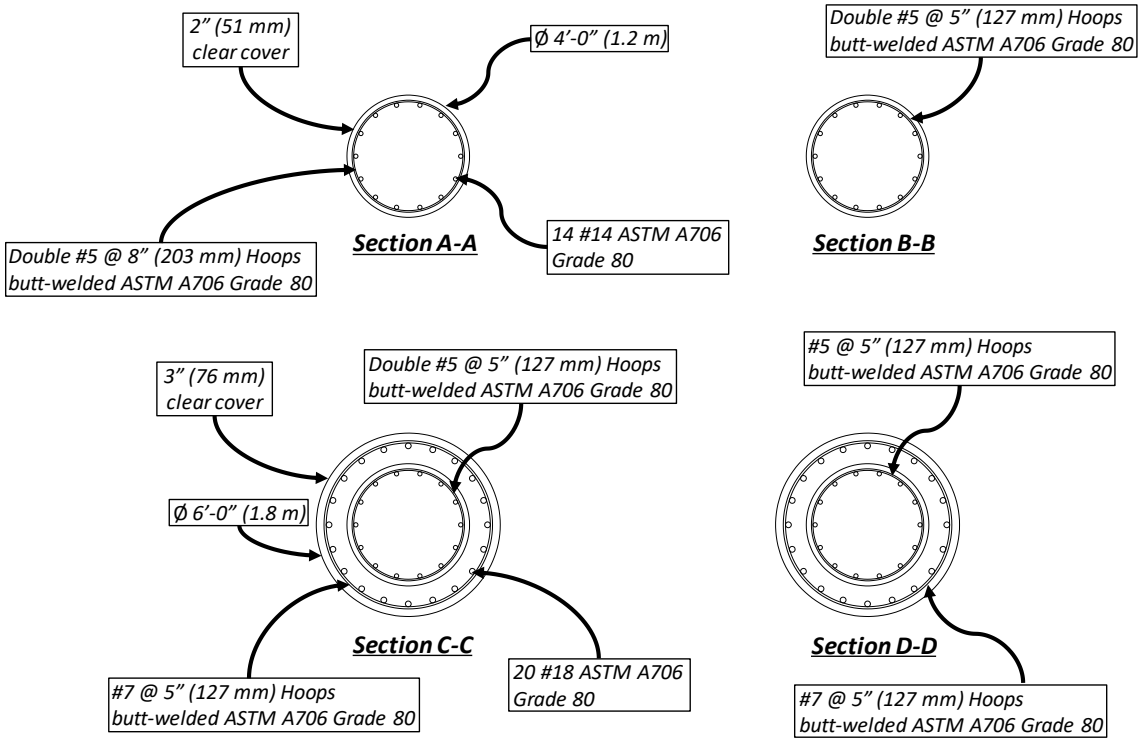

Figure 3.4. Reinforcement Configuration of Test Specimen

Bars from the same heat as those used in the strain penetration and development length set of experiments (Chapter 2) were used as the longitudinal reinforcement in the column and pile. The monotonic stress-strain responses of these bars are shown in Figures 2.2 and 2.3. Since all hoops were butt-welded, validation tests were performed in accordance with Caltrans Test 670[25] to ensure the desired and adequate performance from the column hoops. It should be noted however, since the pile shaft hoops were size #7, due to the limited equipment availability, straightening and performing the necessary validation tests on these hoops was not possible. It was deemed acceptable however, since the hoops in the pile shaft were expected to remain elastic throughout testing. The complete monotonic stress-strain responses of the A706 Grade 80 #5 column hoops are presented in Figure 3.5. The stress-strain response does not show a clear linear branch and yield plateau

since the bars had previously been work-hardened to bend into hoops. Material properties for the reinforcing bars of the specimen is listed in Table 3.1, and Table 3.2 lists the geometric properties for the bars as defined by Metelli and Plizzari[31].

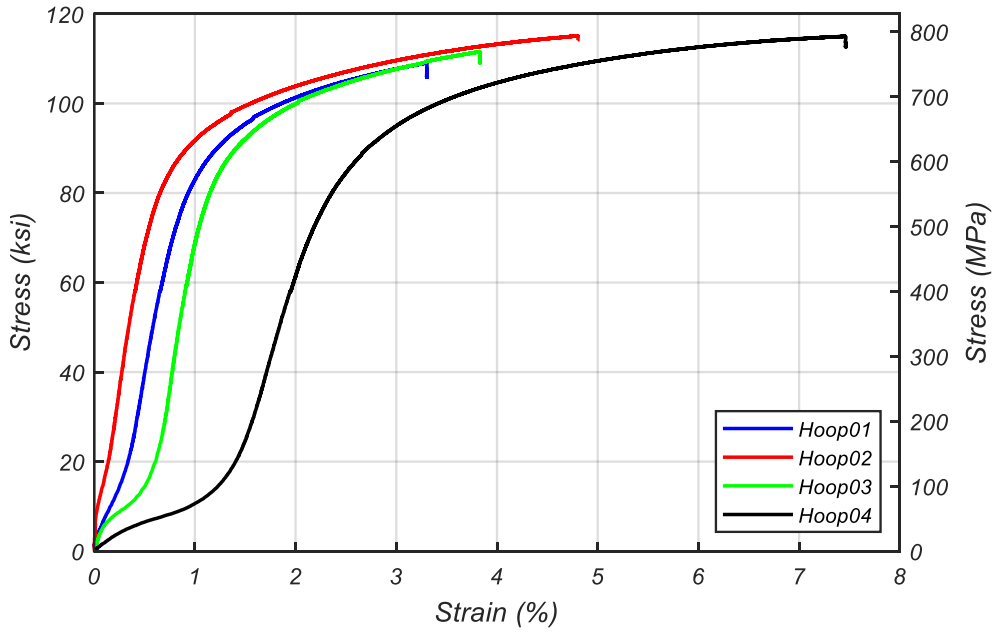

Figure 3.5. Butt-Welded Column Hoop Validation Tensile Tests

Table 3.1. Reinforcing Bars Material Properties

Bar ID	f_y (ksi) [MPa]	$f_{s4\%}$ (ksi) [MPa]	f_{su} (ksi) [MPa]	ε_y (%)	ε_{sh} (%)	ε_{su} (%)	$\frac{f_{su}}{f_y}$	$\frac{f_{s4\%}}{f_y}$	$\frac{f_{su}-f_y}{f_y}$	P
#18	82.1 [566]	103.0 [710]	110.3 [760]	0.28	0.57	10.3	1.34	1.25	0.34	3.09
#14	87.3 [602]	107.9 [744]	114.2 [787]	0.31	0.74	9.0	1.31	1.24	0.31	2.84
#7§	84.6 [583]	-	119.5 [824]	-	-	-	1.41	-	0.41	-
#5§	87.8 [605]	-	115 [793]	-	-	-	1.31	-	0.31	-

§ Information obtained from mill certificate

Table 3.2. Reinforcing Bars Geometric Properties

Bar ID	d_b (in.) [mm]	f_{Rm}	d_e (in.) [mm]	β (degrees)	s (in.) [mm]	a (in.) [mm]
#18	2.257 [57]	0.092	2.379 [60.4]	65	1.136 [28.9]	0.104 [2.6]
#14	1.693 [43]	0.109	1.779 [45.2]	72	0.967 [24.6]	0.107 [2.7]

The test specimen was built with specified 5000 psi (34.5 MPa) concrete compressive strength, cast in stages. To obtain the mechanical properties of the concrete in the test specimen, several 6 in. (152 mm) by 12 in. (305 mm) sample cylinders were taken from each region during concrete placement per ASTM C192-18[27]. The sample cylinders were capped using high-strength gypsum cement paste in accordance with ASTM C617-15[28] and tested in sets of three using the UTM per ASTM C39-18[29] throughout the curing process to monitor the compressive strength gain. Strains were measured using a compressometer with a high precision linear potentiometer as outlined in ASTM C469-14[46], and the compressive stresses were calculated by dividing the recorded forces from the UTM by the cross-section area of the sample cylinders. Figures 3.6, 3.7, and 3.8 show the monotonic stress-strain response of the tested cylinders at day of test (DOT) for the column and pile shaft respectively. The concrete mix properties as well as compressive strength at day of test (DOT) for each casting stage, f_c', are listed in Table 3.3.

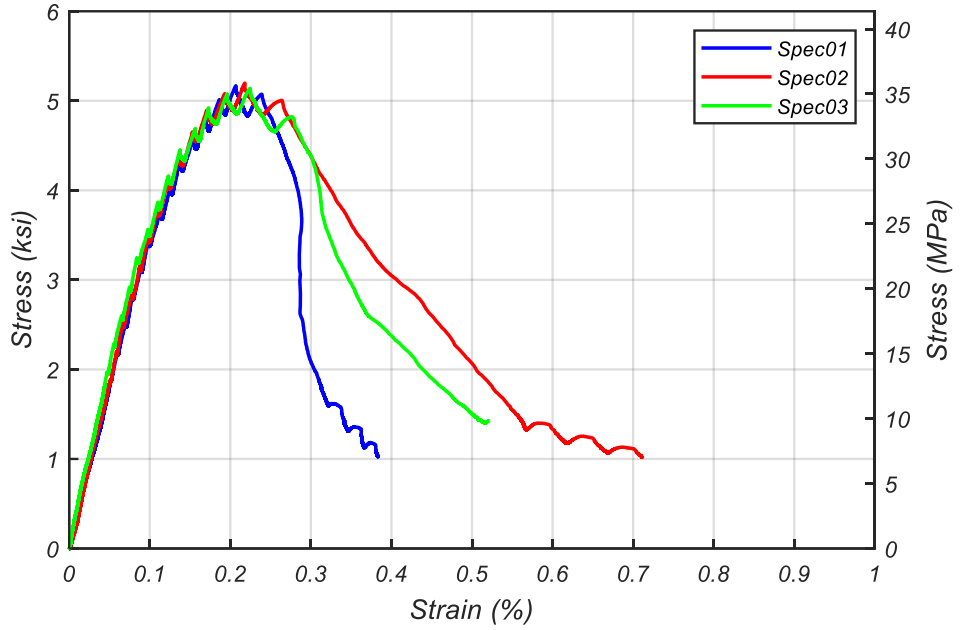

Figure 3.6. Monotonic Stress-Strain Response of Column Plastic Hinge Concrete at DOT

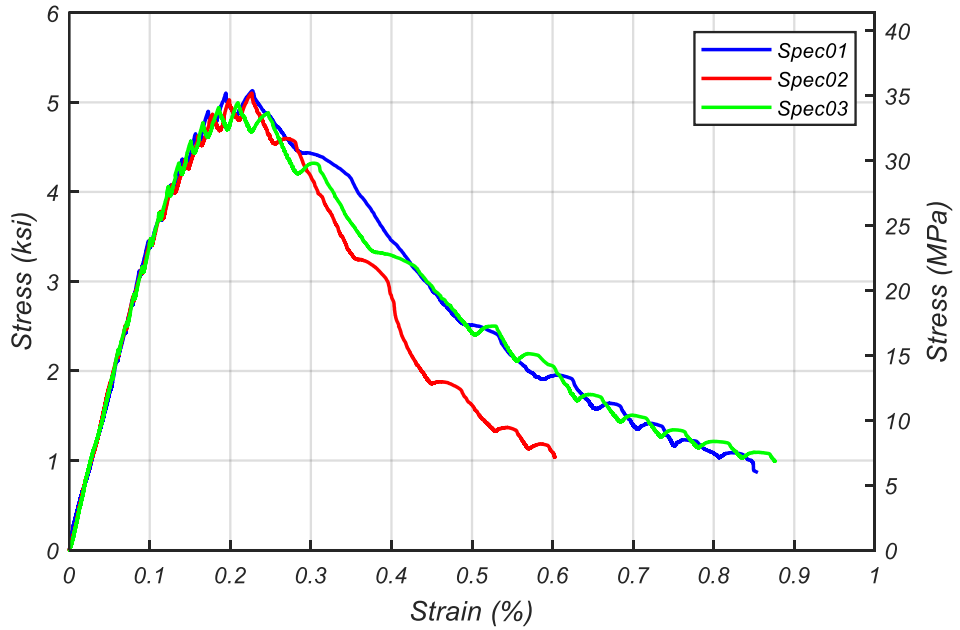

Figure 3.7. Monotonic Stress-Strain Response of Column Elsewhere Concrete at DOT

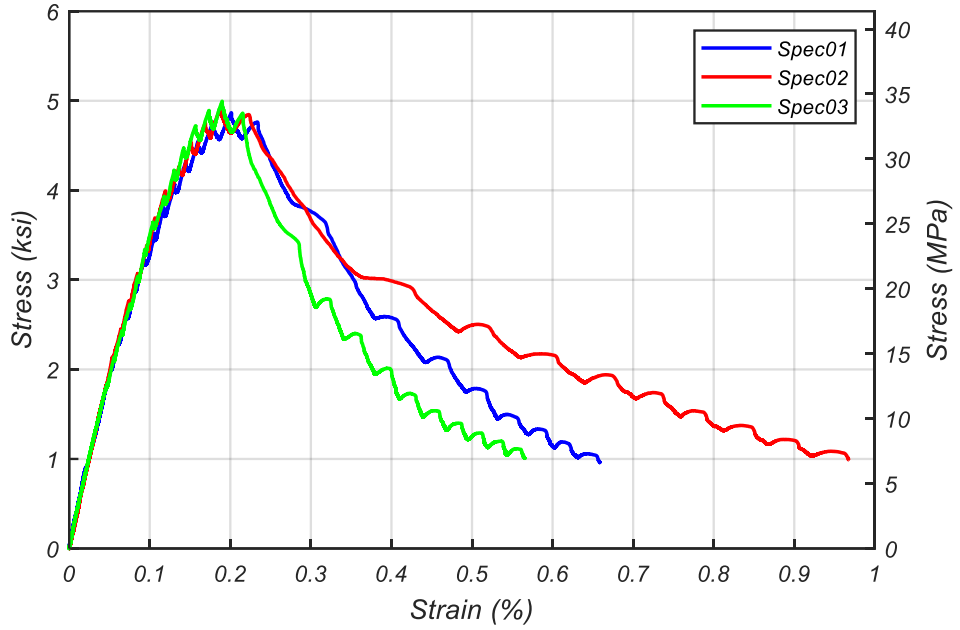

Figure 3.8. Monotonic Stress-Strain Response of Pile Shaft Concrete at DOT

Table 3.3. Test Specimen Concrete Material Properties

Region	Max. Aggregate Size (in.) [mm]	w/cm Ratio (%)	Age of Concrete at DOT (days)	f'_c (ksi) [MPa]
Column Plastic Hinge	0.75 [19]	45	57	5.17 [35.6]
Column Elsewhere	0.75 [19]	45	57	5.08 [35]
Pile	0.75 [19]	45	75	4.93 [34]
Footing	0.75 [19]	45	28[§]	4.55 [31.4]

[§] Footing concrete cylinders tested only at 28 days

Current design guidelines prescribed by AASHTO LRFD Seismic Bridge Design Specifications (SBDS)[1] and Caltrans SDC[22] require embedment lengths of the column longitudinal reinforcement into Type II shafts at substantially longer depths than the tension development length, l_d, specified in AASHTO LRFD Bridge Design Specifications[1]. This increased embedment length is considered to account for the

additional damage which spreads into the bar anchorage region of piles due to plastic deformations at the base of the column. Through an extensive experimental and analytical study, Murcia-Delso et al.[45] expanded on findings from earlier work by McLean and Smith[43] and found that the embedment length of column longitudinal reinforcement into Type II piles may be reduced, while maintaining satisfactory performance, see Equation 3.1.

$$l_e = l_d + s + c \qquad 3.1$$

where c is the thickness of the concrete cover above the top of the pile longitudinal reinforcement, l_d is the tension development length as prescribed in AASHTO LRFD Bridge Design Specifications[1], and s is the bar spacing in the non-contact lap splice.

Following the findings from Murcia-Delso et al.[45], the longitudinal reinforcement of the test column was extended into the pile at a reduced length compared with current design guidelines provided by ACI 318-14[47], AASHTO LRFD Bridge Design Specifications[1], and Caltrans SDC[22], when scaled up using Grade 80 material properties. A comparison of the embedment length of the column longitudinal bars into the pile is presented in Figure 3.9. It should be noted that Caltrans SDC[22] prescribes a staggered configuration for embedment of bars into piles where every other bar extends a longer depth. The test specimen in focus of this research did not make use of this staggered configuration, and instead embedded the longitudinal reinforcement all at the same depth, equal to 60% of the longest or 105% of the shortest length required in the staggered configuration. The chosen embedment length is presented to be on average 77% of that required by Caltrans SDC[22].

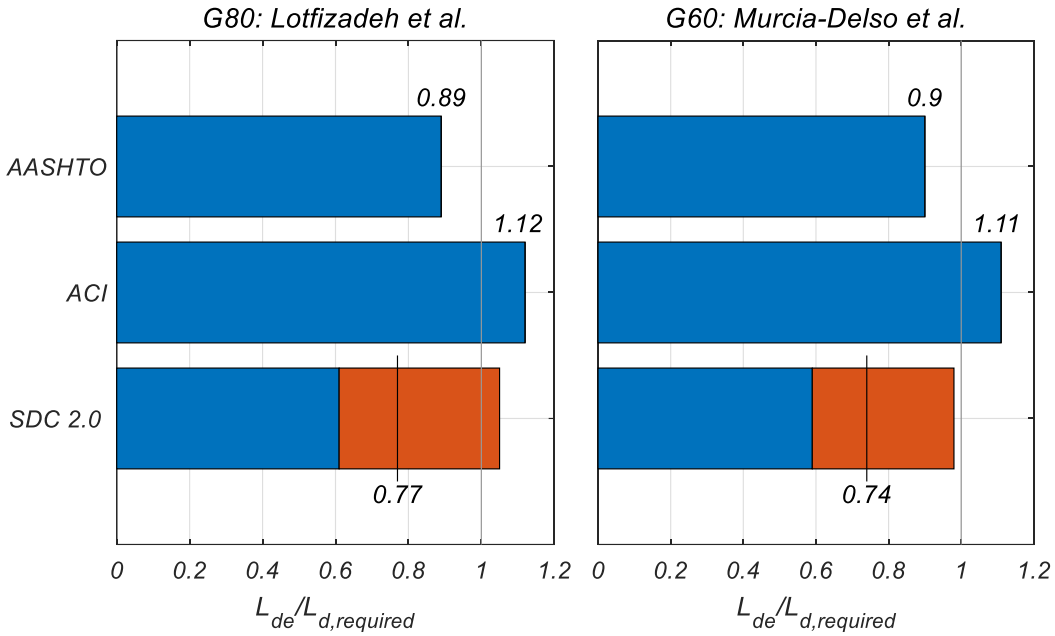

Figure 3.9. Comparison of Column Longitudinal Bar Embedment Length

An additional axial load of 8.9% of $f_c' A_g$ was continuously applied on the specimen using four hydraulically post-tensioned rods attached to the load stub at the top of the column and fixed to the strong floor of the laboratory. Slotted holes were designed in the footing where the post-tensioning rods pass through. These slotted holes prevent any pinching of the post-tensioning rods at high displacements during testing. The lateral load required to cyclically push and pull the top of the column was applied to the load stub using two 220 kip (979 kN) hydraulic actuators. To prevent lateral instability, the two horizontal actuators were mounted parallel one another at the center of the load stub. The overall elevation view of the test setup is presented in Figure 3.10.

(a) (b)

Figure 3.10. Overall Elevation View of Test Setup

The loading protocol was set up to initially perform incremental load-controlled cycles of 20%, 40%, 60%, and 75% of the first yield force, F_y, then the loading scheme was switched to a displacement-controlled scheme which performed three complete push-pull cycles at each displacement ductility level, Δ_y. These increasing magnitude displacement-controlled cycles were repeated until the test was stopped for safety reasons at a displacement ductility of 6 (drift ratio of approximately 11%) after many of the column longitudinal reinforcement had fractured, see Figure 3.11.

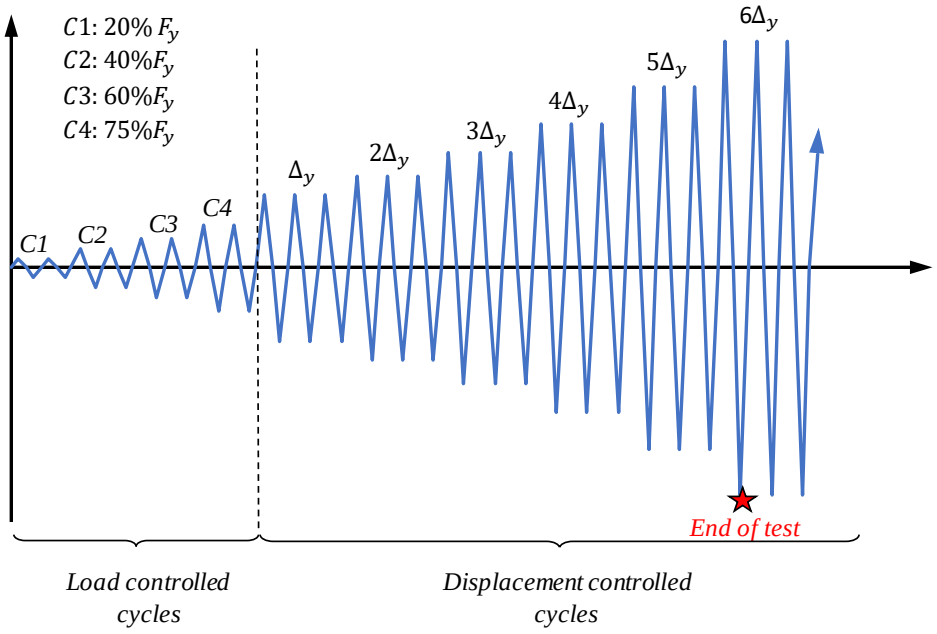

Figure 3.11. Test Loading Protocol

The strains in the longitudinal and transverse reinforcement in the column and pile were monitored with an array of 0.2 in. (5 mm) high-elongation 120 Ohm electrical-foil strain gages. Particular attention was given to the instrumentation of the bars within the plastic hinge region of the column and along the non-contact splice length within the pile. Instrumentation of a representative column longitudinal bar and column hoop are presented in Figure 3.12.

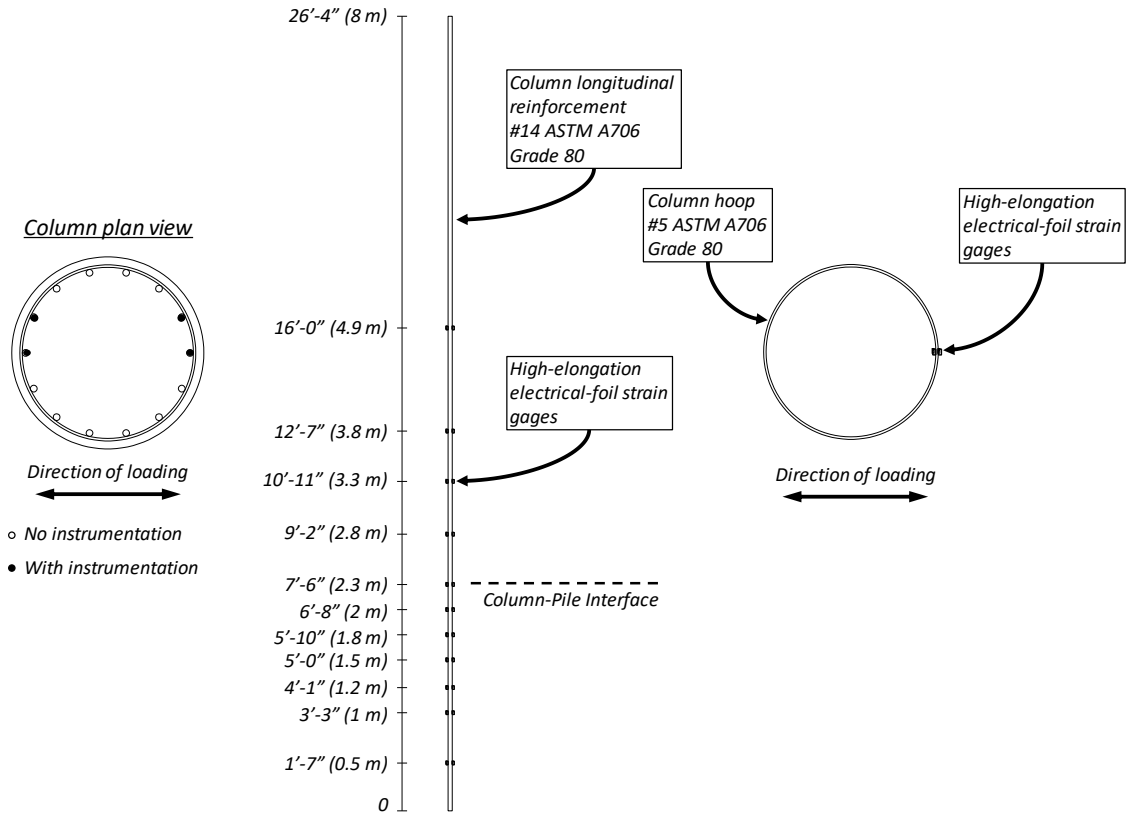

Figure 3.12. Representative Column Longitudinal and Transverse Reinforcement Instrumentation

Similarly, a representative instrumentation layout for the pile can be seen in Figure 3.13. Externally mounted linear potentiometers were used along the height of the column and pile to monitor the deformations of the specimen, as presented in Figure 3.14. Additionally, linear potentiometers were affixed at the column-pile and pile-footing interfaces to monitor the fixed-end rotation of each component. String potentiometers mounted at various heights along the specimen were used to monitor the global displacements during the test, see Figure 3.15. Since the displacements measured internally by the actuators are not as reliable as those measured with string potentiometers, the string

potentiometer at the top of the column was used to control the displacement-controlled push and pull cycles.

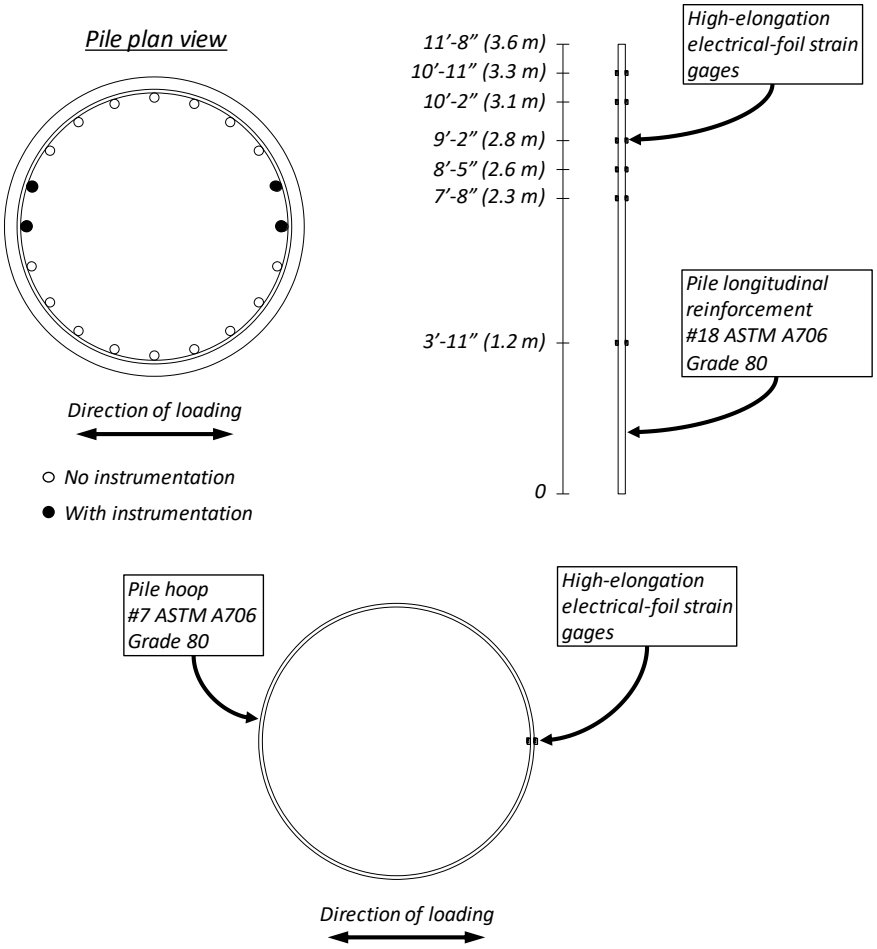

Figure 3.13. Representative Pile Longitudinal and Transverse Reinforcement Instrumentation

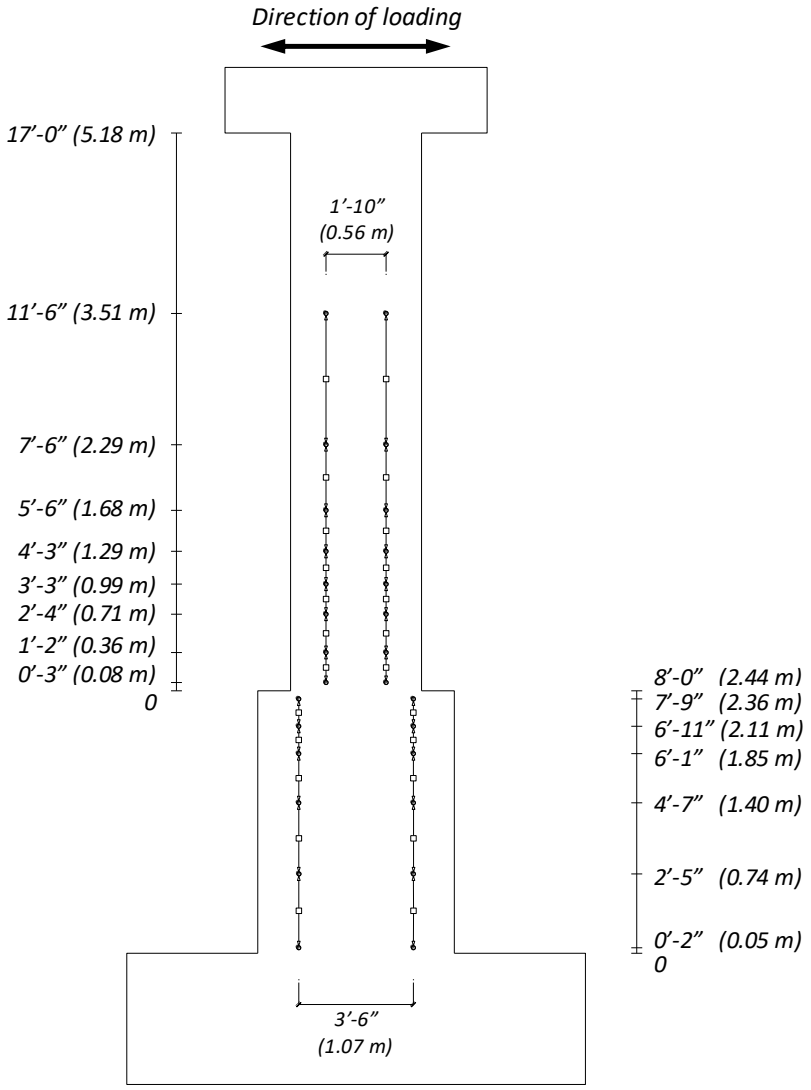

Figure 3.14. Linear Potentiometers Along Height of Test Specimen

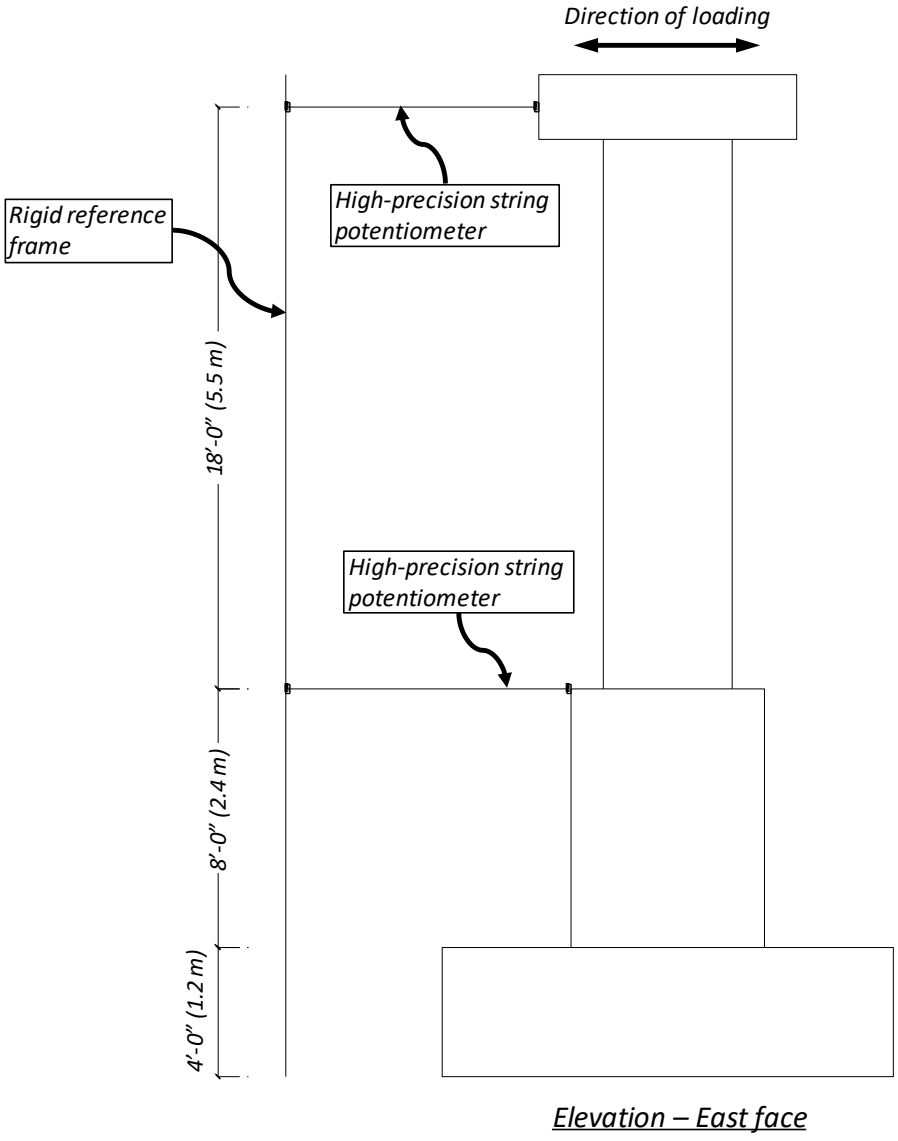

Figure 3.15. String Potentiometers Monitoring Lateral Displacements

Data obtained from this experiment, along with findings from the earlier study investigating the bond-stress of ASTM A706 Grade 80 reinforcement presented in Chapter 2, were used to calibrate and validate a detailed nonlinear finite element model using continuum 3D elements with fracture-plastic constitutive material laws for the concrete, and line elements with uniaxial constitutive materials to characterize the axial stress-strain

response of high-strength reinforcing steel. Detailed explanation of the procedure for calibration and validation of the FE model are presented by Vásquez et al.[48].Observations and results obtained from this research are presented and discussed in the following section.

3.5. Experimental Test Results

The global lateral force-displacement, as well as the normalized base column moment-displacement response of the test specimen identifying some key points along the test are shown in Figures 3.2 and 3.2. The drift ratios presented are measured from the location of the lateral load application (at the center of the load stub), to the column-shaft interface. Loading and displacements are defined as positive for the push cycles, where the load was applied in the southward direction. The base moment is normalized by the ideal moment, M_i, which is the moment capacity computed with simplified flexure theory and using measured material properties.

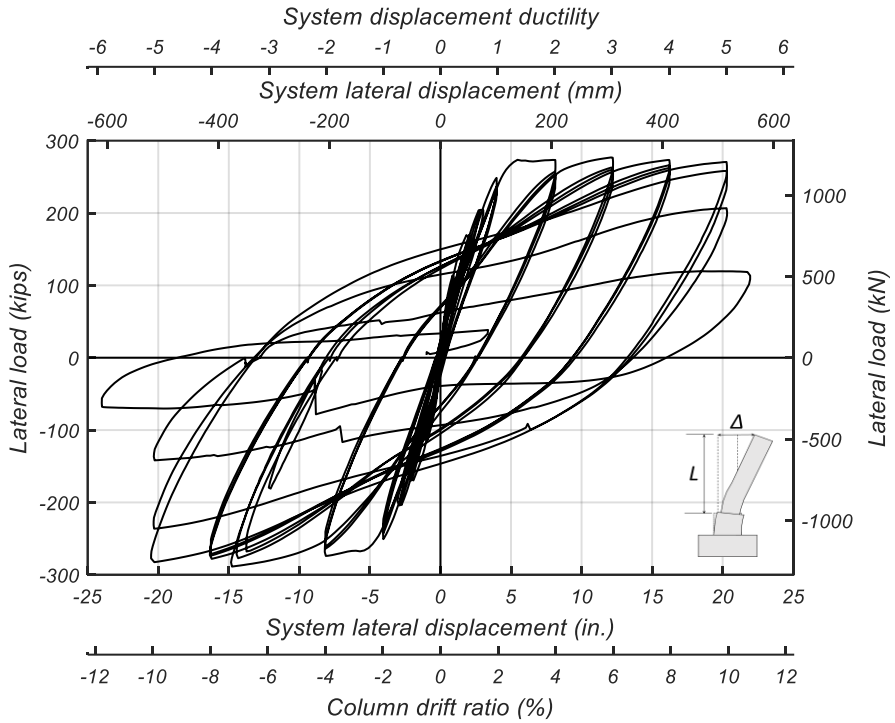

Figure 3.16. Global Lateral Load-Displacement Response of Test Specimen

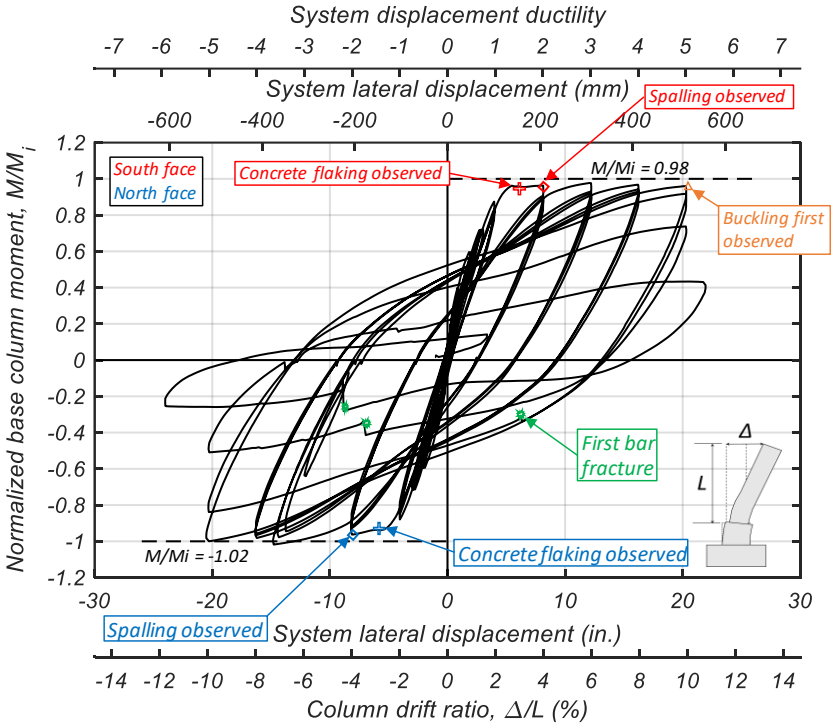

Figure 3.17. Normalized Base Column Moment-Displacement Response of Test Specimen Identifying Key Points During Testing

During the load-controlled cycles at the beginning of the test, before the column longitudinal bars had yielded, flexural cracks with a maximum residual width of 0.008 in. (0.2 mm) developed in the column. By the end of the last load-controlled cycle (75% of F_y) radial splitting cracks extending horizontally from the column base to the edge of the pile were observed. These radial splitting cracks developed as a result of the splitting forces caused by bar slip. The maximum residual width of the radial splitting cracks along the pile was measured to be approximately 0.008 in (0.2 mm).

Just beyond displacement ductility of 1, in both the push and pull load cycles (drift ratio of approximately ±3%), flaking of the concrete is observed in the compressed face of the plastic hinge region. At displacement ductility of 2 (drift ratio of approximately ±4%), spalling of the concrete is observed where concrete flaking had previously occurred.

A small drop in the lateral resistance is noticed mainly due to the P-Delta effect of the externally applied axial load. After several repeated load cycles of gradually increasing displacement demand, several longitudinal reinforcing bars in the column fractured due to fatigue and repeated buckling-straightening. Fracture in the longitudinal bars occurs as the stress concentration in the concave side of a severely buckled bar creates a compression crack along the base of the bar deformations. As the loading is reversed, and the bar begins to straighten, these compression cracks open and propagate through the bar causing fracture. When the longitudinal bars in the column begin to fracture, a substantial drop in the capacity of the column is noticeable, as expected. The column state at key points during the test are shown in Figures 3.18 and 3.19 for the south and north faces respectively.

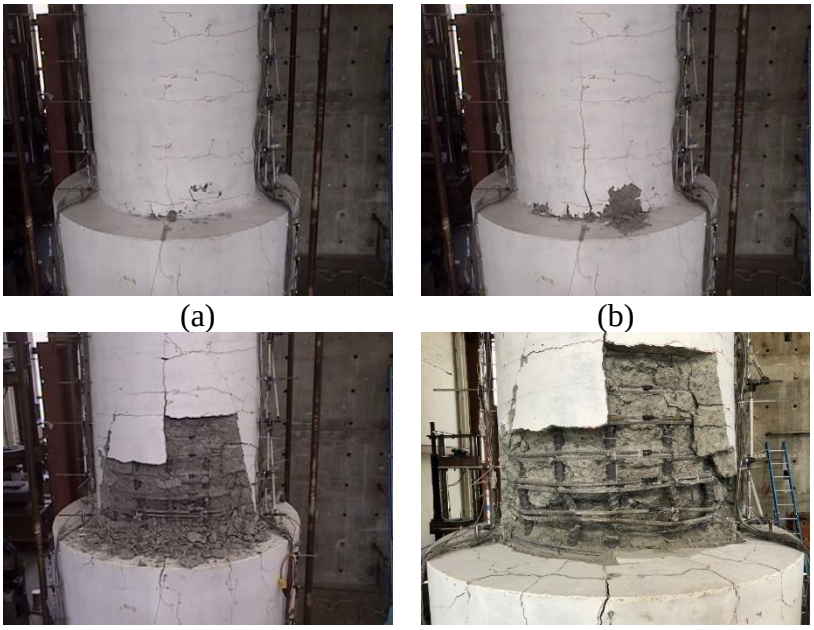

(a) (b)

(c) (d)

Figure 3.18. South Face of Column Plastic Hinge at Key Points During Test; (a) Concrete Flaking; (b) Concrete Spalling; (c) Bar Buckling Exposed; (d) Severe Bar Fracture

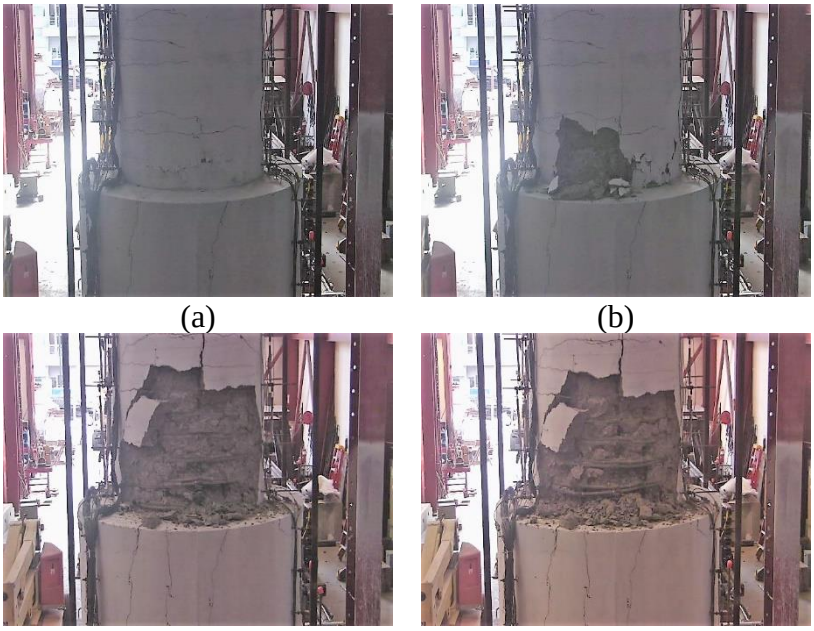

(a) (b)

(c) (d)

Figure 3.19. North Face of Column Plastic Hinge at Key Points During Test; (a) Concrete Flaking; (b) Concrete Spalling; (c) Bar Buckling and Fracture; (d) Severe Bar Fracture and Hoop Dilation

The onset of bar buckling is observed during the second load cycle at a displacement ductility of 5 (drift ratio of approximately 10%). The first bar fracture occurred after the reversal of the loading, shortly after buckling was noticed. The test continued until 9 of the 14 longitudinal reinforcing bars in the column fractured, upon completion of the first push-pull cycle of displacement ductility of 6 (drift ratio of approximately ±11%) when close to 80% of the moment capacity of the column was lost. Upon completion of the test, the column longitudinal bars were carefully extracted for inspection. Figure 3.20 outlines the fractured, buckled, and otherwise straight bars in the column plastic hinge at the end of testing. Along with the longitudinal bars, the hoops in the plastic hinge region were also extracted and examined. Since this column was reinforced with only 14 large diameter bars (#14), the polygon effect, as described by Carreño et al.[10], is clearly noticeable in these hoops, see Figure 3.21. A detailed 360° 3D point cloud model was developed to fully capture and catalog the extent of damage in the plastic hinge region at the end of testing, as presented in Figure 3.22.

The maximum lateral load resistance, effective yield displacement and drift ratio, and displacement ductility capacity of the test specimen are presented in Table 3.4. As the displacement ductility capacity of columns is defined as the maximum ductility attained prior to the first bar fracture, the test specimen attained a ductility capacity of 5.

Table 3.4. Test Specimen Global Response Summary

Maximum Lateral Load (kips) [kN]	Equivalent Yield Displacement, Δ_y (in.) [mm]	Equivalent Yield Drift Ratio (%)	Displacement Ductility Capacity
288.7 [1284]	4.05 [103]	2	5

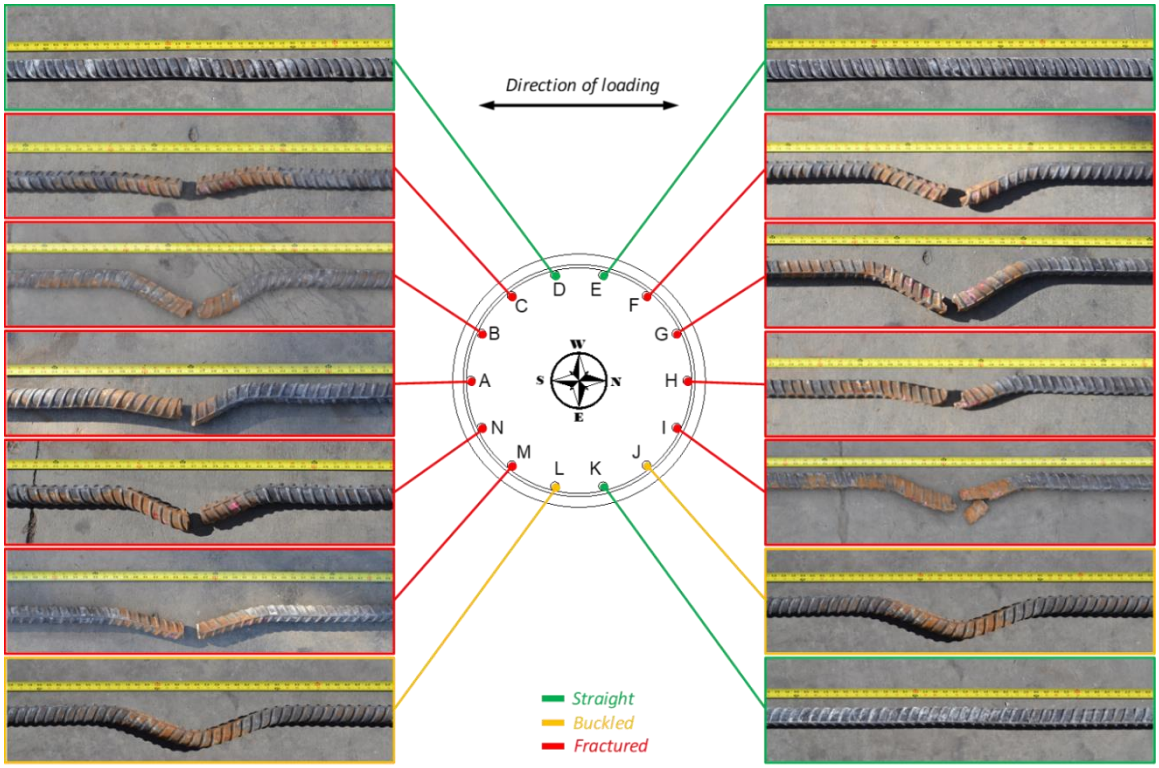

Figure 3.20. Column Longitudinal Bars Extracted from Plastic Hinge Region Post-Test

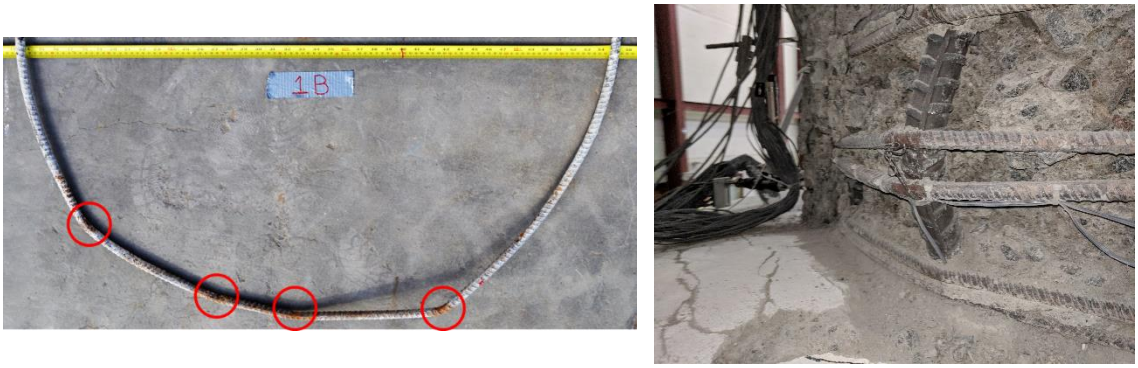

(a) (b)

Figure 3.21. Column Hoop Extracted from Plastic Hinge Region Post-Test Showing "Polygon Effect": (a) Extracted Hoop; (b) Longitudinal Bar Pushing Hoop

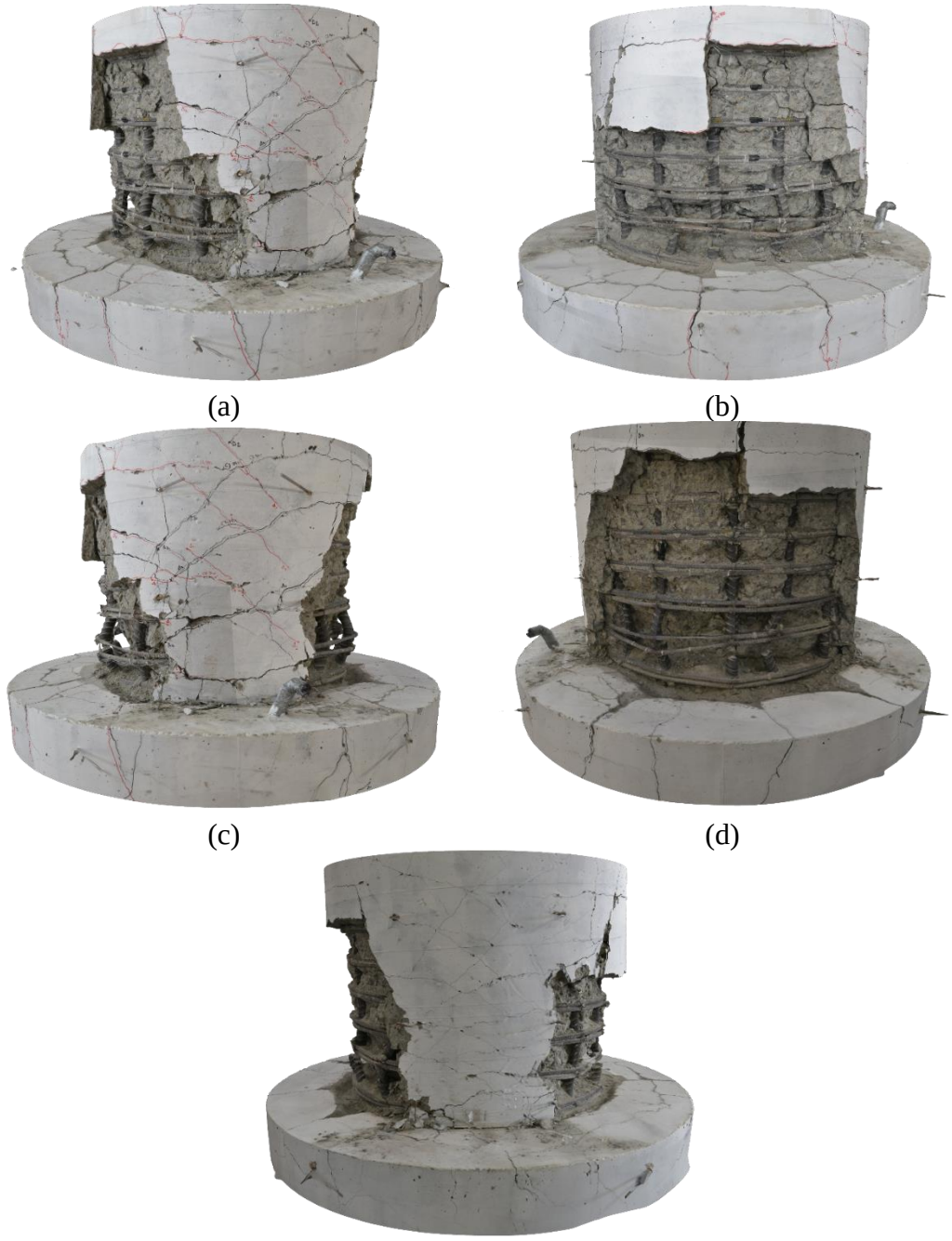

(a) (b)

(c) (d)

(e)

Figure 3.22. 360° Detailed 3D Point Cloud Model Showing Extent of Damage in Column Plastic Hinge Region Post-Test

3.6. Data Processing and Interpretation

Curvatures along the height of the column were obtained using data recorded from panels of vertical linear potentiometers, see Figure 3.14. The simple computational steps required to obtain the curvature from each panel is shown in Equation 3.4.

$$\varepsilon_{Ni} = \frac{\frac{d_{ENi}}{L_i} + \frac{d_{WNi}}{L_i}}{2} \quad 3.2$$

$$\varepsilon_{Si} = \frac{\frac{d_{ESi}}{L_i} + \frac{d_{WSi}}{L_i}}{2} \quad 3.3$$

$$\varphi_i = \frac{\varepsilon_{Si} - \varepsilon_{Ni}}{\delta_i} \quad 3.4$$

where ε_S and ε_N are the average strains within each panel in the south and north side of the column respectively, i refers to the panel number, d_{EN} and d_{ES} are the relative displacements measured by the potentiometers on the north and south side of the east face of the column, d_{WN} and d_{WS} are the relative displacements measured by the potentiometers on the north and south side of the west face of the column, L is the gage length of each corresponding potentiometer, and δ is the distance between north and south potentiometer sets.

Figure 3.23 presents the curvature profile of the column at every displacement ductility level. Since the curvatures were calculated from measurements at discrete locations along the height of the column, they are presented as constant between measurement locations. It should be noted that the curvature profile begins at 3 in. (76 mm) above the column-pile interface. Within the 3 in. (76 mm) above the column-pile interface,

specific linear potentiometers were mounted to measure the fixed-end rotation of the column.

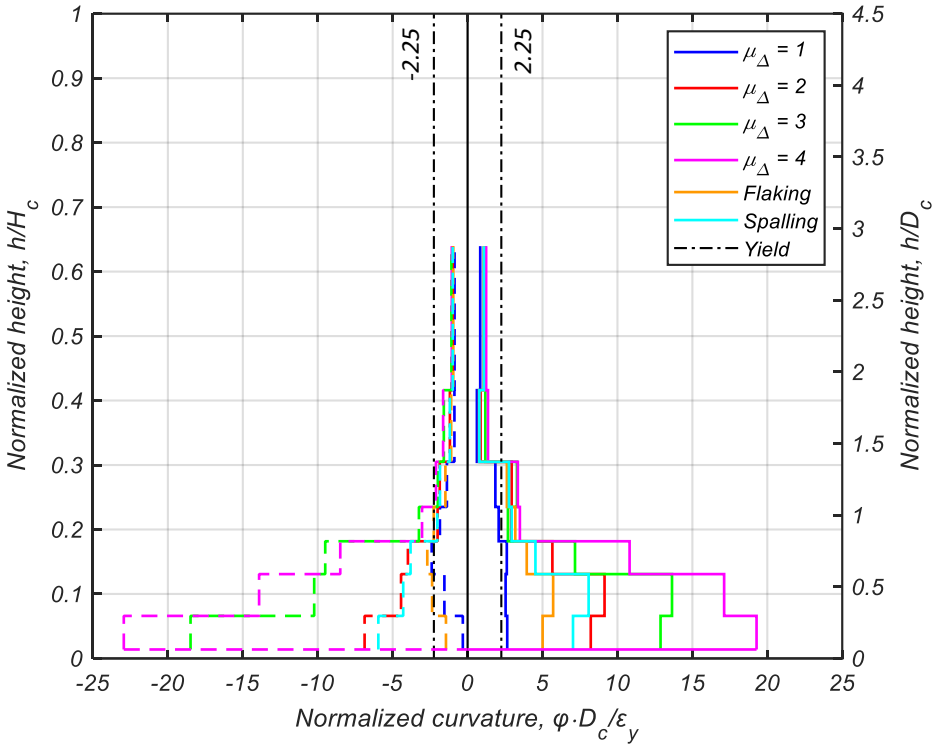

Figure 3.23. Curvature Profile of Column Obtained from Linear Potentiometers

The yield curvature, φ_y, is calculated using the approximate formulation provided by Priestley (2003)[49] for circular columns, see Equation 3.5.

$$\varphi_y = 2.25\frac{\varepsilon_y}{D} \qquad 3.5$$

where ε_y is the yield strain of the longitudinal reinforcing bars, and D is the diameter of the column.

As shown in Figure 3.23, the maximum curvatures observed in the lower 30% of the column exceed the yield curvature. The curvatures along the height of the pile were

similarly computed, however since the curvatures observed in the pile were insignificant and well below the yield curvature, they are not presented.

Similarly, the compressive strain profile of the concrete surface on the south and north side is evaluated at each displacement ductility level and presented in Figures 3.24 and 3.25 respectively. As expected, the concrete in the lower 30% of the column height experienced the most severe compressive strains resulting in crushing of the concrete.

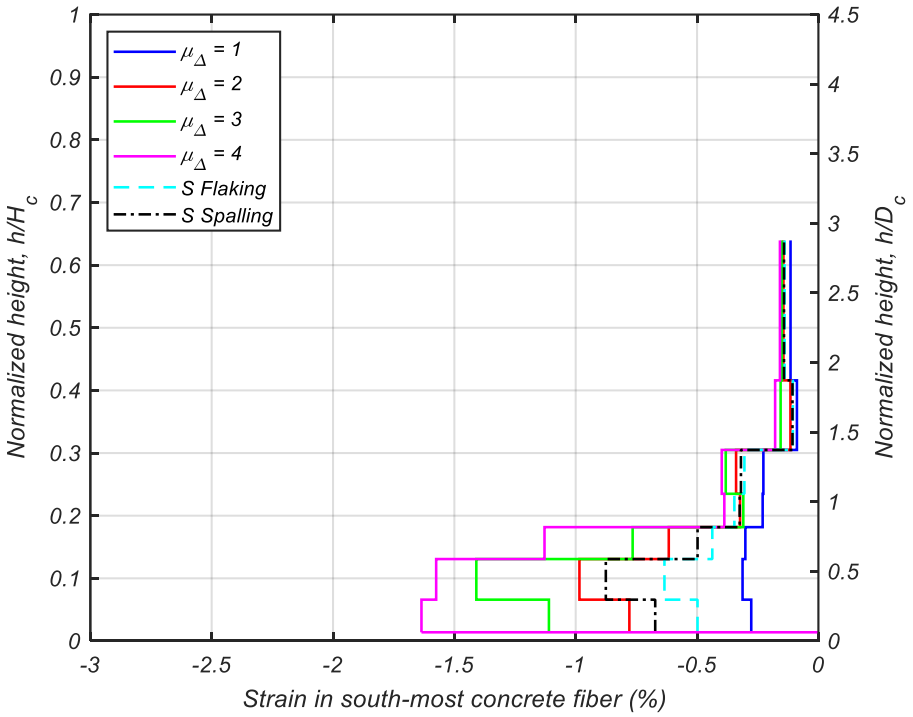

Figure 3.24. Column Concrete Compressive Strain Profile of Southern Face

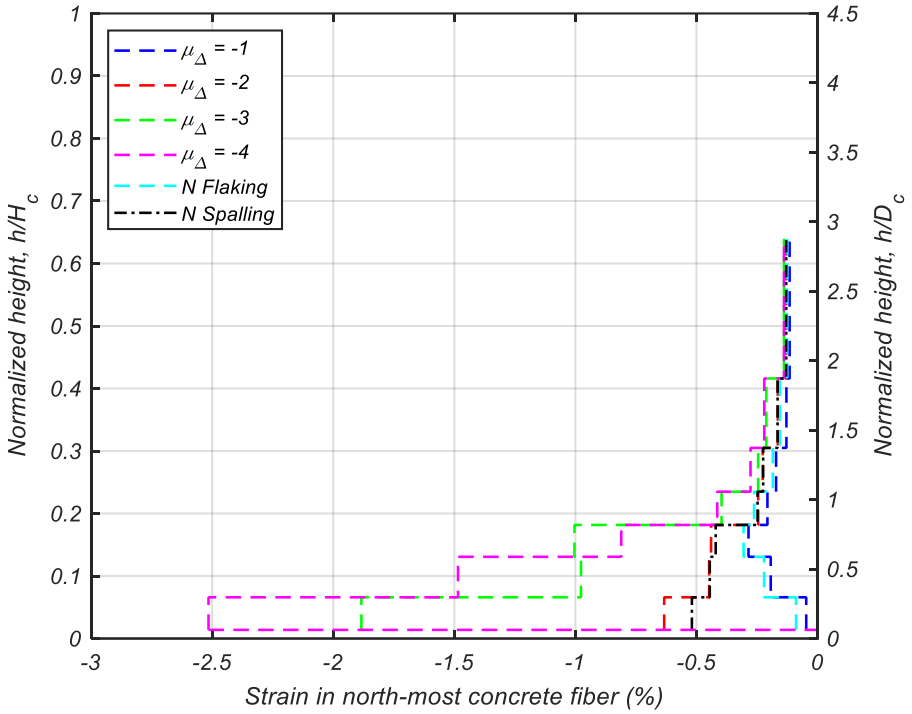

Figure 3.25. Column Concrete Compressive Strain Profile of Northern Face

Similarly, the smeared strains in the longitudinal reinforcing bars on the extreme northern and southern faces of the column are evaluated at every displacement ductility level and presented in Figures 3.26 and 3.27, where all the push cycles are plotted with continuous lines, and all pull cycles with dashed lines. Bar strains in the lower 30% of the column height exceed the measured yield strain, and the gradual decrease in bar strains is observed farther away from the plastic hinge region.

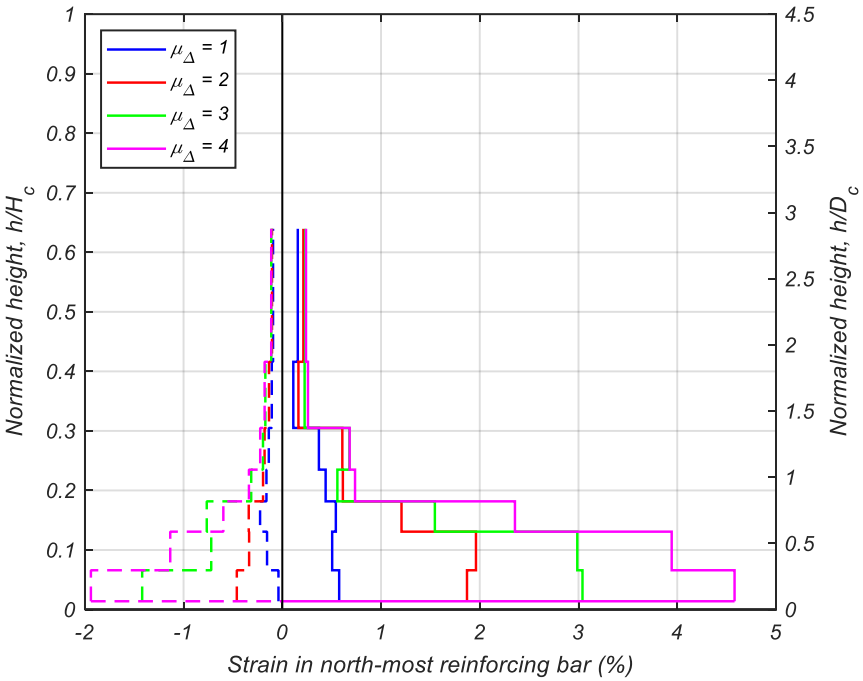

Figure 3.26. Smeared Strain Profile of Northern-Most Column Reinforcing Bar

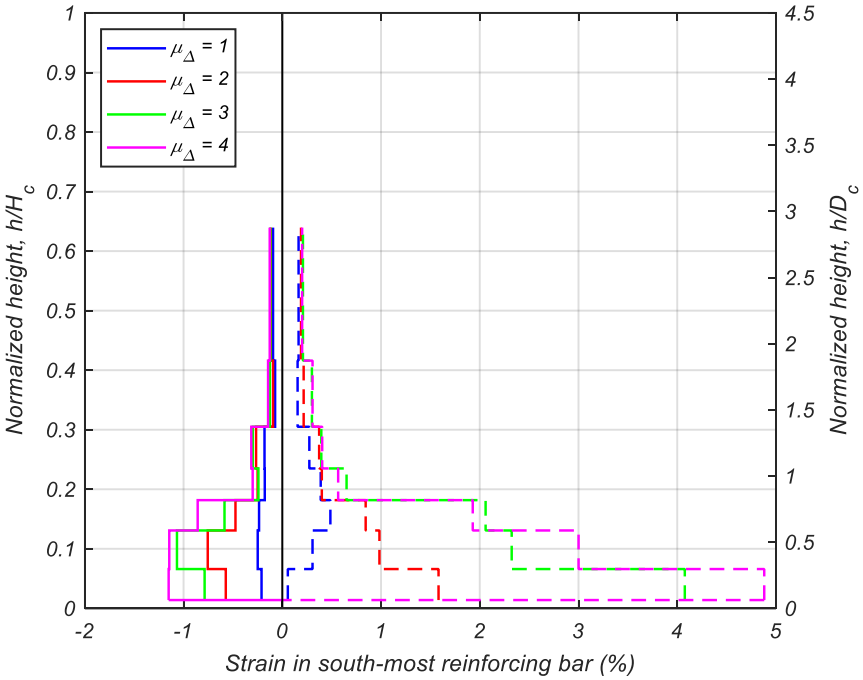

Figure 3.27. Smeared Strain Profile of Southern-Most Column Reinforcing Bar

As mentioned earlier, the displacement at the top of the column was measured using high-precision string potentiometers. The measured displacements at each displacement ductility level were compared with the overall displacement calculated from the data obtained by the linear potentiometers affixed along the height of the column and pile. The top displacement is decoupled into four components: (a) flexure in the column, (b) flexure in the pile, (c) fixed end rotation of the column due to yield penetration and bond slip at the column-pile interface, and (d) shear in the column. The displacements caused by each of these four components is calculated from the data obtained by the potentiometers and compared with the actual lateral displacement recorded during testing, see Figure 3.28. At displacement ductility of 6, since the column concrete had been severely crushed, many of the instrumentation on the test specimen no longer provided reliable readings and therefore could not capture the displacement contributions as accurately as at the lower ductility demand levels. It is observed that the predominant contributor to the lateral displacement is flexure in the column, which accounts for 55% to 65% of the overall displacement in the push cycles, and 40% to 55% in the pull cycles. The fixed end rotation of the column is also a major contributor to the top displacement accounting for 30% to 40% of the overall displacement in the push cycles, and 20% to 40% in the pull cycles. The displacement contributions due to flexure in the pile account for less than 8% of the overall displacement, while the shear in the column contributes even less, at about 1%.

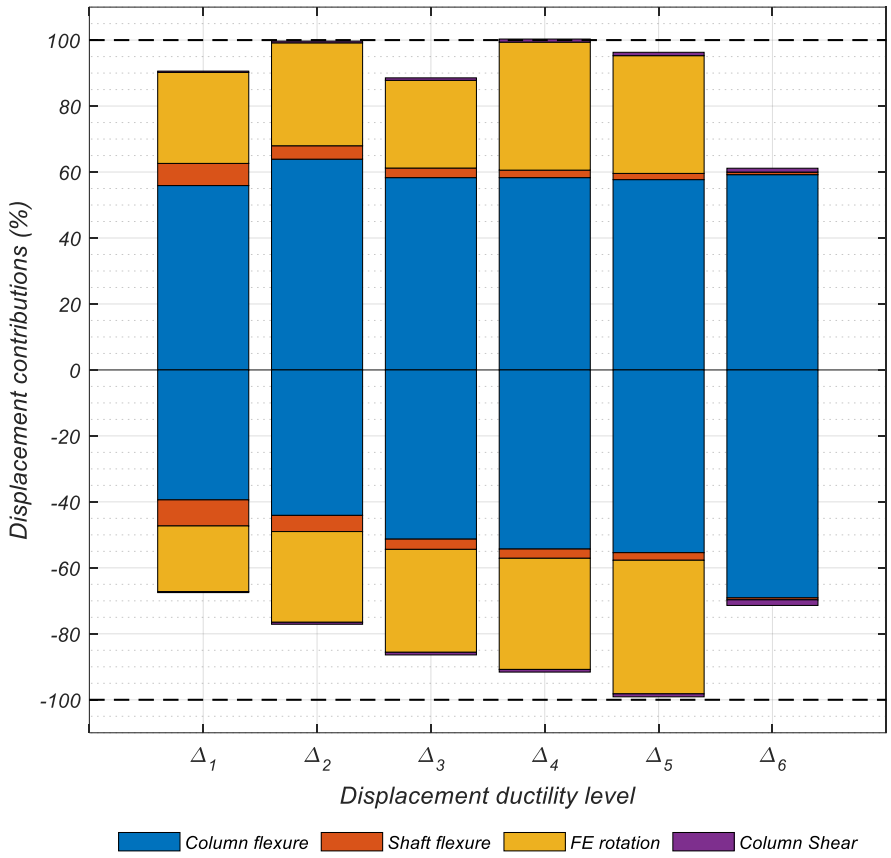

Figure 3.28. Components of Lateral Displacement at Peak Displacement Ductility Levels

Strains in four of the column longitudinal reinforcing bars were monitored with electrical-foil strain gages, two in each the north and south direction, along the direction of loading. Although most of the strain gages or their wires were damaged at high displacement ductility levels, valuable information was obtained regarding the yield strain penetration into the pile. The measured strains of these longitudinal bars at peak displacements of various cycles are presented in Figures 3.29 and 3.30. The maximum yield penetration in the bars occurred at displacement ductility of 5 and was measured to be approximately 3 ft (915 mm) or $21.25d_b$. Since the total embedment length of the

column longitudinal bars into the shaft was 7.5 ft (2.3 m), which is just over $53d_b$, the yield penetration of $21.25d_b$ represents 40% of the total embedment length of the bars. This indicates that the lower $31.75d_b$ of the embedment length was able to develop the yield strength of the bars. A set of strain penetration and development length tests were conducted on individual Grade 80 reinforcing bars embedded in concrete of similar strength and confinement as the specimen of focus in this study (see Chapter 2). Findings from that investigation showed that a length of $20d_b$ is sufficient to develop the yield strength of Grade 80 reinforcing bars in tension. These findings suggest that embedding the column longitudinal bars in the pile at a reduced length of $l_d + s + c$ when scaled up using Grade 80 material properties, the test specimen behaved in a ductile manner and performed adequately. The plastic strain penetration observed in the embedded column longitudinal bars confirm that, similar to the findings by Murcia-Delso et al. (2016)[45] using ASTM A706 Grade 60 bars, this reduced embedment length is sufficient to develop the tensile strength of ASTM A706 Grade 80 longitudinal reinforcement in bridge columns extending into enlarged pile shafts.

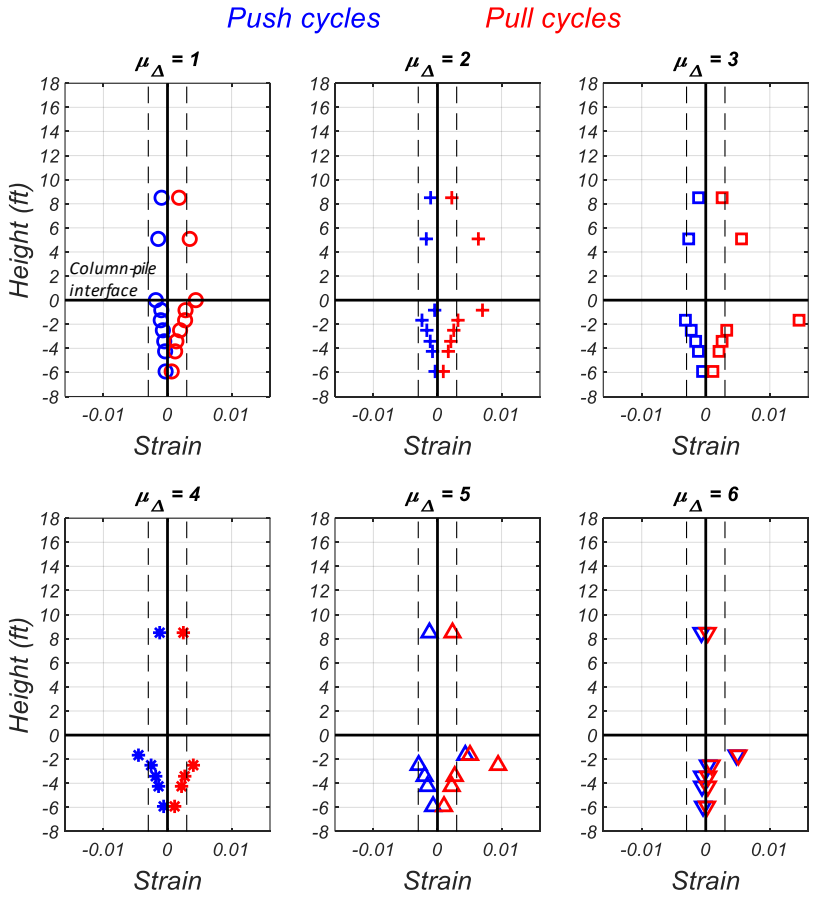

Figure 3.29. Measured Strains of Southern-Most Column Longitudinal Bar (from Strain Gages) at Peak Displacements of Various Cycles

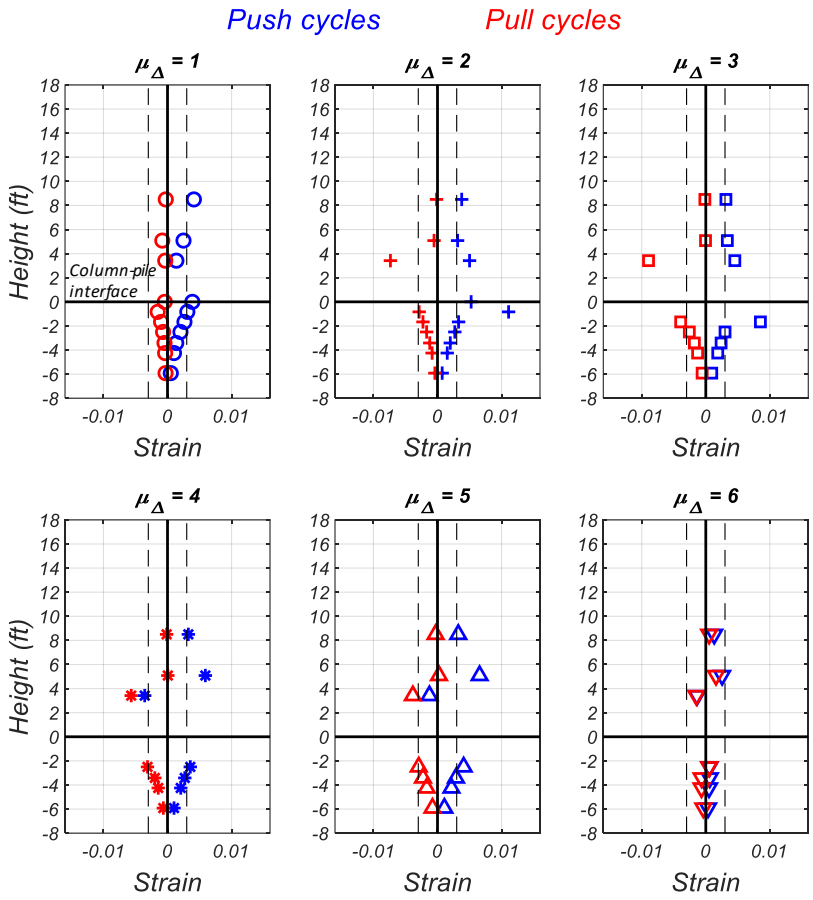

Figure 3.30. Measured Strains of Northern-Most Column Longitudinal Bar (from Strain Gages) at Peak Displacements of Various Cycles

The strain distribution in the pile longitudinal reinforcement was similarly measured. Four bars, two in the north and two in the south sides were instrumented with strain gages along their length. The measured strains of the pile longitudinal bars at peak displacements of various cycles are presented in Figures 3.31 and 3.32. Data from some of the strain gages is not available mainly due to damage incurred on the wires during the test. However, it can still clearly be seen that all bars remained elastic throughout the test. The strain distribution along the non-contact lap splice length with the column longitudinal bars

varies almost linearly suggesting a relatively linear bond stress distribution along the embedded bars, similar to the findings of Murcia-Delso et al. (2016)[45].

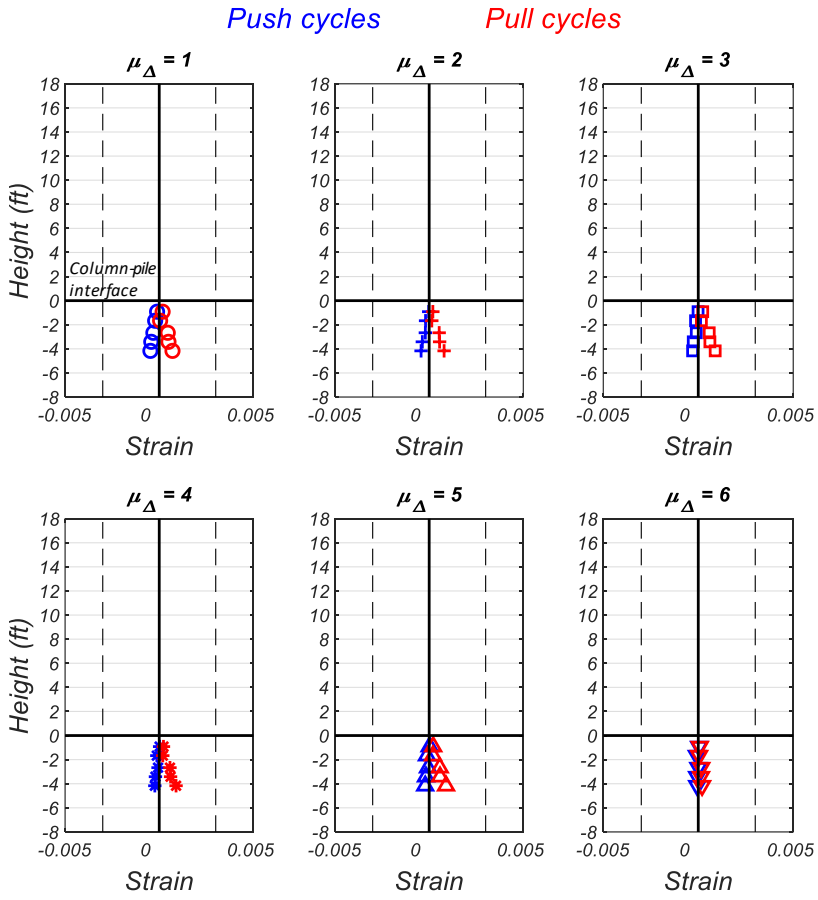

Figure 3.31. Measured Strains of Southern-Most Pile Longitudinal Bar (from Strain Gages) at Peak Displacements of Various Cycles

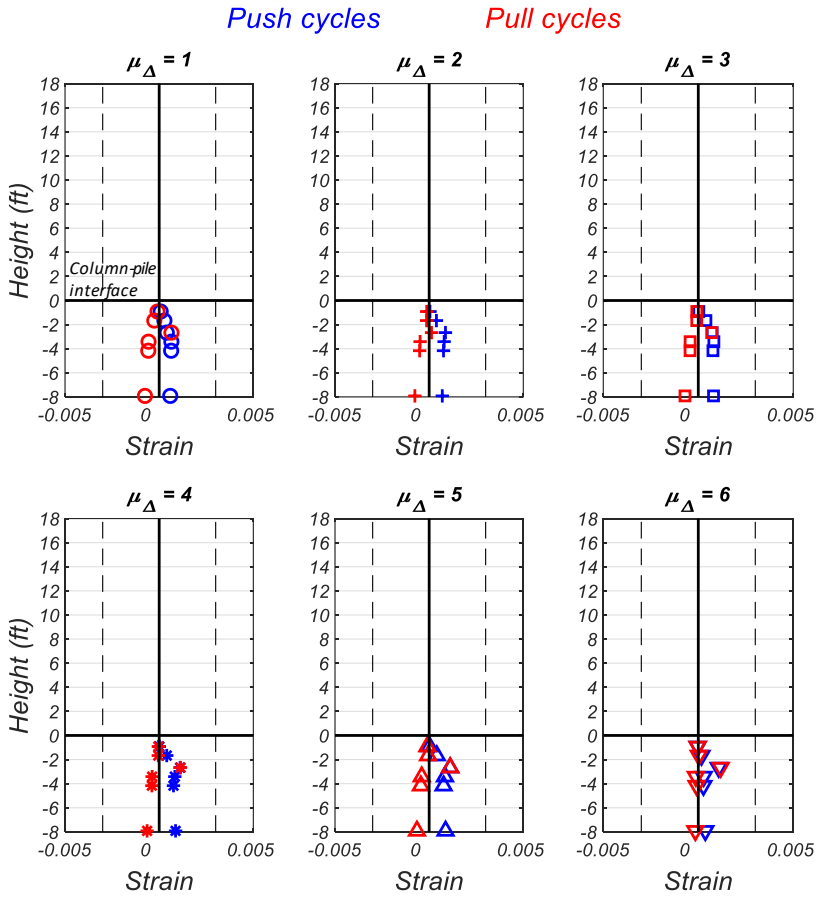

Figure 3.32. Measured Strains of Northern-Most Pile Longitudinal Bar (from Strain Gages) at Peak Displacements of Various Cycles

The strains in the transverse reinforcement of the column were also monitored with electrical-foil strain gages. Since it was expected that the transverse reinforcement in the column would remain elastic throughout most of the load cycles, select hoops were instrumented with strain gages on the south side in the direction of loading, see Figure 3.33. A total of 6 hoops in the plastic hinge region of the column, and 5 hoops within the embedment length inside the pile were monitored. All hoops remained elastic until displacement ductility of 4 (drift ratio of approximately 8%), where the crushing of the concrete and buckling of the longitudinal reinforcing bars in the plastic hinge region caused

the hoops to yield, see Figure 3.34. By the end of testing, due to the large stresses imposed on the hoops by the buckling of the longitudinal bars, some hoops were severely deformed and clearly exhibited the polygon effect yet none of them fractured.

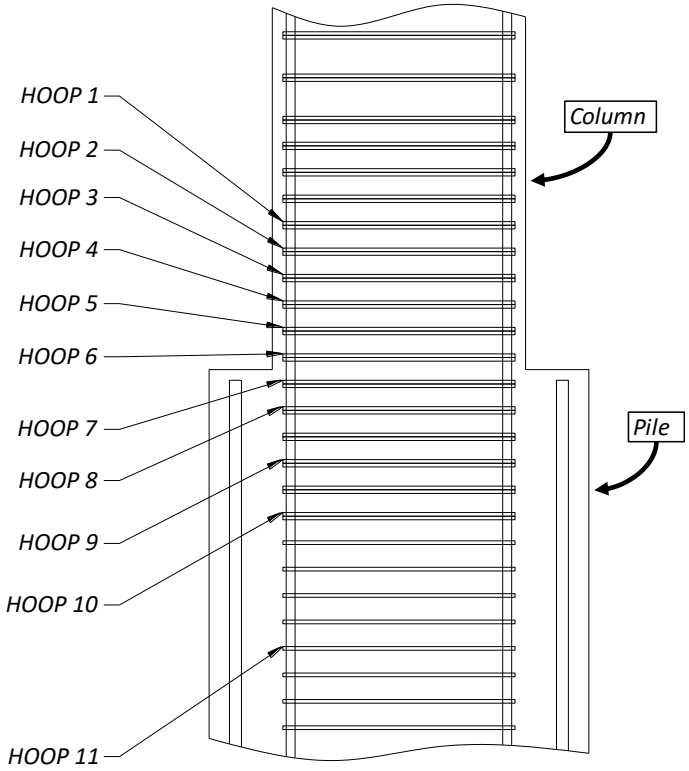

Figure 3.33. Column Hoops Instrumented with High-Elongation Electrical Foil Strain Gages

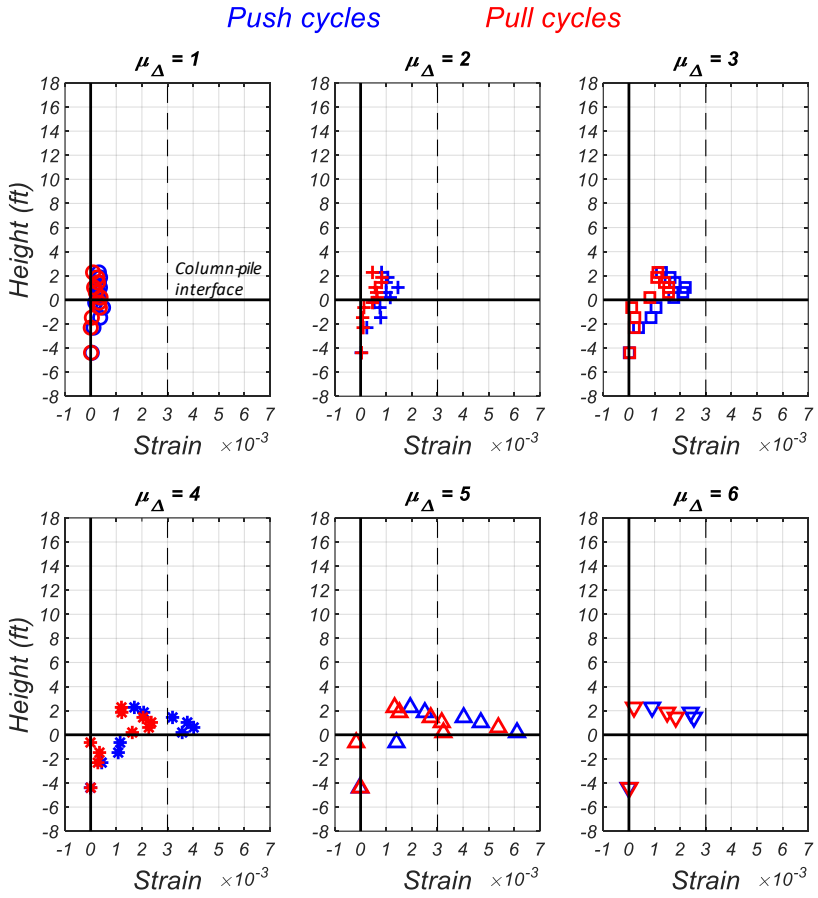

Figure 3.34. Measured Strains of Column Hoops (from Strain Gages) at Peak Displacements of Various Cycles

Seven hoops within the pile were also instrumented with strain gages in a similar manner as the column transverse reinforcement, as shown in Figure 3.35, and the measured strains in these hoops are presented in Figure 3.36. The pile hoops remained elastic throughout testing. The strain distribution of the pile transverse reinforcement shows that the strain decreases along the depth of the pile. Hoops at about half height of the pile experienced practically no strain. At high displacement ductility demand levels, strains in the first two hoop sets – the hoops closest to the column-pile interface – experienced strains close to yielding, yet ultimately, they remained elastic. The higher strains observed in the

upper hoops can likely be attributed to the larger splitting forces exerted by the slippage of the column longitudinal bars in the upper region of the pile.

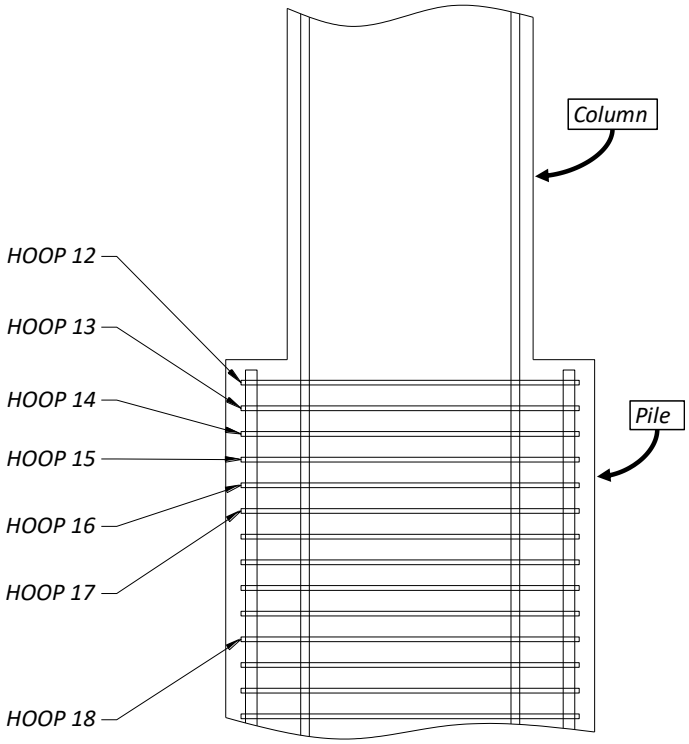

Figure 3.35. Pile Hoops Instrumented with High-Elongation Electrical Foil Strain Gages

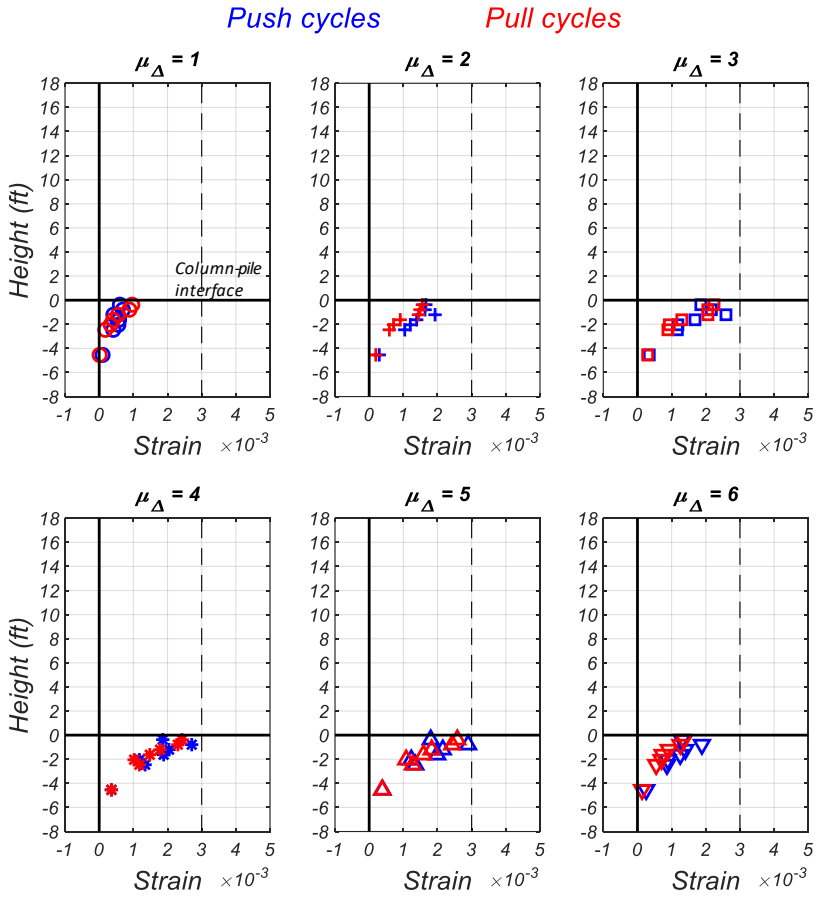

Figure 3.36. Measured Strains of Pile Hoops (from Strain Gages) at Peak Displacements of Various Cycles

3.7. Equivalent Plastic Hinge Length

The equivalent plastic hinge length is defined as the equivalent length along the column over which the plastic curvature is assumed to be constant for the estimation of plastic rotations. This is an important aspect of bridge column seismic design. The plastic hinge length is evaluated by considering the contributions from the spread of plasticity along the column height, and the equivalent length of yield penetration in the longitudinal reinforcement.

Current design guidelines set forth in AASHTO[1] and Caltrans SDC 2.0[22] present an expression to calculate the equivalent plastic hinge length of columns supported on Type II pile shafts, see Equation 3.6, which is comprised of two components: (1) a geometric term related to the spread of plasticity along the column shear span, which in the case of a cantilever column is the column height, and (2) an equivalent yield penetration term dependent of the bar diameter and expected yield strength.

$$L_p = \alpha L + \beta f_{ye} d_b \tag{3.6}$$

$$\text{where: } \alpha = 0.08 \text{ and } \beta = 0.15/\text{ksi} \tag{3.7}$$

Using this expression for the equivalent plastic hinge length has so far been the classical method of obtaining strain histories for the longitudinal reinforcing bars of bridge columns, which can predict the strain amplitudes experienced, and determine the life of the bars. Experimental work by Duck et al.[40] has shown a significant correlation between coefficient α, related to the spread of plasticity, and the displacement ductility demand. This correlation implies that the equivalent plastic hinge length is also correlated with the displacement ductility, as opposed to a constant value assumed in Equation 3.7. Using a ductility independent equivalent plastic hinge length distorts the strain amplitudes at both low and large displacement ductility demands, which affects the prediction of the strain amplitudes experienced by the bars. A smeared strain compatible equivalent plastic hinge length, $L_{p\varepsilon}$, is a more appropriate methodology for predicting the longitudinal strain history of the bars in bridge columns.

3.7.1. Smeared-Strain Compatible Method

The smeared strain compatible method considers that the equivalent plastic hinge experiences a smeared curvature less than the peak curvature, $\bar{\phi} < \phi_k$, such that the measured longitudinal strains on the extreme reinforcement on the tension and compression sides of the column, smeared of the equivalent plastic hinge length, $L_{p\varepsilon}$, equal the strains computed from the moment-curvature analysis at a curvature of $\bar{\phi}$, as demonstrated in Figures 3.37 and 3.38.

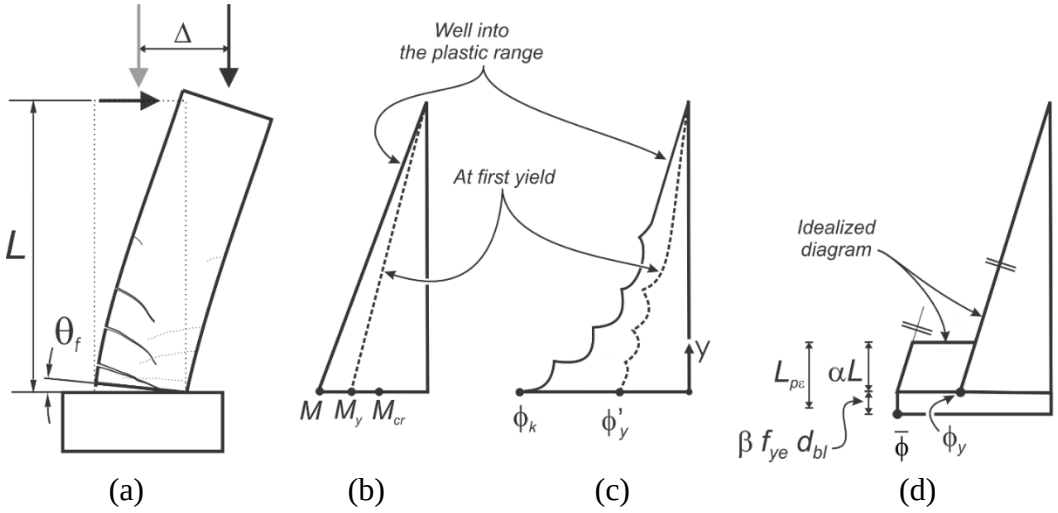

Figure 3.37. Smeared-Strain Compatible Method for Equivalent Plastic Hinge Length: (a) Deformed Column; (b) Bending Moment Diagram; (c) Curvature Diagram; (d) Idealized Curvature Diagram (Duck et al., 2018)

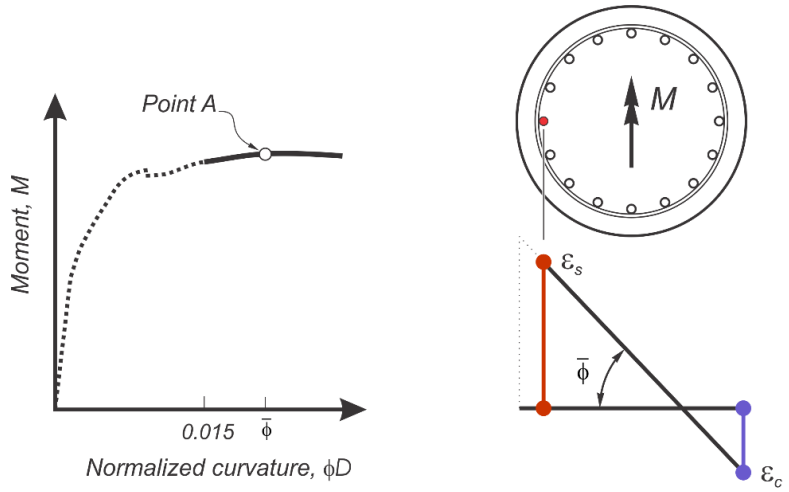

(a) (b)

Figure 3.38. Smeared-Strain Compatible Method for Equivalent Plastic Hinge Length: (a) Domain Used in the Theoretical Moment-Curvature Response; (b) Section Strain Profile at Point "A" (Duck et al., 2018)

For displacements at each ductility level, the top displacement contributions due to the fixed end rotation, Δ_{FE}, and pile shaft flexure and shear displacements, Δ_{cs}, are removed from the measured displacement leaving just the top displacement due to column flexure, Δ_{cf}, see Equation 3.8.

$$\Delta_{cf} = \Delta_c - \Delta_{FE} - \Delta_{cs} \qquad 3.8$$

where Δ_c is the measured top displacement at each displacement ductility level. The top displacement due to fixed end rotation of the column, Δ_{FE}, is evaluated by multiplying the fixed end rotation caused by the yield penetration in longitudinal reinforcement, by the column height, L, see Equation 3.9.

$$\Delta_{FE} = \theta_{FE} \cdot L \qquad 3.9$$

The sets of linear potentiometers placed along the height of the column are considered as “panels” with panel heights denoted by ℓ_i, where the subscript i represents the panel number. The predicted top displacement is calculated by integrating the curvature

profile along the height of the column. The curvature profile consists of two portions as shown in Figure 3.37(d): (1) the curvature profile at first yield, and (2) the plastic curvature developed in the plastic hinge region. The sum of the displacement contributions from both portions of the curvature profile produces the top displacement of the column due to flexure, see Equation 3.10.

$$\Delta_{cf} = \phi_y \cdot \frac{L^2}{3} + \left(\bar{\phi}_i - \phi_y\right) \cdot L_{pi} \cdot \left(L - \frac{L_{pi}}{2}\right) \qquad 3.10$$

where L_{pi} is the assumed smeared height of the plastic hinge, evaluated as the sum of the gage lengths, ℓ_i, of the deformation panels as shown in Equation 3.11.

$$L_{pi} = \sum_{1}^{n} \ell_i \qquad 3.11$$

The expression in Equation 3.8 for each assumed plastic hinge height, L_{pi}, is equated with Equation 3.10, and the smeared curvature, $\bar{\phi}_i$, is evaluated, see Equation 3.12.

$$\bar{\phi}_i = \frac{2 \cdot \phi_y \cdot L^2 + 6 \cdot \phi_y \cdot L \cdot L_{pi} - 3 \cdot \phi_y \cdot L_{pi}^2 + 6 \cdot \Delta_{cf}}{3 \cdot L_{pi} \cdot \left(2 \cdot L - L_{pi}\right)} \qquad 3.12$$

The equivalent yield penetration, $L_{eyp,i}$, is then calculated as the fixed end rotation, θ_{FE}, divided by the maximum smeared curvature, $\bar{\phi}_i$, see Equation 3.13.

$$L_{eyp,i} = \frac{\theta_{FE}}{\bar{\phi}_i} \qquad 3.13$$

The coefficient β_i is the equivalent yield penetration, $L_{eyp,i}$, normalized by the bar diameter, d_b, and the expected bar yield strength, f_{ye}, as presented in Equation 3.14.

$$\beta_i = \frac{L_{eyp,i}}{d_b \cdot f_{ye}} \qquad 3.14$$

Coefficient α_i, the geometric term related to the spread of plasticity, is equivalent to the fraction of the assumed normalized plastic hinge height, L_{pi}, see Equation 3.15.

$$\alpha_i = \frac{L_{pi}}{L} \tag{3.15}$$

For each assumed smeared panel (plastic hinge) height, L_{pi}, coefficient β_i and smeared curvature $\bar{\phi}_i$ are evaluated and compiled. At the peak displacement at every ductility level, and for every smeared curvature, the strains experienced in the bars on the extreme compressed and tensioned sides of the column are obtained from a moment-curvature analysis. The smeared bar axial strains from the moment-curvature analysis are compared with those obtained from the linear potentiometer sets in the experiment, and through an optimization procedure, the coefficient α_i which produces the smallest error between the predicted and experimentally obtained smeared bar strains is obtained, see Figures 3.39 and 3.40. For the optimized α, at which the error between the predicted and measured bar strains is minimal, the values of coefficient β, which have been previously obtained at the peaks of every displacement ductility level, are averaged and an optimum value is obtained, see Figure 3.41. It is shown that the coefficient $\beta = 0.089$ obtained from this analysis and optimization is lower than the value of $\beta = 0.15$ provided by AASHTO[1] and Caltrans SDC 2.0[22].

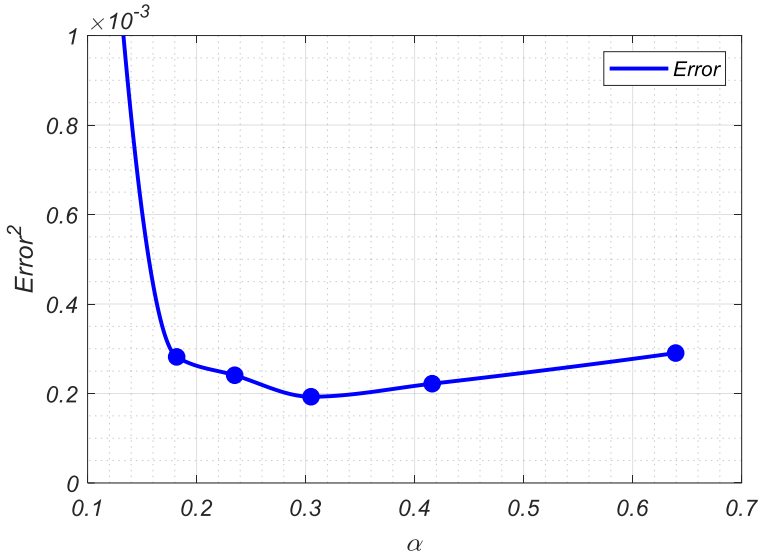

Figure 3.39. Error Between Predicted and Experimental Smeared Strains at Various Plastic Hinge Heights

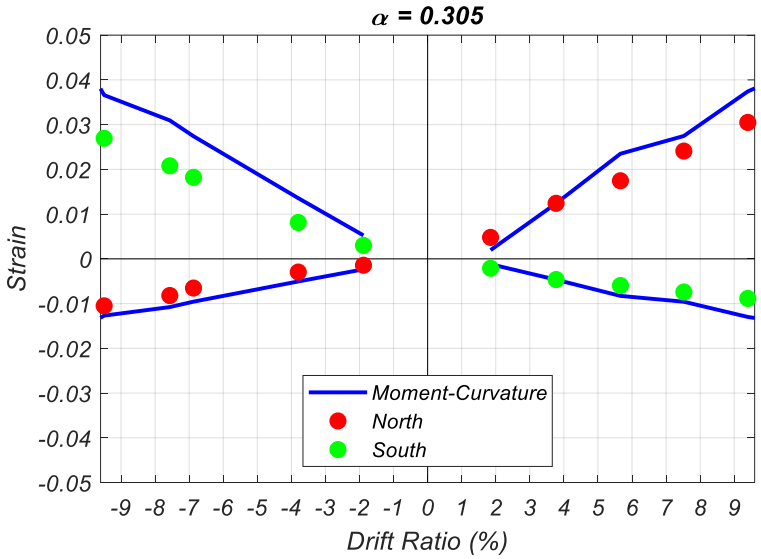

Figure 3.40. Predicted and Experimental Smeared Strains Considering Optimal Plastic Hinge Height

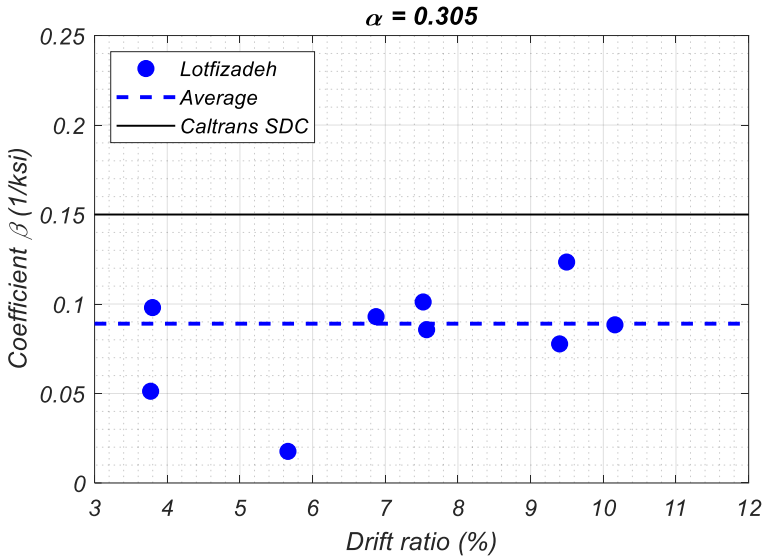

Figure 3.41. Optimal Value of Coefficient β from Test Specimen

To further verify and validate these results, findings from past experiments on columns by Stephan et al.[39] and Schoettler et al.[8] were investigated and a similar smeared strain compatible analysis was performed to obtain the optimized α and β coefficients for each. A brief overview of these test specimens, along with the error optimization and coefficient results for the columns experimented by Stephan et al.[39] and Schoettler et al.[8] are presented in the following sub-sections.

3.7.1.1. Stephan et al., 2003 (Unit 1)

For this investigation, two 35% scale bridge column specimens which represented typical construction of the approach structure for the Oakland Touchdown Substructure of the San Francisco Oakland Bay Bridge were constructed and tested. Unit 1 was built with a specified 8 ksi (55.2 MPa) concrete compressive strength and reinforced with conventional ASTM A706 Grade 60 bars in accordance with Caltrans Bridge Design Specifications (2002)[50]. Unit 2 however, was reinforced with MMFX 2 steel which is a

high strength reinforcing steel with a nominal yield strength of approximately 100 ksi (689 MPa). The primary objective of the experimentation by Stephan et al.[39] was to assess the seismic performance of bridge columns reinforced with high strength Grade 100 reinforcement and compare the behavior and performance with a similar column reinforced with conventional ASTM A706 Grade 60 reinforcing bars. The specimen in focus of this study is Unit 1.

The specimen consisted of a 3 ft (0.9 m) diameter by 8 ft (2.4 m) high column resting on a 9 ft (2.7 m) by 6'-10 ¾" (2.1 m) by 2'-6" (0.8 m) high footing, with a 5'-5" (1.7 m) by 5'-5" (1.7 m) by 2'-11 ½" (0.9 m) deep load stub at the top of the column to apply the necessary loading. The reinforcement layout of this specimen consisted of two reinforcement cages, each containing 42 #5 ASTM A706 Grade 60 bars longitudinally and #3 hoops spaced at 1.56 in. (40 mm), for a reinforcement ratio of $\rho_l = 2.54\%$ and volumetric reinforcement ratio of $\rho_v = 1.74\%$. This dual-cage configuration is typical of columns in the approach structure of the San Francisco Oakland Bay Bridge, see Figure 3.42.

An additional load of 600 kips (2669 kN), simulating an additional gravity load of approximately 7.4% of $f_c' A_g$, was continuously applied on the specimen using four externally post-tensioned rods attached to the load stub at the top of the column and fixed to the strong floor of the laboratory. The lateral load required to cyclically push and pull the top of the column was applied to the load stub using a 500 kip (2224 kN) hydraulic actuator. A loading protocol similar to the one presented earlier, see Figure 3.11, was used for the testing of this specimen. The hysteretic base column moment-drift response for Unit

1 is presented in Figure 3.43. A similar smeared strain compatible analysis was performed to obtain the optimized α and β coefficients for this test specimen and are presented in Figures 3.44 through 3.51.

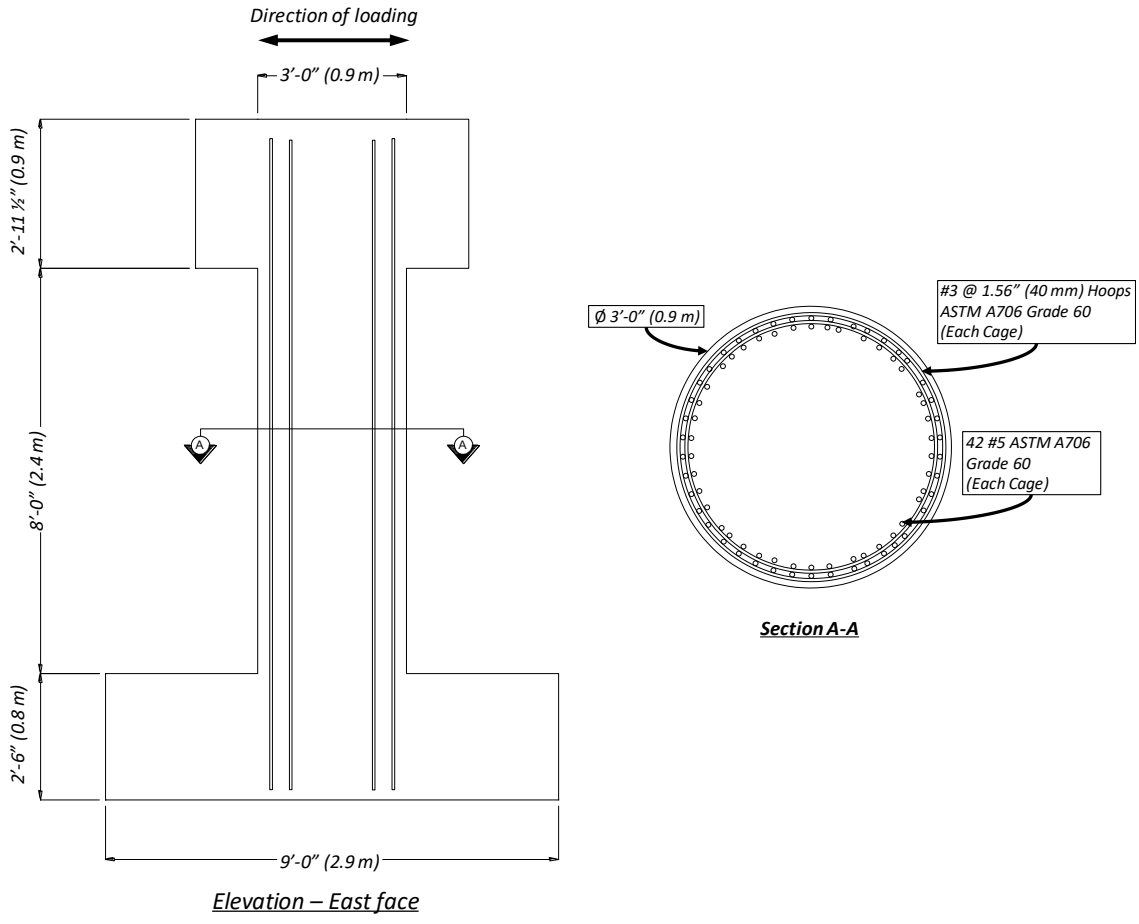

(a) (b)

Figure 3.42. Unit 1 Test Specimen from Stephan et al.; (a) Overall Dimensions; (b) Column Reinforcement Layout

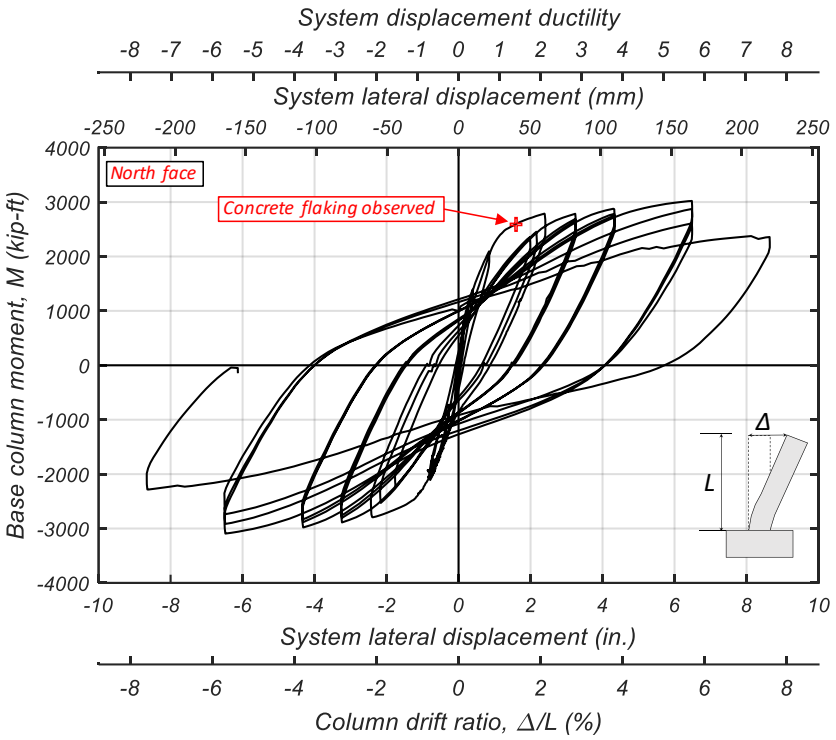

Figure 3.43. Hysteretic Base Column Moment-Drift Response of Stephan Unit 1

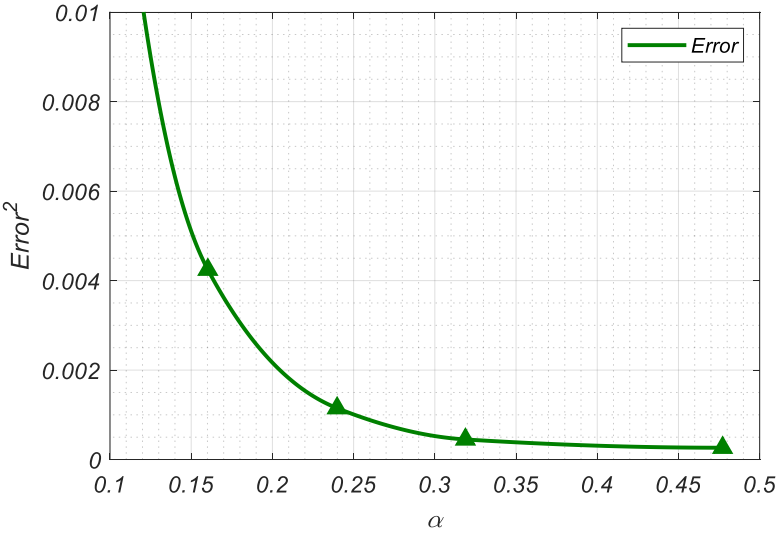

Figure 3.44. Error Between Predicted and Experimental Smeared Strains at Various Plastic Hinge Heights (Stephan Unit 1)

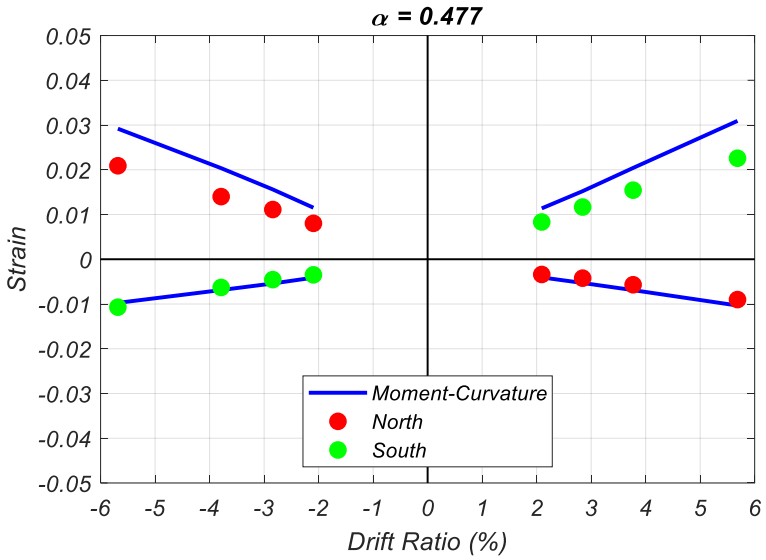

Figure 3.45. Predicted and Experimental Smeared Strains Considering Optimal Plastic Hinge Height (Stephan Unit 1)

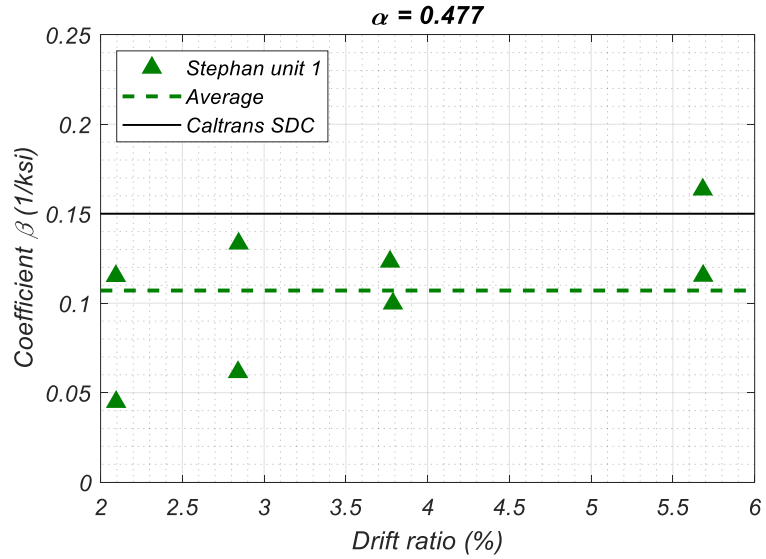

Figure 3.46. Optimal Value of Coefficient β from Test Specimen (Stephan Unit 1)

3.7.1.2. Schoettler et al., 2015 (Large Bridge Column, L.B.C.)

A first-of-its-kind test of a full-scale bridge column was conducted at the Large High-Performance Outdoor Shake Table (LHPOST) at The University of California at San Diego. The test specimen was designed and detailed in accordance with the latest California seismic design provisions and was subjected to ten significant ground motions and tested to failure. Results from this test provide the basis for comparison with small-scale shake table testing which provides great insight into the scale effects under dynamic loading scenarios.

The test specimen consisted of a 4 ft (1.2 m) diameter by 24 ft (7.3 m) high column resting above the 18 ft (5.5 m) long by 6 ft (1.8 m) wide by 4 ft (1.2 m) deep footing. A large mass of 570 kips (2535 kN) was placed at the top of the column (free end) simulating an additional gravity load of approximately 5.3% of $f_c' A_g$ on the column at the day of testing (DOT), see Figure 3.47. The column was reinforced with 18 #11 ASTM A706 Grade 60 bars longitudinally, and butt-welded double #5 ASTM A706 Grade 60 hoops spaced at 6 in. (152 mm) on center, for a reinforcement ratio of $\rho_l = 1.55\%$ and volumetric reinforcement ratio of $\rho_v = 0.95\%$, see Figures 3.47 and 3.48. The specimen was built with a specified concrete compressive strength of 4 ksi (27.6 MPa) with a maximum aggregate size of 1 in. (25 mm). The concrete strength at day of testing (DOT) however, was measured to be 6.1 ksi (42 MPa).

As mentioned earlier, the test specimen was subjected to ten significant ground motions. For the purposes of this investigation, only select ground motions were investigated. The hysteretic base column moment-drift response of specimen due to two

ground motions, *EQ3* and *EQ8* are presented in Figures 3.49 and 3.50. A similar smeared strain compatible analysis was performed to obtain the optimized α and β coefficients for this test specimen and are presented in Figures 3.51 through 3.53.

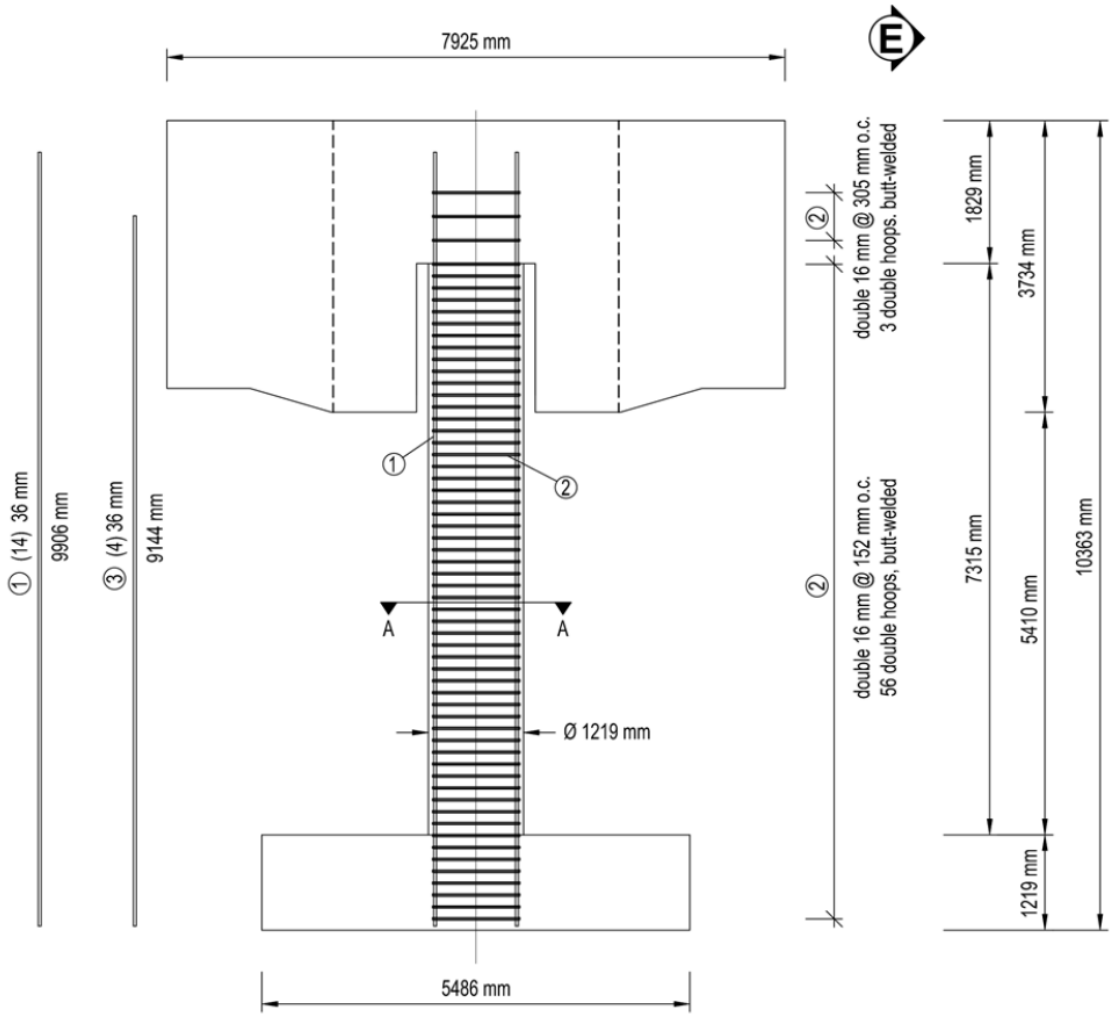

Figure 3.47. Large Bridge Column (L.B.C.) Test Specimen from Schoettler et al., Elevation View; Overall Dimensions and Reinforcement Layout

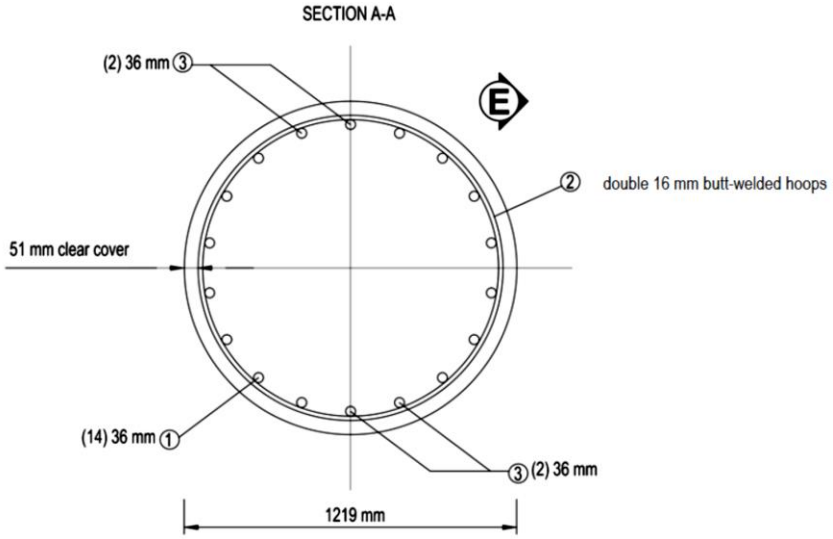

Figure 3.48. Large Bridge Column (L.B.C.) Test Specimen from Schoettler et al., Column Cross-Section

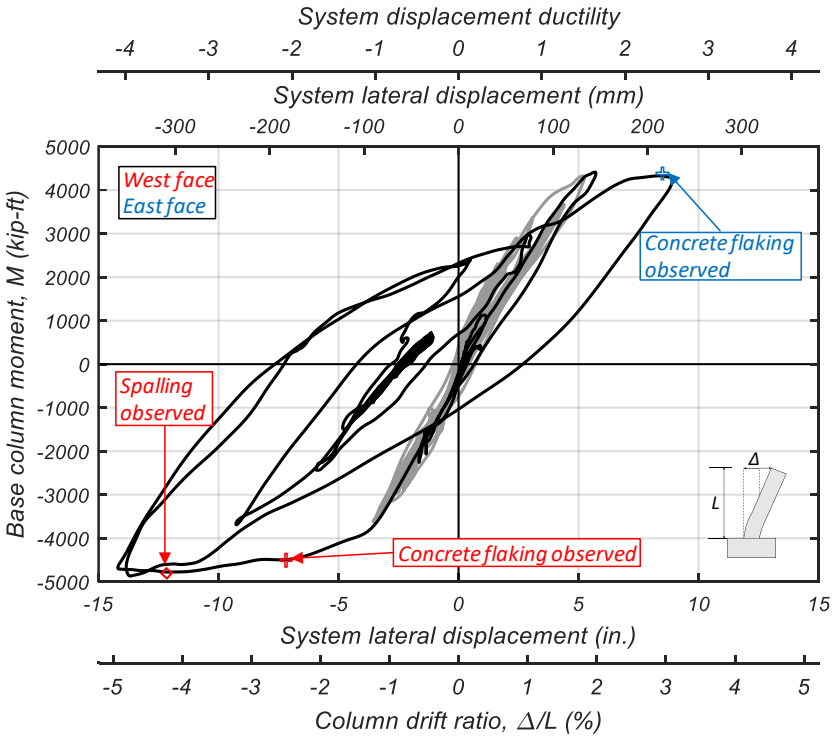

Figure 3.49. Hysteretic Base Column Moment-Drift Response of L.B.C. During EQ3 Excitation

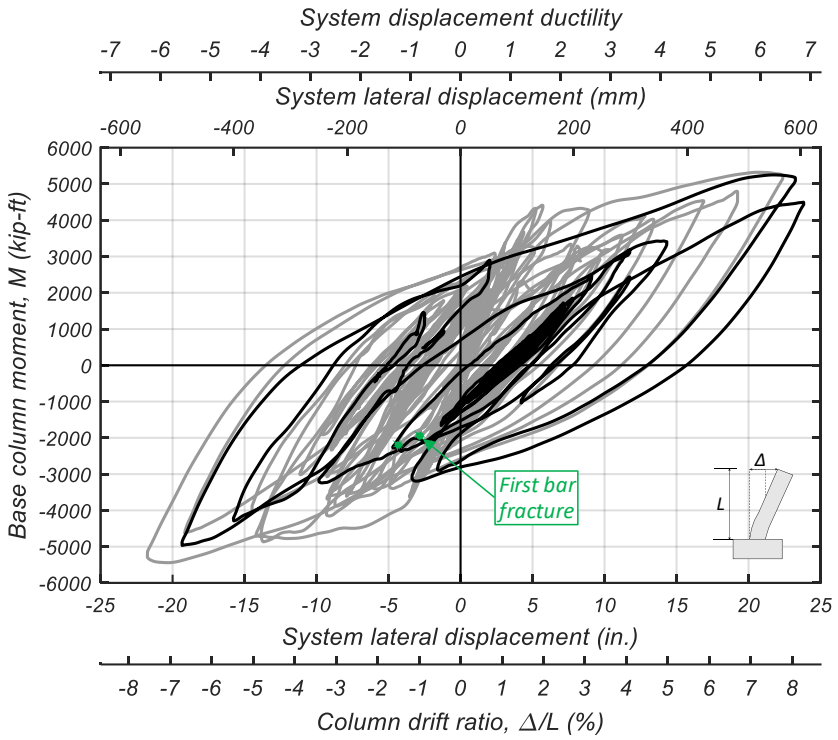

Figure 3.50. Hysteretic Base Column Moment-Drift Response of L.B.C. During EQ8 Excitation

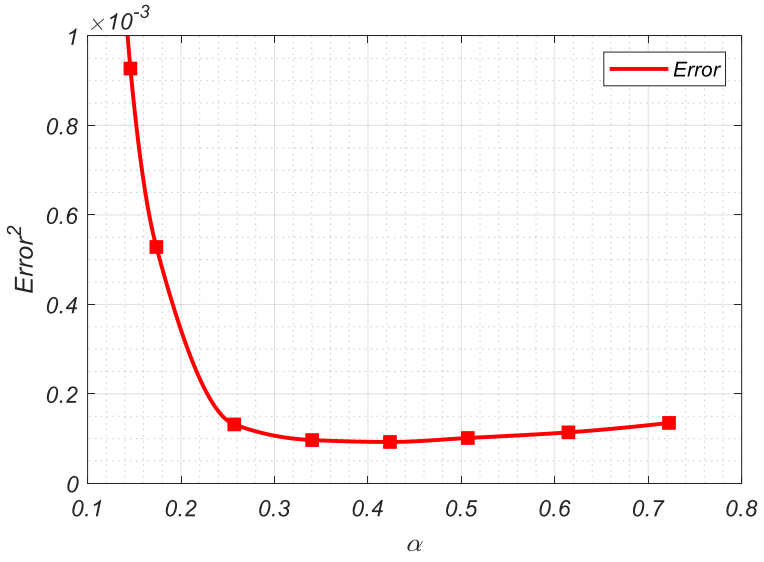

Figure 3.51. Error Between Predicted and Experimental Smeared Strains at Various Plastic Hinge Heights (Schoettler L.B.C.)

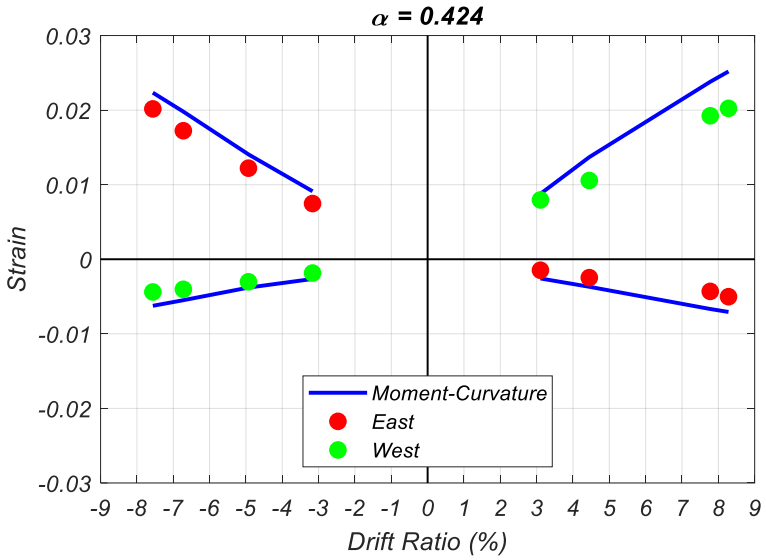

Figure 3.52. Predicted and Experimental Smeared Strains Considering Optimal Plastic Hinge Height (Schoettler L.B.C.)

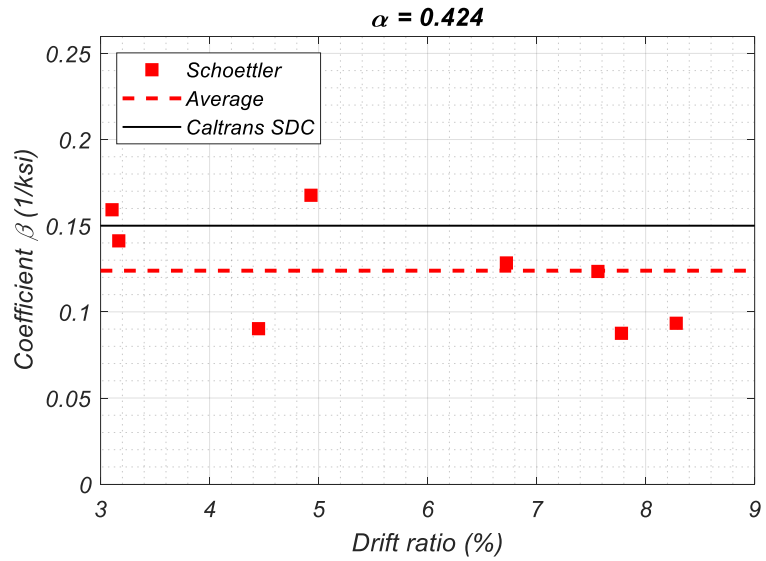

Figure 3.53. Optimal Value of Coefficient β from Test Specimen (Schoettler L.B.C.)

The β coefficients at optimum α values with respect to the drift ratio at the top of the columns are superimposed and presented in Figure 3.54. The statistical variation of the yield penetration term, the β coefficient, obtained from all column tests are presented in Table 3.5.

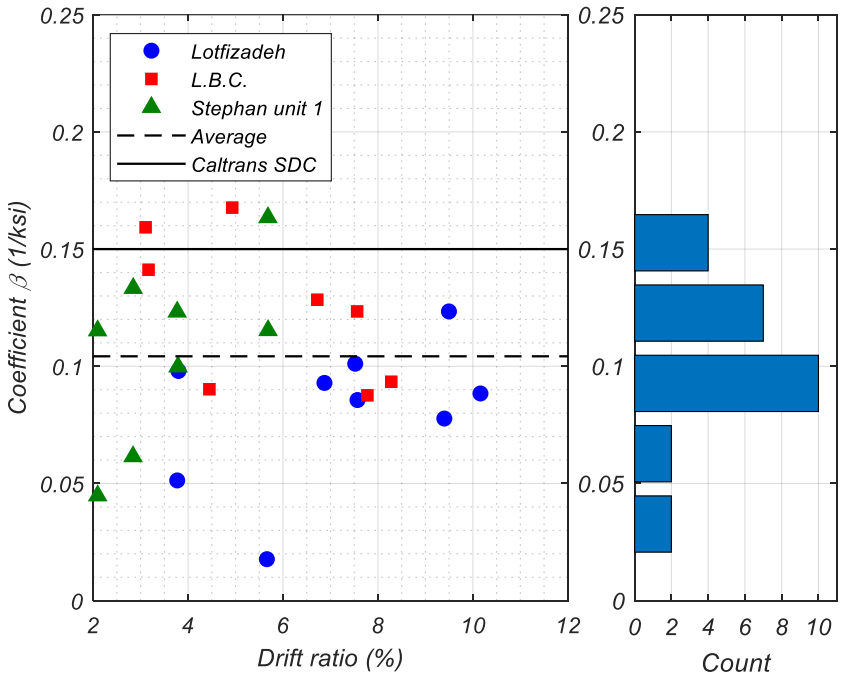

Figure 3.54. Comparison of Coefficient β in Column Tests

Table 3.5. Statistical Variation of Yield Penetration Term Coefficient β

	Mean	Median	STD
β (1/ksi)	0.103	0.0998	0.037

The equivalent yield penetration term was also evaluated for a series of past experiments regarding the bond-slip of ASTM A706 Grade 80 #14 and #18 size bars in confined concrete, as presented in Chapter 2. The findings from that set of experiments are similarly superimposed and presented in Figure 3.55. It should be noted, that in the bond-

slip set of experiments, the tests were set up such that the bars were uniaxially pushed and pulled, therefore there is no drift ratio for comparison. The statistical variation of the yield penetration term, the β coefficient, obtained from the bond-slip tests are presented in Table 3.6. Upon inspection of the results from all columns, the average yield penetration coefficient, $\beta = 0.103$ (1/ksi), is found to be less than the value proposed by Priestley et al.[36] and later adopted by AASHTO[1] and Caltrans SDC 2.0[22] of $\beta = 0.15$ (1/ksi). Also, worth noting, columns reinforced with ASTM A706 Grade 80 bars show less yield penetration than those reinforced with Grade 60 bars.

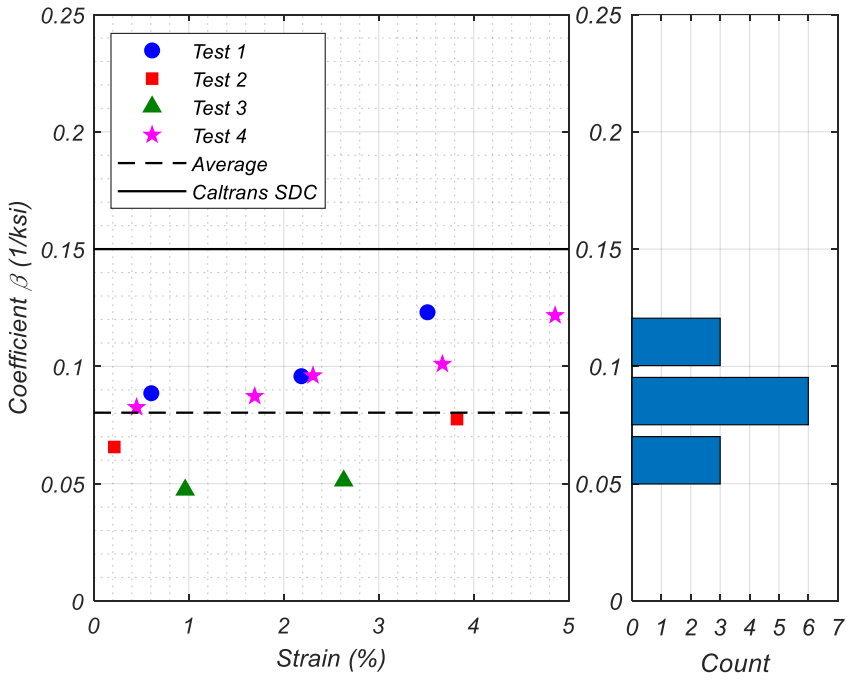

Figure 3.55. Comparison of Coefficient β in Yield Penetration Test Columns

Table 3.6. Statistical Variation of Yield Penetration Term Coefficient β from Yield Penetration Test Columns

	Mean	Median	STD
β (1/ksi)	0.0865	0.0879	0.024

3.8. Finite Element Modeling

A detailed 3D nonlinear finite element model of the test specimen was developed using finite element software ATENA® by Cervenka Consulting. The geometry of the test specimen was modeled with some minor simplifications to improve the analysis speed. The lateral load was applied at a single location within the load stub as opposed to the dual hydraulic actuators used in the actual test, and the sections which were not of focus in the test (the load stub and the footing beneath the pile) were assigned elastic material properties. These simplifications do not alter the findings from the analysis, yet they greatly reduce the required computational power and time. With the geometry of the specimen fully defined, material properties were assigned to each component.

3.8.1. Base Model

Initially, a base model was developed, and material properties were assigned to each component incorporating recommended parameters for the material models. The concrete compressive strength, elastic modulus, and tensile strength values obtained from sample cylinder tests were used. Tension stiffening, aggregate interlock, shear factor, s_F, and the unloading factor, f_U, were not activated in the base model. Due to the lack of experimental data, a fracture energy of $G_{ft}\ (\frac{\mathrm{MN}}{\mathrm{m}}) = 0.000025 f'_t\ (\mathrm{MPa})$ as proposed by Vos (1983)[51] and recommended by ATENA® was assigned. Other parameters were also set for the concrete material which are described in detail by Vásquez et al.[48].

Properties and material model parameters were also defined for the reinforcement in the column and pile, as well as the post-tensioning rods applying the external axial load. The backbone curves characterizing the longitudinal and transverse reinforcement were

discretized as piecewise linear functions. The backbone curve of the transverse reinforcement differs from the longitudinal reinforcement since the hoops have already been work-hardened and present no yield plateau. Miscellaneous parameters were also set for the reinforcement and are outlined in detail by Vásquez et al.[48].

Meshes were assigned to each volume independently, and linear interpolation functions were used between nodes. For the linear elements (i.e. the reinforcement), the software creates a node at each intersection with a volume element. The column and pile were prescribed to have the same mesh in plan, such that every node in the column-pile interface connected both elements, see Figure 3.56. For the volume elements that did not share nodes, such as the column-load stub and pile-footing interfaces, a master-slave condition was applied to connect them, with the master condition assigned to the volume with the coarser mesh.

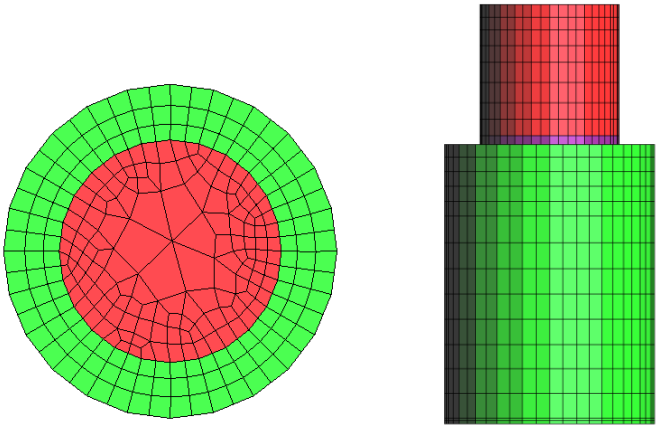

Figure 3.56. Finite Element Model Mesh of Column and Pile

3.8.2. Base Model Results and Comparison

As mentioned earlier, to monitor the behavior, the test specimen was heavily instrumented with linear potentiometers and electrical-foil strain gages. The instrumentation in the test was replicated in the FE model by assigning monitor points at the same locations. However, for modeling convenience, the horizontal distance between the linear potentiometer sets was modified slightly to ease post-processing of the data. The loading pattern applied in the FE model was the same as the experimental load protocol with the exception that the initial load-controlled cycles were ignored and only a single cycle at each displacement ductility demand were applied, see Figure 3.57. Results from the base model analysis are compared with data obtained experimentally.

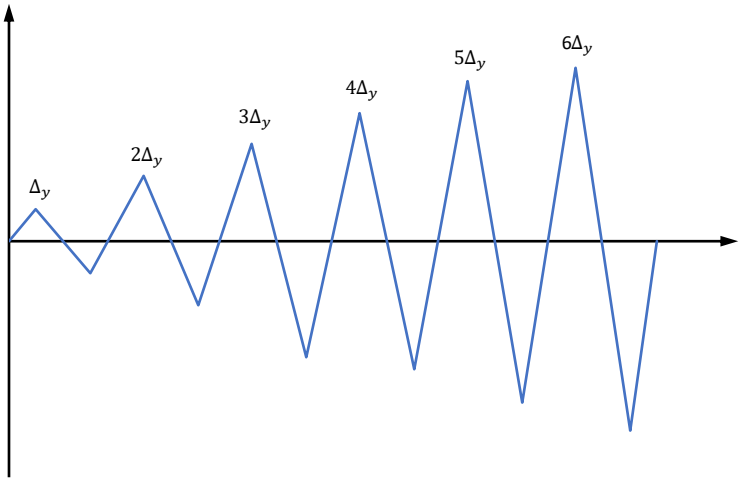

Figure 3.57. Simplified Loading Protocol for Finite Element Model

The analytical model experienced convergence issues prior to the end of the load protocol and was stopped after displacement ductility of 3, at a drift ratio of approximately 7%. The global lateral force-displacement response of the analytical model matches well with the specimen behavior, see Figure 3.58. The energy dissipated in the first cycle of the

model was slightly higher than the test. In the second cycle, the model predicted a strength about 10% higher than the experiment and was not able to accurately capture the change in stiffness in the reloading branch of the cycle. Similarly, in the third cycle, the model was not able to capture the change in stiffness in the reloading branch, however, the strength matched well with the experiment. The comparison between analytical and experimental lateral force-displacement response at each displacement ductility level is presented in Figure 3.59.

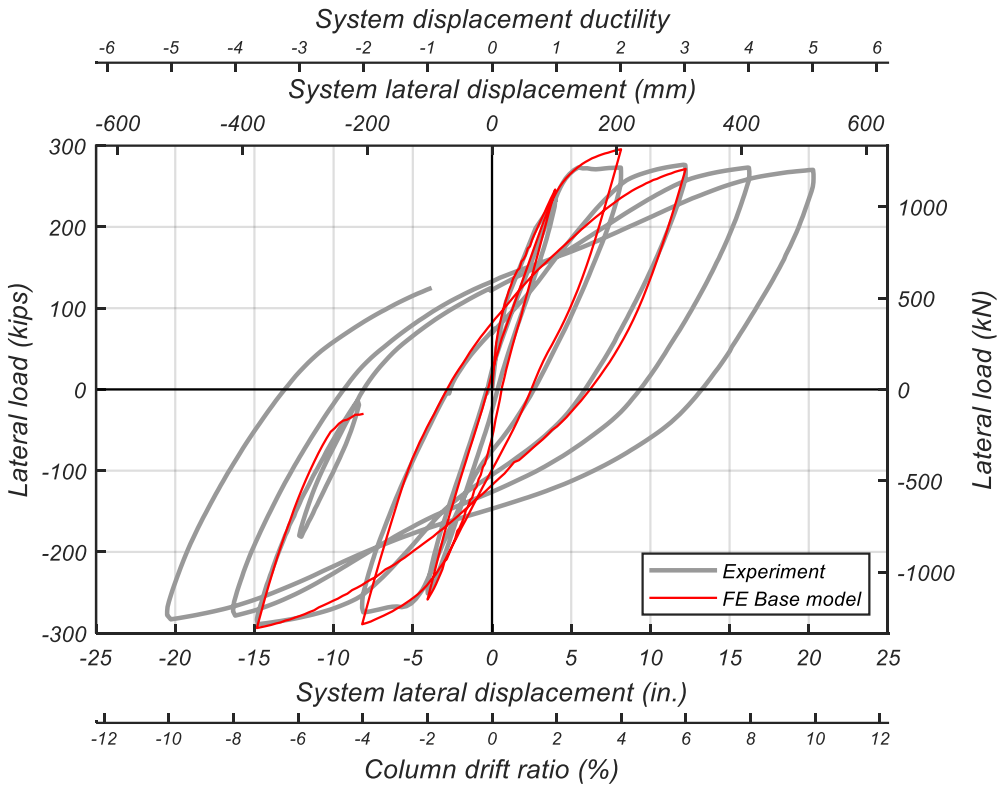

Figure 3.58. Global Lateral Force-Displacement Response Comparison of FE Base Model and Experiment

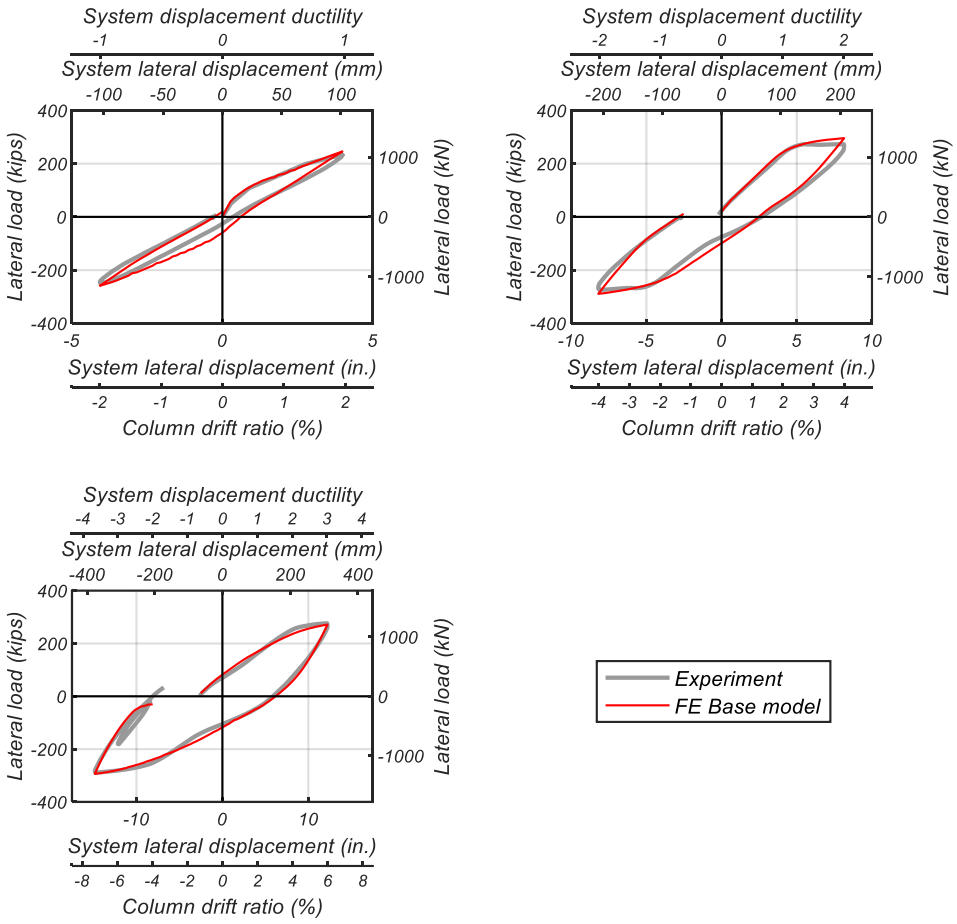

Figure 3.59. Comparison of Global Lateral Force-Displacement Response at Each Displacement Ductility Level

A comparison of the normalized base column moment-curvature response for the first two displacement ductility levels are shown in Figure 3.60. The model successfully predicted the yield curvature as approximated by Priestley[49]. However, experimentally, the test specimen behaved more elastically in the positive displacement cycle, which causes an offset between the predicted and experimental yield curvature. Another shortcoming of the base model is that it had difficulty accurately reproducing the flexural capacity at the peak negative displacement of the third cycle.

Following the same procedure as for the test specimen, the contributions to the top displacement are obtained from the analytical model and compared with those found experimentally, see Table 3.7. Since the analytical base model captured only the first three displacement ductility levels prior to experiencing convergence issues, the displacement contributions are only compared for those load cycles. The analytical base model over-predicts the displacements due to flexure in the pile, while significantly under-predicting the fixed-end rotation of the column. This under-prediction is likely caused by the failure of the base model in properly capturing the yield penetration and bond slip of the column longitudinal reinforcement along the non-contact lap splice length.

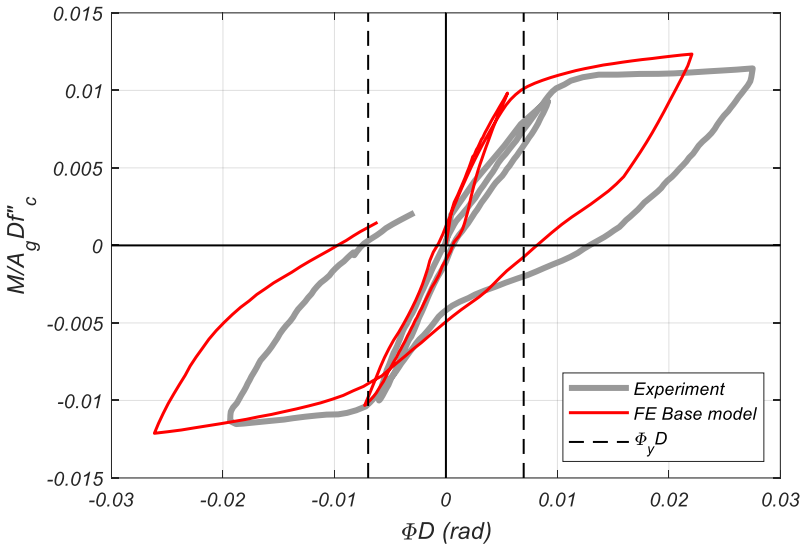

Figure 3.60. Normalized Moment-Curvature Response Comparison of First Two Displacement Ductility Levels

Table 3.7. Comparison of Top Displacement Contributions of Experimental Results and FE Base Model

	Experiment (%)			FE Base Model (%)			Prediction Error (%)		
μ_Δ	1	2	3	1	2	3	1	2	3
Drift Ratio (%)	1.98	4.01	6.64	1.98	4.01	6.64	1.98	4.01	6.64
Column Flexure	55.9	63.9	58.3	46.7	58.4	64.7	-16.5	-8.61	11.0
Pile Flexure	6.71	4.06	2.91	11.7	5.87	3.13	74.4	44.6	7.56
FE Rotation	27.6	31.2	26.6	9.66	8.82	8.44	-65.0	-71.7	-68.3

3.9. Parametric Study and Model Refinement

An extensive and detailed parametric study was conducted to further calibrate and improve the analytical response predicted by the base model. The effects of altering the material parameters for both the concrete and reinforcing steel elements on the behavior of the model were individually inspected, and the results of each alteration were meticulously compared with the experimentally obtained response of the specimen. A brief overview of the observations made from each parameter modification are presented here. A detailed explanation and presentation of all results are provided by Vásquez et al.[48].

3.9.1. Concrete Parameters

The tension stiffening parameter, c_{ts}, represents the relative limiting value of tensile strength in the tension softening branch. The tensile stress in concrete is prevented from reducing beyond $c_{ts}f_{cs}$. Values of 0.4 and 0.25 are recommended by CEB-FIP (1990)[52] for instantaneous, and long-term loading respectively. The analytical base model initially had the tension stiffening parameter disabled which resulted in convergence issues and was only able to complete the analysis for the first three displacement ductility levels.

This parameter was enabled in increments of 0.2, 0.4, and 0.6. Assigning a value of 0.2 to the tension stiffening parameter reduced the convergence issues and allowed the analysis to complete up to the last positive displacement cycle. Worth noting however, is that the analysis again began exhibiting convergence issues at the fifth displacement level. A comparison of the normalized base column moment-curvature of the first five displacement ductility levels with varying tension stiffness parameter values are presented in Figure 3.61. With activation of the tension stiffness parameter, the model captures the strength and curvature more accurately at higher displacement ductility levels for the positive (push direction) load cycles. Importantly, with the tension stiffening parameter activated and set to 0.6, the model most accurately captures the top displacement contribution of the fixed-end rotation at the column-pile interface, as shown in Figure 3.62.

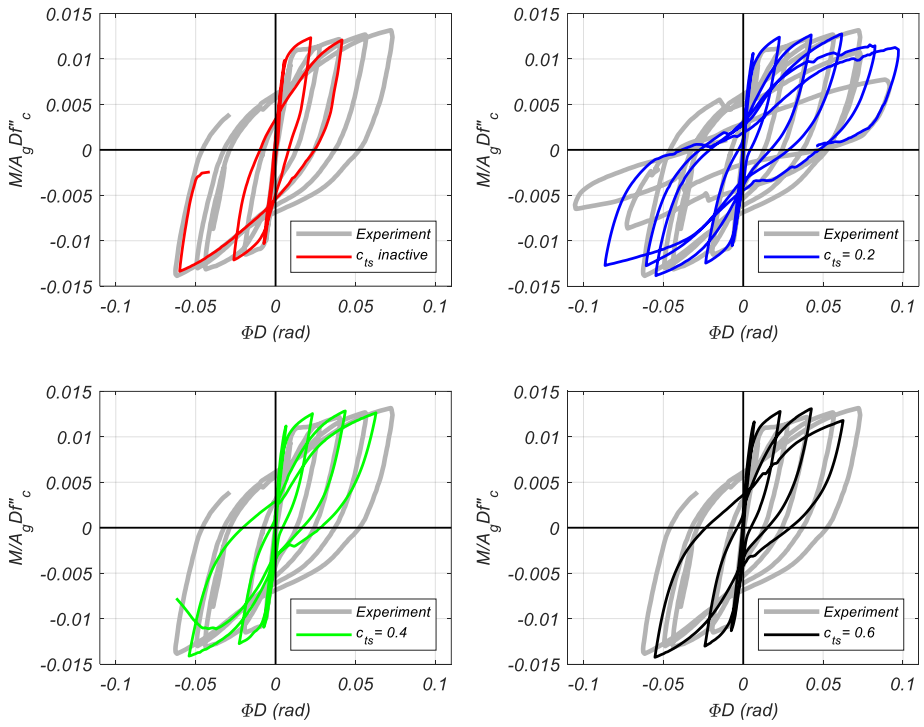

Figure 3.61. Normalized Moment-Curvature Response Comparison Varying c_{ts} Parameter

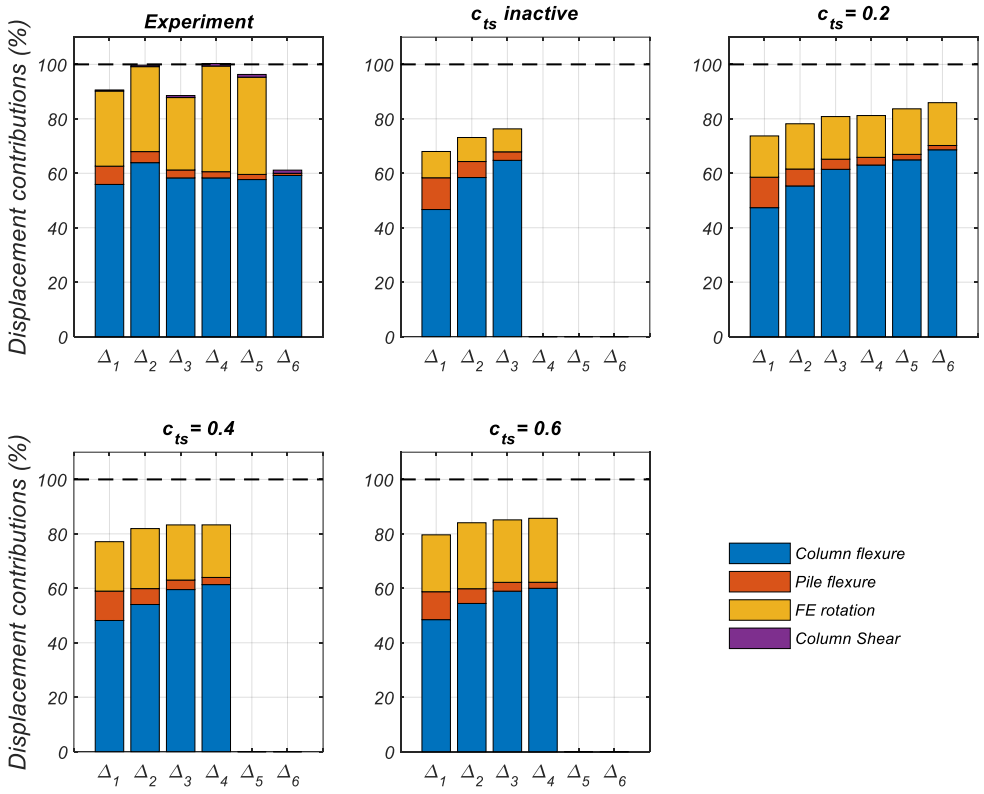

Figure 3.62. Comparison of Components of Lateral Displacement at Peak Displacement Ductility Levels Varying c_{ts} Parameter

Activating the aggregate interlock parameter, which enables the use of the shear strength in cracked concrete calculated using the modified compression field theory by Vecchio and Collins[53], is investigated considering the maximum aggregate size in the concrete of the test specimen. Aside from increasing the analysis run time, and introducing more convergence issues, the overall analytical model response is unchanged with the activation of the aggregate interlock parameter. The top displacement contributions were mainly unchanged as well, and the under-prediction of the fixed-end rotation at the column-pile interface remained.

The shear factor parameter, s_F, links the cracked shear stiffness in mode II to mode I, and is related to the shear retention factor, β, as presented by Havlásek and Kabele[54], see Equation 3.18.

$$D_{II} = s_F D_{I,S} \quad 3.16$$

$$G_c = \beta G \quad 3.17$$

$$\beta = \frac{D_{II}}{D_{II} + G} \quad 3.18$$

where D_i are the stiffness modulus for a smeared formulation in mode I and II (the models assume that the initiation of cracks is made by mode I), G is the elastic shear modulus, and G_c is the effective shear stiffness. Based on experimental work by Walraven in 1981, a value of 20 for the shear factor parameter is recommended by Cervenka et al.[55] and the ATENA® user manual[56], and a value of 200 is suggested in other literature by Cervenka et al.[57]. The effect of assigning both values to the shear factor parameter were investigated. The overall response of the analytical model did not vary by changing this parameter. Regardless of the value selected for the shear factor, the models failed to capture the change in slope at the reloading branch of the loading scheme, mainly due to the closure of the concrete flexural cracks. The top displacement contributions were mostly unchanged with the variation of the shear factor parameter, s_F. It is believed that since the behavior of the specimen is mostly dominated by flexural response in the column, changing the effective shear stiffness after cracking of the concrete does not significantly alter the overall response of the specimen.

The unloading factor, f_U, which controls the crack closure stiffness, was evaluated as 0.99 and 0 and compared with the base model which had not activated this parameter. When the parameter is set to equal 0, the unloading branch goes through the origin, and when set to 1, the unloading direction is parallel to the initial elastic stiffness. While increasing the predicted ductility in the plastic hinge region of the column, activating and varying the unloading factor parameter introduced convergence issues in the model, and was not able to properly capture the fixed-end rotation at the column-pile interface. A noticeable change when enabling this parameter is in the contributions of the flexural displacements in the pile and the upper section of the column, outside the plastic hinge region. It is concluded that if the model does not present convergence issues by enabling the unloading factor parameter, f_U, a value of 0 for this parameter is preferred, as it better captures the change in stiffness at the unloading branch when the cracks close.

Variation of the concrete tensile fracture energy parameter, G_{ft}, was also assessed. The base model used the formulation given by Vos in 1983[51]. Additionally, the relation provided by Nakamura and Higai in 2001[58] which relates the compressive (G_{fc}) and tensile (G_{ft}) fracture energies, see Equation 3.19, was used. The compressive fracture energy was obtained experimentally by testing sample cylinders in the Universal Testing Machine (UTM) following the procedure outlined by Jansen and Shah[59] using a feedback control signal to stably obtain the full stress-strain curve of concrete even when severe snapback occurs.

$$G_{fc} = 250 G_{ft} \qquad 3.19$$

The base model considered a fracture energy of $G_{ft} = 0.44$ lb/in (77.1 N/m) as recommended by Cervenka Consulting. Experimentally, the fracture energy was computed to be $G_{ft} = 0.55$ lb/in (96.3 N/m), and as a comparison a reduced fracture energy of $G_{ft} = 0.1$ lb/in (17.5 N/m) were applied to the model and the results compared. The model exhibited convergence issues with both the lower and higher values of the fracture energy parameter. The higher fracture energy of $G_{ft} = 0.55$ lb/in (96.3 N/m) showed a slightly better match of the strength at the end of the displacement ductility of 2 (drift ratio of ±4%) with the experimental results. However, for the positive peak at displacement ductility of 3 (drift ratio of ±6.6%), all models over-predicted the strength by approximately 3%. Yet, for the negative peak at displacement ductility of 3 (drift ratio of -6.6%), only the model with a fracture energy of $G_{ft} = 0.44$ lb/in (77.1 N/m) was able to complete without convergence issues, and the curvature prediction was over-predicted by approximately 41%. The predicted contributions to the overall top displacement were not affected by changing the fracture energy within the range specified.

The use of a fixed-crack model as opposed to the rotated-crack model was investigated. Using the fixed-crack model caused many convergence issues in the first displacement ductility level, which ultimately proved ineffective for this type of analysis. By comparing the analysis results for the only portion of the loading pattern which completed successfully using the fixed-crack model, it is evident that the fixed-crack model fails to correctly capture the behavior at the column plastic hinge, resulting in a poor overall prediction. It is concluded that the use of a rotated-crack model is advisable to avoid convergence issues.

The critical compression displacement parameter, w_d, was originally selected to be -0.197 in (-5 mm) in the base model which is ten times larger than the value recommended by Cervenka Consulting of -0.0197 in (-0.5 mm). To observe the effects of this parameter on the overall response, other values were applied following recommendations by Nakamura & Higai[58] and Van Mier[60]. It was determined that changing this parameter did not significantly alter the overall response of the model. However, due to the most accurate prediction in the first two displacement ductility levels, a value of -0.0295 in (-0.75 mm) is recommended.

Effects of changing the parameter that reduces the compressive strength due to imposed tensile strain following the Modified Compression Field Theory presented by Collins and Mitchell[61], F_c reduction, were also investigated. As lower values are assigned for F_c reduction, the loss of strength at the subsequent cycles increases, leading to a better prediction of the peak strength of the second cycle, but diverges at the peak of the following displacement cycle. This parameter does not significantly impact the overall response as it does not appear to have a great effect on the prediction of the displacement due to the fixed-end rotation at the column-pile interface.

The plastic flow parameter, β, controls the direction of return of the plastic flow, which is related to the expansion or contraction of the material. ATENA® supports values ranging between -5 and 5 for this parameter. It was found that values greater than 0.5 caused convergence issues early in the analysis and were not considered. Taking into consideration the contraction of the concrete, the model showed an improvement in

capturing the displacement caused by fixed-end rotation at the column-pile interface. It is recommended that a plastic flow parameter of $\beta = -0.1$ be selected.

3.9.2. Reinforcing Steel Parameters

The uniaxial Giuffrè-Menegotto-Pinto constitutive steel model (M-P) is implemented within ATENA®, and the parameters R, c_1, and c_2 are available for adjustment. Several permutations of these parameters were applied and their effects on the model response were investigated. The reinforcement in the column-pile interface play a major role in the behavior at the interface. Properly capturing the reinforcement behavior leads to a more accurate representation of the displacement contribution due to the fixed-end rotation at the column-pile interface. It is concluded that selecting values of $R = 4$, $c_1 = 500$, and $c_2 = 50$ for the M-P parameters most closely predict the overall response of the specimen.

ATENA® also allows for the activation of reinforcement in compression. The effects of enabling this option were investigated. Aside from increasing the processing time, a slight improvement in capturing the displacement due to the fixed-end rotation at the column-pile interface is noticed. No other significant change in the predicted response is observed. Due to the slight improvement in the fixed-end rotation prediction, it is recommended to enable the activation of reinforcement in compression option.

Six configurations for the bond-slip law were investigated, bond-slip provided by CEB-FIP code (1990)[52], Bigaj[62], fixed bar condition considering no bond-slip, and three user-defined memory bond laws. The user-defined laws differed by changing the maximum bond strength and friction unloading parameters, see Table 3.8. At low displacement levels

all bond-slip laws predicted the overall response well, and although they were not able to properly capture the opening and closure of the flexural cracks, the response was not affected by changing the parameters. The bond-slip model that most appropriately captures the displacement contribution due to the fixed-end rotation at the column-pile interface is *BS1c*, with a maximum bond strength of 1000 psi (6.9 MPa) and unloading friction of 200 psi (1.4 MPa), see Table 3.8.

Table 3.8. User-Defined Bond-Slip Laws

User-defined Bond-Slip Law	Maximum Bond Strength (psi) [MPa]	Friction Unloading (psi) [MPa]
BS1a	1000 [6.89]	50 [0.34]
BS1b	2200 [15.2]	50 [0.34]
BS1c	1000 [6.89]	200 [1.38]

3.9.3. Refined Model Results and Comparison

Upon completion of the parametric study, the various parameters are updated in the final model which produced the most accurate overall response of the specimen. Experimentally obtained strain profiles of the extreme northern and southern (direction of loading) column longitudinal reinforcement at the peak displacement ductility levels in the push and pull directions are compared with the base model and the refined final model and presented in Figure 3.63. It should be noted that the experimentally obtained strains on the reinforcement were measured using electrical-foil strain gages at discrete points along the length of the bars and the strains between measurement locations were linearly

interpolated. Also, many strain gages were damaged and lost during the test at higher displacement ductility levels.

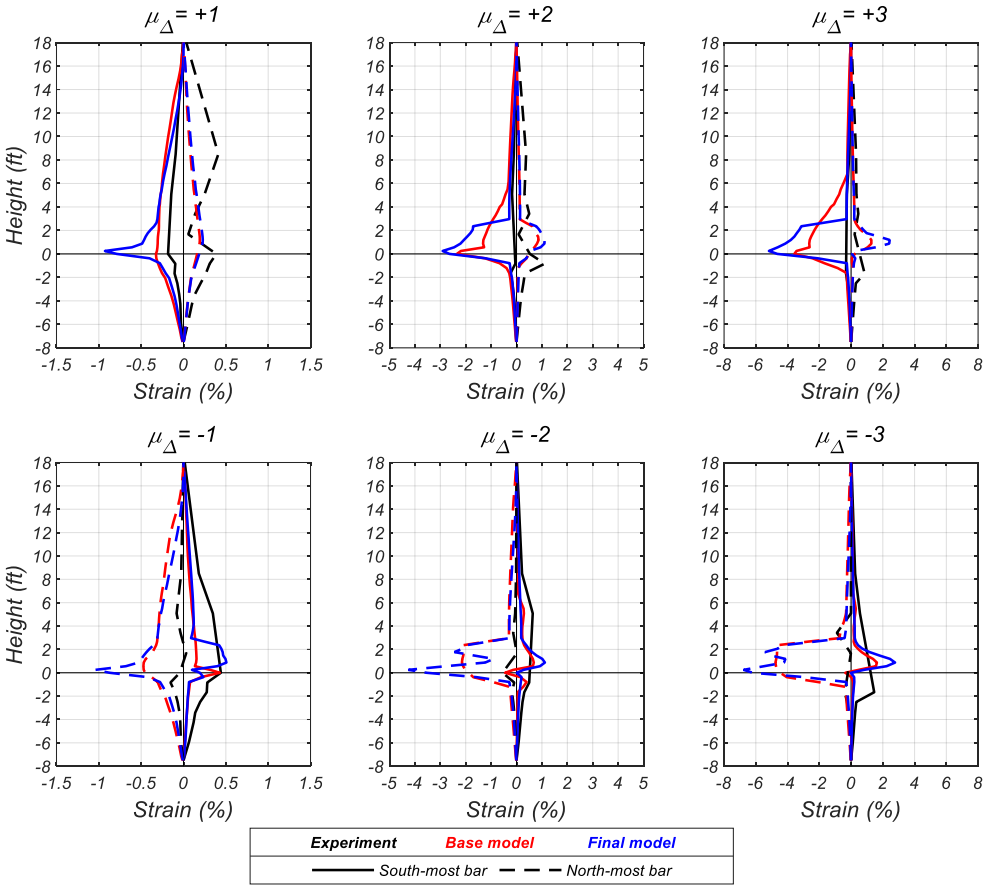

Figure 3.63. Comparison of Experimental Column Longitudinal Bar Strain Profiles with Refined Model

It is evident that the analytical model generally tends to under-predict the tensile strains in the bars for any given displacement cycle. However, the model appears to over-predict the compressive strains in the bars. At displacement ductility of 2, the model properly captures and predicts the localization of the plasticity in the bars on both extreme sides of the column, whereas, the measured strains from the experiment only clearly show this localization in the tensioned side, as shown in Figure 3.63. At displacement ductility

of 3, the model predicts the response in the positive (push) cycle very well. However, in the negative (pull) cycle, experimental strain measurements show a change from tension to compression where the bar should be in tension. The model correctly predicts this change, not in magnitude, but with a change in sign.

The refined model successfully predicts the overall response of the test specimen and can predict some local responses very well. The model falls short however, in accurately reproducing the fixed-end rotation at the column-pile interface due to plastic strain penetration and bond slip of the column longitudinal bars along the non-contact lap splice length.

3.10. Summary and Conclusions

Although extensive experimental and analytical studies have been done in the past, current design guidelines only have prescriptive requirements for the use of ASTM A706 Grade 60 reinforcement in bridge columns extending into Type II piles. A full-scale test specimen was built and tested to investigate the behavior of large diameter ASTM A706 Grade 80 reinforcing bars in the plastic hinge and non-contact splice regions of columns extending into Type II piles. A reduced embedment length of the column longitudinal bars previously proposed by Murcia-Delso et al.[45] was scaled and extrapolated to account for the use of high-strength Grade 80 reinforcement.

Findings from this experiment suggest that the test specimen behaved in a ductile manner and performed adequately even with a reduced embedment length of the column longitudinal bars into the pile. The column was successfully able to sustain a displacement ductility capacity of 5 prior to the first bar fracture and significant loss of capacity.

A detailed 3D nonlinear finite element model of the test specimen was developed using finite element software ATENA® by Cervenka Consulting. The FE model incorporated bond-slip models from previously reported experimental work. An extensive parametric study, investigating the effects of altering the material parameters of the reinforcing steel as well as the concrete, was conducted to further calibrate and improve the FE model. Ultimately, the FE model was able to successfully predict the global response of the test specimen, as well as some local responses. Future studies and improvements are needed to better predict the fixed-end rotation at the column-pile interface primarily due to plastic strain penetration and bond-slip of the bars along the non-contact splice region.

Chapter 3, in part, is currently being prepared for submission for publication of the material. Lotfizadeh, Koorosh H.; Vásquez, Valentina A.; Restrepo, José I. The dissertation author was the primary investigator and author of this material.

Chapter 4.

HIGH-STRENGTH GRADE 80 REINFORCEMENT IN BRIDGE COLUMN-BENT CAP CONNECTIONS

4.1. Abstract

The Department of Transportation of California (Caltrans) funded a large experimental work to validate the use of higher-grade reinforcement, such as Grade 80 reinforcement, in large civil infrastructure projects. A task within this project was to experimentally validate the replacement of ASTM A706 Grade 60 reinforcing steel with large diameter ASTM A706 Grade 80 bars in bridge column-bent cap connections and calibrate a nonlinear finite element analysis model permitting the extrapolation of laboratory tests. This chapter describes the experimental test setup and procedure and presents the main findings and conclusions from this task.

4.2. Introduction

No seismic testing has been performed on integral column-bent cap connections of bridges reinforced with ASTM A706 Grade 80 reinforcement. Practical implementation of

high strength reinforcement such as Grade 80 in California requires experimental validation that the critical components of bridges, such as integral column-bent cap connections, perform adequately when subjected to and exceeding the design earthquake loads. The use of high strength ASTM A706 Grade 80 reinforcement is ideal in cases where the reinforcement ratio of the columns and bent caps are moderate to high. By using higher strength reinforcement, the reinforcement congestion within the members can be mitigated, resulting in lower construction times and cost, while maintaining the same level of performance.

To investigate the behavior and performance of Grade 80 reinforcement in critical components of bridges, an integral column-bent cap connection is built at ¾-scale, cast in place (CIP) in the upright position, and tested. The test specimen represents an exterior bent-cap column connection of a multi-column bent cap and is reinforced entirely with ASTM A706 Grade 80 reinforcement both in the column and cap beam. General dimensions and loading scenario of the test specimen are based on an existing Caltrans bridge bent. The exterior column-bent cap connection was chosen for this investigation due to the added complexity introduced by the variable axial load on the column during cyclic loading.

4.3. Research Significance

The use of high-strength reinforcement such as Grade 80 in the construction of vital civil infrastructure such as bridges will likely reduce reinforcement congestion in column-bent cap joints, thereby reducing construction time and cost without compromising strength and seismic resilience. As many bridges make use of multi-column bent cap configurations,

and the dependability of this civil infrastructure during and after moderate to severe seismic events being crucial, the need for research regarding the use of Grade 80 reinforcement in column-bent cap connections is evident. This investigation provides an insight into the viability of using Grade 80 reinforcement in bridge column-bent cap connections, and by means of experimentation, seeks to reduce the current knowledge-gap.

4.4. Experimental Investigation Test Program

A ¾-scale test specimen was built and tested to investigate the behavior and performance of ASTM A706 Grade 80 reinforcing bars in the exterior column-bent cap connection of a multi-column bridge bent, see Figure 4.1. The specimen consisted of a 3 ft (0.9 m) diameter by 17.5 ft (5.3 m) high column extending into a 3'-5" (1.0 m) by 16'-8.5" (5.1 m) long cap beam at the top. An innovative proprietary hinge mechanism was developed at the base of the column to support the column and cap beam and to create a pinned boundary condition providing minimal bending moment resistance at the base of the column. The hinge was made using 6 #18 size ASTM A706 Grade 60 reinforcing bars with one end embedded in the column, and the other end embedded in the foundation block. The hinge reinforcement was fully developed inside the column to allow the complete transfer of forces without any appreciable bond slip. To ensure no concrete damage occurs at the boundaries of the hinge bars during large rotations, a 1 in. (25 mm) thick steel plate with 2.5 in. (64 mm) inner diameter steel pipes welded onto it were used as a guide for the hinge bars on both the column and foundation interfaces, see Figure 4.2. The gaps between the hinge bars and the steel pipes in the guide were then pumped and filled with high strength grout to ensure no lost bond between the bars and the test specimen. A gap of 6

in. (152 mm) was designed between the column and foundation block to allow unrestricted rotation at the base of the column during testing, see Figure 4.3.

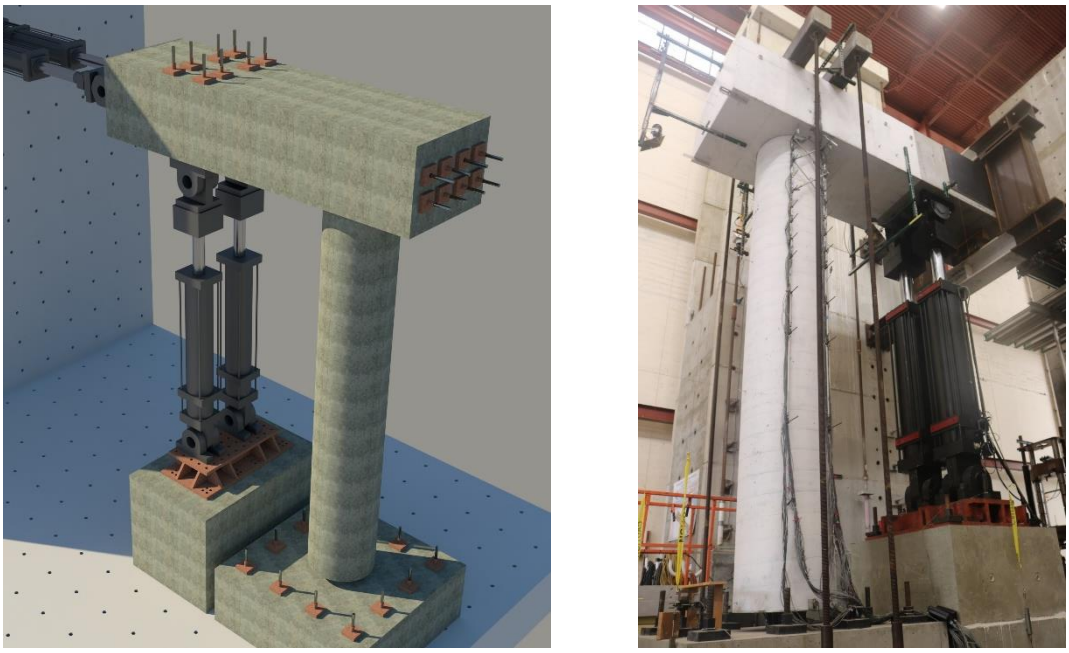

(a) (b)

Figure 4.1. Overall Elevation View of Test Specimen: (a) 3D Rendering; (b) As Built Specimen

Figure 4.2. Built-Up Steel Guide for Hinge at Column Base

Figure 4.3. Proprietary Hinge at Column Base

The specimen was reinforced entirely with ASTM A706 Grade 80 reinforcing bars as shown in Figures 4.4 through 4.6. The column was reinforced with 20 #9 bars with a more smoothed rib-radius compared to commonly available bars, for a longitudinal reinforcement ratio of $\rho_l = 2\%$, and confined by #5 butt-welded hoops at 4 in. (102 mm) on center for a volumetric reinforcement ratio of approximately $\rho_v = 1\%$. The longitudinal column bars were developed into the cap beam at the maximum length available, $33d_b$, extending 10% beyond the requirement prescribed by Caltrans SDC 2.0[22] when scaled to account for the use of Grade 80 reinforcement, $L_{ac}/L_{req} = 1.10$. The principal stresses in the beam-column joint were determined per Caltrans SDC 2.0 (section 7.4.2)[22], as presented in Figure 4.7 and Equations 4.1 and 4.2, and since the principal tension stress

was shown to exceed the $3.5\sqrt{f_c'}$ (psi) limit, joint shear reinforcement was provided by #4 vertical stirrups and horizontal cross-ties.

$$P_t = \frac{(f_h + f_v)}{2} - \sqrt{\left(\frac{f_h - f_v}{2}\right)^2 + v_{jv}^2} \quad 4.1$$

$$P_c = \frac{(f_h + f_v)}{2} + \sqrt{\left(\frac{f_h - f_v}{2}\right)^2 + v_{jv}^2} \quad 4.2$$

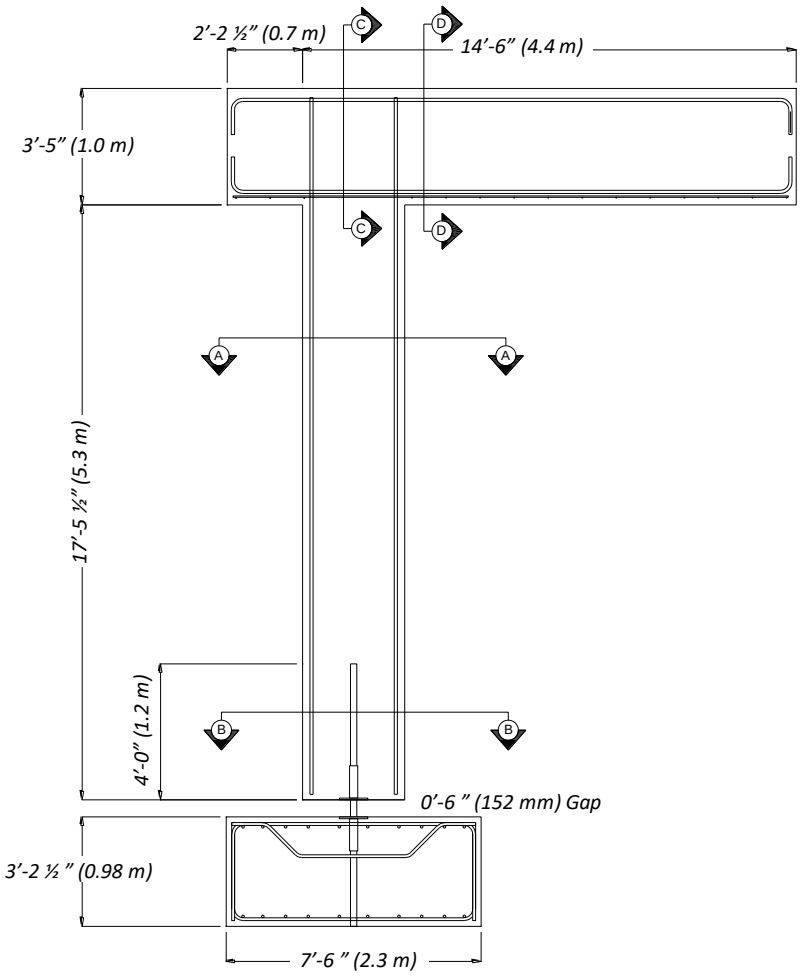

Figure 4.4. General Dimensions of Test Specimen (Elevation View)

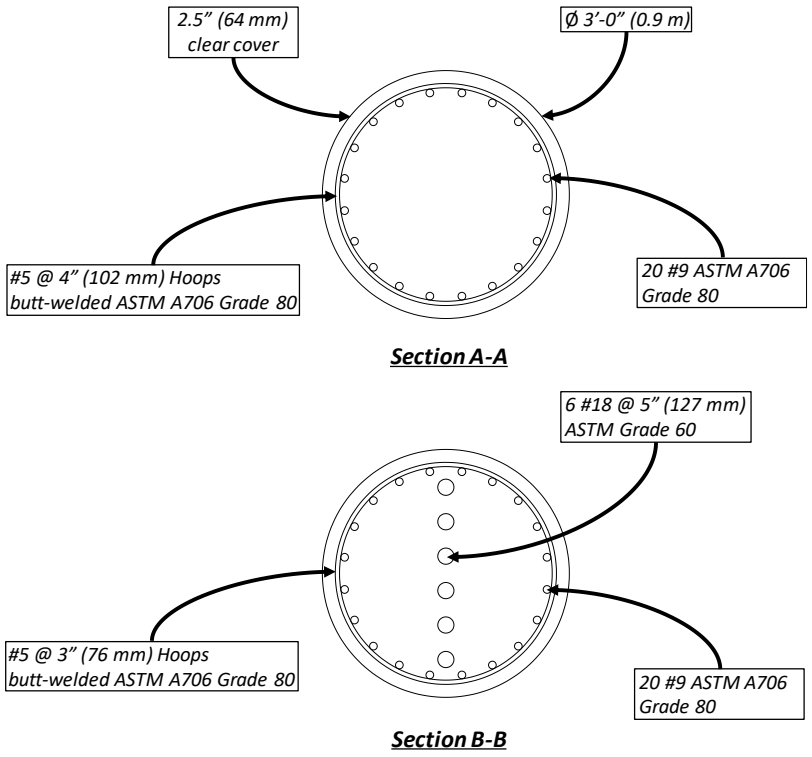

Figure 4.5. Reinforcement Configuration of Column

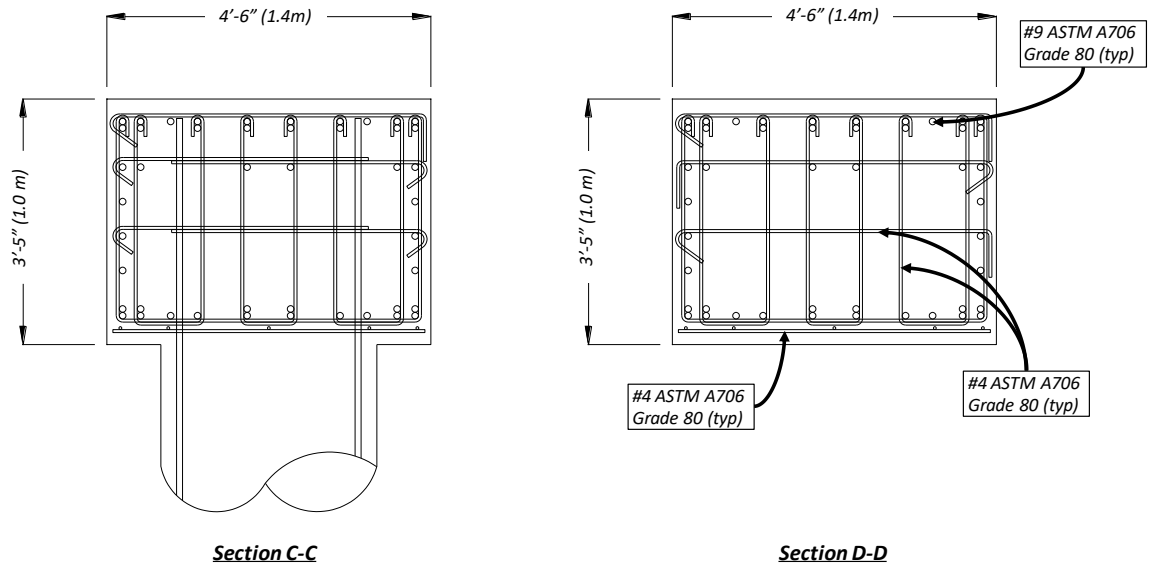

Figure 4.6. Reinforcement Configuration of Cap Beam

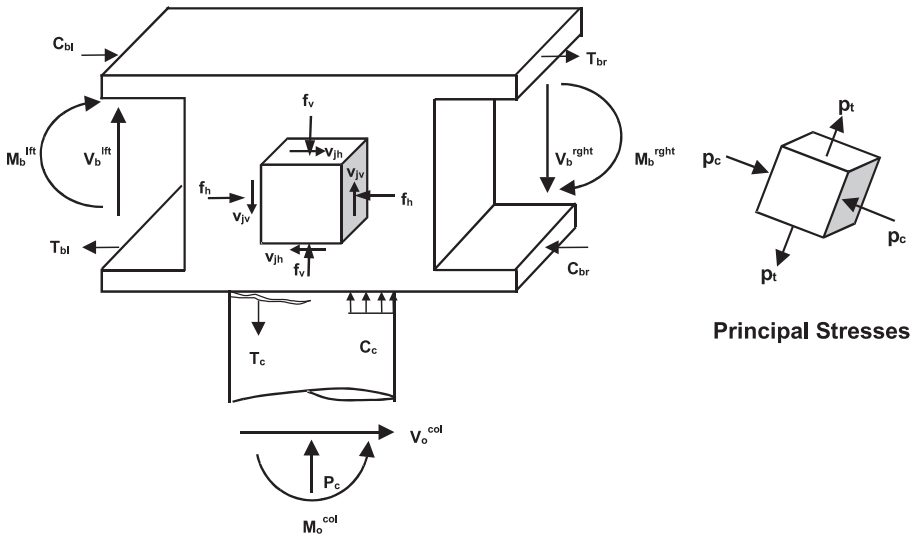

Figure 4.7. Joint Shear Stresses in T-Joints (Caltrans SDC 2.0 Figure C7.4.2-1)

Three monotonic tensile tests were performed on sample bars from the same heat as those used in the test specimen to obtain their mechanical properties. Testing was performed in accordance with ASTM A370-17[23] and ASTM E8-16a[24] using a closed-loop active hydraulic SATEC universal testing machine (UTM). Strains were measured using a 2 in. (51 mm) gage length high-precision extensometer positioned at the center of the bar. Dividing the forces recorded from the UTM by the nominal cross-section area of the bar, stresses were obtained. The complete monotonic stress-strain responses of the A706 Grade 80 #9 column longitudinal bars are presented in Figure 4.8. Key mechanical properties including the power term, *P*, obtained from a least-squares optimization between each recorded strain hardening branch and the formulation for the corresponding curve proposed by Mander[26], are listed in Table 4.1. Table 4.2 lists the geometric properties for the bars as defined by Metelli and Plizzari[31].

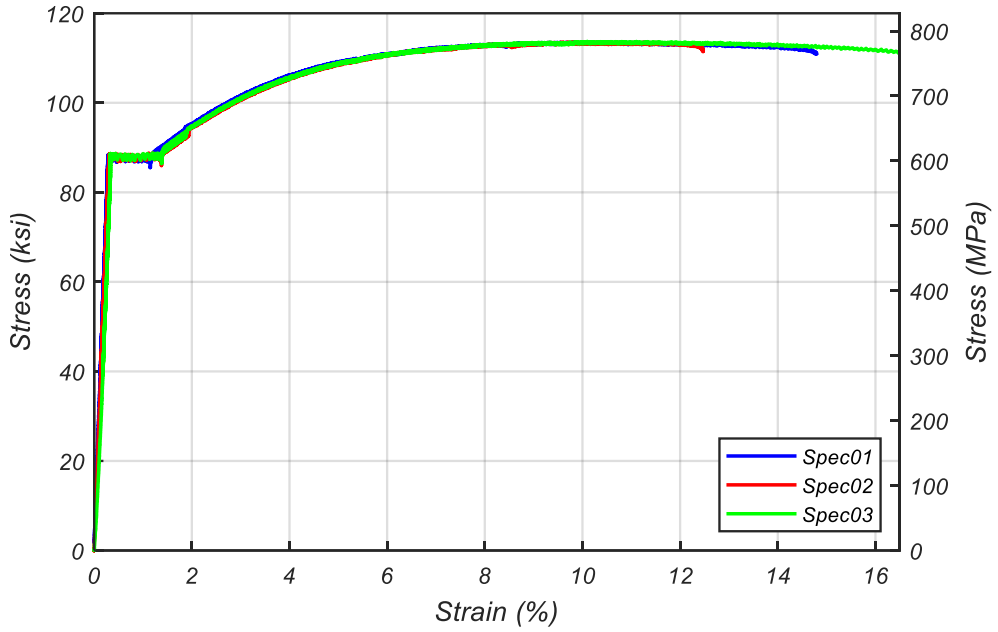

Figure 4.8. ASTM A706 Grade 80 #9 Column Longitudinal Smoothed-Rib-Radii Bar Tensile Tests

Table 4.1. Reinforcing Bars Mechanical Properties

Bar ID	f_y (ksi) [MPa]	$f_{s4\%}$ (ksi) [MPa]	f_{su} (ksi) [MPa]	ε_y (%)	ε_{sh} (%)	ε_{su} (%)	$\frac{f_{su}}{f_y}$	$\frac{f_{s4\%}}{f_y}$	$\frac{f_{su}-f_y}{f_y}$	P
#9†	87.9 [606]	105.5 [727]	113.7 [784]	0.32	1.34	10.1	1.29	1.20	0.29	3.38
#9‡§	85.2 [587]	N/A	113.7 [784]	N/A	N/A	N/A	1.33	N/A	0.33	N/A
#5§	89.3 [616]	N/A	114.0 [786]	N/A	N/A	N/A	1.28	N/A	0.28	N/A
#4§	80.5 [555]	N/A	114.5 [789]	N/A	N/A	N/A	1.42	N/A	0.42	N/A

† Smoothed-rib-radii column longitudinal reinforcement

‡ Commonly available cap-beam longitudinal reinforcement

§ Information obtained from mill certificate

Table 4.2. Column Longitudinal Reinforcement Geometric Properties

Bar ID	d_b (in.) [mm]	f_{Rm}	d_e (in.) [mm]	β (degrees)	s (in.) [mm]	a (in.) [mm]
#9†	1.128 [29]	0.107	1.195 [30.4]	68	0.717 [18.2]	0.078 [2]

† Smoothed-rib-radii column longitudinal reinforcement

Since all hoops were butt-welded, validation tests were performed in accordance with Caltrans Test 670[25] to ensure the desired and adequate performance from the column hoops. The complete monotonic stress-strain responses of the A706 Grade 80 #5 column hoops are presented in Figure 4.9. The stress-strain response does not show a clear elastic linear branch and yield plateau since the bars had previously been work-hardened to bend into hoops.

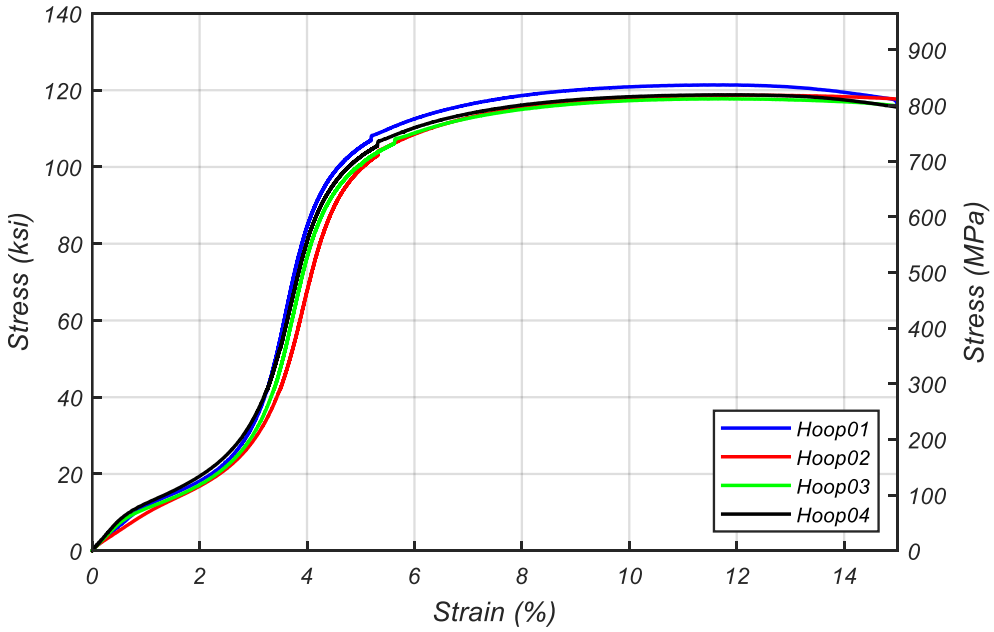

Figure 4.9. Butt-Welded Column Hoop Validation Tensile Tests

The test specimen was built with a specified 5000 psi (34.5 MPa) concrete compressive strength, cast in stages. To obtain the mechanical properties of the concrete in the test specimen, several 6 in. (152 mm) by 12 in. (305 mm) sample cylinders were taken from each region during concrete placement per ASTM C192-18[27]. The sample cylinders were capped using high-strength gypsum cement paste in accordance with ASTM C617-15[28] and tested in sets of three using the UTM per ASTM C39-18[29] throughout the curing process to monitor the compressive strength gain. Strains were measured using a compressometer with a high precision linear potentiometer as outlined in ASTM C469-14[46], and the compressive stresses were calculated by dividing the recorded forces from the UTM by the cross-section area of the sample cylinders. Figure 4.10 shows the monotonic stress-strain response of the tested cylinders at day of test (DOT) for the column in the plastic hinge region. The splitting tensile strength of the cap beam concrete was also obtained by performing split-cylinder tests in accordance with ASTM C496-17[30]. The concrete mix properties as well as compressive strength at day of test (DOT) for each casting stage, f_c', are listed in Table 4.3.

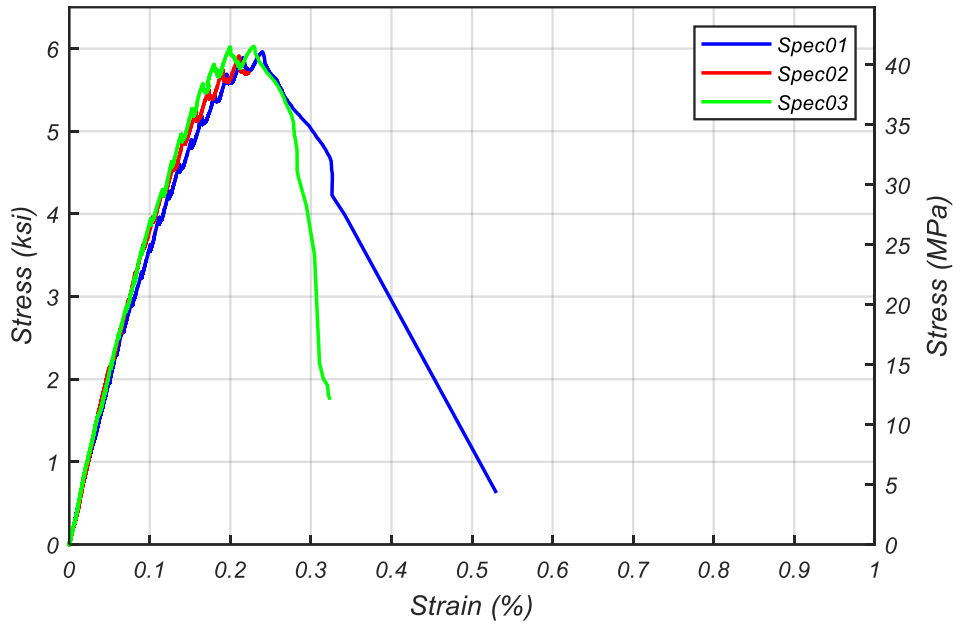

Figure 4.10. Monotonic Stress-Strain Response of Column Plastic Hinge Concrete at DOT

Table 4.3. Test Specimen Concrete Material Properties

Region	Max. Aggregate Size (in.) [mm]	w/cm Ratio (%)	Age of Concrete at DOT (days)	f'_c (ksi) [MPa]
Column Plastic Hinge	0.75 [19]	45	65	5.97 [41.2]
Column Elsewhere	0.75 [19]	45	21†	5.10 [35.2]
Cap Beam	0.75 [19]	45	6‡	4.44 [30.6]
Footing	0.75 [19]	45	15§	4.42 [30.5]

† Concrete cylinders tested only at 21 days after placement
‡ Concrete cylinders tested only at 6 days after placement
§ Concrete cylinders tested only at 15 days after placement

The cyclic lateral load was applied at the center height of the cap beam at the free end using two servo-controlled 220 kip (979 kN) hydraulic actuators. To prevent lateral instability, the hydraulic actuators were mounted parallel one another. Ensuring that the lateral loads are applied at a distance from the column-bent cap connection and not

influencing the behavior of the reinforcement in the joint, a special steel loading frame was fabricated and embedded in the free end of the cap beam to evenly transfer the actuator loads to the beam, see Figure 4.11.

Figure 4.11. Steel Loading Frame to Evenly Transfer Lateral Loads into Cap Beam

Two 500 kip (2224 kN) servo-controlled hydraulic actuators mounted parallel one another 5.5 ft (1.7 m) away from the face of the column apply the necessary additional axial load required while testing to prevent rotations of the cap beam during the push and pull load cycles. Simulating the scaled loads on the actual bridge, an additional external axial load of 337.5 kip (1501 kN), which equates to approximately 6.6% of $f_c' A_g$, was continuously applied on the specimen using four hydraulically post-tensioned rods attached to loading beams directly above the column-bent cap joint and fixed to the strong floor of the laboratory.

The loading protocol was set up to initially perform incremental load-controlled cycles of 25%, 50%, and 75% of the first yield force, F_y, after which the loading scheme was switched to a displacement-controlled scheme that performed three complete push-pull cycles at each incrementally increasing displacement ductility level, Δ_y. These increasing magnitude displacement-controlled cycles were repeated until the test was stopped for safety reasons after the first positive (push) peak at displacement ductility of +6 after many of the column longitudinal reinforcement had fractured and a significant loss in capacity was observed, see Figure 4.12.

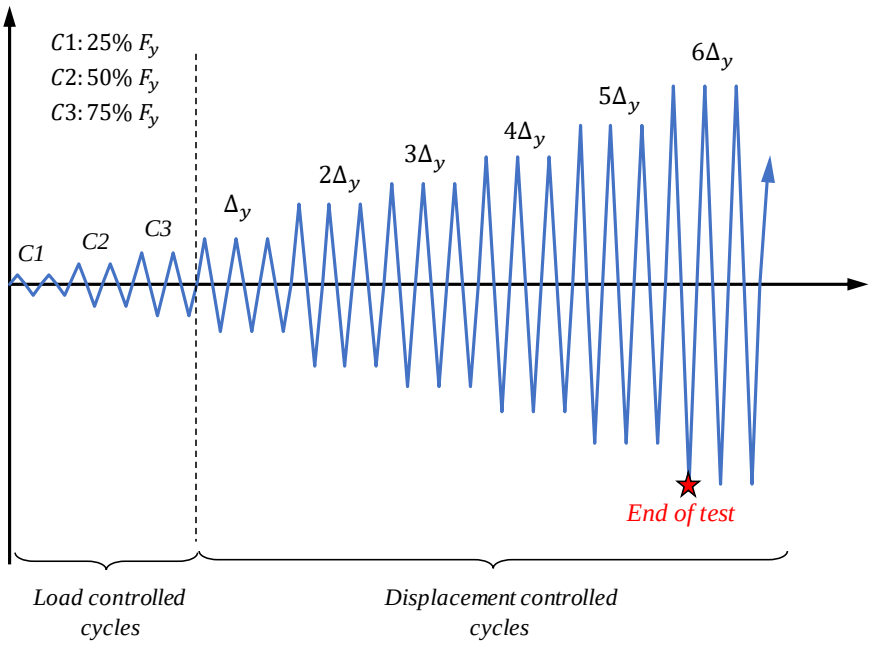

Figure 4.12. Test Specimen Loading Protocol

Strains in the longitudinal and transverse reinforcement of the column were monitored with an array of 0.2 in. (5 mm) high-elongation 120 Ohm electrical-foil strain gages. Particular attention was given to the instrumentation of the bars within the plastic hinge region of the column just below the cap beam, and along the column-bent cap joint.

A total of four longitudinal bars, two on each extreme side of the column in the direction of loading were instrumented with strain gages. Similarly, strain gages were applied to nine transverse hoops, four hoops in the joint and five hoops along the plastic hinge length of the column. To save space, instrumentation of a representative column transverse hoop and longitudinal bar are presented in Figures 4.13 and 4.14 respectively. Externally mounted linear potentiometers were used along the height of the column to monitor the deformations of the specimen, as presented in Figure 4.15. Additionally, linear potentiometers were affixed at the column-bent cap interface to monitor the fixed-end rotation of the column joint. String potentiometers mounted at various heights along the specimen were used to monitor the global displacements during the test, see Figure 4.16. Since the displacements measured internally by the actuators are not as reliable as those measured with string potentiometers, the string potentiometer at mid-height of the cap beam was used to control the displacement-controlled push and pull cycles.

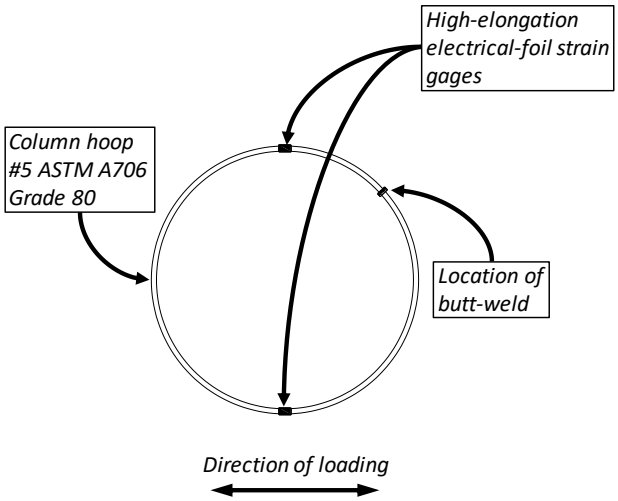

Figure 4.13. Representative Column Hoop Instrumentation

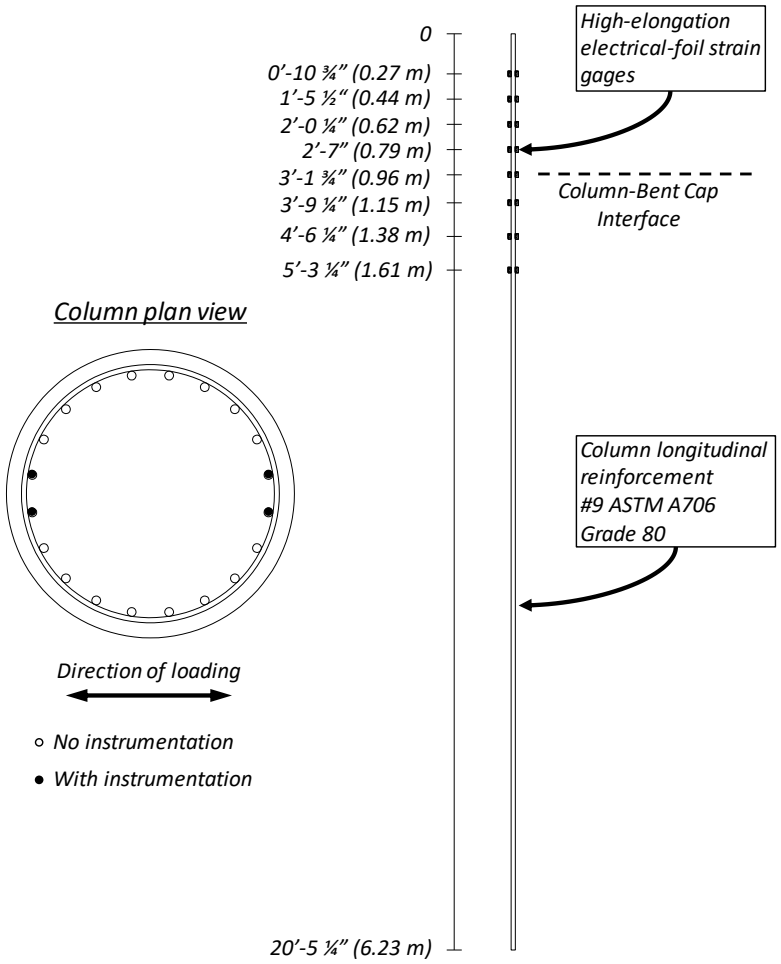

Figure 4.14. Representative Column Longitudinal Reinforcement Instrumentation

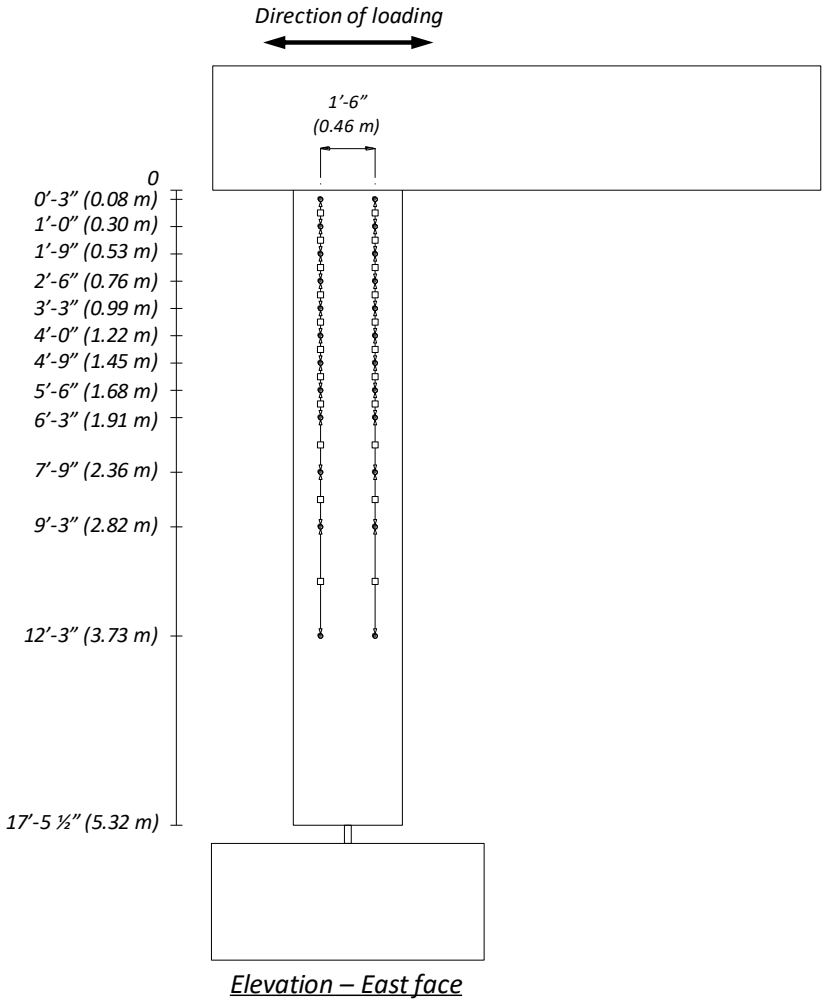

Figure 4.15. Linear Potentiometers Mounted Along Height of Test Specimen

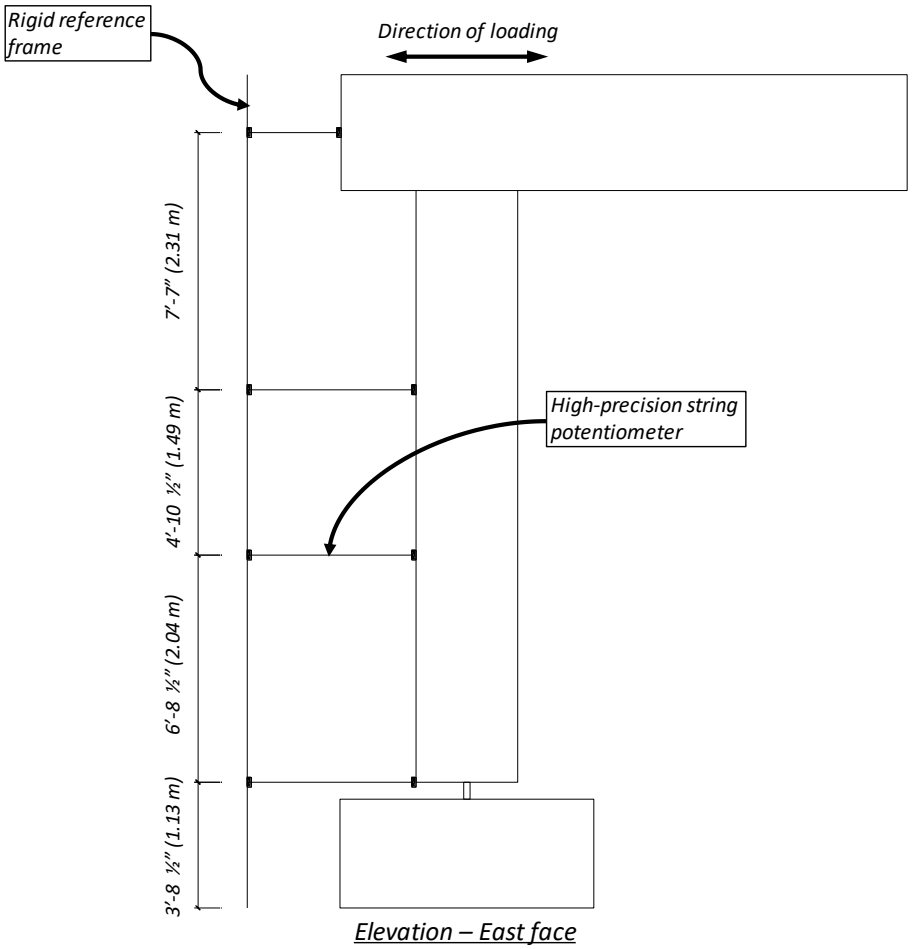

Figure 4.16. High-Precision String Potentiometers Used to Monitor Lateral Displacements

4.5. Experimental Test Results

The global lateral force-displacement, as well as the normalized column moment-displacement response of the test specimen identifying some key points along the test are shown in Figures 4.17 and 4.18 respectively. The drift ratios presented are measured from the location of the lateral load application (at the center height of the cap beam), to the base of the column immediately above the proprietary hinge. Loading and displacements are

defined as positive for the push cycles, where the lateral load was applied in the southward direction. The column moment is normalized by $A_g D_c f_c'$, and for comparison, the ideal moment, M_i, which is the column moment capacity computed with simplified flexure theory using the measured materials properties, is provided. The onset of bar buckling was observed during the reloading branch of the last cycle of displacement ductility of 4 (at a drift ratio of approximately -1%). In the moment-lateral displacement response, Figure 4.18, the column showed a sustained moment capacity up until the fracture of the first longitudinal bar occurred after the first reversal following the peak displacement at ductility of +5 (drift ratio of approximately -4%), after which drops in moment capacity are observed upon buckling and fracture of other longitudinal bars. In the lateral load-displacement response, Figure 4.17, the P-Delta effect plays a significant role in the observed response. During the push loading cycles, the high axial load ratio of approximately 12% of $f_c' A_g$ reduces the lateral force capacity with increasing levels of displacement. This decrease is observed by the negative slope of the ideal lateral force-displacement line, F_i, which is the lateral load-displacement response calculated using the ideal moment, M_i, of the column, incorporating the actual axial load observed during the test, see Equation 4.3.

$$F_i = \frac{-P \cdot \Delta}{L} + \frac{M_i}{L} \qquad 4.3$$

In the pull loading cycles however, due to the negligibly small axial load, the lateral force capacity remains mostly constant and consistent with the behavior observed in the moment-displacement response. The loss of capacity observed in the moment-

displacement response, caused by the buckling and fracture of the column longitudinal reinforcement, translates into the force displacement peaks falling below the ideal lateral force-displacement lines in Figure 4.17.

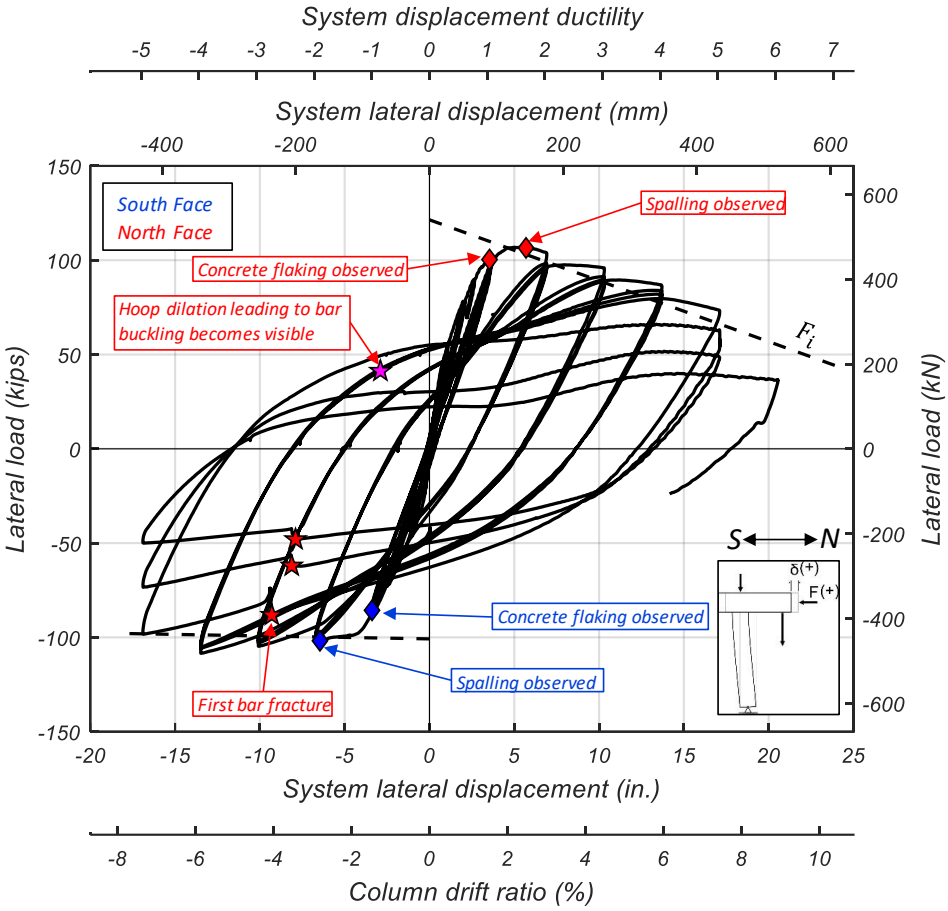

Figure 4.17. Global Lateral Load-Displacement Response of Test Specimen

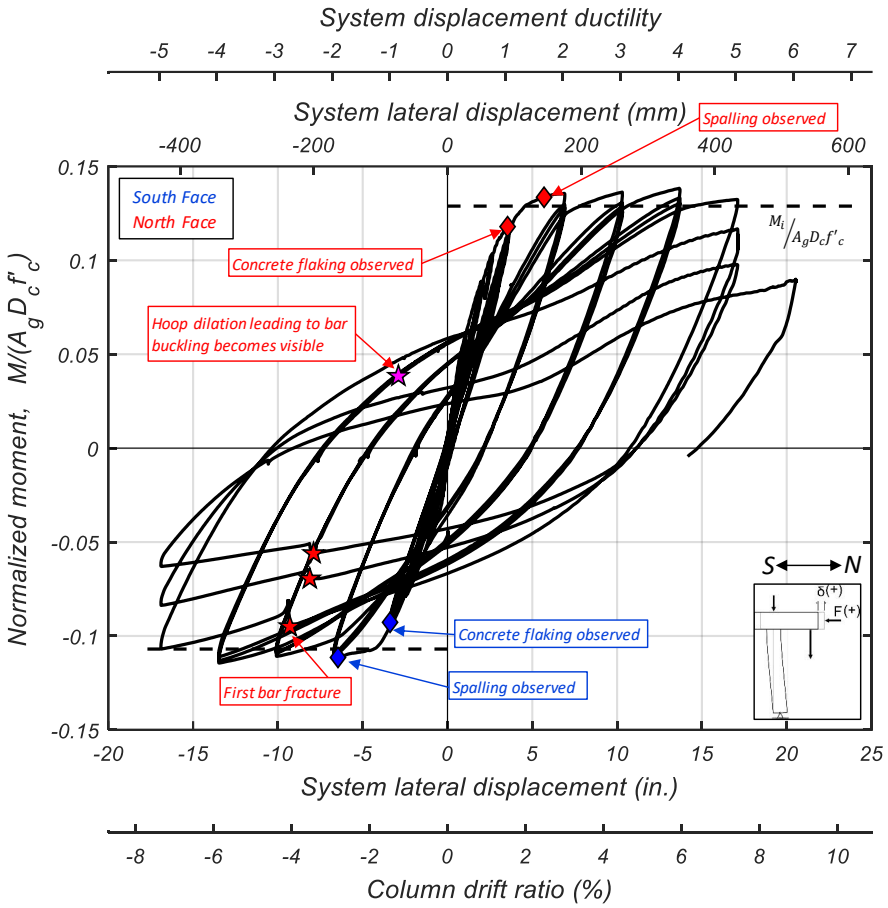

Figure 4.18. Normalized Column Moment-Displacement Response of Test Specimen

Throughout testing, the column developed a plastic hinge beneath the joint and sustained severe damage. Flaking and spalling of the concrete cover, buckling, and fracture of the column longitudinal reinforcing bars were observed in the plastic hinge region. The north face of the column plastic hinge, which was under compression during the push cycles, exhibited more damage due to the increased axial load and moment demands. Damage observed in the south face of the column plastic hinge was far less severe predominantly due to the lower axial load on the column during the pull cycles where the south face was under compression. The column state at key points during the test are shown in Figures 4.19 and 4.20 for the north and south faces respectively.

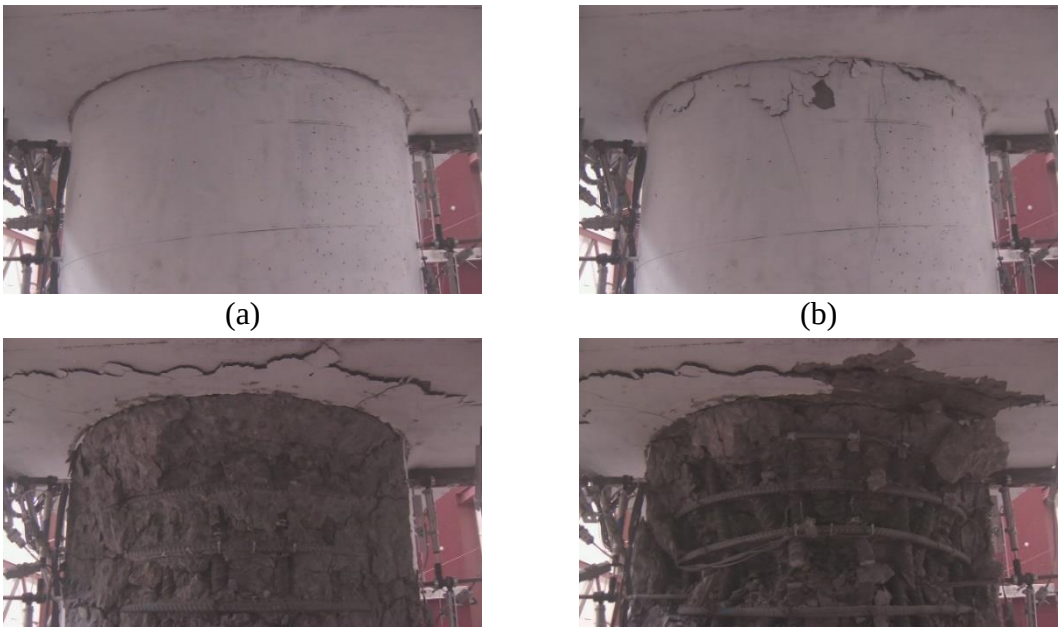

(a) (b)

(c) (d)

Figure 4.19. North Face of Column Plastic Hinge at Key Points During Test: (a) Concrete Flaking; (b) Concrete Spalling; (c) Reinforcing Bars Exposed; (d) Severe Buckling and Bar Fracture

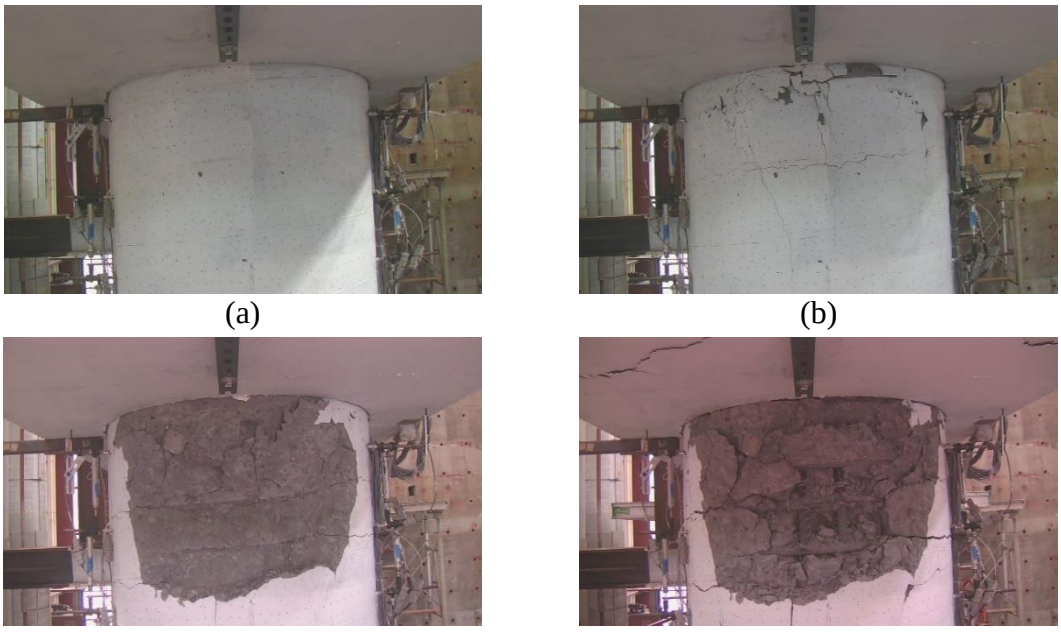

(a) (b)

(c) (d)

Figure 4.20. South Face of Column Plastic Hinge at Key Points During Test: (a) Concrete Flaking; (b) Onset of Concrete Spalling; (c) Severe Concrete Spalling; (d) Reinforcing Bars Exposed

During the load-controlled cycles at the beginning of the test, prior to yielding in the column longitudinal reinforcement, minor flexural cracks with a maximum residual width of 0.008 in. (0.2 mm) developed along the height of the column. By the end of the last load-controlled cycle (75% of F_y) the maximum residual width of the cracks remained largely unchanged and remained at approximately 0.008 in. (0.2 mm) wide. Flaking of the concrete in the north and south faces occurred at the first cycle peak of displacement ductility ±1 (drift ratio of approximately 1.5%). At a displacement ductility of ±2 (drift ratio of approximately 2.5%), spalling of the concrete was observed at the locations where flaking had previously occurred. As much of the cover concrete had spalled off in the plastic hinge region, hoop dilation leading to bar buckling in the north side of the column became visible during the reloading push cycle of displacement ductility +5. After the reversal, and prior to reaching the pull peak of displacement ductility -5, the first longitudinal bar fracture occurred and a sharp decline in strength capacity was noticeable. As the test continued, in the remaining cycles, more bar buckling, and subsequent fracture occurred resulting in a steady strength capacity decline until the test was stopped.

Overall, damage was largely isolated in the column plastic hinge, and only minor shear cracking was observed in the joint corresponding to the direction of loading. Figure 4.21 shows the state of the west face of the column-bent cap joint at displacement ductility of ±4 (drift ratio of approximately +6% and -5.9%). A detailed 360° 3D point cloud model was developed to fully capture and catalog the extent of damage in the plastic hinge region of the column at the end of testing, as presented in Figure 4.22.

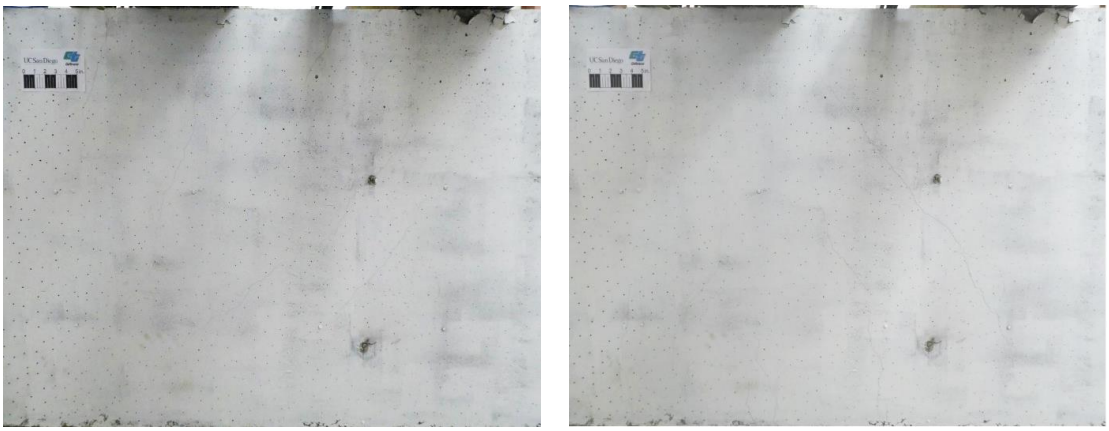

(a) (b)

Figure 4.21. Minor Shear Cracking Observed in West Face of Bent Cap Joint at: (a) Peak of Displacement Ductility +4; (b) Peak of Displacement Ductility -4

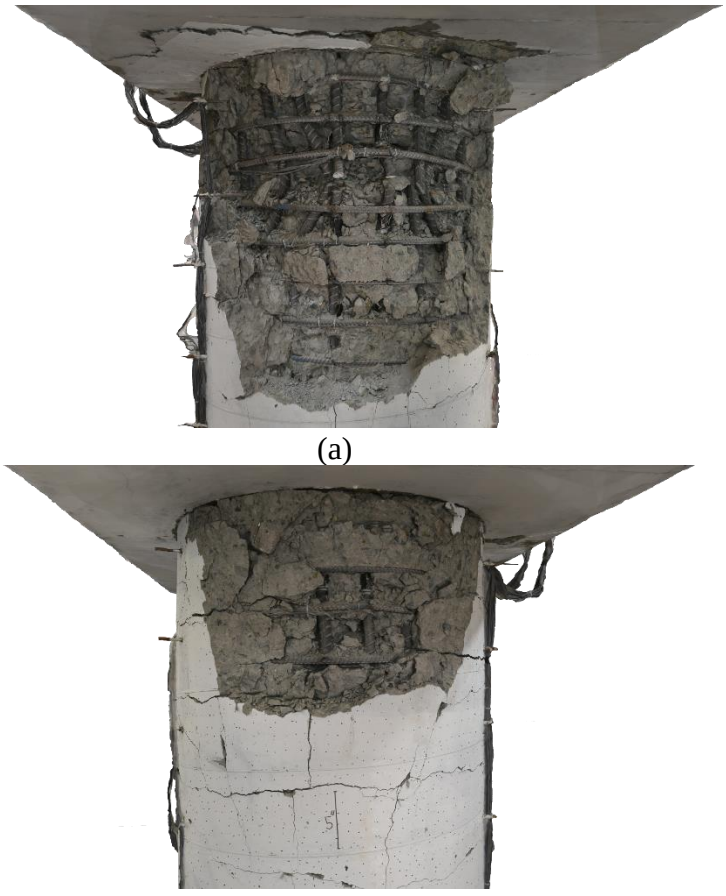

(a)

(b)

Figure 4.22. 360° Detailed 3D Point Cloud Model Showing Extent of Damage in Column Plastic Hinge Region Post-Test; (a) Interior Face of Column; (b) Exterior Face of Column

The maximum lateral load resistance, effective yield displacement and drift ratio, and displacement ductility capacity of the test specimen are presented in Table 4.4. Given that the displacement ductility capacity of columns is defined as the maximum ductility attained prior to the first bar fracture, the test specimen attained a ductility capacity of 5.

Table 4.4. Test Specimen Global Response Summary

Loading Direction	Maximum Lateral Load (kips) [kN]	Equivalent Yield Displacement, Δ_y (in.) [mm]	Equivalent Yield Drift Ratio (%)	Displacement Ductility Capacity
Push	106.8 [475]	3.61 [92]	1.56	5
Pull	108.4 [482]	3.39 [86]	1.47	5

4.6. Data Processing and Interpretation

Curvatures along the height of the column were calculated using data recorded from panels of vertical linear potentiometers presented in Figure 4.15. The simple computational steps performed to obtain the curvature from each panel is outlined in Equation 4.6.

$$\varepsilon_{Ni} = \frac{\frac{d_{ENi}}{L_i} + \frac{d_{WNi}}{L_i}}{2} \quad 4.4$$

$$\varepsilon_{Si} = \frac{\frac{d_{ESi}}{L_i} + \frac{d_{WSi}}{L_i}}{2} \quad 4.5$$

$$\varphi_i = \frac{\varepsilon_{Si} - \varepsilon_{Ni}}{\delta_i} \quad 4.6$$

where ε_S and ε_N are the average strains within each panel in the south and north side of the column respectively, i refers to the panel number, d_{EN} and d_{ES} are the relative displacements measured by the potentiometers on the north and south side of the east face

of the column, d_{WN} and d_{WS} are the relative displacements measured by the potentiometers on the north and south side of the west face of the column, L is the gage length of each corresponding potentiometer, and δ is the distance between north and south potentiometer sets.

The curvature profile of the column, normalized by D_c/ε_y, at various displacement ductility levels is presented in Figure 4.23. Since the curvatures were calculated from measurements at discrete locations along the height of the column, they are presented as constant between measurement locations. It should be noted that the curvature profile begins at 3 in. (76 mm) below the column-bent cap interface, as the linear potentiometers mounted at that level were used to measure the fixed-end rotation of the column. The yield curvature, φ_y, is calculated using the approximate formulation provided by Priestley[49], as shown in Equation 4.7.

$$\varphi_y = 2.25\frac{\varepsilon_y}{D_c} \qquad 4.7$$

where ε_y is the yield strain of the longitudinal reinforcing bars, and D_c is the diameter of the column. The curvature profile presented in Figure 4.23 shows that the maximum curvatures observed in the upper 25% to 30% of the column beneath the column-bent cap interface exceed the yield curvature.

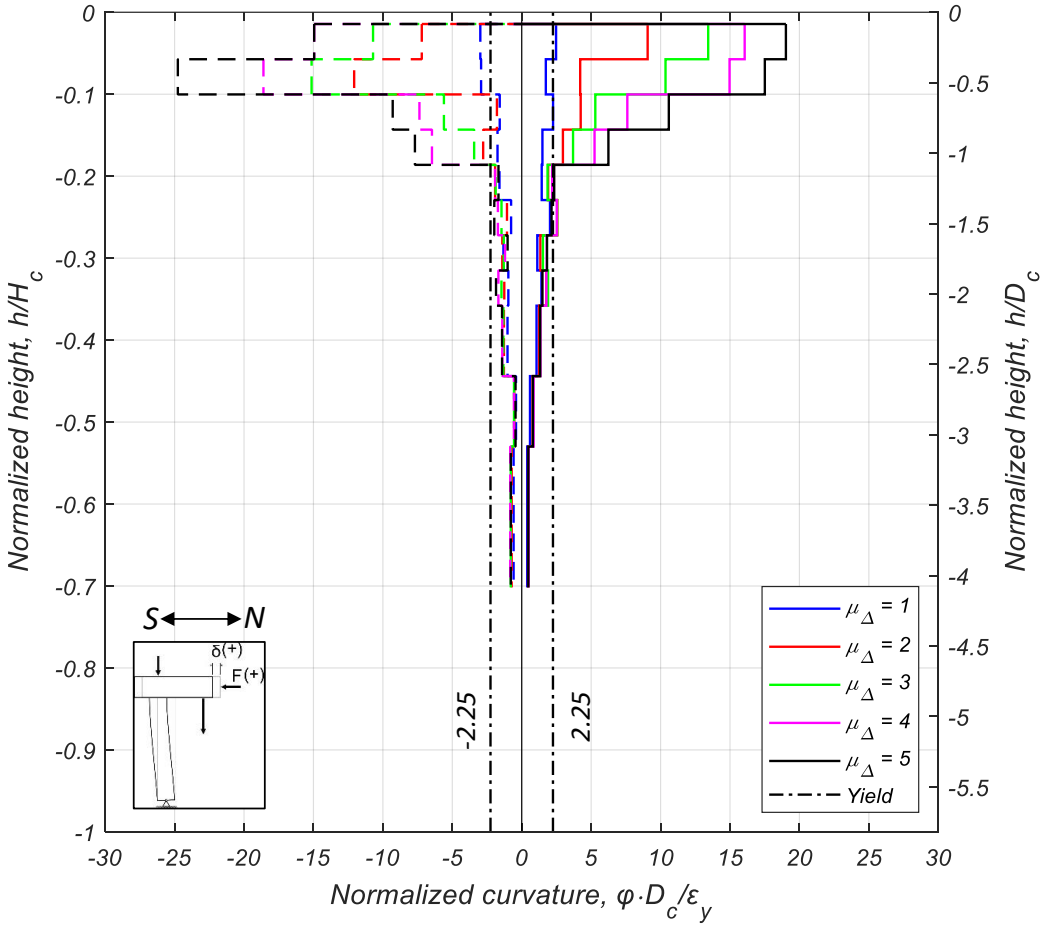

Figure 4.23. Curvature Profile of Column Obtained from Linear Potentiometers

The northern face of the column undergoes compression during the push (positive) loading cycles, whereas the southern face of the column experiences compressive forces during the pull (negative) loading cycles. The compressive strain profile of the concrete surface on both the north and south face is evaluated at each displacement ductility level and presented in Figures 4.24 and 4.25 respectively. As expected, based on the curvature profile of the column, the concrete in the upper 20% of the column beneath the column-bent cap interface experienced the most severe compressive strains resulting in crushing of the concrete.

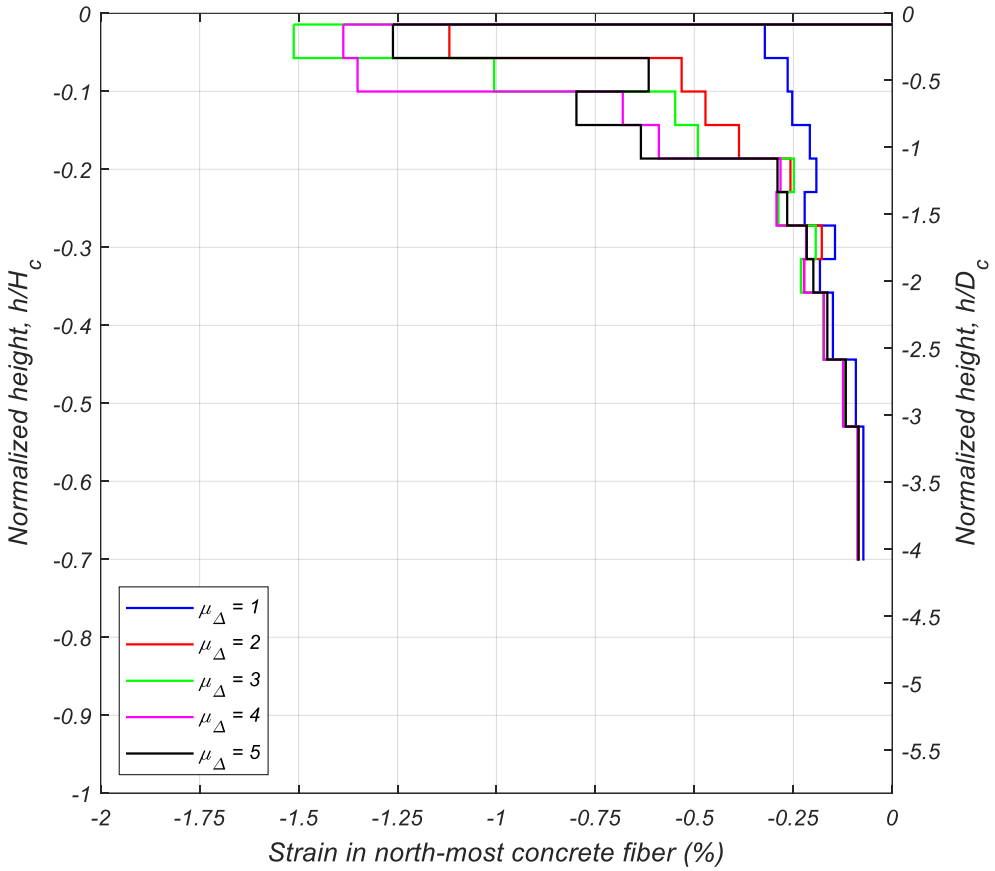

Figure 4.24. Column Concrete Compressive Strain Profile of Northern Face

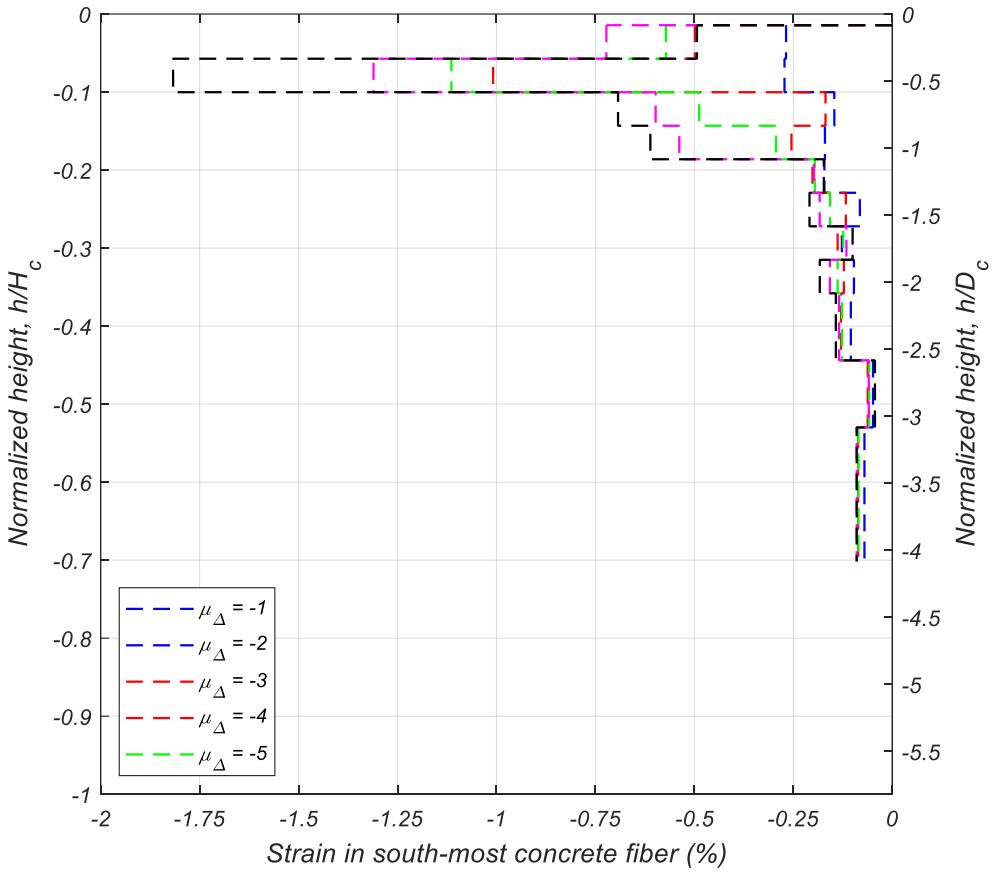

Figure 4.25. Column Concrete Compressive Strain Profile of Southern Face

Similarly, the smeared strains in the longitudinal reinforcing bars on the extreme northern and southern faces of the column are evaluated at every displacement ductility level and presented in Figures 4.26 and 4.27, where all the push cycles are plotted with continuous lines, and all pull cycles with dashed lines. Bar strains in the upper 20% of the column height exceed the measured yield strain, and the gradual decrease in bar strains is observed farther away from the plastic hinge region.

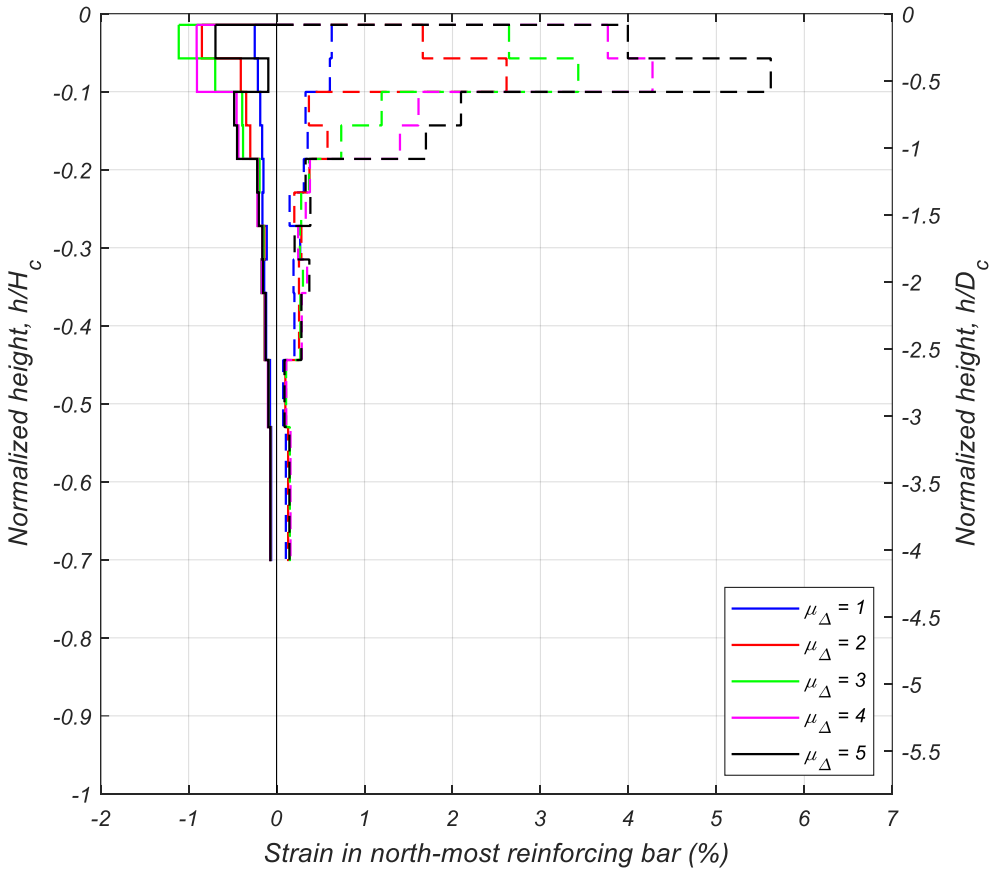

Figure 4.26. Smeared Strain Profile of Northern-Most Column Reinforcing Bar

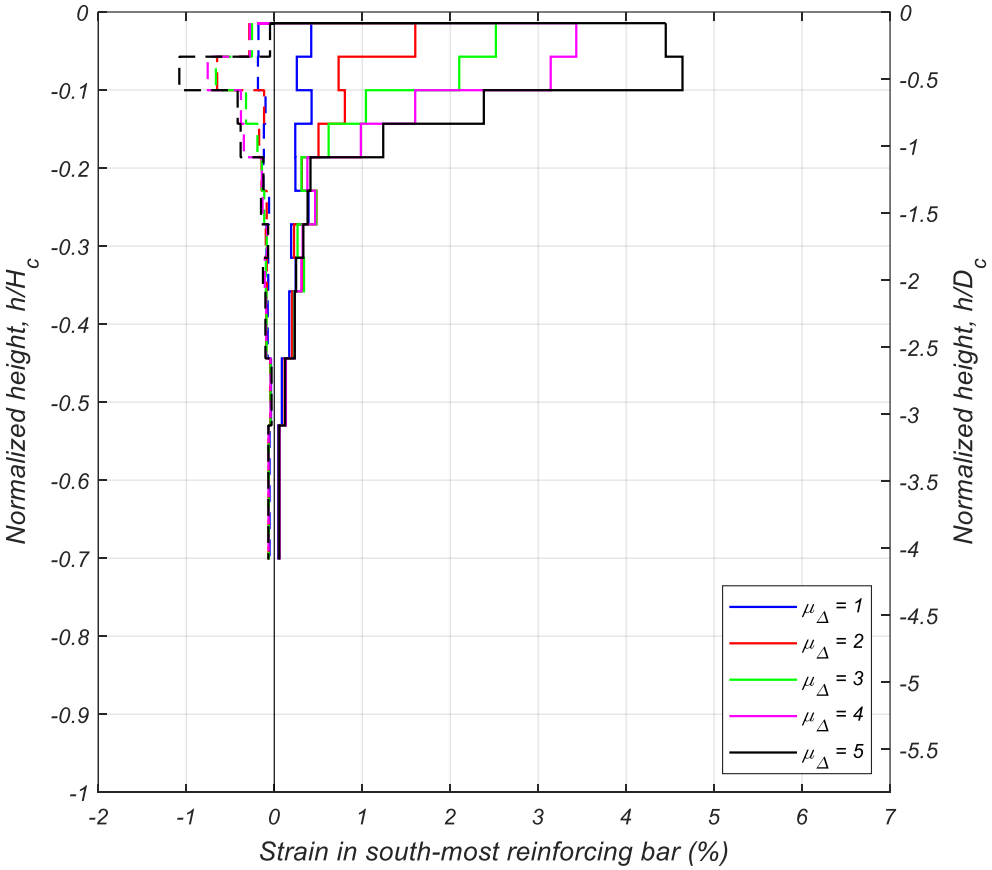

Figure 4.27. Smeared Strain Profile of Southern-Most Column Reinforcing Bar

The column longitudinal bar strains were also monitored at various discrete points along their length using high elongation electrical-foil strain gages as described earlier. Electrical-foil strain gages provide very accurate strain measurements, albeit with some significant drawbacks. The measurements obtained from strain gages represent a very localized strain, which is not necessarily an accurate representation of the actual behavior of the bar, especially during cyclic loading events where buckling of the bar may occur. Another major drawback with using strain gages is their fragility and sensitivity to damage. Strain gages, or often their wires, get damaged rather easily during construction, and since they are embedded within the specimen, repairs and replacements are not possible.

Although most of the strain gages or their wires were damaged at high displacement ductility levels during the test, valuable information was obtained regarding the yield strain penetration into the cap beam. The measured strains of these longitudinal bars at peak displacements of various cycles are presented in Figures 4.28 and 4.29. The maximum yield penetration in the bars occurred at displacement ductility of -5 and was measured to be approximately 1'-6" (457 mm) or $16d_b$. Since the total embedment length of the column longitudinal bars into the cap beam was 37.5 in. (0.95 m), which is approximately $33d_b$, the yield penetration of $16d_b$ represents about 49% of the total embedment length of the bars.

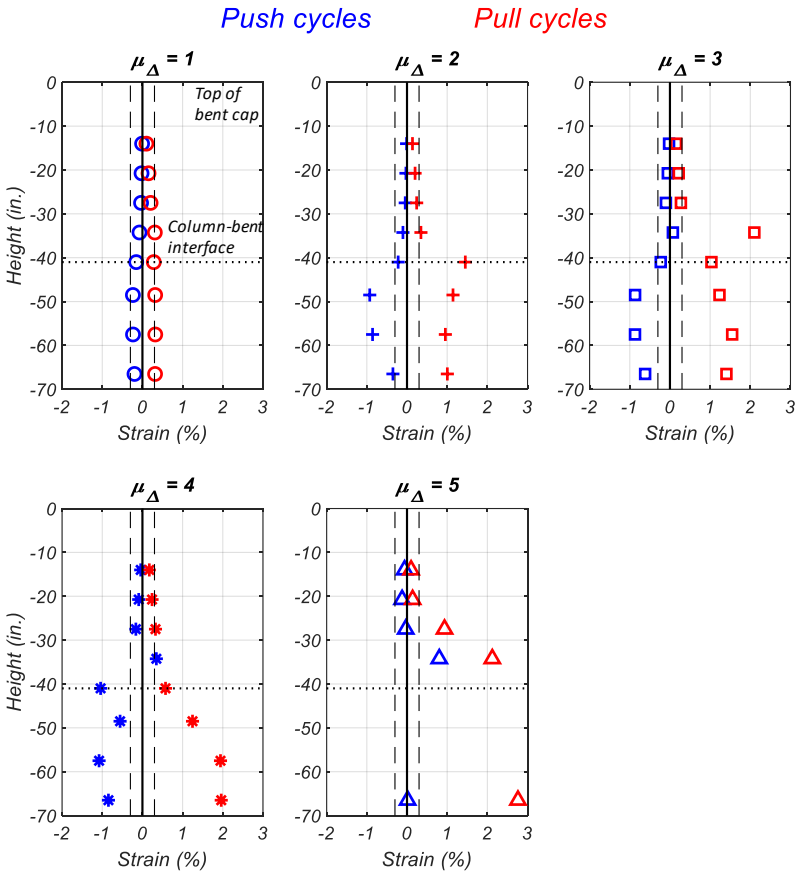

Figure 4.28. Measured Strains of Northern-Most Column Longitudinal Bars (from Strain Gages) at Peak Displacements of Various Cycles

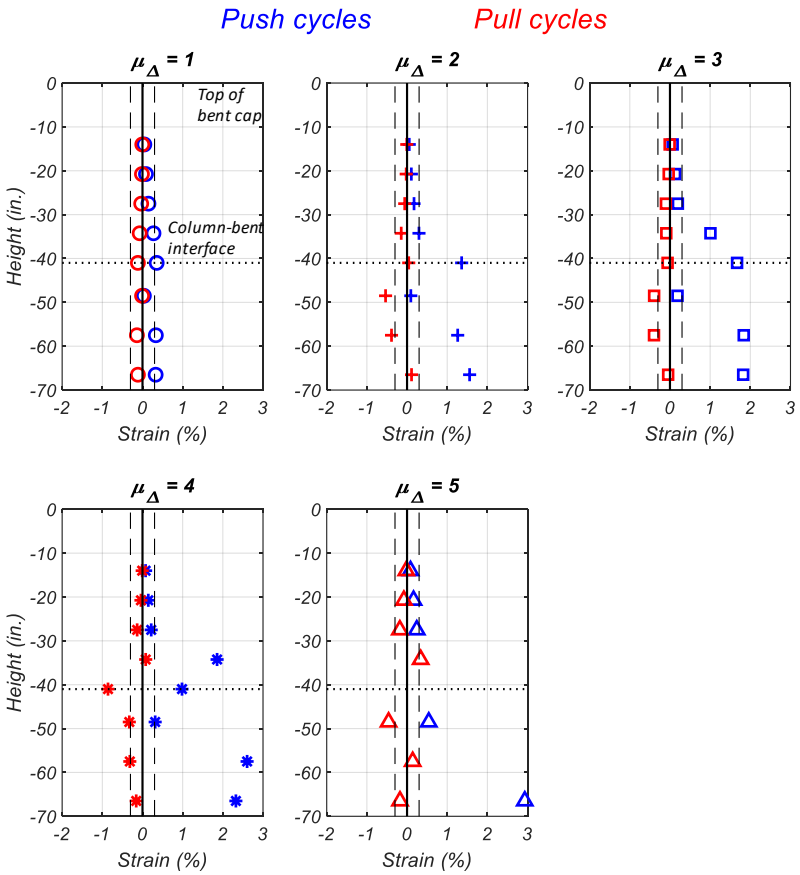

Figure 4.29. Measured Strains of Southern-Most Column Longitudinal Bars (from Strain Gages) at Peak Displacements of Various Cycles

The displacements measured at each displacement ductility level using high-precision string potentiometers were compared with the overall displacement calculated from the data obtained by the linear potentiometers affixed along the height of the column and pile. The top displacement is decoupled into three primary components: (a) flexure in the column, (b) fixed end rotation of the column due to yield penetration and bond slip at the column-bent cap interface, and (c) shear in the column. The displacements caused by each of these four components is calculated from the data obtained by the potentiometers and compared with the actual lateral displacement recorded during testing, see Figure 4.30. At displacement ductility of -3, since the concrete at the interface surface had been severely

crushed, the linear potentiometers placed at that location to measure the fixed-end rotation of the column no longer provided reliable readings and therefore could not capture the displacement contribution from the fixed-end rotation. It is observed however, that the predominant contributor to the lateral displacement is flexure in the column, which accounts for 56% to 68% of the overall displacement in the push cycles, and 57% to 71% in the pull cycles. The fixed end rotation of the column is also a major contributor to the top displacement accounting for approximately 27% of the overall displacement in the push cycles, and 26% to 32% in the pull cycles where instrumentation was still available. Shear deformations in the column, however, contribute very little to the overall top displacement, at about 1%.

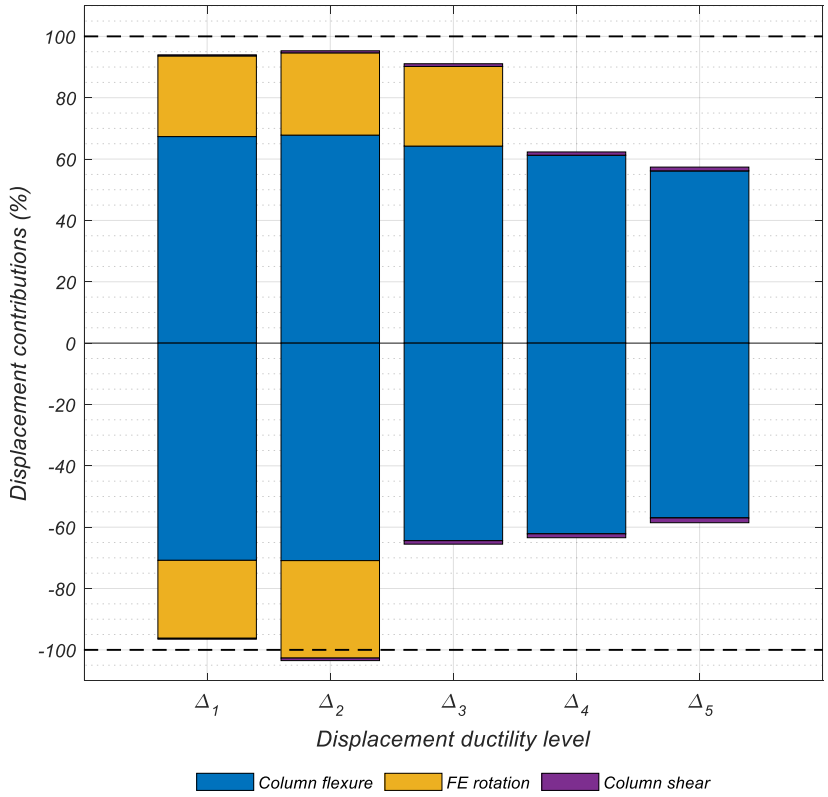

Figure 4.30. Components of Lateral Displacement at Peak Displacement Ductility Levels

4.7. Summary and Conclusions

Although the test specimen was scaled down in size, and the prescribed design recommendations were scaled to incorporate the use of Grade 80 reinforcement, the ¾-scale bridge column-bent cap connection test specimen performed satisfactorily. The specimen achieved extensive drift ratios in both push and pull loading directions (high axial load, and virtually no axial load respectively) with negligible strength degradation. P-Delta effects were pronounced in the push loading cycles where the column axial load was greatest, while in the pull loading cycles due to minimal column axial load, P-Delta effects were negligible. Extensive plastic hinging occurred in the column as expected, and the column-bent cap joint behaved in an essentially elastic manner, with only minor cracks that closed upon returning the specimen to its steady-state.

The in-house designed proprietary hinge at the base of the column performed spectacularly, behaving as a hinge in the direction of loading, reducing the base moment to effectively zero. By grouting the bars within the steel guiding frame, the hinge performed as desired, and no measurable slippage was observed in the hinge bars. The use of this proprietary hinge mechanism substantially reduced construction time and cost.

Chapter 4, in part, is currently being prepared for submission for publication of the material. Lotfizadeh, Koorosh H.; Bustamante, Ricardo; Restrepo, José I. The dissertation author was the primary investigator and author of this material.

Chapter 5.

PLASTIC BUCKLING-STRAIGHTENING FATIGUE OF HIGH-STRENGTH GRADE 80 REINFORCEMENT

5.1. Abstract

Fracture in the longitudinal reinforcement of bridge columns after buckling is a very common failure mode. Observing the behavior of columns from various tests, and real-world applications, it is seen that the longitudinal reinforcement often buckles along several sets of hoops and not necessarily between only two adjacent hoops. While many have studied the bar buckling phenomena between a set of hoops, limited research has been conducted to characterize the response of reinforcement buckling along several sets of hoops[10],[26],[40],[63]–[66]. Taking into consideration however, that most research to date has been carried out regarding Grade 60 reinforcement, the buckling behavior and fatigue life of Grade 80 reinforcement remains to be studied. The use of A706 Grade 80 reinforcement in seismic critical members (SCM) requires extensive investigation. This chapter discusses both the experimental research conducted on large diameter ASTM A706 Grade 80

reinforcement to characterize the buckling behavior, post-buckling fracture mechanism, and cyclic fatigue life of the bars, as well as the extensive finite element analysis study conducted to develop a simplified expression for design purposes to prevent premature plastic buckling and subsequent fracture of column longitudinal reinforcement.

5.2. Introduction

Restrepo-Posada et al.[67] found that as bars buckle, microscopic compression cracks develop at the base of bar deformations due to "low-cycle" fatigue. As the bar begins to buckle, a large concentration of shear strains develops resulting in a rearrangement of the steel microstructure. Microscopic cracks initially invisible to the naked eye begin to form at the base of the deformations on the concave side of the buckled bar, Figure 5.1, where the stress concentration is most prevalent. Under cyclic loading, the propagation of these cracks due to unloading and straightening of the bar, ultimately leads to bar fracture.

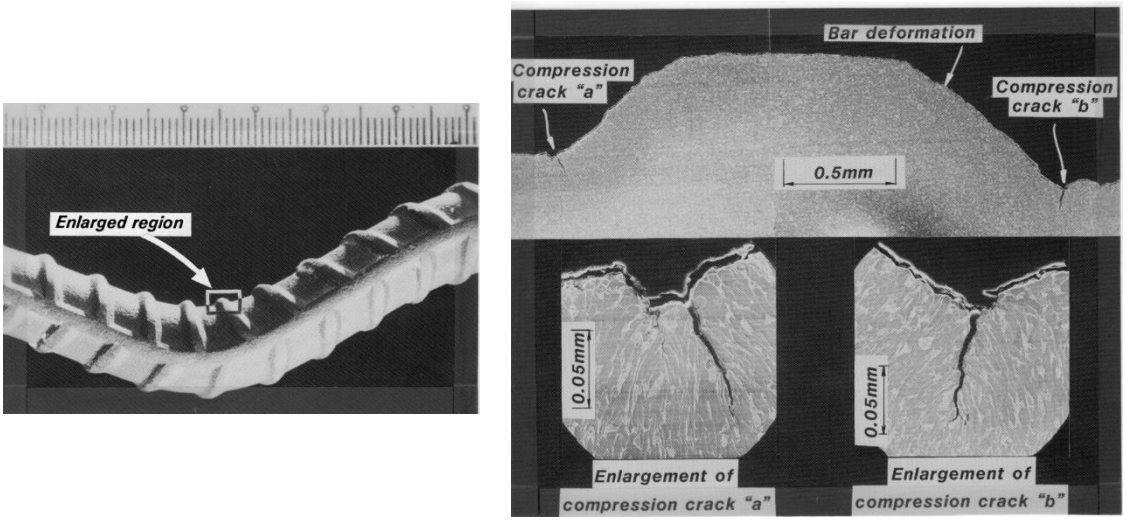

(a) (b)

Figure 5.1. Microscopic Image of a Longitudinal Section Cut of Buckled Reinforcing Bar Showing Compressive Crack Formation: (a) Buckled Bar (Scale in mm); (b) Cracks Developed at Root of Bar Rib (Restrepo-Posada et al., 1994)

Many researchers have attempted to characterize the behavior of reinforcement under large amplitude cyclic strains with varying levels of success. Most have been unable to experimentally characterize this buckling-straightening phenomenon mainly due to boundary condition issues such as bond-slip and rotation at the gripped ends of the bar. To properly investigate this behavior while avoiding issues with bar gripping experienced by other researchers, Duck et al.[40] designed and fabricated an innovative test apparatus which used a highly confined sulfur-based concrete substitute to grip the ends of the bar, see Figure 5.2. The sulfur-based concrete was selected for the apparatus since it has a high strength and fatigue resistance, can be melted and re-used, and it solidifies and gains strength rapidly upon cooling which prove useful for performing multiple tests using the same apparatus without the wasted material. The loading apparatus was carefully designed to allow the testing of large diameter ASTM A706 Grade 60 #18 bars under large strain amplitude cyclic loading and was made rigid enough to sustain the buckling of these large diameter bars while maintaining near full fixity at the gripped ends. The apparatus remains elastic while allowing a maximum rotation at the top grip of 1.61×10^{-4} radians, or approximately 8.1% of the maximum allowable rotation of 0.002 radians. As detailed by Duck et al.[40], a lateral bracing system was implemented which allowed the movement and removal of the upper pipe, while preventing excessive out of plane rotation during testing, see Figure 5.3. To simulate the restraint provided by the transverse reinforcement in a column, as well as the cone formed at the base of columns after cyclic loading, 4 in. (102 mm) thick circular steel blocks with a 2.5 in. (64 mm) center hole were placed around the bar at the interface on both ends, see Figure 5.4, similar to the investigation by Mander[26].

The axial load is applied by two 500 kip (2224 kN) hydraulic actuators positioned on either side of the apparatus and connected by a heavily reinforced built-up steel spreader beam, as shown in Figure 5.5. The design of the test apparatus is thoroughly explained by Duck et al.[40].

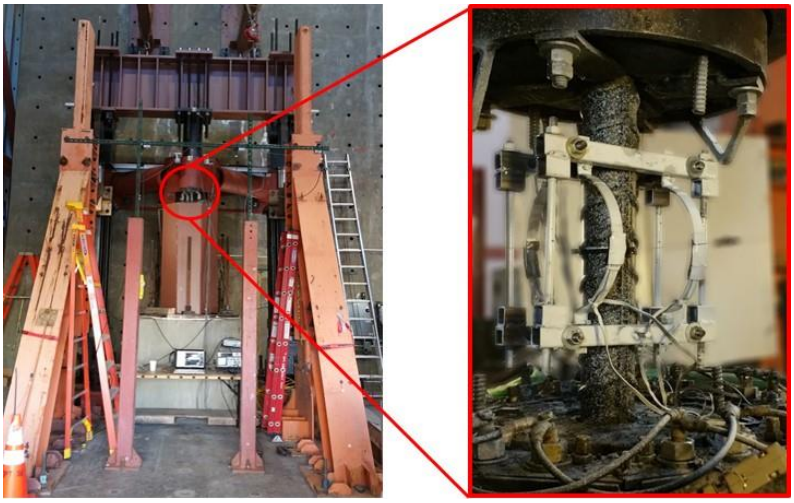

Figure 5.2. Test Apparatus Using Highly Confined Sulfur-Based Concrete Substitute for Bar Grips (Duck et al., 2018)

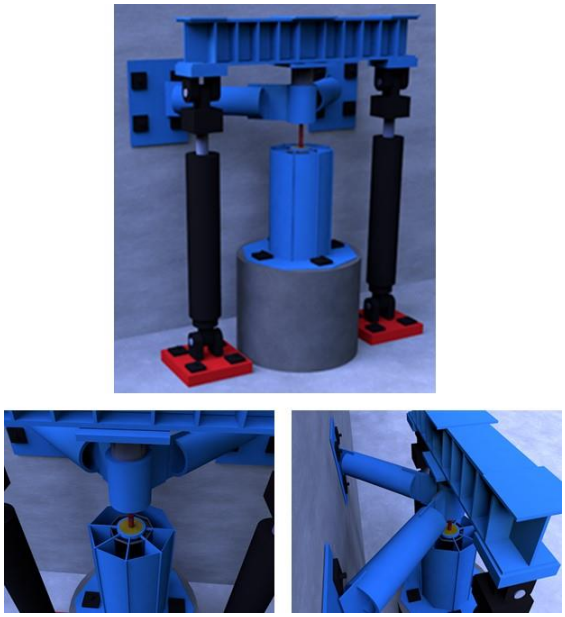

Figure 5.3. 3D Rendering of Test Apparatus Highlighting the Lateral Bracing System (Duck et al., 2018)

Figure 5.4. Circular Steel Blocks Used at Each End of Gripped Bar (Duck et al., 2018)

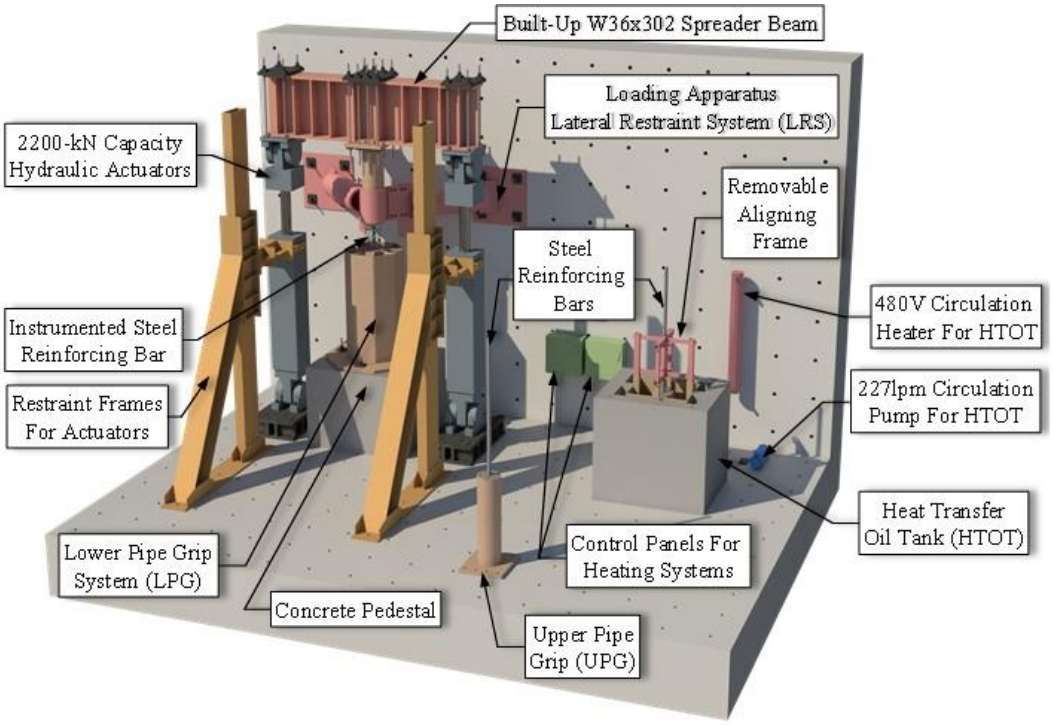

Figure 5.5. Detailed 3D Rendering of Test Setup Identifying Key Components (Duck et al., 2018)

5.3. Research Significance

Characterizing the buckling and subsequent fracture mechanism of high-strength reinforcement, such as Grade 80, is critical in determining the suitability of using such reinforcement in seismic critical members (SCMs). Although exhaustive experimental and analytical research has been conducted on Grade 60 large-diameter bars in the past, no such research is available for higher-strength reinforcement such as Grade 80. The incorporation of Grade 80 large diameter reinforcement in seismic critical members in design guidelines such as Caltrans SDC requires that the mechanical and low-cycle fatigue characteristics of this reinforcement to be well established and validated through experimental investigations.

5.4. Experimental Investigation Test Program

To characterize and investigate the plastic buckling-straightening fatigue (PBSF) life of large diameter #14 ASTM A706 Grade 80 reinforcing bars under large-amplitude cyclic strain amplitudes, the test apparatus designed by Duck et al.[40] was modified to accommodate the testing of #14 bars, and a series of tests with varying strain amplitudes were performed. In order to reduce the effect of compressive stress concentration at the base of the bar deformations on the concave side during buckling, the same series of tests were performed for both conventional reinforcing bars available in the market, as well as the proposed and newly developed smoothed-rib-radii bars, see Figure 5.6.

(a)

(b)

Figure 5.6. Reinforcing Bar Deformations of: (a) Commonly Available "Normal" A706 Grade 80 #14 Bars, (b) Proposed Smoothed-Rib-Radii A706 Grade 80 #14 Bars

5.4.1. Loading Protocol

A total of four loading protocols were used in the test program, as outlined Table 5.1. The first load protocol consisted of a series of increasing strain amplitudes ranging from 0.75% to 9%, where each strain amplitude cycle was repeated twice. The remaining three loading protocols were constant amplitude tests ranging from 3% to 4%, performed to establish a relationship between deformation amplitude and the number of cycles to failure which allows for the comparison to existing fatigue models. All tests began with a series of three elastic cycles with a strain amplitude approximately equivalent to half of the expected yield strain of the bars, after which the strain loading protocols were applied until fatigue failure in the bars occurred. The loading protocols are presented visually in Figure 5.7. For consistency, all tests were performed for a constant aspect ratio of $\ell/d_b = 5$.

Table 5.1. Key Details of Loading Protocol Strain Histories

Protocol	Identifier	ε_{min} (%)	ε_{max} (%)	ε_{amp} ** (%)
SH1	Variable Amplitude	-	-	Variable
SH2	(3%, -0.5%)	-0.5	2.5	3
SH3	(4%, -1%)	-1	3	4
SH4	(3%, -1%)	-1	2	3

** $\varepsilon_{amp} = \varepsilon_{max} - \varepsilon_{min}$

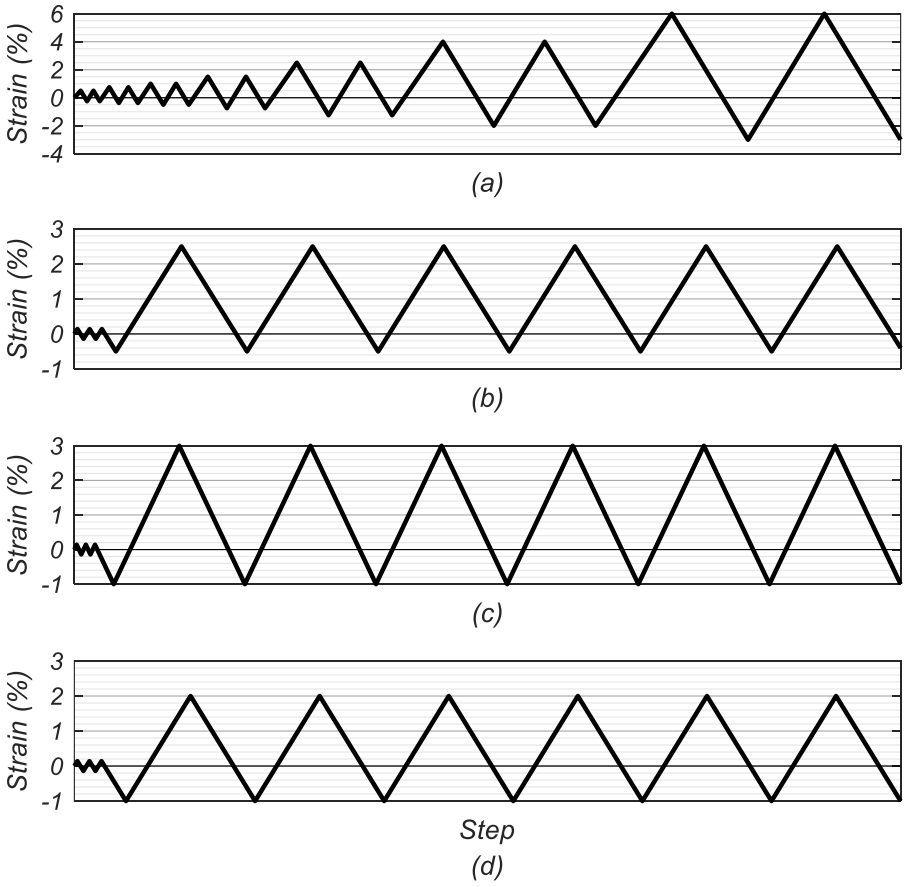

Figure 5.7. Loading Protocol Strain Histories: (a) SH1: Variable Amplitude; (b) SH2: (3%, -0.5%); (c) SH3: (4%, -1%); (d) SH4: (3%, -1%)

5.4.2. Reinforcing Bar Properties

A set of three monotonic tensile tests were performed for both the regular and smoothed-rib-radii bars to determine their respective mechanical properties, shown in Figures 5.8 and 5.9. Strain measurements were taken with a 2 in. (51 mm) gage length extensometer and a specially designed and in-house fabricated clip gage. The resulting bar mechanical properties obtained from these monotonic tests are presented in Table 5.2. It is shown that although both bar types were ASTM A706 Grade 80, their yield and tensile strength vary noticeably. An average yield strength of 80.4 ksi (554 MPa) and 87.3 ksi (602 MPa) is observed for the smoothed-rib-radii and the common bar respectively. Similarly, an average tensile strength of 107.7 ksi (743 MPa) and 114.2 ksi (787 MPa) is measured for the smoothed-rib-radii and the common bar respectively. Table 5.3 lists the geometric properties for both these types of bars as defined by Metelli and Plizzari[31].

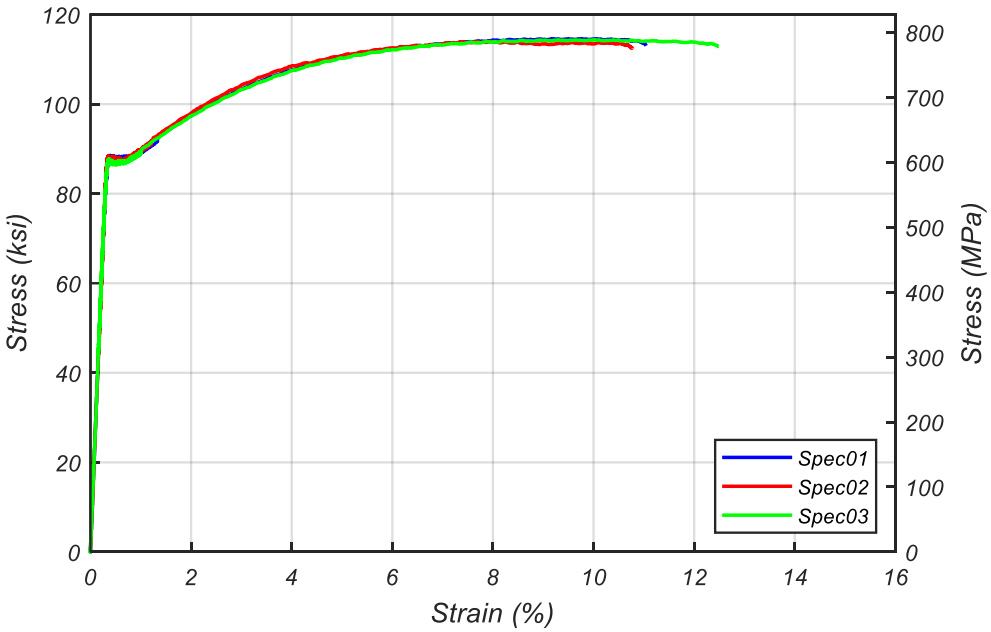

Figure 5.8. Normal #14 ASTM A706 Grade 80 Tensile Test Data

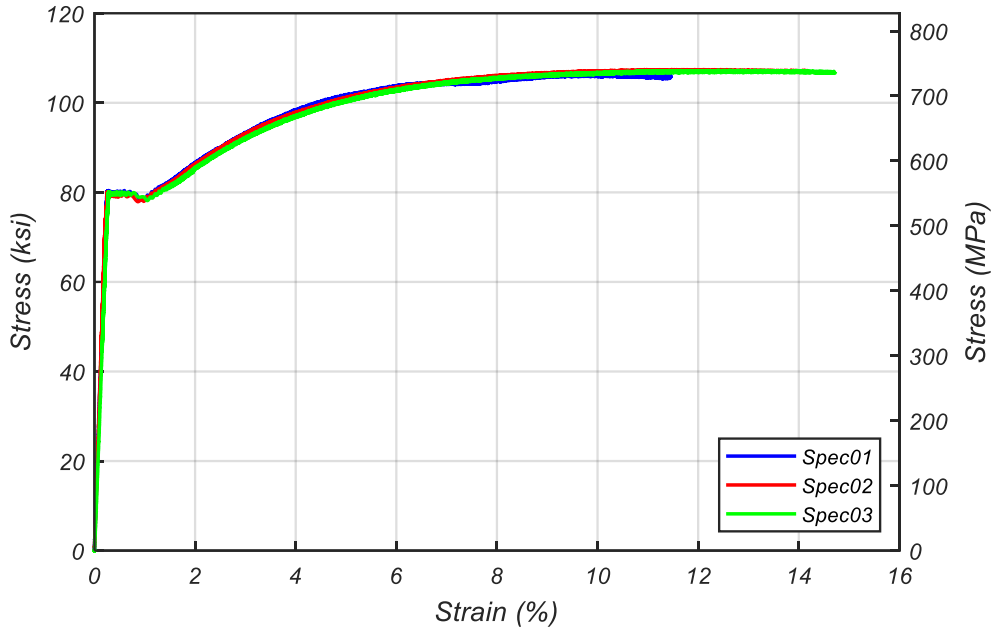

Figure 5.9. Smoothed-Rib-Radii #14 ASTM A706 Grade 80 Tensile Test Data

Table 5.2. Reinforcing Bars Mechanical Properties

Bar ID	f_y (ksi) [MPa]	$f_{s4\%}$ (ksi) [MPa]	f_{su} (ksi) [MPa]	ε_y (%)	ε_{sh} (%)	ε_{su} (%)	$\frac{f_{su}}{f_y}$	$\frac{f_{s4\%}}{f_y}$	$\frac{f_{su}-f_y}{f_y}$	P
#14‡	87.3 [602]	107.9 [744]	114.2 [787]	0.31	0.74	9.0	1.31	1.24	0.31	2.84
#14†	80.4 [554]	98.1 [676]	107.7 [743]	0.28	0.91	10.9	1.34	1.22	0.34	3.04

‡ Commonly available ASTM A706 reinforcement

† Smoothed-rib-radii ASTM A706 reinforcement

Table 5.3. Reinforcing Bars Geometric Properties

Bar ID	d_b (in.) [mm]	f_{Rm}	d_e (in.) [mm]	β (degrees)	s (in.) [mm]	α (in.) [mm]
#14‡	1.693 [43]	0.109	1.779 [45.2]	72	0.967 [24.6]	0.107 [2.7]
#14†	1.693 [43]	0.094	1.803 [45.8]	64	1.032 [26.2]	0.097 [2.5]

‡ Commonly available ASTM A706 reinforcement
† Smoothed-rib-radii ASTM A706 reinforcement

5.4.3. Instrumentation

Following the design procedure provided by Carreño et al.[10] and Duck et al.[40], a clip gage strain measuring device was designed and fabricated with dimensions and properties suitable for this series of tests. The clip gage consists of two sets of diametrically opposite 0.063 in. (1.5 mm) thick aluminum 7075-T6 semi-circular arches mounted on steel frames, which affix to the reinforcing bar at four contact points using hardened steel tips along the bar's vertical ribs at the theoretical inflection points of the buckled shape, see Figure 5.10. Each arch is instrumented with two 0.2 in. (5 mm) high-elongation 120 Ohm electrical-foil strain gages, one on the convex and one on the concave side of the arch. The thickness and radius of the arches were selected such that at a maximum expected bar elongation of 6% during the test, the maximum strain induced in the arches remained below 50% of the aluminum yield strain. By limiting the strain in the arches, the clip gage was designed to be re-usable. The clip gage was calibrated by performing a series of monotonic tensile tests using the clip gage as a measurement device and comparing the strain measurements to those obtained using a commercially available 2 in. (51 mm) gage length

extensometer. A calibration factor between the axial strain of the clip gage arches and the axial strain in the bar was determined.

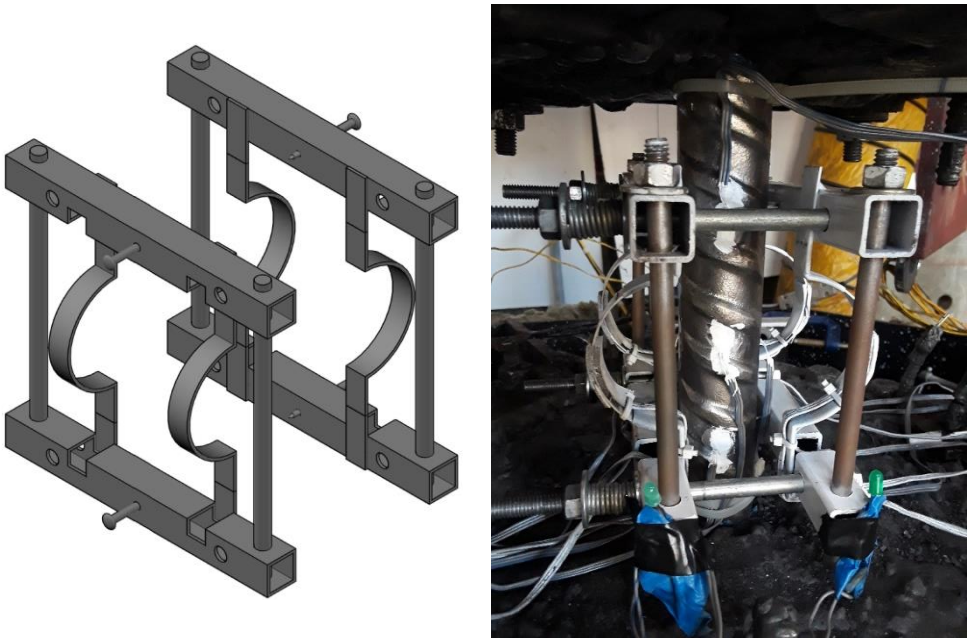

(a) (b)

Figure 5.10. In-House Designed Clip Gage Strain Measuring Device: (a) 3D Rendering; (b) Assembled on Test Bar

While the clip gage is an excellent device for accurately measuring the smeared strains on the bar, local strains along the unsupported length of the bar are measured using 0.2 in. (5 mm) high-elongation 120 Ohm electrical-foil strain gages. Sets of two diametrically opposite strain gages are placed between the bar deformations at the theoretical inflection points of the buckled shape, along with a set of four strain gages, two along the vertical rib, and two between the bar deformations, placed at mid-height. Ideally, more than four strain gages would be applied at mid-section. However, due to the limited available surface area of a #14 bar, a maximum of four strain gages could be affixed. Information provided by these strain gages, used in conjunction with Bernoulli's

hypothesis that plane sections remain plane under bending, the average strains in both the convex and concave sides as well as the curvature at the mid-section of the bar are obtained. The limitation to this process is that strain gages get damaged and fail at various points throughout the test, which poses a potential issue where after some loading cycles, not enough healthy strain gages remain to allow for the solution of a plane equation (which requires three known points).

Vertical displacement of the spreader beam transferring the load from the hydraulic actuators to the upper grip is measured using four string potentiometers, one on each corner of the beam. The rotation of the beam is also monitored using sets of inclinometers mounted orthogonal to each other, measuring rotations in both in-plane and out-of-plane directions. Monitoring these displacements and rotations in critical to ensure a proper test where no unexpected motion is occurring.

5.4.4. Test Setup

As previously mentioned, the test apparatus designed and built by Duck et al.[40] was re-purposed for this series of experiments. Some modifications were made to make the setup compatible with #14 Grade 80 bars. One such modification was to the circular steel block used at the gripped ends of the bar. The blocks were designed with a 2.5 in. (64 mm) hole at their center to accommodate a #18 bar. These blocks were modified, and the hole size reduced to 1.75 in. (45 mm) to provide a better boundary at the base of the bar. Similarly, the aligning metal frame used to keep the bar plumb and centered during installation in the upper grip was also modified for the use of #14 bars. Preparations for

each test consisted of various steps over the course of four days. A brief description of the day-to-day procedure is provided in the following section.

5.4.4.1. Day 1: Embedment of Bar into Upper Pipe

The upper grip pipe is placed in the concrete tank filled with heat transfer fluid and heated over the course of approximately 4-5 hours, depending on the ambient temperature. This allows the sulfur-concrete inside the pipe to fully melt and liquify. If any previously tested bar is still embedded in the upper pipe, a 1 in. (25 mm) bolt and nut are welded to the exposed end of the bar, and using lifting straps attached to a powered gantry crane, the bar is extracted from the molten sulfur-concrete mixture. To facilitate the embedment of the next test bar, the circular steel block at the interface is lifted and removed from the pipe, and using an auger with a 4 in. (102 mm) wide bit, the sulfur-concrete is drilled at the center all the way down the length of the upper pipe. This displaces all sulfur-aggregate mix within the pipe and ensures all material is uniformly distributed and molten with no separation between the liquid sulfur and solid aggregate. After thorough drilling and mixing of the sulfur-concrete, the circular steel block is re-inserted in the pipe, and the aligning steel frame is mounted atop the concrete tank in preparation for the insertion of the new test bar, see Figure 5.11.

Figure 5.11. Test Bar Embedded in Upper Pipe Grip Using the Aligning Steel Frame

The new test bar is cut to the desired length and embedded vertically in the upper pipe using the steel aligning frame as a guide to ensure plumbness. Bars for all tests were embedded 48 in. (1219 mm) into the upper pipe which is equivalent to $28.4d_b$. Since the circular steel block does not allow proper development of the bar along its depth, the 4 in. (102 mm) thickness of the block is not considered for the development length of the bars, leaving approximately 44 in. (1118 mm) or $26d_b$ of actual development length for the bars in the upper grip. To ensure a proper bond between the sulfur-concrete and the bar, all air pockets and voids were removed by using a formwork vibrator attached to the exposed end of the bar to induce vibrations within the upper pipe. At this point, liquid sulfur is poured into the upper pipe to account for the sulfur lost due to the extraction of the previously tested bar. Special care and attention is given to the orientation of the embedded bar within

the upper pipe, the vertical ribs of the bar are aligned to be in the East-West direction to ensure that the bar will buckle in the weaker direction (North-South).

After successfully embedding the bar in the upper pipe, the heating system for the concrete tank is shut down and the system is set to passively cool overnight. The pipe is not moved out of the concrete tank as to not disturb the bar orientation while the sulfur-concrete is still molten.

5.4.4.2. Day 2: Embedment of Bar into Lower Pipe

By the next morning, the upper grip pipe has cooled enough that the sulfur-concrete inside the pipe is no longer liquid. At this time the pipe is removed from the concrete tank and allowed to cool to ambient temperature. Meanwhile, the heating system of the lower pipe grip is activated, and the lower pipe is heated for approximately 5-6 hours, again depending on the ambient temperature, to melt the sulfur-concrete mixture. Once the sulfur-concrete in the lower pipe grip is molten, if any previously tested bar is still embedded, a bolt and nut are welded to the exposed end of the bar, and the bar is removed from the grip following a similar procedure as the upper pipe grip. The circular steel block is removed, and again using an auger with a 4 in. (102 mm) wide bit, the molten sulfur-concrete is drilled at the center of the pipe along the entire length of the lower pipe grip, approximately 60 in. (1524 mm) deep. After thorough drilling and mixing of the sulfur-concrete, the circular steel block is reinserted in the pipe. The temperature inside the lower pipe grip is monitored to ensure that the material remains molten, and the heating system is activated accordingly.

While the sulfur-concrete mix is still molten, the upper pipe grip (now in thermal equilibrium with the ambient temperature) is hoisted through bracing sleeve atop the lower pipe grip and the bar is aligned with the hole at the center of circular steel block. Using just the self-weight of the upper pipe grip, the bar is embedded several inches through the circular block into the lower pipe. The remaining required embedment depth of the bar into the lower pipe is achieved by attaching the spreader beam to the top of the upper pipe grip and applying downward load using the hydraulic actuators. This load application is done very carefully and incrementally to avoid any premature buckling and deformation of the bar during embedment. Bars for all tests were embedded between 56 and 57.5 in. (1422 and 1461 mm) into the lower pipe which is equivalent to $33.1d_b$ and $34d_b$. Again, since the circular steel block does not allow proper development of the bar along its depth, the 4 in. (102 mm) thickness of the block is not considered for the development length of the bars, leaving approximately 53 in. (1346 mm) or $31.3d_b$ of actual development length for the bars in the lower grip. To ensure a proper bond between the sulfur-concrete and the bar, all air pockets and voids were removed by using a formwork vibrator attached to the lower pipe housing to induce vibrations within the lower pipe. At this point, liquid sulfur is poured into the lower pipe to account for the sulfur lost due to the extraction of the previously tested bar.

After successful embedment of the bar into the lower pipe grip, the heating system is shut down and the system is set to cool overnight. To help expedite the cooling process, the thermal insulation surrounding the lower pipe is removed, and cooling fans are positioned around the system. Prior investigation by Duck et al.[40] and Carreño et al.[10]

has shown that even though sulfur-concrete has a very rapid strength gain, it also has a very low thermal conductivity. Since the outer region inside the pipe cools more rapidly than the core, to ensure that all the sulfur-concrete inside the grip has cooled evenly, the system is left to cool for at least 24 hours.

5.4.4.3. Day 3: Instrumentation and Test Preparation

Due to the violent nature of the embedment process, as well as the high temperature of the surroundings, and since the strain gages are rather delicate and sensitive, they must be applied to the bar after embedment to ensure their survival. After the lower pipe grip has cooled enough to allow safe human contact, the strain gages are meticulously applied at the locations previously identified, inflection points of the buckled shape, and the mid-section of the unsupported length, see Figure 5.12. Four small punch marks were made along the vertical ribs of the bar, two on each side, at the theoretical points of inflection on the buckled shape. These punch marks are placed as a guide for the hardened steel tips of the clip gage to mount and remain in place after severe elongation and shortening of the bar during testing. The clip gage is then attached to the bar, see Figure 5.10. Other external instrumentation, such as the inclinometers and string potentiometers, are also attached, connected, and verified. Upon completion of the instrumentation, an overall inspection is performed to ensure proper functionality of all measurement devices. The strain gages are then balanced and shunted in the data acquisition system in preparation for testing. Lastly, the camera array used to visually monitor and inspect the behavior during testing is assembled and prepared. With all instrumentation and test preparation completed, the

system is left to cool until thermal equilibrium with ambient temperature is achieved, which often requires several hours.

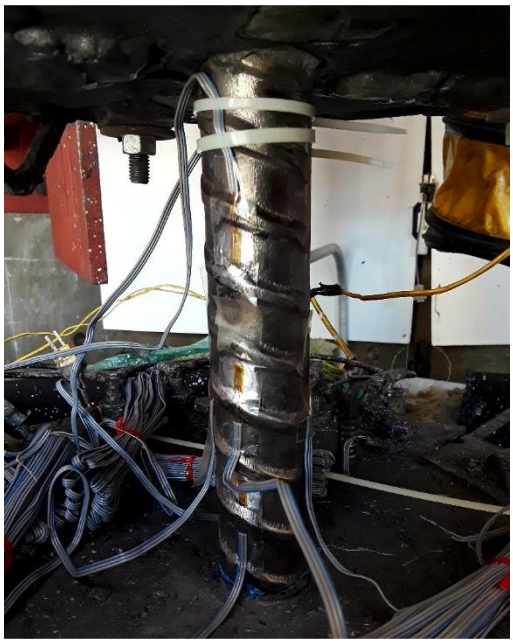

Figure 5.12. Electrical-Foil Strain Gages Applied to Test Bar

5.4.4.4. Day 4: Testing and Disassembly

Cyclic testing is performed using the measurements from the clip gage as the control system for the loading protocol. Depending on the load protocol, the test duration varies for every specimen, ranging between 2 hours and sometimes more than 6 hours. Upon completion of the test, as the tested bar fractures due to plastic buckling-straightening fatigue, all instrumentation is removed, and the spreader beam is de-tensioned from the upper pipe grip and the pipe is hoisted out of the bracing sleeve and placed inside the concrete tank for re-heating. This procedure is repeated for every test specimen.

5.5. Experimental Test Results

Continuing and expanding on the experimental work done by Duck & Carreño[40], a series of 15 tests were performed on two types of #14 ASTM A706 Grade 80 reinforcing bars, commonly available "normal", and the proposed and newly developed smoothed-rib-radii bars. The primary objective of this investigation was to characterize the plastic buckling-straightening fatigue behavior of commercially available large diameter Grade 80 reinforcement, compared with the smoothed-rib-radii bars. It is expected that with a more smoothed rib radius, the reduction of compressive strain concentration at the base of the bar deformations will improve the fatigue life of the bars. For consistency, all tests were performed with an unsupported length of $5d_b$, and an in-house designed clip gage with a gage length equal to one half of the unsupported length, $2.5d_b$, was used to measure the smeared strains between the theoretical points of inflection on each bar. For comparison, the same strain history load protocol was applied to both types of bars.

Several of the tests were unsuccessful due to bar pullout or instrumentation failure and are omitted from the analysis presented here. The main properties and outcomes of all completed tests are summarized in Table 5.4.

Table 5.4. Test Matrix Identifying Key Properties and Test Outcomes

Test ID	Embedment Length (in) [mm]		Bar Type	Strain History	Test Outcome	Final Cycle
	Upper Grip	Lower Grip				
Spec01	48 [1219]	56 [1422]	Normal	SH1	Successful	Amp. 8
Spec02	48 [1219]	56 [1422]	Smoothed	SH1	Instrumentation*	Amp. 8
Spec03	48 [1219]	56 [1422]	Normal	SH2	Successful	13
Spec04	48 [1219]	56 [1422]	Smoothed	SH2	Successful	29
Spec05	48 [1219]	56 [1422]	Normal	SH3	Bar Pullout	3
Spec06	48 [1219]	56.5 [1435]	Normal	SH3	Successful	8
Spec07	48 [1219]	56.5 [1435]	Smoothed	SH3	Instrumentation*	7
Spec08	48 [1219]	57 [1448]	Smoothed	SH3	Successful	17
Spec09	48 [1219]	57 [1448]	Normal	SH4	Bar Pullout	7
Spec10	48 [1219]	57.5 [1461]	Smoothed	SH1	Successful	Amp. 12
Spec11	48 [1219]	57.5 [1461]	Smoothed	SH4	Bar Pullout	15
Spec12	48 [1219]	57.5 [1461]	Smoothed	SH4	Successful	30
Spec13	48 [1219]	57.5 [1461]	Normal	SH4	Bar Pullout	3
Spec14	48 [1219]	57.5 [1461]	Normal	SH4	Bar Pullout	7
Spec15	48 [1219]	57.5 [1461]	Normal	SH4	Successful	19

* Clip gage was knocked off the bar as buckling occurred

The effects of compressive stress concentration at the base of the bar deformations is clearly noticeable when comparing the response of the “normal” and smoothed-rib-radii bars tested with the same strain history. Figures 5.14 through 5.17 show the response of both types of bars for all strain history loading protocols. In these figures, each test is identified using a coding system for organization. The coding system is defined in Figure 5.13.

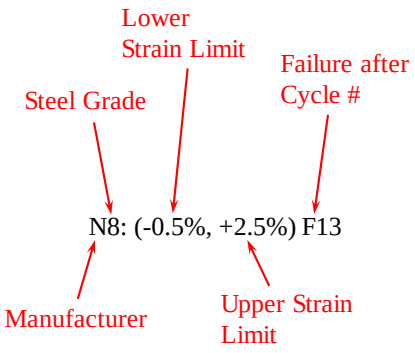

Figure 5.13. Coding System for Identifying Test Bars

Results from the variable strain amplitude load protocol show that the bars with more smoothed rib radii can undergo larger strain amplitude cycles prior to fracture, but little information is gained regarding their fatigue life. Comparing the response for the constant strain amplitude load protocols, a gradual reduction in stress for the same strain target is observed in all tested bars. The formation and propagation of fatigue cracks occur at an earlier stage for the "normal" bars, leading to a reduced fatigue life. A summary of the test results for the constant strain amplitude tests comparing the fatigue life each bar type is presented in Table 5.5.

All observed cracks began at the base of the bar deformations on the concave side of the buckled bar and propagated through towards the convex side. The cracks gradually expand, and failure occurs when the applied loads are no longer able to transfer through the bar. No necking is observed prior to fracture in any of the tested specimens. The fracture surface showing the stable and unstable cracks as defined by Duck & Carreño[40] for every load protocol are presented in Figures 5.18 through 5.21.

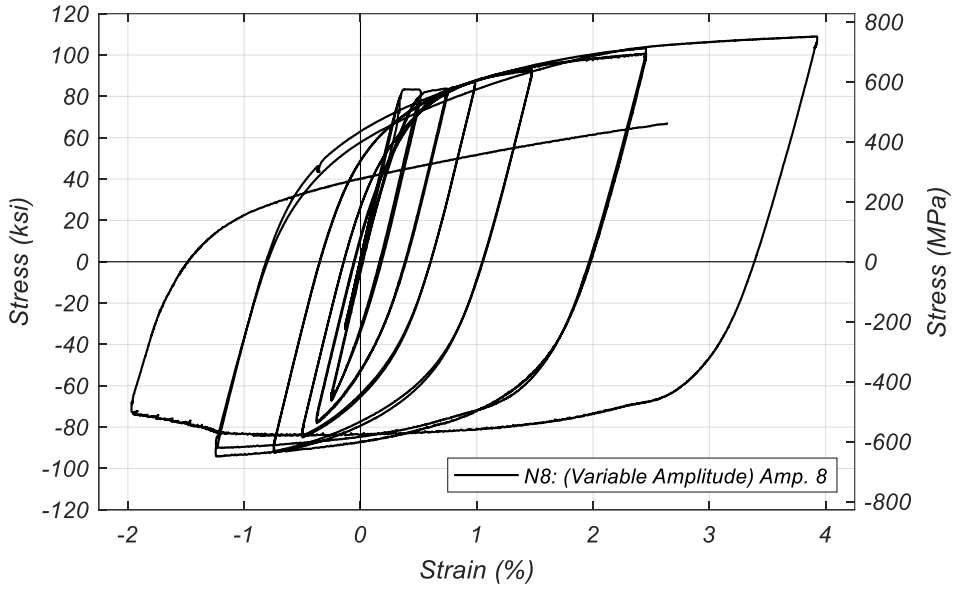

(a)

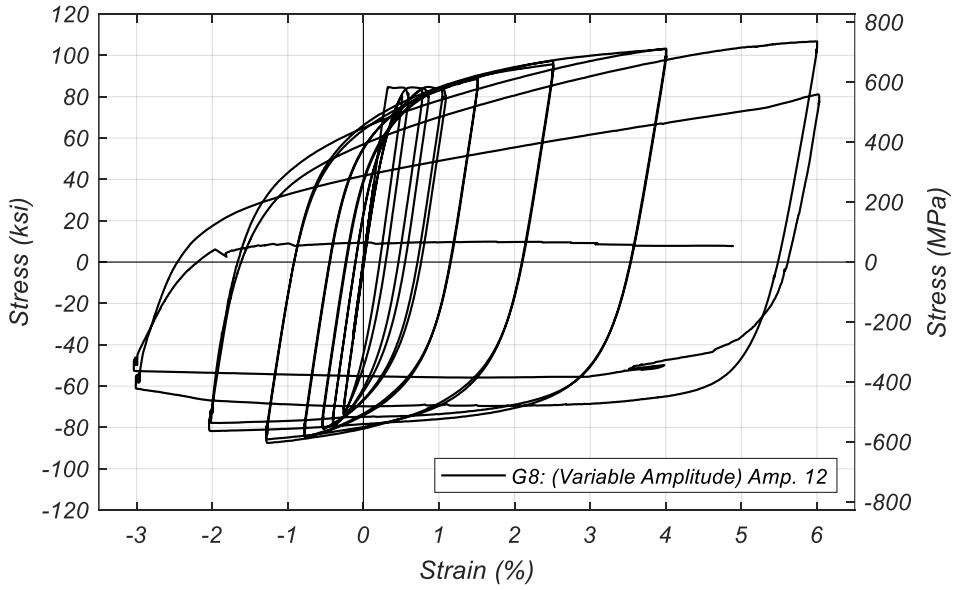

(b)

Figure 5.14. Hysteretic Response of: (a) Normal; (b) Smoothed-Rib-Radii Test Bars to Loading Protocol SH1

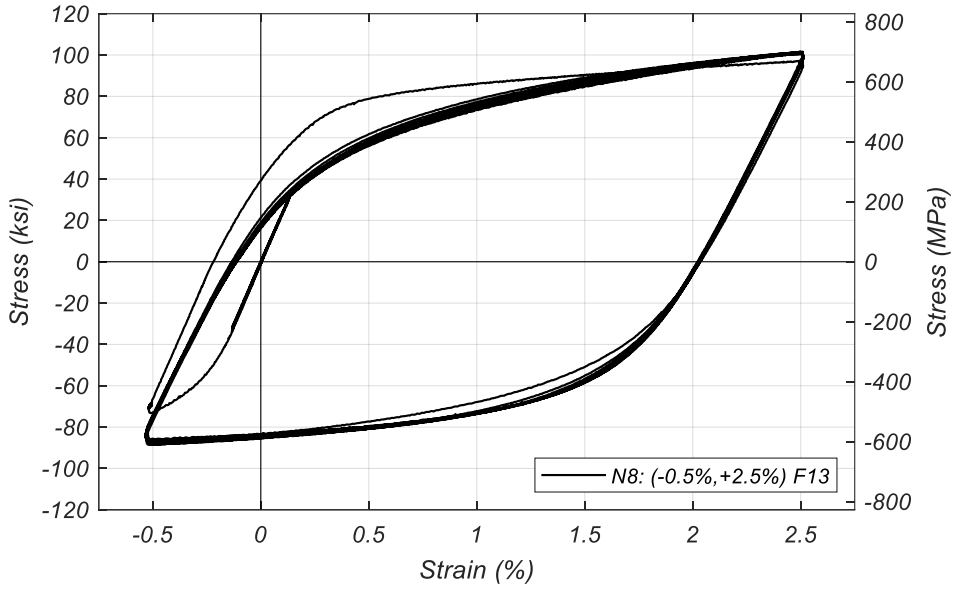

(a)

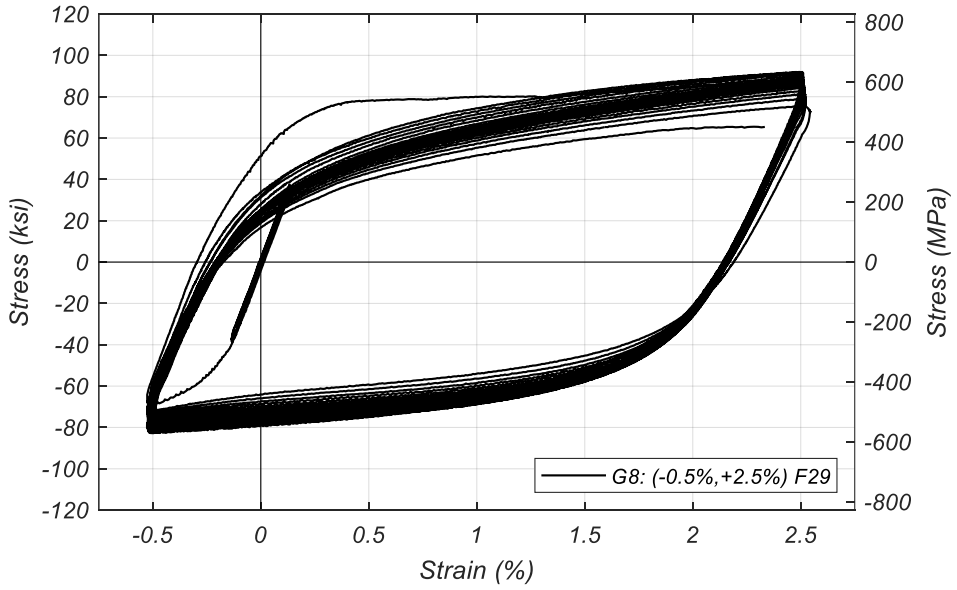

(b)

Figure 5.15. Hysteretic Response of: (a) Normal; (b) Smoothed-Rib-Radii Test Bars to Loading Protocol SH2

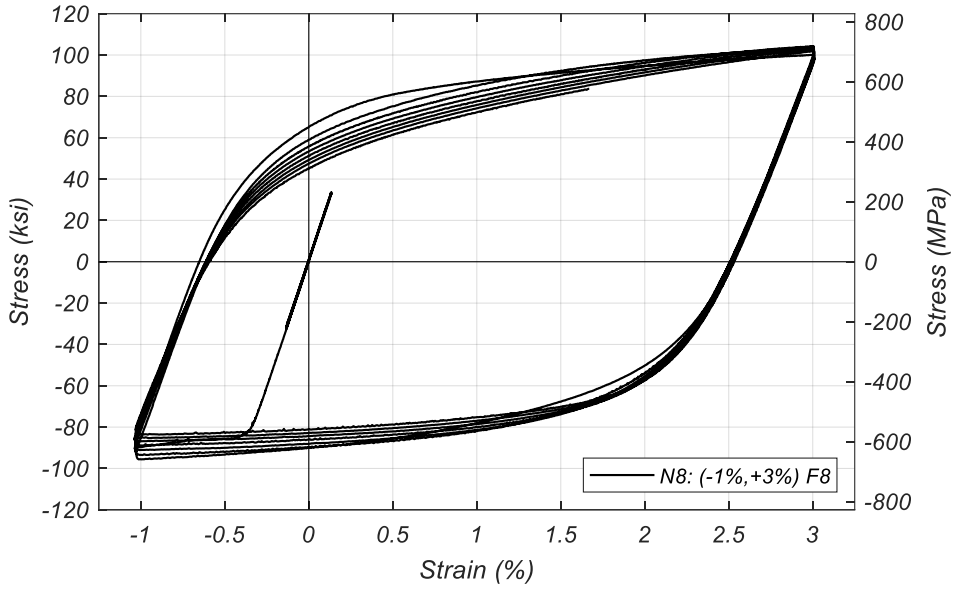

(a)

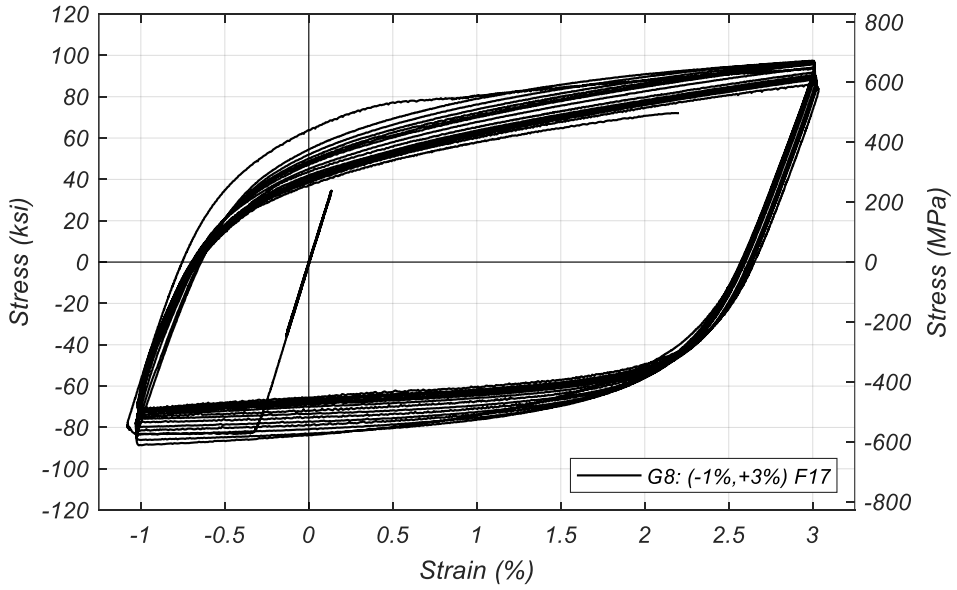

(b)

Figure 5.16. Hysteretic Response of: (a) Normal; (b) Smoothed-Rib-Radii Test Bars to Loading Protocol SH3

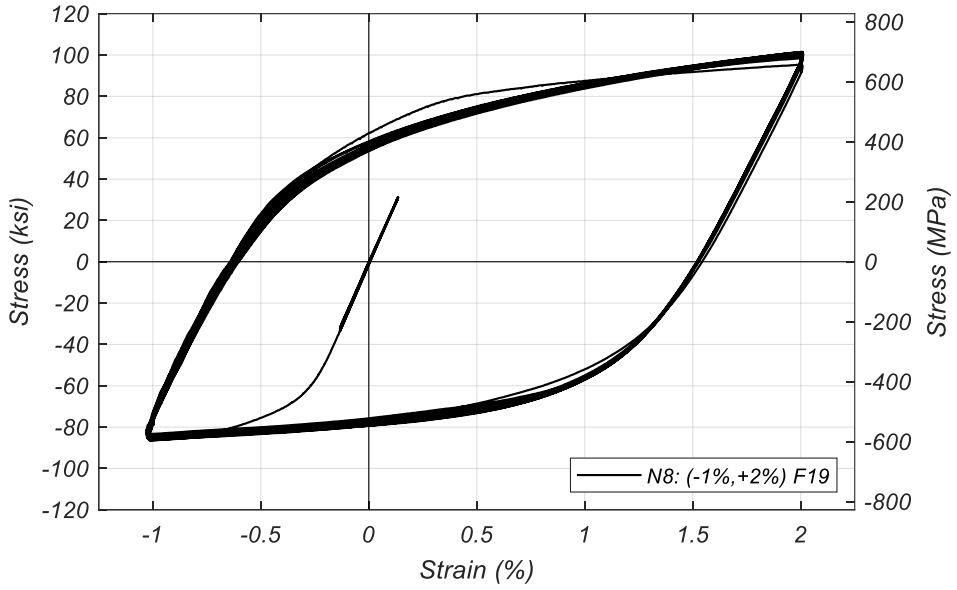

(a)

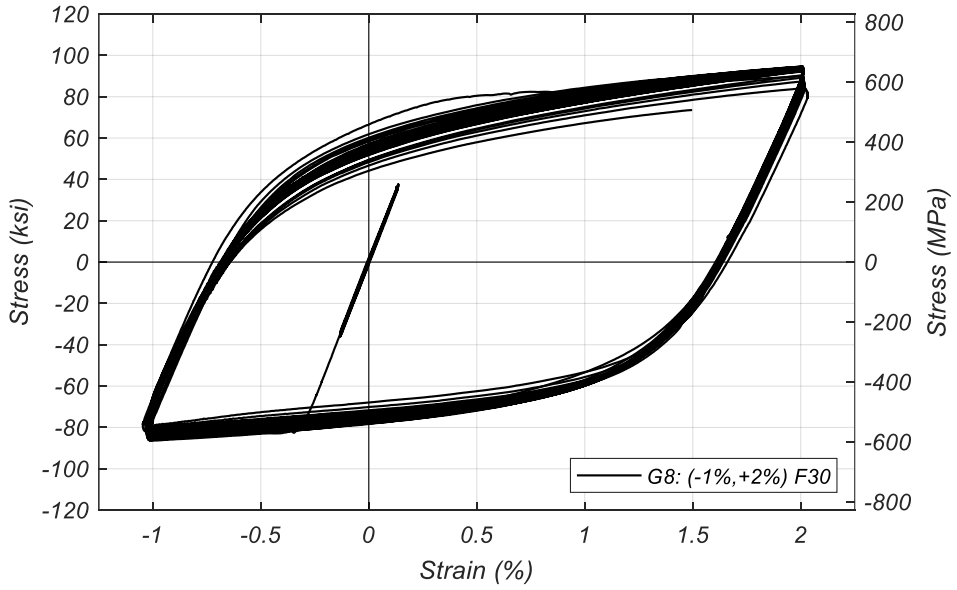

(b)

Figure 5.17. Hysteretic Response of: (a) Normal; (b) Smoothed-Rib-Radii Test Bars to Loading Protocol SH4

Table 5.5. Summary of Constant Strain Amplitude Tests Comparing Fatigue Life

Protocol	ε_{min} (%)	ε_{max} (%)	ε_{amp} (%)	Test ID	Bar Type	$2N_f$	W_{ft} (ksi) [MPa]
SH2	-0.5	2.5	3	Spec03	Normal	13	43.1 [297]
				Spec04	Smoothed	29	79.2 [546]
SH3	-1	3	4	Spec06	Normal	8	38.9 [268]
				Spec08	Smoothed	17	66.5 [459]
SH4	-1	2	3	Spec15	Normal	19	62.5 [431]
				Spec12	Smoothed	30	85.9 [593]

(a) (b)

Figure 5.18. Fracture Surface of (a) Spec01 (SH1); (b) Spec10 (SH1)

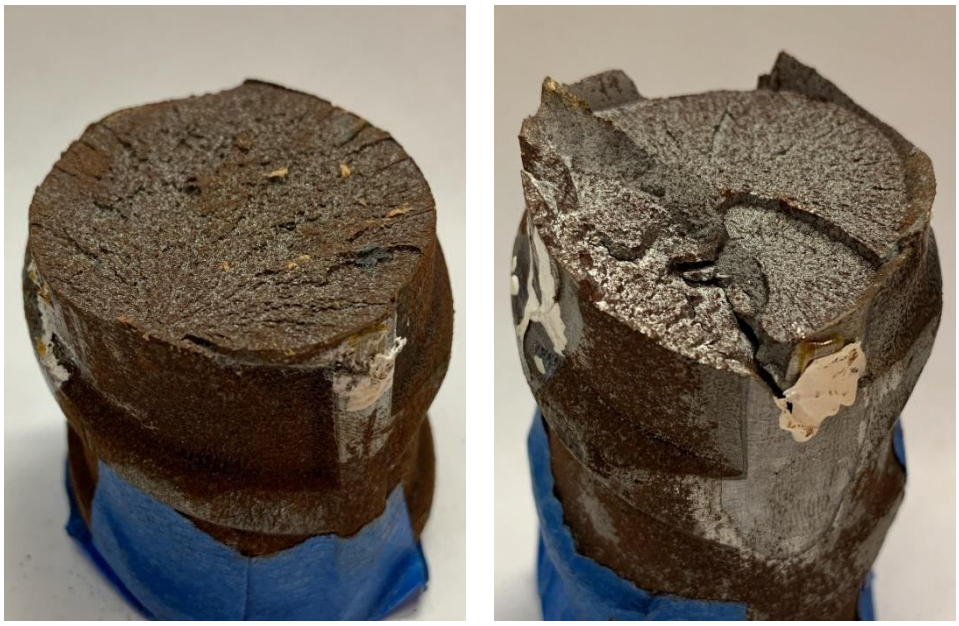

(a) (b)

Figure 5.19. Fracture Surface of (a) Spec03 (SH2); (b) Spec04 (SH2)

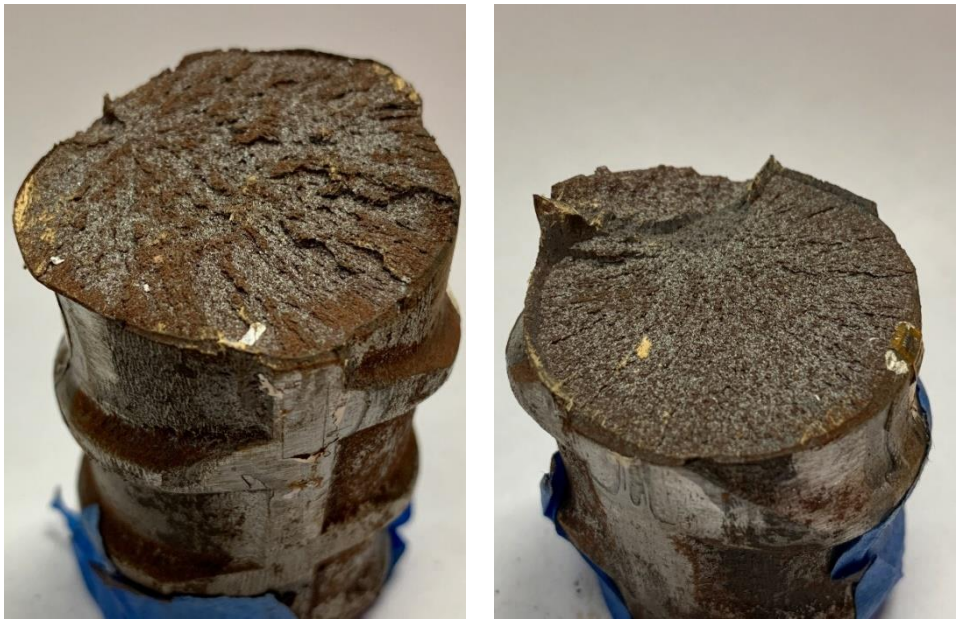

(a) (b)

Figure 5.20. Fracture Surface of (a) Spec06 (SH3); (b) Spec08 (SH3)

(a) (b)

Figure 5.21. Fracture Surface of (a) Spec12 (SH4); (b) Spec15 (SH4)

5.6. Transverse Hoop-Longitudinal Reinforcement Interaction

Longitudinal bar fracture following buckling upon repeated large-amplitude strain reversals, is commonly observed in experimental testing of circular columns designed per the prescriptive requirements in Caltrans SDC[22]. While many researchers have investigated the response of reinforcing bars after buckling, most of the emphasis has been regarding the buckling of the longitudinal bars between a set of adjacent hoops, and very few have assessed the behavior of bars buckling along a set of several hoops instead. Carreño et al.[10] developed a series of finite element models using OpenSees by McKenna et al.[68] which represented various combinations of column diameter, longitudinal and transverse reinforcement, and material properties to better understand the interaction between longitudinal and transverse reinforcement beyond the onset of buckling.

Through the extensive finite element analysis which was validated using experimentally obtained data from Schoettler et al.[8], Carreño et al.[10] investigated the interaction between the column longitudinal reinforcement and circular hoops after the onset of buckling in columns designed in accordance with Caltrans SDC[22], and provided simplified formulaic relations to predict the geometry of the buckled reinforcement (d_{POI} and d_{CR}), the characteristic strain limits (ε_{E-C} and ε_{vK}), and the amplification factors between smeared and local strains (λ_{CR}). It was shown that the relation between the smeared and local strains in the bar after the onset of buckling are highly correlated to the reinforcement configuration parameters ρ_s, $\sqrt[3]{n_{bar}}$, s/d_b , and T/Y. Ultimately, Carreño et al.[10] provided a simplified expression for design purposes to ensure reliable performance against plastic buckling-straightening fatigue in the column longitudinal reinforcement. The expression states that the strain demand of the reinforcing bars shall remain below the von Karman strain amplitude in order to prevent large strain concentrations between centers of rotation of the buckled shape, see Equation 5.1.

$$\Delta\varepsilon'_{vK} = 0.11 + \min\left(0.054, 0.032 \cdot \rho_s(\%)\right) - 0.0175 \cdot \left|\sqrt[3]{n_{bar}} - 2.93\right| - 0.054 \cdot \frac{T}{Y} \quad 5.1$$

5.7. Finite Element Model

All investigations to date, including the extensive work done by Carreño et al.[10] have been regarding ASTM A706 Grade 60 reinforcement. Carreño et al.[10] modeled and analyzed the behavior of a combination of 33 different cage configurations with 18 different material property sets for the longitudinal and transverse reinforcement. The primary focus of this investigation is to extend this methodology and adapt it to ASTM

A706 Grade 80 reinforcement, to observe and characterize the plastic buckling-straightening fatigue life of high-strength reinforcement in bridge columns. To this end, Carreño's finite element model framework was modified to analyze Grade 80 reinforcing cages, and rather than building each model based on existing reinforcement cage configurations, which encompasses columns with similar configurations, a set of non-dimensional normalized reinforcement cages were developed and investigated. Using normalized parameters ensures that every cage configuration analyzed is unique and the results obtained allow for a more complete understanding of the bar behavior in all possible configurations. The development and setup of the models is outlined in the following sections.

5.7.1. Description of Finite Element Model

To account for the axial and bending capacity of the reinforcement, each longitudinal bar and hoop is modeled as a single displacement-based beam-column element, discretized along its length into multiple sub-elements. An initial lateral imperfection with a magnitude of 0.01 in. (0.25 mm) is introduced to all longitudinal reinforcing bars at the center height of the cage to ensure the occurrence of buckling. This imperfection is so minute that it has a negligible effect on the model response aside from ensuring buckling. Each longitudinal bar is sub-divided such that the same number of sub-elements exist between all sets of adjacent hoops. The hoops are sub-divided with less sub-elements in hoops away from the defined buckling region at the center height of the cage, increasing incrementally for hoops closer to the buckling region. This non-uniform sub-division of the hoop elements is chosen to increase the speed of the analysis since the hoops

far from the buckling region experience very little strains, therefore require less beam-column sub-elements for the analysis, see Figure 5.22.

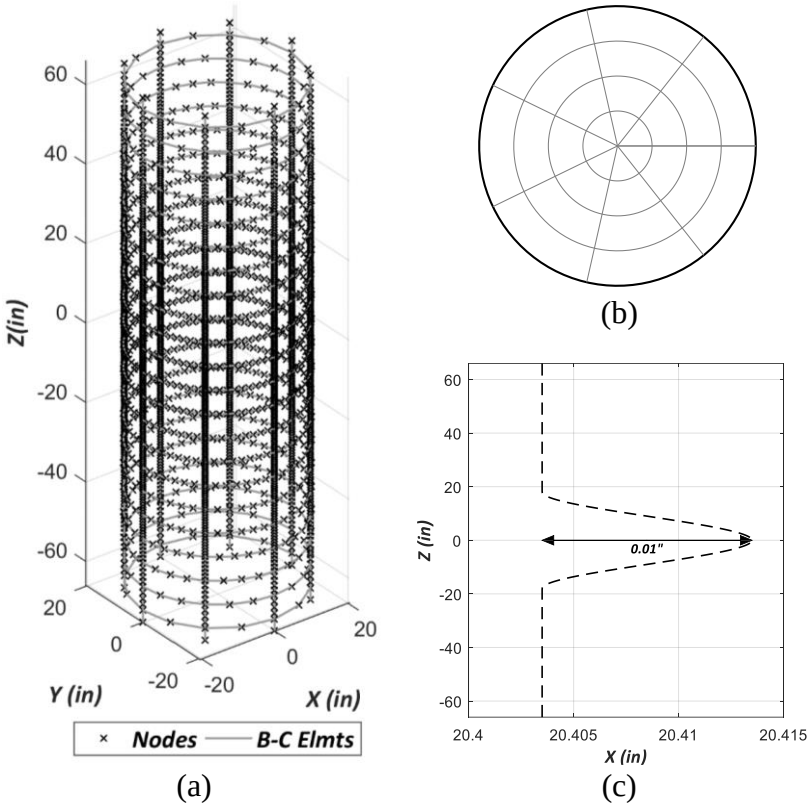

Figure 5.22. OpenSees Model: (a) 3D Cage Layout; (b) Reinforcing Bar Cross-Section; (c) Initial Imperfection in Longitudinal Bar; (Carreño et al., 2018)

The cross section of each element is sub-divided into 4 radial, and 7 circumferential fibers, and using the steel model by Dodd and Restrepo[69], the non-linear behavior of steel is included in the material fibers. Geometric non-linearities, which are of great importance in the buckling phenomenon, are accounted for by corotational geometric transformations in every sub-element of the model (Crisfield[70]), and shear deformations are accounted for by a linear model with a shear modulus, G, computed for a Poisson's ratio of $\nu = 0.26$, see Carreño et al.[10]. Some simplifications were made to increase the analysis speed. The concrete cover is neglected, as it does not influence the buckling behavior of the

longitudinal reinforcement. The concrete core, however, may play an important role in the response by preventing the longitudinal bars from buckling inward towards the column core, as well as exerting outward pressure on the reinforcement cage from the lateral expansion due to dilation. This phenomenon is prevalent in columns where the neutral axis is deep, however, since bridge columns generally tend to have moderate reinforcement ratios and low axial compression, the effects of the concrete core are also neglected and a model of a bare column reinforcing cage was chosen to conduct the analysis.

The boundary conditions are defined such that all displacements and rotations in the nodes at the bottom of the reinforcement cage, and all but the vertical displacement in the nodes at the top of the cage are restrained. The total axial load is divided evenly and applied in a triangularly distributed pattern along each longitudinal bar at the hoop locations, with the maximum force being applied at the top and bottom nodes, see Figure 5.23. This loading pattern was chosen as it results in the maximum force being concentrated at the mid-height of the column over a length of at least three hoop spacings, forcing the first buckling mode to occur at this location. A more detailed and thorough explanation of the finite element model is provided by its developer, Carreño et al.[10]

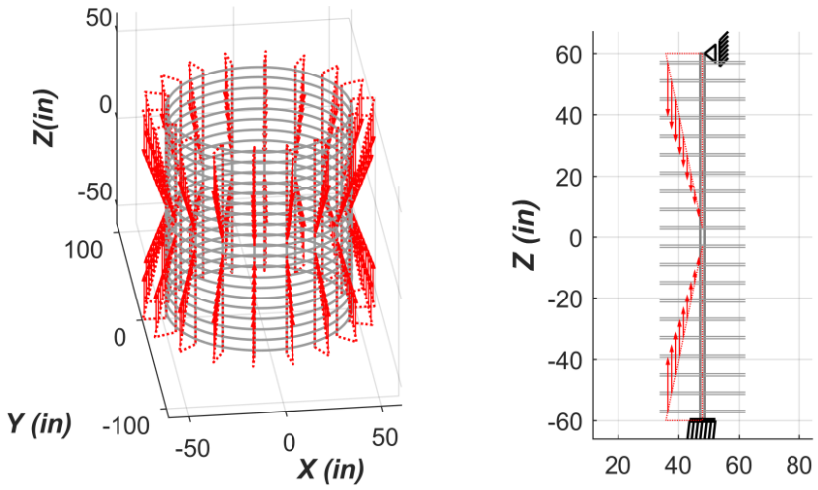

(a) (b)

Figure 5.23. Loading Configuration and Boundary Conditions: (a) 3D Model Loading; (b) Single Bar Boundary Conditions; (Carreño et al., 2018)

5.7.2. Reinforcement Cage Configuration

To obtain buckling behavior results and characterize the response of any generic column reinforcement configuration, a set of non-dimensional normalized reinforcement cages were developed and modeled for the analysis. The column diameter, D_c, of all cages were considered to remain constant since through the prior investigation by Carreño et al.[10] it was found that the buckling response is not directly correlated with the column diameter.

Considering a constant column diameter for all models, artificial bar sizes were numerically selected to mimic certain longitudinal reinforcement ratios, ρ_l, as well as artificial hoop spacing, s/d_b, and therefore volumetric reinforcement ratios, ρ_s. The models were first categorized by the hoop spacing, s/d_b, ranging from an unrealistically tightly-spaced cage configuration of $s/d_b = 1.5$, incrementally increasing to an unrealistically widely-spaced $s/d_b = 12$. Furthermore, within each spacing group, the

cages were grouped by the ratio of longitudinal to volumetric reinforcement ratios, ρ_s/ρ_l, ranging from a poorly-confined $\rho_s/\rho_l = 15\%$, incrementally increasing to a very well-confined $\rho_s/\rho_l = 90\%$. To observe the effect of the number of longitudinal bars (n_{bar}) on the response of each cage, for each ρ_s/ρ_l ratio, 4 configurations were developed with 8, 12, 18, and 30 longitudinal bars in each.

Overall, a total of 176 unique column cage configurations were developed. To compare the plastic buckling-straightening response and determine the correlation, if any, of the material properties with the response, analysis was performed for both ASTM A706 Grade 80 as well as Grade 60 mean expected material properties obtained from numerous tensile tests. The cages in the $s/d_b = 12$ set were only analyzed for Grade 60 reinforcement since that spacing is unrealistic for columns reinforced with Grade 80 bars. A summary of the column cage configurations developed for this analysis are presented in Table 5.6, and Figure 5.24 shows the basic geometry of the column cages in this investigation. It is believed that this large selection of normalized generic cage configurations represents a majority of commonly designed columns, providing invaluable insight on the plastic buckling-straightening fatigue life of most columns.

Table 5.6. Column Model Categories by Reinforcement Configuration

Case	n_{bar}	ρ_s/ρ_l (%)	s/d_b	Case	n_{bar}	ρ_s/ρ_l (%)	s/d_b
1	8	15	1.5	***25***	8	60	3.0
2	12			***26***	12		
3	18			***27***	18		
4	30			***28***	30		
5	8	30		***29***	8	75	
6	12			***30***	12		
7	18			***31***	18		
8	30			***32***	30		
9	8	45		***33***	8	90	
10	12			***34***	12		
11	18			***35***	18		
12	30			***36***	30		
13	8	15	3.0	***37***	8	15	3.5
14	12			***38***	12		
15	18			***39***	18		
16	30			***40***	30		
17	8	30		***41***	8	30	
18	12			***42***	12		
19	18			***43***	18		
20	30			***44***	30		
21	8	45		***45***	8	45	
22	12			***46***	12		
23	18			***47***	18		
24	30			***48***	30		

Table 5.6. Column Model Categories by Reinforcement Configuration (continued)

Case	n_{bar}	ρ_s/ρ_l (%)	s/d_b	Case	n_{bar}	ρ_s/ρ_l (%)	s/d_b
49	8	60	3.5	***73***	8	60	4.0
50	12			***74***	12		
51	18			***75***	18		
52	30			***76***	30		
53	8	75		***77***	8	75	
54	12			***78***	12		
55	18			***79***	18		
56	30			***80***	30		
57	8	90		***81***	8	90	
58	12			***82***	12		
59	18			***83***	18		
60	30			***84***	30		
61	8	15	4.0	***85***	8	15	4.5
62	12			***86***	12		
63	18			***87***	18		
64	30			***88***	30		
65	8	30		***89***	8	30	
66	12			***90***	12		
67	18			***91***	18		
68	30			***92***	30		
69	8	45		***93***	8	45	
70	12			***94***	12		
71	18			***95***	18		
72	30			***96***	30		

Table 5.6. Column Model Categories by Reinforcement Configuration (continued)

Case	n_{bar}	ρ_s/ρ_l (%)	s/d_b	Case	n_{bar}	ρ_s/ρ_l (%)	s/d_b
97	8	60	4.5	***121***	8	60	6.0
98	12			***122***	12		
99	18			***123***	18		
100	30			***124***	30		
101	8	75		***125***	8	75	
102	12			***126***	12		
103	18			***127***	18		
104	30			***128***	30		
105	8	90		***129***	8	90	
106	12			***130***	12		
107	18			***131***	18		
108	30			***132***	30		
109	8	15	6.0	***133***	8	15	8.0
110	12			***134***	12		
111	18			***135***	18		
112	30			***136***	30		
113	8	30		***137***	8	30	
114	12			***138***	12		
115	18			***139***	18		
116	30			***140***	30		
117	8	45		***141***	8	45	
118	12			***142***	12		
119	18			***143***	18		
120	30			***144***	30		

Table 5.6. Column Model Categories by Reinforcement Configuration (continued)

Case	n_{bar}	ρ_s/ρ_l (%)	s/d_b
145	8	60	8.0
146	12		
147	18		
148	30		
149	8	75	
150	12		
151	18		
152	30		
153	8	90	
154	12		
155	18		
156	30		
157	8	7.5	12.0
158	12		
159	18		
160	30		
161	8	15	
162	12		
163	18		
164	30		
165	8	22.5	
166	12		
167	18		
168	30		

Case	n_{bar}	ρ_s/ρ_l (%)	s/d_b
169	8	60	12.0
170	12		
171	18		
172	30		
173	8	75	
174	12		
175	18		
176	30		

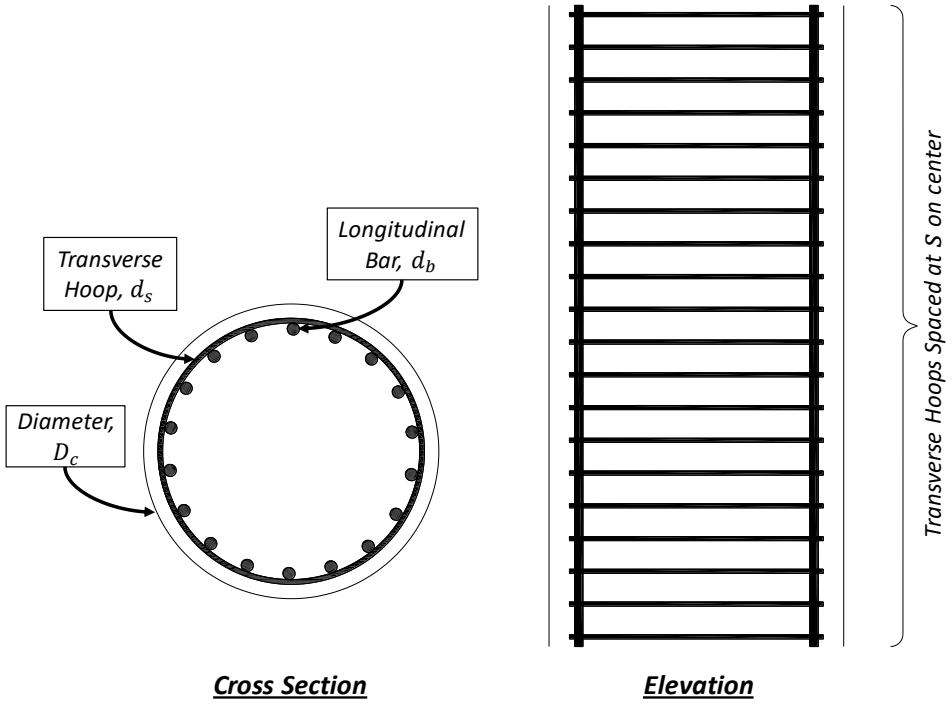

Figure 5.24. Column Reinforcement Cage Configuration

5.7.3. Material Properties

The constitutive stress-strain relationship developed by Dodd and Restrepo[69] was assigned and used in the uniaxial fibers of the finite element model to simulate the non-linear behavior of all reinforcing bars. As most of the parameters in this constitutive relationship can be extracted from monotonic tensile tests, the Dodd and Restrepo[69] material model is an attractive option for this type of analysis. The shape of the strain hardening backbone curve and the Bauschinger effect are controlled by additional parameters P, and Ω_{fac} respectively.

Mechanical properties were gathered from 27 sets of experiments on ASTM A706 Grade 80 reinforcing bars varying in size between #5 and #18, and the mean values of f_y, f_{su}, ε_y, and ε_{su} parameters were used in the constitutive stress-strain relationship.

Restrepo-Posada et al.[71] suggests that the Ω_{fac} parameter is correlated with the carbon content in the steel. However, since prior investigation by Carreño et al.[10] showed no direct effect of this parameter on the plastic buckling-straightening fatigue behavior of the bars, and due to the limited availability of milling certificates for the monotonically tensile tested bars, a suggested approximate value of $\Omega_{fac} = 0.92$ was selected. Similarly, due to the limited availability of complete monotonic stress-strain curves for the bars, an approximate value of $P = 3.3$ was selected. For comparison, the expected mechanical properties suggested by Caltrans SDC 2.0 (Section 3.3.3)[22] were used for all Grade 60 reinforcement. As Caltrans SDC[22] does not provide suggested values for the Ω_{fac} and P parameters, and to simplify the comparison with Grade 80, the same values were selected for this set of analyses. A summary of these material properties is presented in Table 5.7. The strain at the onset of strain-hardening for the longitudinal bars was set as $\varepsilon_{shl} = 4 \cdot \varepsilon_y$, whereas since the hoops were already work-hardened and no longer present a clear yield plateau, the onset of strain-hardening in the transverse reinforcement was selected to be only slightly larger than the yield strain at $\varepsilon_{sht} = 1.1 \cdot \varepsilon_y$.

Table 5.7. Material Properties Assigned to All Reinforcement Configurations

Type	f_y (ksi) [MPa]	f_{su} (ksi) [MPa]	ε_y (%)	ε_{su} (%)	P	Ω_{fac}
Grade 80	84.6 [583]	118.4 [816]	0.29	10.3	3.3	0.92
Grade 60	68 [469]	95 [655]	0.28	10.5	3.3	0.92

5.7.4. Loading Protocol

To properly achieve the buckling response sought after in this investigation, a cyclic loading protocol was considered where the longitudinal reinforcement of the cage is initially placed in tension well beyond the yielding strain, after which the loading is reversed and the cage is placed under compression until buckling occurs in the longitudinal reinforcement. Data available from prior research suggests that the extreme tensile strains observed in the reinforcement at the plastic hinge region of reinforced concrete columns, with a typically low axial load ratio, is in the order of 4.5%. To confirm that the results of the analysis are not influenced by the extreme tensile strain, a subset of the cage configurations were analyzed with loading protocols with maximum tensile strains of 3%, 4.5%, and 6%, and the results were compared, see Table 5.8. Results from this initial analysis show that the maximum tensile strain has a negligible effect on the buckling response of the bars. Based on experience and engineering judgment, a maximum tensile strain of 4.5% was selected for the loading protocol for all analyses, see Figure 5.25.

Table 5.8. Comparison of von Karman Strain Amplitude, $\Delta\varepsilon_{vK}$, Results by Changing Maximum Tensile Strain in Loading Protocol

Case	ASTM A706 Grade 80			ASTM A706 Grade 60		
	$\varepsilon_{st} = 3\%$	$\varepsilon_{st} = 4.5\%$	$\varepsilon_{st} = 6\%$	$\varepsilon_{st} = 3\%$	$\varepsilon_{st} = 4.5\%$	$\varepsilon_{st} = 6\%$
7	0.030	0.032	0.029	0.030	0.032	0.030
31	0.028	0.029	0.028	0.028	0.029	0.026
46	0.048	0.050	0.049	0.049	0.052	0.047
56	0.023	0.024	0.024	0.022	0.023	0.023
69	0.037	0.035	0.032	0.034	0.033	0.033

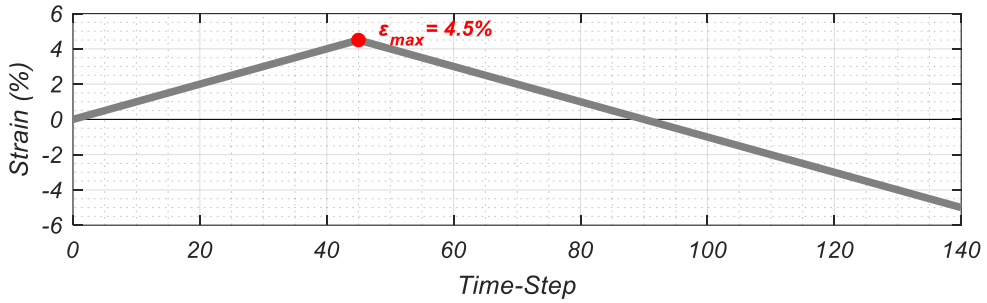

Figure 5.25. Loading Protocol Strain History for FE Analysis

5.7.5. Analysis Results

FE model analyses were performed for all column cage configurations considering both Grade 80 and 60 material properties as outlined in Tables 5.6 and 5.7. As determined through prior investigation, all analyses were performed using the same loading protocol, see Figure 5.25. The longitudinal bars in all computational analyses experienced significant buckling deformations, and the analysis successfully captured their behavior.

Several key characteristic states of the analysis are identified using the strains recorded in the concave, ε_{kv}, and convex, ε_{kx}, sides of the critical plastic hinge in the buckled shape of the bars. These characteristic points are defined by Carreño et al.[10], and described as the following:

1) Zero stress state following the maximum reversal in tension, ε_0. This point is identified in the figures using the symbol ×.
2) Bifurcation point where the difference in strain in the concave and convex sides of the critical plastic hinge in the buckled bar, ε_{kv} and ε_{kx} respectively, increases beyond 10%. This point represents the onset of buckling and is henceforth referred

to as the Engesser-Considère strain, ε_{EC}. This point is identified in the figures with the symbol ○.

3) The peak stress in compression is reached, when the segments outside of the buckled shape begin unloading in tension. The smeared strain at this point is identified as the von Karman strain, ε_{vK}, and is represented in the figures by the symbol Δ.

4) The state at which the natural strain in the concave side of the buckled bar, when shifted by the plastic strain $\varepsilon'_0(1)$, reaches one-half of the uniform strain in compression ($\varepsilon'_{kv} = \varepsilon'_0 - \varepsilon'_u/2$). This point is identified by the symbol □.

5) The state at which the natural strain in the concave side of the buckled bar, when shifted by the plastic strain ε'_0, reaches the uniform strain in compression ($\varepsilon'_{kv} = \varepsilon'_0 - \varepsilon'_u$). This point is identified in the figures by the symbol ◊.

6) The analysis step half-way between states 4) and 5), which is used for the measurement of characteristic dimensions in the buckled shape. This point is represented in the figures by the symbol ∗.

Figures 5.26 through 5.29 show results from the finite element analysis for a sample column reinforced with ASTM A706 Grade 80 bars, $n_{bar} = 30$, $s/d_b = 3$, and $\rho_s/\rho_l = 0.6$, outlining the key characteristic analysis states outlined above.

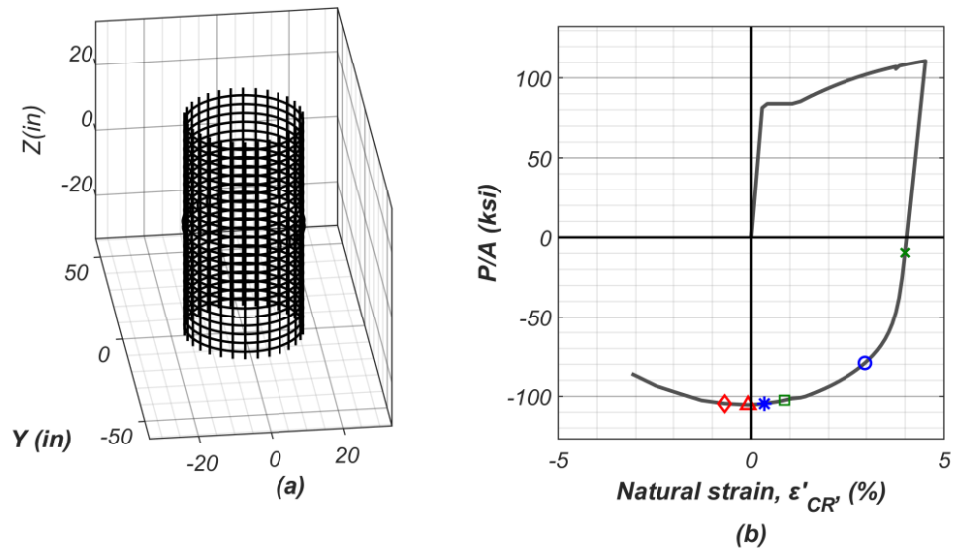

Figure 5.26. Global Response of FE Model, Case 28: (a) 3D Representation of Buckled Shape; (b) Smeared Natural Strain vs Stress in a Single Longitudinal Bar Identifying Key Analysis Steps

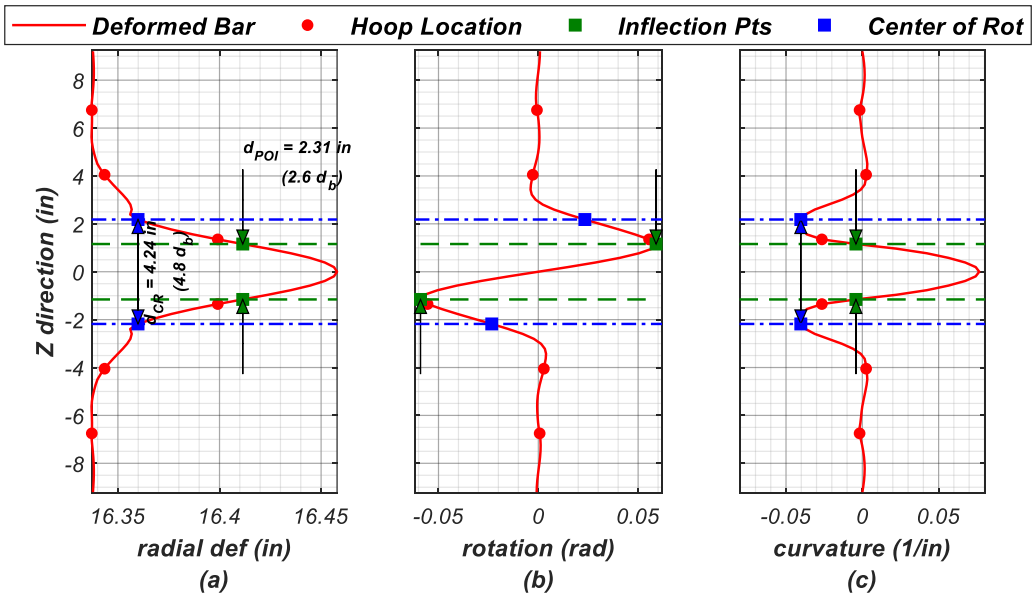

Figure 5.27. Deformed Shape of Buckled Reinforcement, Case 28: (a) Lateral Deformation; (b) Node Rotations; (c) Curvature Distribution

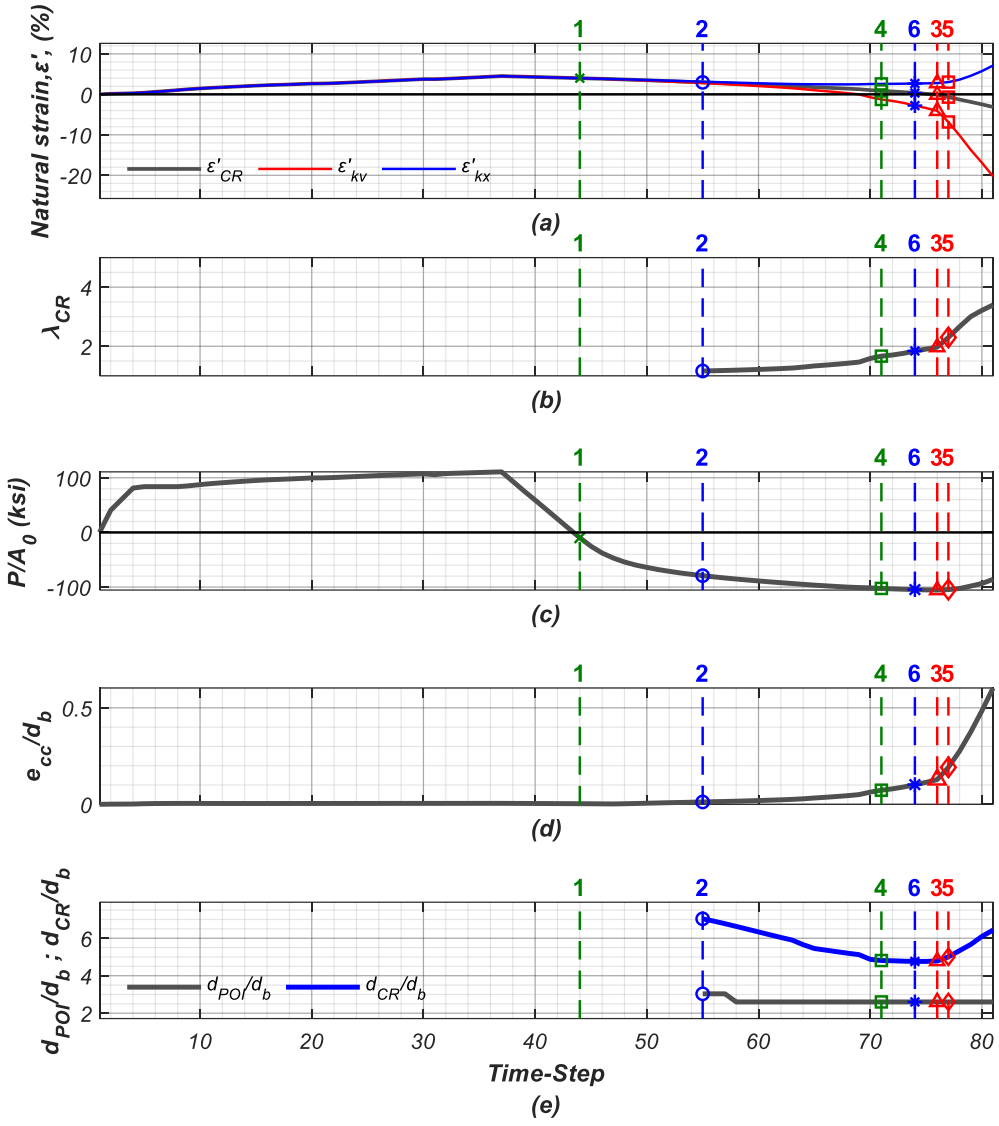

Figure 5.28. Variation of Parameters in Buckled Reinforcement at Each Time-Step, Case 28: (a) Strain History; (b) Ratio Between Local and Smeared Strains; (c) Average Axial Stress; (d) Lateral Deformation/Eccentricity of Buckled Bar, e_{cc}; (e) Distance Between POIs and CRs

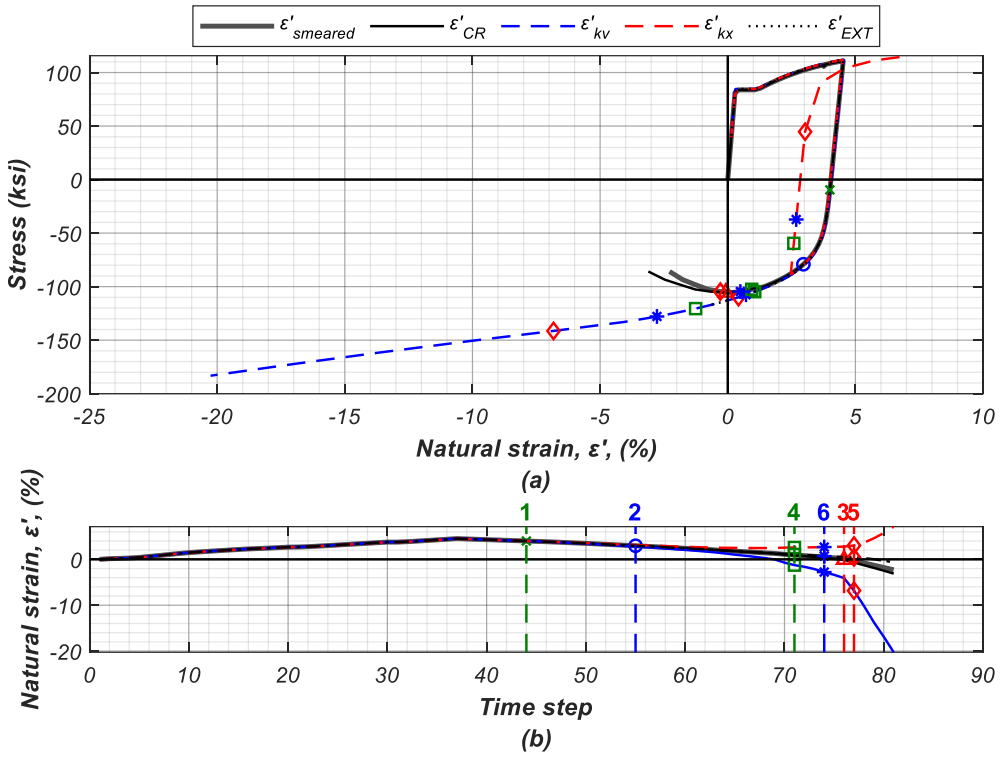

Figure 5.29. Local vs Smeared Response in Buckled Reinforcement, Case 28: (a) Natural Strain vs Stress; (b) Natural Strain Time-History

An appropriate measure of the plastic buckling-straightening fatigue life in reinforced concrete bridge columns is the von Karman strain amplitude, $\Delta\varepsilon_{vK} = \varepsilon_{st} - \varepsilon_{vK}$, which defines the upper bound strain demand limit for reinforcing bars in order to prevent large strain concentrations between centers of rotation in the buckled shape, ultimately leading to failure due to fatigue. This upper-bound strain amplitude limit, $\Delta\varepsilon_{vK}$, is obtained for all combinations of cage configuration and material properties through the analyses, and the results are presented in Figure 5.30. Since the cage configurations were non-dimensionalized, the results are grouped in categories as explained in the previous section. Through this grouping, a clear trend is observed. By increasing the confinement, ρ_s/ρ_l,

while maintaining the same hoop spacing ratio, s/d_b, the von Karman strain amplitude, $\Delta\varepsilon_{vK}$, increases. This increase occurs linearly, within each hoop spacing category, up to a certain confinement level, after which the von Karman strain amplitude behaves asymptotically and remains relatively constant. This behavior is more pronounced in columns with large hoop spacing (e.g. $s/d_b = 6$).

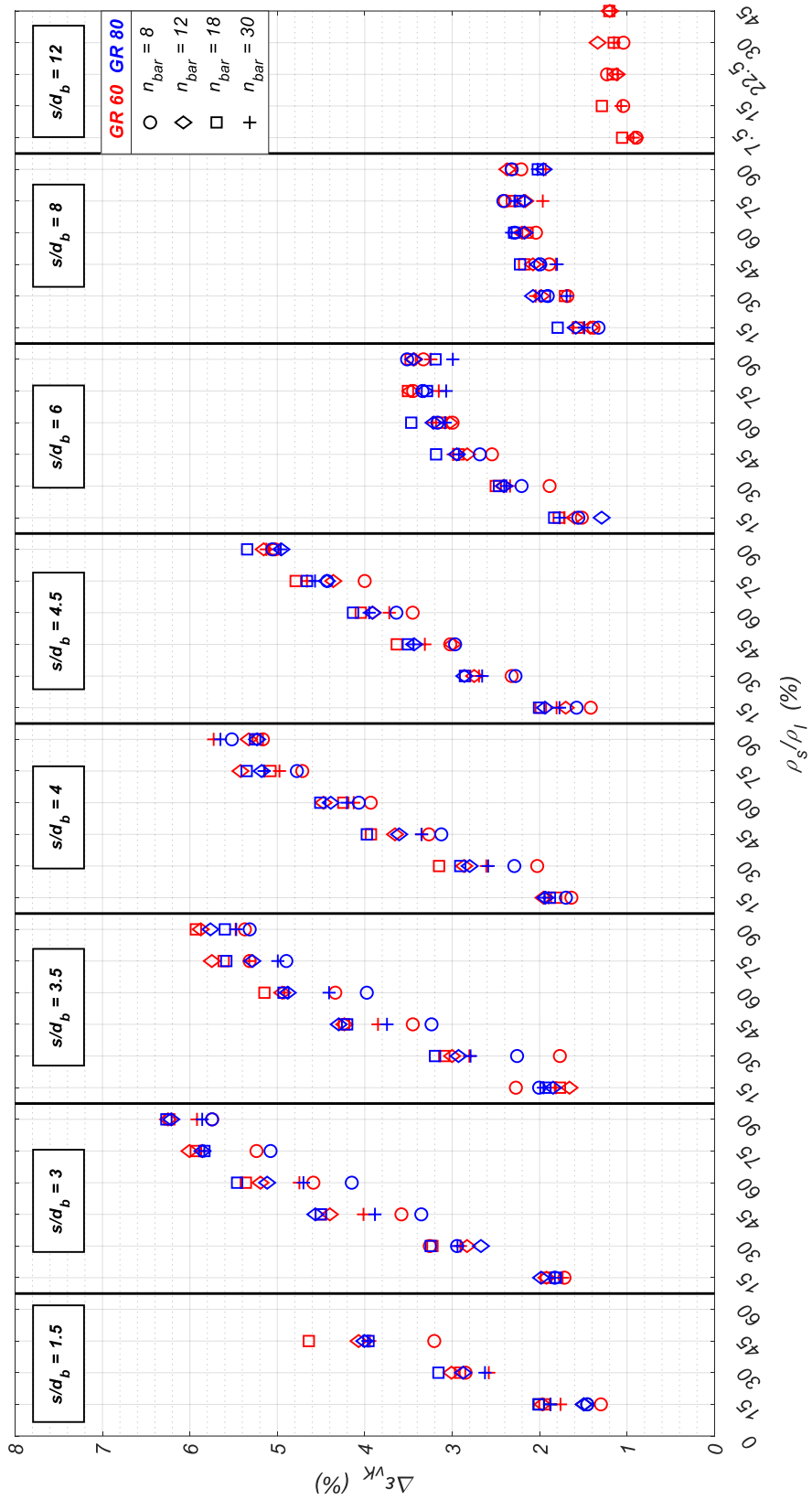

Figure 5.30. von Karman Strain Amplitude Comparison for ASTM A706 Grade 80 and Grade 60 Reinforcement Cages

Changing the number of longitudinal bars (n_{bar}) in a column while maintaining the same hoop spacing (s/d_b) and confinement (ρ_s/ρ_l) ratios, changes the von Karman strain amplitude. The effect of n_{bar} on the buckling response is attributed to two primary factors. First, to increase n_{bar} while maintaining a constant reinforcement ratio, the bar diameter must be reduced, increasing the slenderness of the bars, which results in a decrease in buckling resistance. Second, and more prominent in bridge columns with large diameter longitudinal bars, is the "polygon effect" as described by Carreño et al.[10], which refers to the phenomenon where the lateral deformations of the longitudinal reinforcement after the onset of buckling push the hoops at very discrete locations, forcing the circular hoops to develop noticeable kinks and deform like a polygon with vertices at the location of every longitudinal bar, see Figure 3.21. Transverse hoops are most effective at restraining lateral deformations when working in pure tension, and as the hoops are deformed due to the "polygon effect", their effectiveness in restraining the lateral deformations is reduced due to bending. As expected, the "polygon effect" in the hoops is more pronounced in columns with fewer longitudinal bars. By comparison it is also shown that the von Karman strain amplitude is not directly correlated with the material properties such as f_y and f_{su}, and does not show a noticeable difference for Grade 80 bars as opposed to Grade 60, see Figure 5.30.

A statistical analysis of the computational results showed that the characteristic strain limit, von Karman strain amplitude ($\Delta\varepsilon_{vK}$) is highly correlated to the reinforcement configuration parameters s/d_b, ρ_s/ρ_l, and to a lesser extent only for very high confinement ratios, ε_{su}. Since varying the number of longitudinal bars, n_{bar}, produced

only minor variations in the strain amplitude within each analysis category, the variable was removed from the analysis for simplicity. Through a regression analysis of the finite element model results, a simple expression to predict the von Karman strain amplitude, $\Delta\varepsilon_{vK}$, is developed and presented in Equation 5.2, which provides a strain limit for reliable performance against plastic buckling-straightening fatigue of longitudinal column reinforcement.

$$\Delta\varepsilon_{vK} = \min\begin{cases} \dfrac{0.21}{\max\left(\dfrac{3.6}{\dfrac{s}{d_b}}\right)} \cdot \dfrac{\rho_s}{\rho_l} + 0.01 \\ 0.75 \cdot \varepsilon_{su} \\ \dfrac{1}{2 \cdot \left(\dfrac{s}{d_b}\right)^{1.5}} \end{cases} \qquad 5.2$$

The mean and standard deviation of the ratio between the finite element model and the regression analysis results, at $\mu = 1.02$ and $\delta = 10.15\%$ respectively, indicate a high level of accuracy attained by the regression function, see Figures 5.31 and 5.32. This simplified expression for the von Karman strain amplitude with respect to the column cage configuration parameters is useful for design purposes and is explained in the following section.

Take for example the two test units presented in Chapters 3 and 4, the Column Extending into Type II Pile Shaft, and the Column-Bent Cap Connection. The column-pile specimen (Chapter 3) had a transverse hoop spacing of $s/d_b = 3$ and a reinforcement ratio of $\rho_l = 1.74\%$. The volumetric reinforcement ratio required by Equation 5.2 to prevent

premature bar fracture due to PBSF is $\rho_{s,PBSF} = 0.96\%$. A volumetric reinforcement ratio of $\rho_s = 1.14\%$ was provided in that test unit. As described in Chapter 3, the test showed excellent ductile behavior. No bar buckling was observed at displacement ductility of 4. The onset of bar buckling was observed during the second load cycle at displacement ductility of 5 (drift ratio of approximately 10%), and the first bar fracture occurred in the following load cycle.

The column-bent cap specimen (Chapter 4) had a transverse hoop spacing of $s/d_b = 3.5$ and a reinforcement ratio of $\rho_l = 2\%$. The volumetric reinforcement ratio required by Equation 5.2 to prevent premature bar fracture due to PBSF is $\rho_{s,PBSF} = 0.89\%$. A volumetric reinforcement ratio of $\rho_s = 1\%$ was provided in that test unit. As described in Chapter 4, the test showed excellent behavior. The onset of bar buckling was observed during the third reloading cycle after achieving a displacement ductility of 4 (at a drift ratio of approximately -1%), and the first bar fracture occurred in the first unloading cycle after the specimen had achieved a displacement ductility of 5 (at a drift ratio of approximately -4%).

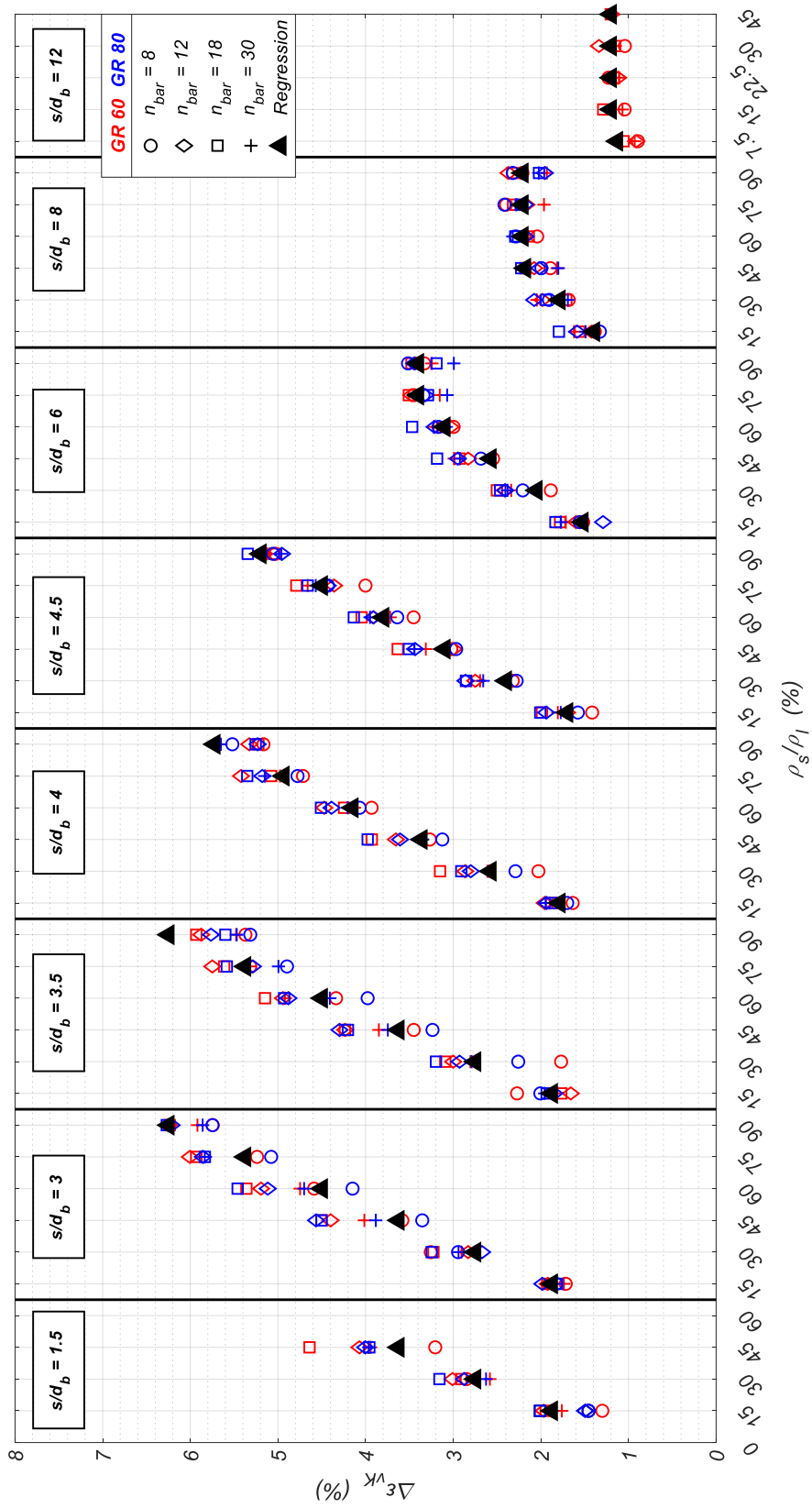

Figure 5.31. von Karman Strain Amplitude Comparison for ASTM A706 Grade 80 and Grade 60 Reinforcement Cages with Simplified Expression from Regression Analysis

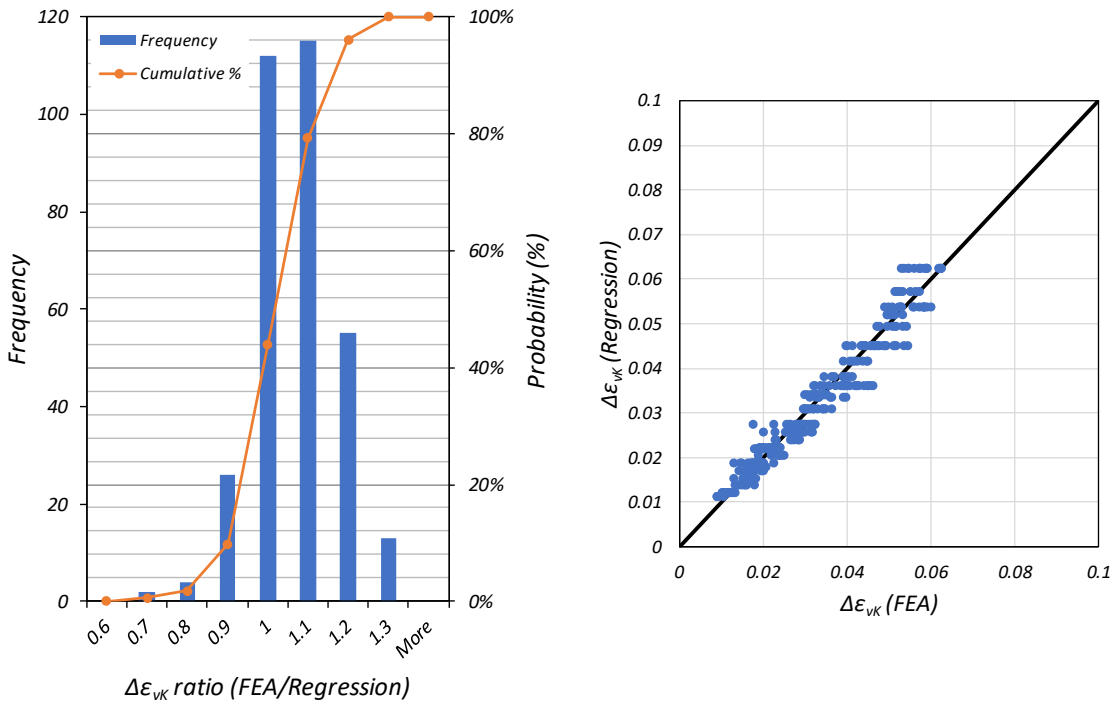

(a) (b)

Figure 5.32. Regression Results for $\Delta\varepsilon_{vK}$: (a) Fragility Curve for Ratio Between Regression and FE Model Results; (b) Regression vs FE Model Results

5.8. Proposed Updated Design Procedure

As per Caltrans SDC[22], the collapse limit state in ductile bridge columns is defined by one of two strain limits in the Moment-Curvature analysis of the plastic hinge region: 1) crushing of the concrete core, and 2) fracture of the longitudinal reinforcement. Caltrans SDC[22] provides a step-by-step procedure for the design of fixed-base bridge columns which determines the collapse limit state using a monotonic Moment-Curvature analysis considering expected material properties and confinement of the concrete core, see Figure 5.33. Although the current prescribed design procedure includes a reduced ultimate strain limit for the longitudinal reinforcement, ε_u^R, this limit does not account for fracture due to

the plastic buckling-straightening fatigue. An update to the design procedure is therefore proposed to include considerations mitigating the effects of plastic buckling-straightening fatigue bar fracture in bridge columns.

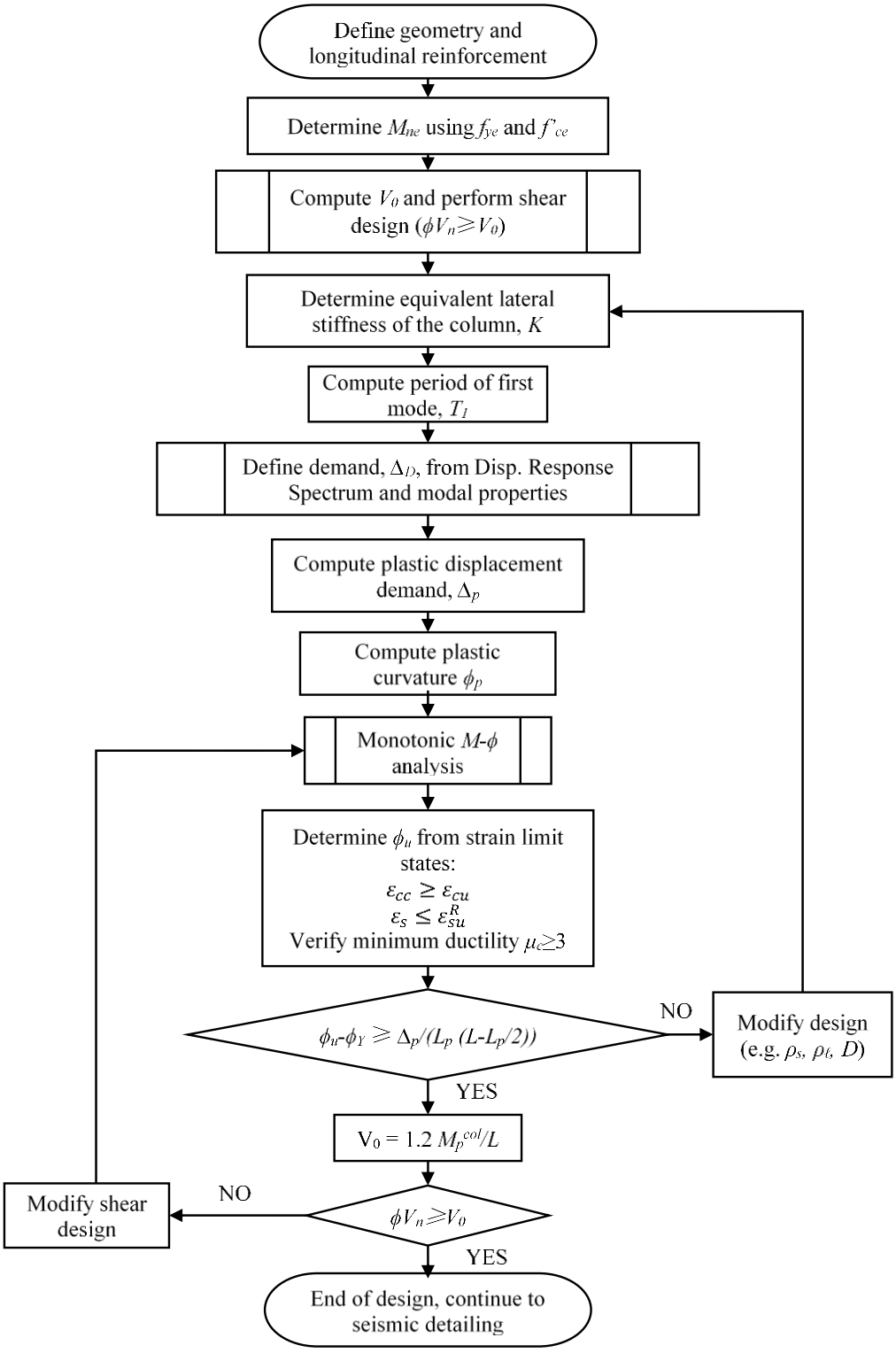

Figure 5.33. Design Flowchart for Ductile Cantilever Bridge Columns per Caltrans SDC, (Carreño et al., 2018)

The strain amplitudes (peak tensile to peak compressive strain) averaged over the plastic hinge length at the first cycle of displacement ductility 4 were obtained from experimental work presented in Chapters 3 and 4, see Figures 3.26-3.27 and 4.26-4.27 to simplify Equation 5.2. The average strain $\Delta\varepsilon_{t-c} = 3.6\%$ was found for the two specimens, with little variation between cycles to positive and negative displacements and between the two specimens. Equation 5.3 is derived by substituting $\Delta\varepsilon_{vK} = \Delta\varepsilon_{t-c}$ and $s/d_b = 4$ within Equation 5.2,

$$\rho_{s,PBSF} \geq 0.5 \cdot \rho_l \qquad 5.3$$

The tests described in Chapter 3 and 4 and used in the calibration of Equation 5.2 were tested with a prescribed loading protocol with symmetry in the applied displacements. To extend the concept, the displacement ductility used above should be understood as a mean displacement ductility (i.e. positive minus negative displacement ductilities over two), which can be used to capture column responses with unsymmetrical positive and negative lateral displacement demands (or displacement ductilities).

5.9. Validation of Proposed Design Procedure

As an independent validation for the proposed design method, results from the tests reported by Moyer and Kowalsky[66] are used. Moyer and Kowalsky tested four columns reinforced with Grade 60 reinforcing bars. Although all reinforcing steel was specified as ASTM A615 Grade 60 by the manufacturer, all the material specifications satisfied the criteria for ASTM A706 Grade 80 as well[72]. All test units were identically reinforced, with the only variable among the tests being the loading protocol, which is very advantageous for validating this proposed design procedure.

Each specimen consisted of a circular reinforced concrete column 18 in. (457 mm) in diameter with a height of 8 ft (2.44 m), reinforced longitudinally with 12 #6 (19 mm diameter) Grade 60 reinforcing bars, and #3 (9.5 mm diameter) spiral bars at 3 in. (76 mm) pitch for transverse reinforcement for a ratio of $s/d_b = 4$, see Figure 5.34. These specimens had a longitudinal reinforcement ratio of $\rho_l = 2.07\%$ and a volumetric ratio of transverse reinforcement of $\rho_s = 0.93\%$.

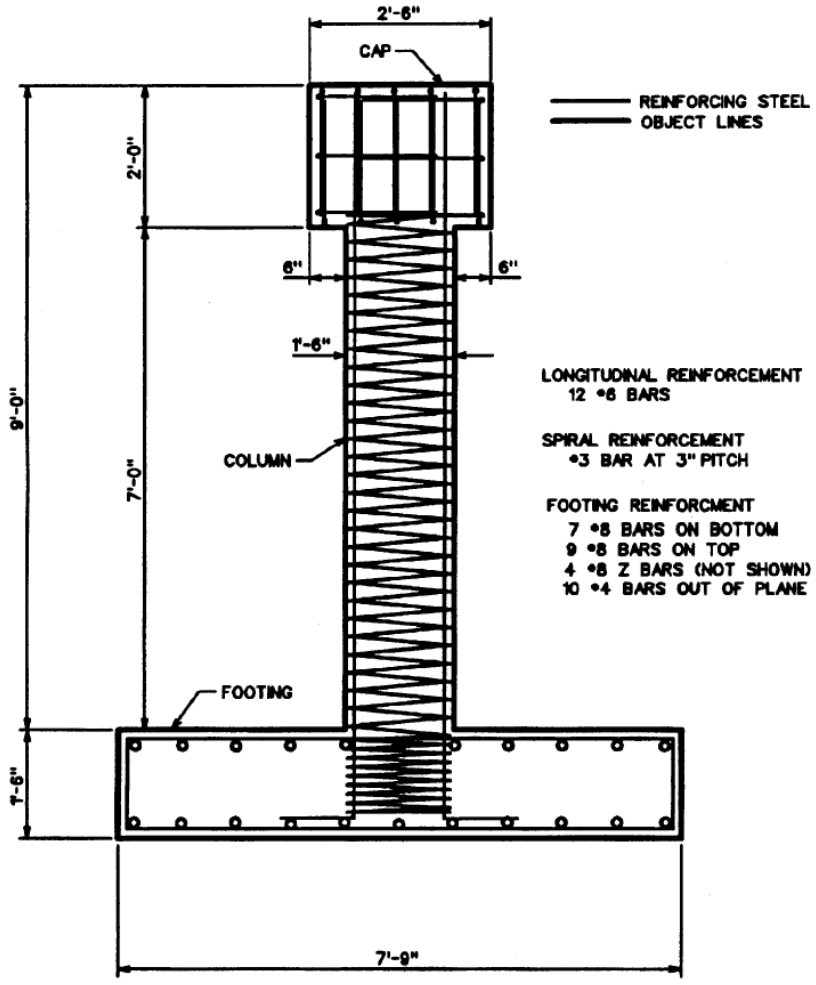

Figure 5.34. Typical Test Specimen Dimensions and Reinforcement Layout (Moyer and Kowalsky, 2003)

Test results from Unit 1 show that the column was able to sustain a displacement ductility of 4 prior to any observable bar buckling. The first bar buckling was observed after the third cycle of displacement ductility 4, as shown in the hysteretic response in Figure 5.35 where "X" marks approximately where buckling was first noted during the response. The specimen successfully attained a displacement ductility of +4 in one direction and -4 in the reverse direction prior to bar buckling.

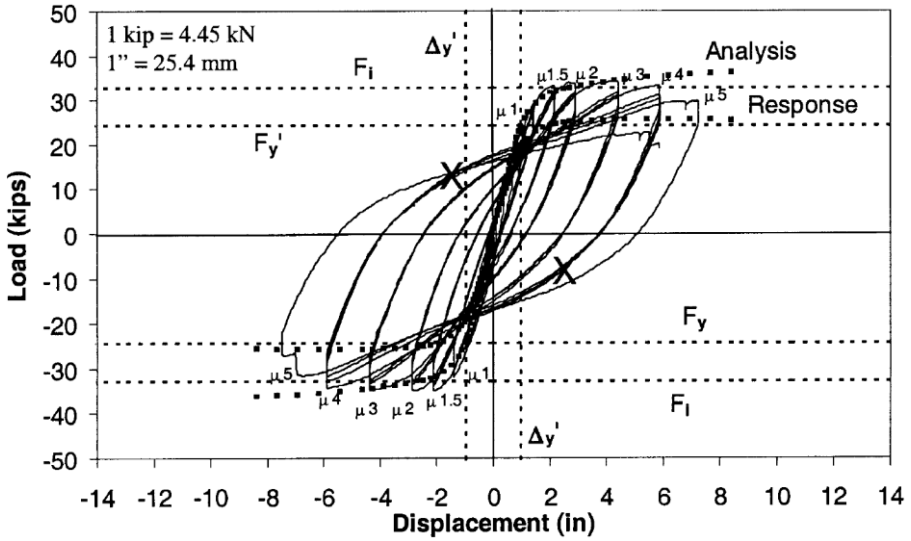

Figure 5.35. Force-Displacement Hysteretic Response of Unit 1 (Moyer and Kowalsky, 2003)

Results from Unit 2 show that the column was able to sustain a displacement ductility of 7 prior to any observable bar buckling. The first bar buckling was observed after the first cycle of displacement ductility 7, as shown in the hysteretic response in Figure 5.36. The specimen successfully attained a displacement ductility of +7 in one direction and bar buckling was observed upon the first return cycle afterwards.

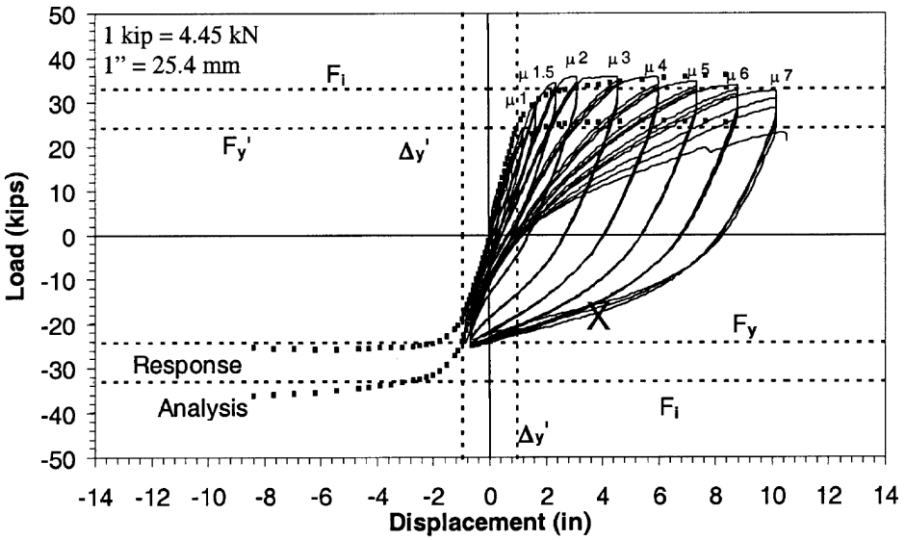

Figure 5.36. Force-Displacement Hysteretic Response of Unit 2 (Moyer and Kowalsky, 2003)

Unit 3 was able to sustain a deformation of equal amount in the opposing direction prior to bar buckling. The first bar buckling was observed after the reversal from the return cycle. The specimen successfully attained a displacement ductility of 7 in both directions after which the first bar buckling was observed, as presented in Figure 5.37.

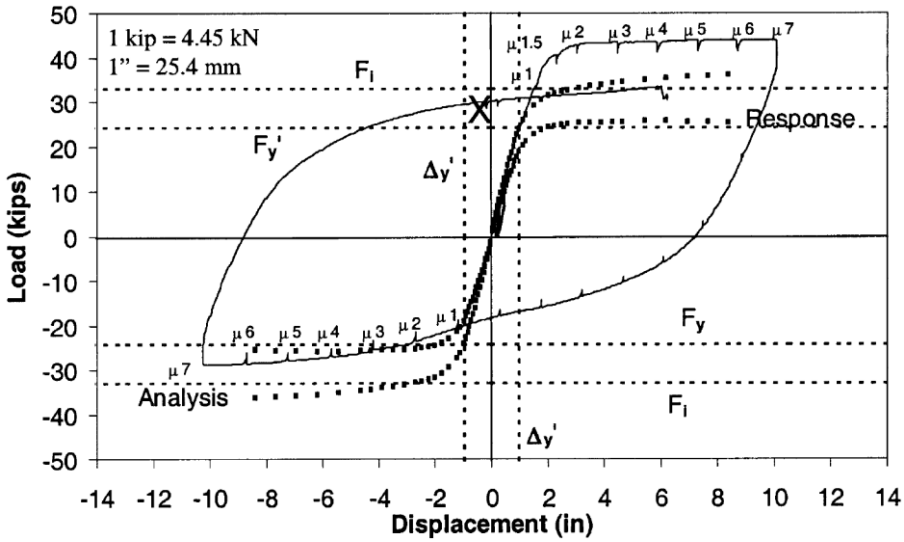

Figure 5.37. Force-Displacement Hysteretic Response of Unit 3 (Moyer and Kowalsky, 2003)

The loading protocol for Unit 4 was similar to Unit 3, except that the final displacement ductility level was increased from 7 to 9. First bar buckling was observed upon reversal from a displacement ductility of 9 prior to the point at which the cracks closed, see Figure 5.38.

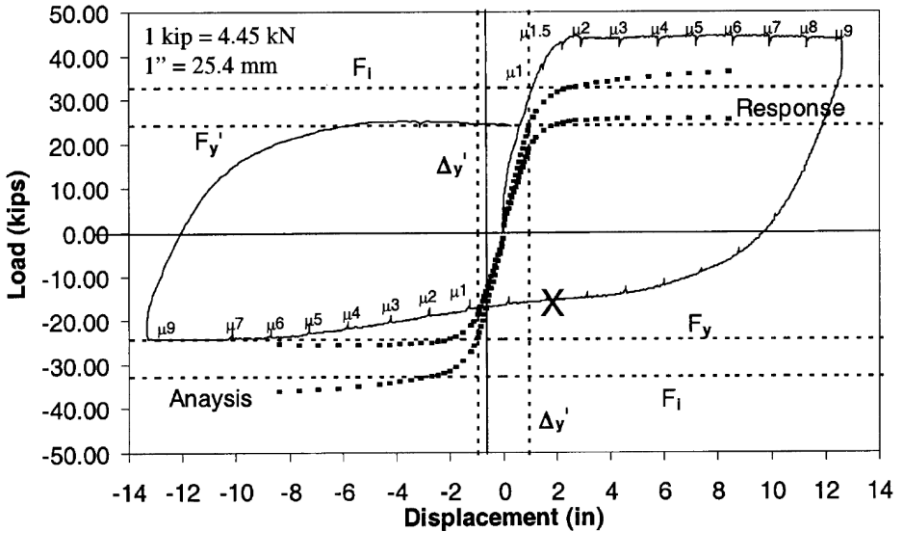

Figure 5.38. Force-Displacement Hysteretic Response of Unit 4 (Moyer and Kowalsky, 2003)

Using the expression provided in Equation 5.2 and the proposed strain amplitude of 3.6%, in conjunction with known design parameters ρ_l and s/d_b for these test units, the required volumetric reinforcement ratio to prevent premature bar buckling leading the fracture due to PBSF at a mean displacement ductility of 4 is found to be:

$$\left(\frac{\rho_s}{\rho_l}\right)_{PBSF,req} = 0.444 \qquad 5.4$$

The provided reinforcement ratio for these specimens is:

$$\left(\frac{\rho_s}{\rho_l}\right)_{Provided} = 0.449 \qquad 5.5$$

which is just slightly greater than the required reinforcement ratio. The provided reinforcement ratio being greater than the required reinforcement ratio predicts that these columns should not exhibit bar buckling prior to attaining a mean displacement ductility of 4. The mean displacement ductility attained in all test units are tabulated in Table 5.9. It is shown that except for Unit 3, the proposed design expression correctly predicts the mean displacement ductility a column can sustain prior to bar buckling. Unit 4 attained a mean displacement ductility slightly below the predicted value, which may not coincide with the definition of ε_{vK} which defines the onset of stress degradation. Furthermore, Unit 3 attained a greater displacement ductility than that predicted by the proposed equation, which further confirms the conservativeness of this proposed expression.

Table 5.9. Mean Displacement Ductility Levels Attained Prior to Bar Buckling (Moyer and Kowalsky, 2003)

	Displacement Ductility Level		
Unit	**Maximum**	**Minimum**	**Mean**
1	4	-4	4
2	7	-1	4
3	7	-7	7
4	9	1.8	3.6

Using this independent set of tests, the proposed design expression preventing premature bar buckling leading to fracture due to PBSF for circular columns is validated.

5.10. Summary and Conclusions

A series of cyclic tests with large strain amplitudes were performed on large diameter #14 ASTM A706 Grade 80 bars and newly developed #14 Grade 80 reinforcing

bars with a more smoothed-rib-radius. A total of four loading protocols were used in testing, the first being a variable strain amplitude protocol with increasing strain amplitudes, and the remaining three loading protocols were constant strain amplitude tests. Both bar types were tested with each loading protocol to properly characterize and compare the plastic buckling-straightening fatigue life of the bars. All specimens were tested with and unsupported length equal to $5d_b$ for consistency. Smeared strains were measured in all tests using an in-house design clip gage with a fixed gage length equal to half of the unsupported length of the test specimen. Results obtained from these tests show the gradual strength degradation of the bars due to the formation of compressive fatigue cracks developing at the base of the bar deformations. It is shown that bars with more smoothed-rib-radii can undergo more loading cycles and have longer fatigue life when compared with conventional ASTM A706 #14 Grade 80 bars, predominantly due to the delayed development and subsequent propagation of fatigue cracks leading to bar fracture. It is also shown that the strain amplitude plays a significant role in the fatigue life of bars, as the tests performed with a higher strain amplitude loading protocol showed that both types of bars endured substantially less cycles prior to fracture. These findings are in agreement with observations made in prior investigations.

The nonlinear finite element analysis framework developed by Carreño et al.[10] was adapted for Grade 80 reinforcement. A total of 176 unique column cage configurations representing the majority of commonly designed columns were modeled using both ASTM A706 Grade 80 and Grade 60 material properties. The models capture the behavior of column longitudinal reinforcing bars well beyond the onset of buckling, while taking into

consideration their interaction with the column hoops. The characteristic strain limit, $\Delta\varepsilon_{vK}$, defined as the strain amplitude between the maximum tensile strain and the strain at which maximum compressive stresses are exhibited on the bar, is determined to be the critical characteristic in plastic buckling-straightening fatigue life of column longitudinal bars. To confirm that the von Karman strain amplitude, $\Delta\varepsilon_{vK}$, is not influenced by the extreme tensile strain, a subset of analyses was performed with various maximum tensile strains. It is shown that the extreme tensile strain, thereby the loading protocol, has a negligible effect on the buckling response of the bars. A statistical analysis of the computational results showed that the characteristic strain limit, $\Delta\varepsilon_{vK}$, is highly correlated to the reinforcement configuration parameters s/d_b and ρ_s/ρ_l, as well as ε_{su}, the strain at ultimate strength of the reinforcing bars. An expression is developed from a regression analysis of the finite element model results to predict the von Karman strain amplitude, $\Delta\varepsilon_{vK}$. Lastly, a recommendation for design is proposed, which provides an expression to select the appropriate volumetric reinforcement ratio and transverse hoop spacing to prevent undesirable plastic buckling-straightening fatigue fracture of the column longitudinal reinforcement.

Chapter 5, in part, is currently being prepared for submission for publication of the material. Lotfizadeh, Koorosh H.; Carreño, Rodrigo; Restrepo, José I. The dissertation author was the primary investigator and author of this material.

Chapter 6.

CONCLUSIONS

The research presented in this dissertation focused on characterizing the behavior of ASTM A706 Grade 80 reinforcement and validating the use of prescriptive requirements in current design codes by extrapolation in seismic critical members of large civil infrastructure projects such as bridge substructures, power stations, and large mat footings. To that end, this research work was sub-divided in four tasks.

For the first task of this research, the development of high strength ASTM A706 Grade 80 large diameter (#14 and #18) bars in confined concrete is investigated. Four full-scale specimens, all entirely reinforced with A706 Grade 80 reinforcement, were built and tested to investigate the strain penetration and bar development of #14 and #18 size ASTM A706 Grade 80 bars embedded in well-confined concrete. These experiments confirmed that the extrapolation of current prescriptive requirements for the development of A706 Grade 80 reinforcement is satisfactory in design. Despite their significantly shorter development length than specified by SDC 2.0[22] and ACI 318-19[21], bars in all tests behaved desirably, were able to sustain significant inelastic strain and reach ultimate

strength without pulling out of the concrete. The bond stress-slip relationship of the test bars embedded in 5000 psi (34.5 MPa) and 8000 psi (55.2 MPa) concrete were also investigated. Some minor variation between the average bond stress for similar size bars embedded in concrete with different compressive strength is observed. However, due to the lack of data from more tests, no conclusions can be made regarding what the main variables causing this slight variation are.

The currently prescribed expression for calculating the analytical plastic hinge length of columns supported on footings or extended Type II pile shafts is updated and a simplified expression for the equivalent strain penetration term, normalized with respect to the reinforcement strength to allow its use for both ASTM A706 Grade 80 and Grade 60 reinforcement, is proposed.

A full-scale column extending into a Type II pile shaft, entirely reinforced with ASTM A706 Grade 80 bars is tested to investigate the behavior of high-strength large diameter reinforcement in the plastic hinge region of the column, as well as the non-contact splice region within the pile shaft. The test specimen was designed with a reduced embedment length of the column longitudinal bars into the pile shaft than prescribed requirements in current design codes when scaled and extrapolated to account for the use of Grade 80 reinforcement. The specimen behaved in a ductile manner and performed satisfactorily. A smeared-strain compatible approach is used to determine the equivalent strain penetration term for the test specimen, as well as two other columns tested in the past by Stephan et al.[39] and Schoettler et al.[8], and a statistical mean value for the equivalent strain penetration term lower than currently prescribed in design codes is obtained. Results

from this investigation validate future implementation of Grade 80 reinforcement in large civil infrastructure projects. Data obtained from this test was used to calibrate a detailed 3D nonlinear finite element model using commercially available software, ATENA® by Cervenka Consulting, which will prove useful for future predictive analyses.

Further validating the replacement of Grade 60 reinforcing bars with A706 Grade 80 in seismic bridge design, a proof-of-concept ¾-scale bridge column-bent cap connection was tested. The specimen was designed based on an existing bridge in California. The exterior column of a multi-column bent, reinforced entirely with ASTM A706 Grade 80 bars was chosen for this test due to the variable axial loads experienced in such columns. A unique hinge mechanism was used at the base of the column to ensure minimal bending moment resistance while properly transferring the required shear forces. The test specimen behaved satisfactorily with an extensive plastic hinge developing in the column beneath the bent cap, and minimal cracking in the column-bent cap joint. Results from this test show that bridge columns and bent caps reinforced with Grade 80 reinforcement, when detailed properly, perform in a ductile manner, and can achieve high drift ratios with negligible strength degradation.

With some modifications, the innovative sulfur-based bar gripping test apparatus designed by Duck et al.[40] was used to successfully perform first-of-its-kind cyclic testing of #14 size ASTM A706 Grade 80 reinforcing bars. The test results from this investigation provide the first successful experimental evaluation of the fatigue life of such large diameter high-strength reinforcement. Comparing the effect of compressive stress concentrations at the base of bar deformations during buckling, the same strain amplitude

loading protocol tests were performed on both conventional and commercially available ASTM A706 Grade 80 #14 bars, as well as the proposed and newly developed Grade 80 bars with a more smoothed rib radius. For consistency, all tests were performed with equal unsupported bar lengths of $5d_b$. Results from this set of experiments show a clear relation between the strength degradation of the bars due to the formation and propagation of compression fatigue cracks, with the geometric properties of the bar and the loading strain amplitude. Bars with more smoothed-rib-radii generally show longer fatigue life due to the delayed development and subsequent propagation of fatigue cracks. It is also shown that, both bar types tested with higher strain amplitude loading endured substantially less cycles prior to fracture.

The nonlinear finite element analysis framework developed by Carreño et al.[10] using the OpenSees analysis software platform[68] was used to assess the buckling behavior of column longitudinal reinforcing bars interacting with transverse hoops. A total of 176 uniquely defined column reinforcement cages representing the majority of commonly designed bridge columns were modeled using both ASTM A706 Grade 60 and Grade 80 material properties. From regression analysis, it is shown that the characteristic strain limit (von Karman strain amplitude, $\Delta\varepsilon_{vK}$) is highly correlated to the reinforcement configuration parameters s/d_b and ρ_s/ρ_l, as well as ε_{su}, the strain at ultimate strength of the reinforcing bars. An expression is provided to predict the von Karman strain amplitude, $\Delta\varepsilon_{vK}$, for columns with any reinforcement cage configuration. Lastly, a recommendation for design is proposed, which provides an expression to select the appropriate volumetric

reinforcement ratio and transverse hoop spacing to prevent undesirable plastic buckling-straightening fatigue fracture of the column longitudinal reinforcement.

REFERENCES

[1] American Association of State Highway and Transportation Officials (AASHTO) "AASHTO LRFD Bridge Design Specifications (8th Edition)," Washington, D.C., 2017.

[2] NZS 3101 "Concrete Structures Standard," *Standards New Zealand: Wellington*, 1995.

[3] NZS 3101 "The Design of Concrete Structures," *Standards New Zealand: Wellington*, 2006.

[4] Aoyama, H. "Design of Modern Highrise Reinforced Concrete Structures," v. vol. 3, London, United Kingdom, Imperial College Press, 2001.

[5] NEHRP Consultants Joint Venture "Use of high-strength reinforcement in earthquake-resistant concrete structures," Gaithersburg, MD, National Institute of Standards and Technology, 2014.

[6] Trejo, D., Barbosa, A. R., and Link, T. "Seismic performance of circular reinforced concrete bridge columns constructed with grade 80 reinforcement.," No. FHWA-OR-RD-15-02, 2014.

[7] Caltrans, S. "Caltrans Seismic Design Criteria Version 1.6," *California Department of Transportation, Sacramento*, 2010.

[8] Schoettler, M. J., Restrepo, J. I., and Guerrini, G. "A Full-Scale, Single-Column Bridge Bent Tested by Shake-Table Excitation," n.d., p. 153.

[9] Murcia-Delso, J., and Benson Shing, P. "Bond-Slip Model for Detailed Finite-Element Analysis of Reinforced Concrete Structures," *Journal of Structural Engineering*, V. 141, No. 4, 2015, p. 04014125.

[10] Carreño, R. "Characterization of Large Diameter Reinforcement Under Large Strain Cyclic Reversals." Doctoral Dissertation, University of California, San Diego, La Jolla, California, 2018.

[11] Kelly, D. J., Lepage, A., Mar, D., et al. "ATC-98 Project on Seismic Design of Concrete Structures with High-Strength Reinforcement," *Special Publication*, V. 313, 2017, pp. 1–10.

[12] Rautenberg, J. M., Pujol, S., Tavallali, H., et al. "Drift Capacity of Concrete Columns Reinforced with High-Strength Steel," *ACI Structural Journal*, V. 110, No. 2, 2013, p. 307.

[13] Tavallali, H., Lepage, A., Rautenberg, J. M., et al. “Concrete Beams Reinforced with High-Strength Steel Subjected to Displacement Reversals,” *ACI Structural Journal*, V. 111, No. 5, 2014.

[14] Cheng, M.-Y., Hung, S.-C., Lequesne, R. D., et al. “Earthquake-Resistant Squat Walls Reinforced with High-Strength Steel,” *ACI Structural Journal*, V. 113, No. 5, 2016.

[15] Barbosa, A. R., Link, T., and Trejo, D. “Seismic Performance of High-Strength Steel RC Bridge Columns,” *Journal of Bridge Engineering*, V. 21, No. 2, 2016, p. 04015044.

[16] Barbosa, A. R., Trejo, D., and Nielson, D. “Effect of High-Strength Reinforcement Steel on Shear Friction Behavior,” *Journal of Bridge Engineering*, V. 22, No. 8, 2017, p. 04017038.

[17] Barbosa, A. R., Trejo, D., Nielson, D., et al. “High strength reinforcing steel bars : low cycle fatigue behavior : final report - part B.,” No. FHWA-OR-RD-17-09, 2017.

[18] Overby, D., Kowalsky, M., and Seracino, R. “Stress-strain response of A706 grade 80 reinforcing steel,” *Construction and Building Materials*, V. 145, 2017, pp. 292–302.

[19] Sperry, J., Yasso, S., Searle, N., et al. “Conventional and High-Strength Hooked Bars—Part 1: Anchorage Tests,” *ACI Structural Journal*, V. 114, No. 1, 2016.

[20] Ghannoum, W. M., and Slavin, C. M. “Low-Cycle Fatigue Performance of High-Strength Steel Reinforcing Bars,” *ACI Materials Journal*, V. 113, No. 6, 2016.

[21] ACI Committee 318, and American Concrete Institute (ACI) “Building code requirements for structural concrete (ACI 318-19): an ACI standard and commentary on building code requirements for structural concrete (ACI 318R-19),” Farmington Hills, Michigan, American Concrete Institute, ACI, 2019.

[22] Caltrans (California Department of Transportation). “Caltrans Seismic Design Criteria (SDC), version 2.0.” Available at: http://www.dot.ca.gov/hq/esc/earthquake_engineering/sdc/documents/SDC2.0_April-2019_final.pdf. Accessed June 24, 2019.

[23] ASTM International. “ASTM A370-17 Standard Test Methods and Definitions for Mechanical Testing of Steel Products,” West Conshohocken, PA, 2017.

[24] ASTM International. “ASTM E8-16a Standard Test Methods for Tension Testing of Metallic Materials,” West Conshohocken, PA, 2016.

[25] Caltrans (California Department of Transportation). “California Test 670 Method of Tests for Mechanical and Welded Reinforcing Steel Splices,” Sacramento, CA, California Department of Transportation (Caltrans), 2013.

[26] Mander, J. B. “Seismic Design of Bridge Piers.” Doctoral Dissertation, University of Canterbury, Christchurch, New Zealand, 1983.

[27] ASTM International. “ASTM C192-18 Standard Practice for Making and Curing Concrete Test Specimens in the Laboratory,” West Conshohocken, PA, 2018.

[28] ASTM International. “ASTM C617-15 Standard Practice for Capping Cylindrical Concrete Specimens,” West Conshohocken, PA, 2015.

[29] ASTM International. “ASTM C39-18 Standard Test Method for Compressive Strength of Cylindrical Concrete Specimens,” West Conshohocken, PA, 18.

[30] ASTM International. “ASTM C496-17 Standard Test Method for Splitting Tensile Strength of Cylindrical Concrete Specimens,” West Conshohocken, PA, 2017.

[31] Metelli, G., and Plizzari, G. A. “Influence of the relative rib area on bond behaviour,” *Magazine of Concrete Research*, V. 66, No. 6, 2014, pp. 277–94.

[32] Murcia-Delso, by J., Stavridis, A., and Shing, P. B. “Tension Development Length of Large-Diameter Bars for Severe Cyclic Loading,” *ACI Structural Journal*, V. 112, No. 6, 2015.

[33] Alavi-Fard, M., and Marzouk, H. “Bond behavior of high strength concrete under reversed pull-out cyclic loading,” *Canadian Journal of Civil Engineering*, V. 29, No. 2, 2002, pp. 191–200.

[34] BS8110, B. “Structural Use of Concrete, Part 1: Code of Practice for Design and Construction,” *British Standards Institution, UK*, 1985.

[35] Park, R., and Paulay, T. “Strength and Ductility of Concrete Substructures of Bridges.” vol. 1. Christchurch, New Zealand, Road Research Unit, Transit New Zealand, 1990. p. 30.

[36] Priestley, M. J. N., Seible, F., Calvi, G. M., et al. “Seismic Design and Retrofit of Bridges,” John Wiley & Sons, 1996, 704 pp.

[37] Lepage, A., Huq, M. S., Weber-Kamin, A. S., et al. “High-Strength Steel Bars in Earthquake-Resistant T-Shaped Concrete Walls,” The University of Kansas Center for Research Inc., Lawrence, Kansas, 2018.

[38] Sokoli, D., Limantono, A., and Ghannoum, W. M. “Plasticity Spread in Columns Reinforced With High Strength Steel.” vol. Paper #234. Santiago, Chile, Pankow Foundation, 2017. p. 11.

[39] Stephan, B., Restrepo, J., and Seible, F. “Seismic Behavior of Bridge Columns Built Incorporating MMFX Steel,” La Jolla, California, University of California, San Diego, 2003.

[40] Duck, D. E., Carreño, R., and Restrepo, J. I. “Plastic Buckling-Straightening Fatigue of Large Diameter Reinforcing Steel Bars,” La Jolla, California, University of California, San Diego, 2018.

[41] Lukose, K., Gergely, P., and White, R. N. “Behavior of Reinforced Concrete Lapped Splices for Inelastic Cyclic Loading,” *ACI Journal Proceedings*, V. 79, No. 5, 1982.

[42] Sagan, V. E., Gergely, P., and White, R. N. “Behavior and Design of Noncontact Lap Splices Subjected to Repeated Inelastic tensile loading,” *ACI Structural Journal*, V. 88, No. 4, 1991.

[43] McLean, D. I., and Smith, C. L. “Noncontact Lap Splice in Bridge Column-Shaft Connections,” Washington State University, Pullman, WA, Washington State Transportation Center, 1997.

[44] Tran, H. V., Stanton, J. F., and Eberhard, M. O. “Precast Bent System for High Seismic Regions: Laboratory Tests of Column-to-Drilled Shaft Socket Connections,” Federal Highway Administration, 2013.

[45] Murcia-Delso, J., Liu, Y., and Shing, P. B. “Development of Bridge Column Longitudinal Reinforcement in Oversized Pile Shafts,” *Journal of Structural Engineering*, V. 142, No. 11, 2016, p. 04016114.

[46] ASTM International. “ASTM C469-14 Standard Test Method for Static Modulus of Elasticity and Poisson’s Ratio of Concrete in Compression,” West Conshohocken, PA, 2014.

[47] ACI Committee 318, and American Concrete Institute (ACI) “Building code requirements for structural concrete (ACI 318-14): an ACI standard and commentary on building code requirements for structural concrete (ACI 318R-14),” Farmington Hills, Michigan, American Concrete Institute, ACI, 2014.

[48] Vásquez, V. A. “Detailed Finite Element of a Type II Bridge Column Shaft Reinforced with High-Strength Steel.” Thesis, University of California, San Diego, La Jolla, California, 2019.

[49] Priestley, M. J. N. “Myths and Fallacies in Earthquake Engineering, Revisited The Ninth Mallet Milne Lecture, 2003,” n.d., p. 98.

[50] Caltrans (California Department of Transportation). “Bridge Design Specifications Manual,” Sacramento, CA, 2002.

[51] Vos, E. “Influence of Loading Rate and Radial Pressure on Bond in Reinforced concrete. A Numerical and Experimental Approach,” Delft, Netherlands, Delft University Press, 1983.

[52] CEB-FIP. “CEB-FIP Model Code 1990 Design Code,” *Comite Euro International du Beton*, 1990.

[53] Vecchio F. J., and Collins M. P. “Compression Response of Cracked Reinforced Concrete,” *Journal of Structural Engineering*, V. 119, No. 12, 1993, pp. 3590–610.

[54] Havlasek, P., and Kabele, P. “A detailed description of the computer implementation of SHCC material model in OOFEM.,” Prague, Czech Republic, Czech Technical University in Prague, 2017.

[55] Cervenka, J., Cervenka, V., and Laserna, S. “On crack band model in finite element analysis of concrete fracture in engineering practice,” *Engineering Fracture Mechanics*, V. 197, 2018, pp. 27–47.

[56] Cervenka, V., Jendele, L., and Cervenka, J. “ATENA program documentation, Part 1: Theory,” *Cervenka Consulting, Prague*, 2018.

[57] Cervenka, V., Cervenka, J., Pukl, R., et al. “Prediction of Shear Failure of Large Beams Based on Fracture Mechanics.” Proceedings of the 9th International Conference on Fracture Mechanics of Concrete and Concrete Structures. Prague, Czech Republic, 2016.

[58] Nakamura, H., and Higai, T. “Compressive Fracture Energy and Fracture Zone Length of Concrete,” 2001, pp. 471–87.

[59] Jansen, D. C., and Shah, S. P. “Effect of Length on Compressive Strain Softening of Concrete,” *Journal of Engineering Mechanics*, V. 123, No. 1, 1997, pp. 25–35.

[60] Van Mier, J. G. M. “Strain-Softening of Concrete Under Multiaxial Loading Conditions,” Netherlands, Eindhoven University of Technology, Netherlands, 1984.

[61] Collins, M. P., and Mitchell, D. “Prestressed Concrete Structures,” v. vol. 9, Prentice Hall Englewood Cliffs, NJ, 1991.

[62] Bigaj, A. J. “Structural Dependence of Rotation Capacity of Plastic Hinges in RC Beams and Slabs,” *Delft University of Technology, Netherlands*, 1999.

[63] Tanaka, H. “Effect of lateral confining reinforcement on the ductile behaviour of reinforced concrete columns.” University of Canterbury, New Zealand, 1990.

[64] Zahn, F. A. “Design of reinforced concrete bridge columns for strength and ductility.” University of Canterbury, New Zealand, 1985.

[65] Rodriguez, M. E., Botero, J. C., and Villa, J. “Cyclic Stress-Strain Behavior of Reinforcing Steel Including Effect of Buckling,” *Journal of Structural Engineering*, V. 125, No. 6, 1999, pp. 605–12.

[66] Moyer, M. J., and Kowalsky, M. J. “Influence of tension strain on buckling of reinforcement in concrete columns,” *ACI Structural Journal*, V. 100, No. 1, 2003, pp. 75–85.

[67] Restrepo-Posada, J. I. “Seismic behaviour of connections between precast concrete elements,” *University of Canterbury, Christchurch, New Zealand*, 1993.

[68] McKenna, F., Fenves, G. L., and Scott, M. H. “Open system for earthquake engineering simulation,” *University of California, Berkeley, CA*, 2000.

[69] Dodd, L. L., and Restrepo-Posada, J. I. “Model for Predicting Cyclic Behavior of Reinforcing Steel,” *Journal of Structural Engineering*, V. 121, No. 3, 1995, pp. 433–45.

[70] Crisfield, M. A. “Non-linear finite element analysis of solids and structures,” Wiley, 1997.

[71] Restrepo-Posada, J. I., Dodd, L. L., Park, R., et al. “Variables Affecting Cyclic Behavior of Reinforcing Steel,” *Journal of Structural Engineering*, V. 120, No. 11, 1994, pp. 3178–96.

[72] Kowalsky, M. “Personal Communication,” 2019.